

UNIVERSITY OF SÃO PAULO
POLYTECHNIC SCHOOL
DEPARTMENT OF NAVAL AND OCEAN ENGINEERING

CEZAR AUGUSTO BELLEZI

STUDIES OF NONLINEAR HYDRODYNAMICS BASED ON MOVING
PARTICLES SEMI-IMPLICIT METHOD:
DEVELOPMENT AND APPLICATIONS

Revised Version

São Paulo

2020

CEZAR AUGUSTO BELLEZI

**STUDIES OF NONLINEAR HYDRODYNAMICS BASED ON MOVING
PARTICLES SEMI-IMPLICIT METHOD:
DEVELOPMENT AND APPLICATIONS**

Revised Version

(versão original encontra-se na unidade que aloja o Programa de Pós-graduação)

(original version is located in the unit of the Graduate Program)

Thesis submitted to the Polytechnic School of
Engineering of the University of São Paulo for
the partial fulfillment of the requirements for the
degree of Doctor of Science

Supervisor: Prof. Dr. Cheng Liang-Yee

São Paulo

2020

Autorizo a reprodução e divulgação total ou parcial deste trabalho, por qualquer meio convencional ou eletrônico, para fins de estudo e pesquisa, desde que citada a fonte.

Este exemplar foi revisado e corrigido em relação à versão original, sob responsabilidade única do autor e com a anuência de seu orientador.

São Paulo, _____ de _____ de _____

Assinatura do autor: _____

Assinatura do orientador: _____

Catálogo-na-publicação

Bellezi, Cezar Augusto

Studies of nonlinear hydrodynamics based on Moving Particles Semi Implicit method: development and applications / C. A. Bellezi -- versão corr. -- São Paulo, 2020.
270 p.

Tese (Doutorado) - Escola Politécnica da Universidade de São Paulo. Departamento de Engenharia Naval e Oceânica.

1.Dinâmica dos fluídos computacional 2.Hidrodinâmica não-linear 3.Método de partículas 4.Sloshing 5.Gap effect I.Universidade de São Paulo. Escola Politécnica. Departamento de Engenharia Naval e Oceânica II.t.

*I dedicate this thesis to my wife Regina, for
her companionship, love and patience.*

ACKNOWLEDGEMENTS

I would like to express my sincere gratitude to prof. Cheng Liang-Yee, who has been supervising my scientific activities since the undergraduate level for more than ten years. I am grateful for his support, guidance, knowledge and patience during the development of this thesis. Foremost, I owe to him the enthusiasm for the knowledge and discovery and the virtues that a researcher should have.

Besides, I am grateful to prof. Dr. Kazuo Nishimoto, my advisor during the first part of the doctorate, for the numerous opportunities and enthusiasm. I am also indebted to prof. Dr. Makoto Arai, from the Yokohama National University (YNU), who gave me the opportunity to experience research abroad for two brief spells and first suggested the practical application cases which were studied in the present work.

I am very thankful to the current and former members that contributed to the MPS group of the Numerical Offshore Tank (TPN) laboratory during the past five years, especially to Dr. Fabio Kenji Motezuki and MSc. Rubens Augusto Amaro Junior for the fruitful discussions and partnership. A special thanks to Dr. Marcio Michiharu Tsukamoto, who provided valuable assistance during the development of the multi-resolution MPS technique.

Furthermore, I would like to extend my gratitude to the members of the Thesis Defense Committee by their valuable suggestions and careful review of the present work, which greatly improved the revised version of this Thesis. Namely, Prof. Dr. Celso Kazuyuki Morooka, from the State University of Campinas (UNICAMP), Prof. Dr. Celso Pupo Pesce, from the Polytechnic School of the University of São Paulo

(USP), prof. Dr. José Luis Drummond Alves, from the Federal University of Rio de Janeiro (UFRJ) and Prof. Dr. Joel Roberto Guimarães Vasco, from the Federal University of Goiás (UFG).

Finally, I am most grateful to my family, who gave me all the support during this very long academic journey full of difficult moments. To my wife Regina, my mother Diva, my father Augusto and my sister Larissa.

This work had financial support from Coordenação de Aperfeiçoamento de Pessoal de Nível Superior – Brasil (CAPES) – Finance Code 001.

This work was partially funded by the Office of Naval Research Global (ONRG) – Grant number N62909-16-1-2181.

ABSTRACT

BELLEZI, Cezar Augusto. **STUDIES OF NONLINEAR HYDRODYNAMICS BASED ON MOVING PARTICLES SEMI-IMPLICIT METHOD: Development and Applications.** Revised Version. 2020. 270 p. Doctorate (Thesis) – Department of Naval and Ocean Engineering, Polytechnic School, University of São Paulo, São Paulo, 2020.

The present work is focused on the development and application of the Moving Particles Semi-Implicit (MPS) method to the investigation of complex nonlinear hydrodynamics problems in naval and offshore engineering. This work is divided into three different studies that share this background and each one presents its own original contribution:

PART 1: The first study consists in the proposal of a perforated swash bulkhead with optimized geometry in order to mitigate the sloshing in rectangular tanks. The first step of the investigation comprises the assessment of the effects of the bulkhead open-area ratio in the sloshing flow based on a comprehensive parameter analysis. Then, a function of the optimized open-area ratio as function of the filling ratio is proposed. Three different swash bulkhead models with optimized geometry are evaluated and successfully mitigated the sloshing resonance in the frequency range encompassing the three first sloshing resonant modes for different filling ratios. This investigation resulted in technological innovation, as a highly effective engineering solution with simple implementation was achieved.

PART 2: In the second study, the resonance within narrow gaps between naval and offshore structures is investigated by MPS simulations. It consists on a parameter analysis of a simplified two-dimensional barge with imposed harmonic sway motion. Different widths of the gap, motion frequencies and amplitudes were considered. Two different resonant modes in the gap were observed from the particle-based simulations:

the piston-mode and the sloshing-mode. In particular, two peaks in the frequency domain were observed for the piston-mode resonant flow. The behavior of the second peak resembled a syphon U-tube flow and it was not previously reported in the literature. Then, two simple mechanical models, with 1 DOF and 2 DOF were adopted in order to explain these two peaks.

PART 3: In the third study of this thesis, a multiresolution technique called “border mapping” is proposed for the MPS method. The border mapping technique aims to obtain an “equivalent particle distribution” in the truncated boundary between two sub-domains with different resolutions and it is divided into two steps: the refinement of the coarse region of the border and the simplification of the fine region of the border. The main aspect of the proposed approach is to use the actual irregular particle distribution in the border region, which enhances the numerical stability. The preliminary tests of the proposed technique were promising, as the pressure was correctly calculated, the mass of the system was properly conserved and the computational cost could be substantially reduced in relation to a single-resolution simulation. This study is a contribution to the state-of-the-art of the meshless methods in computational fluid dynamics.

Keywords: nonlinear hydrodynamics, computational fluid dynamics, particle-based method, multiresolution, hydrodynamic impact, sloshing, gap resonance.

RESUMO

BELLEZI, Cezar Augusto. **ESTUDOS EM HIDRODINÂMICA NÃO-LINEAR POR MÉTODO MOVING PARTICLES SEMI-IMPLICIT**: Desenvolvimento e Aplicações. Versão Revisada. 2020. 270 f. Doutorado (Tese) – Departamento de Engenharia Naval e Oceânica, Escola Politécnica, Universidade de São Paulo, São Paulo, 2020.

Esta tese foca-se no desenvolvimento e aplicação do método de partículas Moving Particles Semi-Implicit (MPS) para a investigação de complexos problemas de hidrodinâmica não-linear no contexto da engenharia naval e oceânica. A mesma é dividida em três diferentes trabalhos que partilham deste contexto, sendo que cada trabalho apresenta suas próprias contribuições originais:

PARTE 1: O primeiro estudo da presente tese consiste na proposta de uma geometria otimizada de antepara perfurada para a mitigação do fenômeno de sloshing em tanques retangulares. Investigou-se os efeitos da razão de abertura das anteparas perfuradas no fenômeno de sloshing por meio de uma abrangente análise paramétrica. Com base nos resultados obtidos, é proposta uma relação de razão de abertura otimizada em função do nível de preenchimento. Três modelos de antepara com geometria otimizada são então testados com sucesso para a mitigação de sloshing a diferentes níveis de preenchimento para frequências englobando os três primeiros modos de ressonância do fenômeno de sloshing. Trata-se de um estudo que resultou em inovação tecnológica, ao propor uma solução em engenharia bastante efetiva e de simples implementação.

PARTE 2: No segundo estudo, o método de partículas foi empregado na investigação do fenômeno de ressonância de fluido confinado entre estruturas próximas, conhecido como “gap effect”. É realizada uma análise paramétrica do fenômeno de ressonância no gap em modelos bidimensionais de uma barcação com movimento harmônico imposto de “sway”. Gaps com diferentes dimensões e movimentos com diferentes frequências e

amplitudes foram considerados. As simulações numéricas capturam os diferentes modos de ressonância no gap: o modo pistão e modo sloshing. Dois diferentes picos no domínio da frequência foram observados para a ressonância no modo pistão. O segundo deles se assemelha a um escoamento em tubo em U, o qual não havia sido previamente reportado na literatura. Por fim, o comportamento do escoamento em cada um deles foi explicado por uma analogia a sistemas mecânicos simples, um com 1 e outro com 2 graus de liberdade.

PARTE 3: No terceiro estudo, propôs-se uma nova técnica multirresolução para o método de partículas denominada técnica de “mapeamento da borda”. A técnica de mapeamento da borda consiste em obter distribuições de partícula equivalentes em cada lado da fronteira truncada entre dois sub-domínios de resoluções diferentes, a qual pode ser dividida em duas etapas: o “refinamento” da borda de baixa-resolução e a “simplificação” da borda de alta-resolução. Diferentemente de outras técnicas propostas na literatura, o mapeamento baseia-se na atual distribuição irregular de partículas na região de borda, o que aumenta a estabilidade numérica. Os testes preliminares da técnica proposta mostram que a pressão pode ser calculada adequadamente, os algoritmos do mapeamento conservam a massa do sistema e o tempo de processamento pode ser significativamente reduzido em relação às simulações de resolução única. Este estudo é uma contribuição ao estado-da-arte dos métodos sem malhas para dinâmica dos fluidos computacional.

Palavras-chave: hidrodinâmica não-linear, dinâmica dos fluidos computacional, método de partículas, multirresolução, impacto hidrodinâmico, sloshing, ressonância em gap.

LIST OF FIGURES

| | |
|---|----|
| Figure 1.1 – (a) Global energy demand share and (b) Regional supply of liquid energy sources | 29 |
| Figure 1.2 – Track record of Brazilian oil production per environment | 30 |
| Figure 1.3 – Wave impact phenomena on floating offshore structures..... | 31 |
| Figure 1.4 – Snapshots of a MPS simulation of green water phenomenon | 34 |
| Figure 1.5 – Sloshing in prismatic tank – MPS simulation x experiment..... | 35 |
| Figure 2.1 – Duration of numerical and physical impulsive phenomenon | 51 |
| Figure 2.2 – Sketch of the neighborhood of a fluid particle..... | 56 |
| Figure 2.3 – Sketch of the modeling of the free solid..... | 57 |
| Figure 2.4 – Flowchart of the MPS method algorithm..... | 59 |
| Figure 3.1– Main dimensions and the positions of the pressure probes of the validation case with perforated baffle (based on Xue et al (2017))..... | 69 |
| Figure 3.2 – Pressure time series for the tank with perforated baffle– $\omega = 1.32\omega_1$, $A = 0.01m$ – computed results and experimental data (Xue, Zheng, Lin, & Yuan, 2017) | 71 |
| Figure 3.3 – Maximum dynamic pressure as a function of motion frequency: computed results and experimental data (Xue, Zheng, Lin, & Yuan, 2017) | 72 |
| Figure 3.4 – Configuration and main dimension of the tank models..... | 74 |
| Figure 3.5 – Swash bulkhead perforation arrangement – Model A..... | 75 |
| Figure 3.6 – Swash bulkhead perforation arrangement – Model B..... | 75 |
| Figure 3.7 – Swash bulkhead perforation arrangement – Model C..... | 76 |
| Figure 3.8 – Numerical tank: center of rotation and location of the probes (dimensions in mm)..... | 78 |
| Figure 3.9 – Typical sloshing resonant modes | 79 |

| | |
|---|----|
| Figure 3.10 - Time series of free surface height on (left) tank left wall ($H1$) and (right) bulkhead left wall ($H2$): first mode of sloshing motion ($n1$)..... | 82 |
| Figure 3.11 – Time series of free surface height on (left) tank left wall ($H1$) and (right) bulkhead left wall ($H2$): second mode sloshing motion ($n2$)..... | 84 |
| Figure 3.12 – Dimensionless amplitude of free surface elevation in the tank wall ($H1$) in the frequency domain, pitch motion, $\theta = 6^\circ$ | 85 |
| Figure 3.13 - Dimensionless longitudinal dynamic force in the frequency domain, pitch motion, $\theta = 6^\circ$ | 86 |
| Figure 3.14 - Dimensionless amplitude of free surface elevation in the tank wall ($H1$) in the frequency domain, surge motion, $A = 1\% \times L$ | 87 |
| Figure 3.15 - Dimensionless longitudinal dynamic force in the frequency domain, surge motion, $A = 1\% \times L$ | 88 |
| Figure 3.16 – Frequency of the first ($n1$) and the second resonant peak ($n2$) as a function of submerged open area ratio | 90 |
| Figure 3.17 – Dimensionless longitudinal dynamic force as a function of the excitation frequency, pitch motion – Model P0 and Model P100 | 93 |
| Figure 3.18 – Dimensionless longitudinal dynamic force as a function of the excitation frequency, pitch motion – A2x2-C-P11 and A2x2-C-P69..... | 94 |
| Figure 3.19 – Dimensionless longitudinal dynamic force as a function of the excitation frequency, surge motion – Model P0 and Model P100 | 95 |
| Figure 3.20 – Dimensionless longitudinal dynamic force as a function of the excitation frequency, surge motion – A2x2-C-P11 and A2x2-C-P69..... | 96 |
| Figure 3.21 – Open area ratios as a function of filling level – comparison considering circular and square shaped holes | 98 |
| Figure 3.22 – Time series of pressure at probe P1 (filtered) – first mode ($n1$): $hH = 25\%$, $f = 0.675Hz$, $\theta = 6^\circ$ – comparison considering circular and square shaped holes..... | 99 |

| | |
|--|-----|
| Figure 3.23 – Longitudinal dynamic force as function of the frequency, $\theta = 60^\circ$ – comparison considering circular and square shaped | 100 |
| Figure 3.24 – Open area ratios as a function of filling ratio – comparison considering different hole arrangements | 101 |
| Figure 3.25 – Time series of pressure at probe P1 (filtered) – first mode ($n1$): $hH = 25\%$, $f = 0.675Hz$, $\theta = 60^\circ$ – comparison considering different hole arrangements | 102 |
| Figure 3.26 – Longitudinal dynamic force as function of excitation frequency, $\theta = 60^\circ$ – comparison considering different hole arrangements | 103 |
| Figure 3.27 – Surge added mass coefficient ($Ca, 11$) in the frequency domain, surge motion, $A = 1\% \times L$ | 107 |
| Figure 3.28 – Surge damping coefficient ($Cb, 11$) in the frequency domain, surge motion, $A = 1\% \times L$ | 108 |
| Figure 3.29 – Dimensionless longitudinal dynamic force of the first ($n1$) and second resonant peak ($n2$) as functions the open area ratio, pitch motion..... | 112 |
| Figure 3.30 – Dimensionless free surface elevation of the first ($n1$) and second resonant peak ($n2$) as functions of the open area ratio, pitch motion | 113 |
| Figure 3.31 – Dimensionless longitudinal dynamic force of the first ($n1$) and second resonant peak ($n2$) as functions the open area ratio, surge motion | 114 |
| Figure 3.32 – Dimensionless free surface elevation of the first ($n1$) and second resonant peak ($n2$) as functions of the open area ratio, surge motion..... | 115 |
| Figure 3.33 – Optimum open area ratios for sloshing mitigation as a function of the filling ratio hL , pitch motion..... | 118 |
| Figure 3.34 – Optimum open area ratios for sloshing mitigation as a function of the filling ratio hL , surge motion..... | 118 |
| Figure 3.35 – Geometry of the models of bulkheads with optimum open area ratio... | 121 |

| | |
|--|-----|
| Figure 3.36 – Relation between open area ratio distribution of the optimized swash bulkheads and the filling level | 122 |
| Figure 3.37 – Snapshots of particle simulation – $hL = 0.167$, non-compartmented first mode ($n1$) | 123 |
| Figure 3.38 – Snapshots of particle simulation – $hL = 0.5$, compartmented second mode ($n2$) | 124 |
| Figure 3.39 – Optimized swash bulkheads: dimensionless free surface elevation in frequency domain..... | 126 |
| Figure 3.40 – Diagram of the dimensionless longitudinal dynamic force in the tank in the frequency domain: optimized..... | 127 |
| Figure 3.41 – Diagram of the dimensionless longitudinal dynamic force in the tank in the frequency domain – analysis of scaling effects..... | 130 |
| Figure 4.1 – Sketch of the two-dimensional modeling of the problem | 141 |
| Figure 4.2 – Dimensions of the validation model..... | 144 |
| Figure 4.3 – Time series of free surface elevation at wave probe: $h_0 = 20cm$ (experimental data from Maisondieu et al. (2001))..... | 145 |
| Figure 4.4 – (a) Time series of the free surface elevation at probe and (b) FFT of the free surface elevation: $h_0 = 15cm$, $\Delta h = 10cm$ (experimental data from Maisondieu et al. (2001)), 0-th order gradient model..... | 146 |
| Figure 4.5 – (a) Time series of the free surface elevation at probe and (b) FFT of the free surface elevation: $h_0 = 15cm$, $\Delta h = 10cm$ (experimental data from Maisondieu et al. (2001)), 1-st order gradient model | 146 |
| Figure 4.6 – Dimensions of the numerical model of the parameter analysis..... | 150 |
| Figure 4.7 – Dimensionless free surface elevation height in relation to sway period: convergence analysis – $L_{gap} = 10m$, $Asway = 0.05 \times B$ | 153 |
| Figure 4.8 – Time series of the free surface elevation: convergence analysis - $L_{gap} = 10m$, $Asway = 0.05 \times B$, 1-st order gradient model. | 154 |

| | |
|--|-----|
| Figure 4.9 – Dimensionless free surface height as function of the particle resolution - $L_{gap} = 10m$, $A_{sway} = 0.05 \times B$, 1-st order gradient model..... | 155 |
| Figure 4.10 – Time series of free surface elevation in the barge right wall (left) and its FFT (right) for 32 cycles of sway motion – $L_{gap} = 50m$, $A_{sway} = 0.05 \times B$ | 157 |
| Figure 4.11 – Contour map of the dimensionless wave height as function of the length of the gap and the sway period | 159 |
| Figure 4.12 – Snapshots of the particle simulation – $L_{gap} = 10m$, $T = 13.0s$, $A_{sway} =$ $0.05 \times B$ | 161 |
| Figure 4.13 – Free surface profile and envelope – $L_{gap} = 10m$, $T = 13.0s$, $A_{sway} =$ $0.05 \times B$ | 162 |
| Figure 4.14 – Snapshots of the particle simulation – $L_{gap} = 60m$, $T = 9.0s$, $A_{sway} =$ $0.05 \times B$ | 164 |
| Figure 4.15 – Snapshots of the particle simulation – $L_{gap} = 60m$, $T = 6.25s$, $A_{sway} =$ $0.05 \times B$ | 165 |
| Figure 4.16 – Free surface profile and envelope – $L_{gap} = 60m$, $T = 9.0s$, $A_{sway} =$ $0.05 \times B$ | 166 |
| Figure 4.17 – Free surface profile and envelope – $L_{gap} = 60m$, $T = 6.25s$, $A_{sway} =$ $0.05 \times B$ | 166 |
| Figure 4.18 – Dimensionless free surface elevation height in relation to sway period: piston mode flow..... | 168 |
| Figure 4.19 – (a) Amplitude of the crest ($\Delta h +$) and the trough ($\Delta h -$) of the free surface elevation and (b) phase of free surface elevation at barge wall as function of the sway period – $L = 10m$ | 169 |
| Figure 4.20 – (a) Amplitude of the crest ($\Delta h +$) and the trough ($\Delta h -$) of the free surface elevation and (b) phase of free surface elevation at barge wall as function of the sway period – $L = 12m$ | 170 |

| | |
|--|-----|
| Figure 4.21 – (a) Amplitude of the crest ($\Delta h +$) and the trough ($\Delta h -$) of the free surface elevation and (b) phase of free surface elevation at barge wall as function of the sway period – $L = 14m$ | 171 |
| Figure 4.22 – Layout and coordinates of (a) the U-tube mechanical model and (b) the equivalent model for the piston-flow in the gap..... | 175 |
| Figure 4.23 – Period of free surface elevation peaks: analytical and numerical estimations..... | 177 |
| Figure 4.24 – Sketch of the simplified mechanical models..... | 178 |
| Figure 4.25 – Diagram of the magnitude of the two free surface height peaks in relation to the width of the gap..... | 179 |
| Figure 4.26 – Snapshots of the vortex in the lower edge of the barge: vorticity and flow direction (left column) free surface profile and velocity magnitude (right column) – $L_{gap} = 10m, T = 13.0s, A_{sway} = 0.05 \times B$ | 181 |
| Figure 4.27 – Contour map of the dimensionless wave height as function of the length of the gap and the sway period – sloshing-type resonance..... | 183 |
| Figure 4.28 – Dimensionless free surface elevation in relation to sway period: sloshing mode..... | 184 |
| Figure 4.29 – (a) Amplitude of the crest ($\Delta h +$) and the trough ($\Delta h -$) of the free surface elevation and (b) phase of free surface elevation at barge wall as function of the sway period – $L = 40m$ | 186 |
| Figure 4.30 – (a) Amplitude of the crest ($\Delta h +$) and the trough ($\Delta h -$) of the free surface elevation and (b) phase of free surface elevation at barge wall as function of the sway period – $L = 50m$ | 187 |
| Figure 4.31 – (a) Amplitude of the crest ($\Delta h +$) and the trough ($\Delta h -$) of the free surface elevation and (b) phase of free surface elevation at barge wall as function of the sway period – $L = 60m$ | 188 |

| | |
|---|-----|
| Figure 4.32 – Diagrams of the resonant period for sloshing modes: Analytical estimation and numerical results | 189 |
| Figure 5.1 – Inside an LNG MarkIII membrane tank with corrugations..... | 198 |
| Figure 5.2 – Neighborhood of particles with different sizes | 202 |
| Figure 5.3 – Splitting and merging algorithm – Tanaka et al. (2009)..... | 203 |
| Figure 5.4 – Neighborhood of particles | 204 |
| Figure 5.5 – Neighborhood of particles– Chen et al. (2015) | 206 |
| Figure 5.6 – Splitting algorithm – Chen et al. (2015)..... | 207 |
| Figure 5.7 – Merging algorithm – Cheng et al. (2015)..... | 207 |
| Figure 5.8 – Border between two sub-domains..... | 210 |
| Figure 5.9 – Conceptual scheme of the “border mapping” technique..... | 211 |
| Figure 5.10 – Conceptual scheme of the simplification..... | 213 |
| Figure 5.11 – Conceptual scheme of the refinement | 215 |
| Figure 5.12 – Creation of a fictitious particle | 216 |
| Figure 5.13 – Algorithm of the multi-resolution and single-resolution MPS | 219 |
| Figure 5.14 – Layers of the border region – Explicit calculation..... | 221 |
| Figure 5.15 – Neighborhood of a low-resolution particle close to the border..... | 222 |
| Figure 5.16 – Neighborhood of a high-resolution particle close to the border | 224 |
| Figure 5.17 – Neighborhood of a “fictitious particle” close to the border..... | 225 |
| Figure 5.18 – Sketch of different typical particle distributions..... | 227 |
| Figure 5.19 – Different arrangements on a Dam-Break simulation | 228 |
| Figure 5.20 – Histogram of the distance between neighbor particles..... | 229 |
| Figure 5.21 – Algorithm 1 of simplification – distance between particles..... | 231 |
| Figure 5.22 – Algorithm 2 of simplification: set operations | 232 |
| Figure 5.23 – Simplification of a particle grid from a MPS simulation | 234 |
| Figure 5.24 – Simplified particles in the border of a MPS simulation..... | 234 |
| Figure 5.25 – Refinement algorithm..... | 235 |

| | |
|---|-----|
| Figure 5.26 – Refinement of a particle grid from a MPS simulation | 236 |
| Figure 5.27 – Fictitious particles in the border of a MPS simulation..... | 237 |
| Figure 5.28 – Pressure field of a hydrostatic case..... | 238 |
| Figure 5.29 – Initial conditions of the test case..... | 238 |
| Figure 5.30 – Pressure distribution of the test case: single resolution case and multi- resolution case..... | 239 |
| Figure 5.31 – Non-zero elements of the PPE matrix of coefficients..... | 240 |
| Figure 5.32 – Dimensions of the Dam Break test case..... | 241 |
| Figure 5.33 – Division of the computational domain – Dam Break case..... | 242 |
| Figure 5.34 – Snapshots of the MPS simulation – Dam Break case | 243 |
| Figure 5.35 – Time series of (a) the number and (b) the total area of the particles of each resolution – Dam Break case..... | 244 |
| Figure 5.36 – Refinement at the free-surface | 245 |
| Figure 5.37 – Dimensions of the still water rectangular tank..... | 245 |
| Figure 5.38 – Division of the computational domain – still water rectangular tank ... | 246 |
| Figure 5.39 – Processing time for the still water rectangular tank in multi-resolution simulation | 247 |

LIST OF TABLES

| | |
|---|-----|
| Table 3.1 – Bulkhead with circular holes dimensions and open-area ratio | 77 |
| Table 3.2 – Bulkhead with square holes – dimensions and open-area ratio..... | 77 |
| Table 3.3 – Filling levels and analytical natural frequencies | 79 |
| Table 4.1 – Oscillation frequency of the free oscillation test – numerical, analytical and experimental data – (MPS, 0-th order gradient model)..... | 148 |
| Table 4.2 – Oscillation frequency of the free oscillation test – numerical, analytical and experimental data – (MPS, 1-st order gradient model)..... | 148 |
| Table 5.1 – Features of the multi-resolution techniques for MPS method | 209 |

CONTENTS

| | | |
|----------|---|-----------|
| 1 | CHAPTER ONE: INTRODUCTION..... | 27 |
| 1.1 | INTRODUCTION..... | 29 |
| 1.1.1 | Background..... | 29 |
| 1.1.2 | Hydrodynamic loads on naval and offshore structures..... | 30 |
| 1.1.3 | Approaches for the investigation of hydrodynamic loads..... | 32 |
| 1.1.4 | Application of meshless methods for nonlinear hydrodynamics | 33 |
| 1.1.5 | Outline of the Thesis | 36 |
| 1.2 | OBJECTIVES..... | 38 |
| 1.3 | TEXT OUTLINE..... | 40 |
| 2 | CHAPTER TWO: THEORETICAL FRAMEWORK: THE MOVING PARTICLES SEMI-IMPLICIT (MPS) METHOD..... | 43 |
| 2.1 | GOVERNING EQUATIONS..... | 43 |
| 2.2 | DISCRETE DIFFERENTIAL OPERATORS..... | 44 |
| 2.3 | ALGORITHM OF THE INCOMPRESSIBLE FLOW | 46 |
| 2.4 | IMPLICIT CALCULATION OF PRESSURE..... | 47 |
| 2.4.1 | PPE source term with restricted compressibility | 49 |
| 2.4.2 | Divergence-free condition for PPE source term..... | 50 |
| 2.4.3 | PPE source term with time-scale correction | 50 |
| 2.5 | PRESSURE GRADIENT..... | 52 |
| 2.5.1 | Improved gradient model..... | 52 |
| 2.5.2 | First-order gradient model..... | 52 |
| 2.6 | FREE-SURFACE DETECTION TECHNIQUES | 53 |
| 2.6.1 | Original free-surface detection | 53 |

| | | |
|----------|--|-----------|
| 2.6.2 | Free-surface detection by number of neighbor particles..... | 54 |
| 2.6.3 | Free-surface detection by neighbor particle centroid deviation (NPCD) | 54 |
| 2.7 | RIGID SOLID BOUNDARY CONDITION | 56 |
| 2.7.1 | Floating body..... | 57 |
| 2.8 | ALGORITHM OF THE METHOD..... | 58 |
| 3 | CHAPTER THREE: SLOSHING MITIGATION BY PERFORATED SWASH BULKHEAD WITH OPTIMIZED GEOMETRY | 61 |
| 3.1 | ABSTRACT..... | 61 |
| 3.2 | INTRODUCTION..... | 63 |
| 3.3 | LITERATURE REVIEW | 65 |
| 3.4 | OBJECTIVES | 68 |
| 3.5 | VALIDATION | 69 |
| 3.6 | CASE OF STUDY..... | 74 |
| 3.7 | RESULTS..... | 81 |
| 3.7.1 | Effect of the open-area ratio: General Behavior..... | 81 |
| 3.7.2 | Effects of excitation amplitude..... | 91 |
| 3.7.3 | Effects of the geometry of the holes | 97 |
| 3.7.4 | Effects of the arrangement of the holes..... | 101 |
| 3.7.5 | Discussion of the damping effects of the perforated bulkheads..... | 104 |
| 3.8 | OPTIMUM OPEN AREA RATIO OF SWASH BULKHEAD FOR SLOSHING MITIGATION..... | 111 |
| 3.9 | TEST CASE: SWASH BULKHEADS WITH OPTIMUM OPEN AREA RATIO | 120 |
| 3.9.1 | Models..... | 120 |
| 3.9.2 | Results..... | 122 |
| 3.9.3 | Full scale test case..... | 128 |
| 3.10 | CONCLUSIONS..... | 131 |

| | | |
|----------|--|------------|
| 4 | CHAPTER FOUR: INVESTIGATION OF THE RESONANT BEHAVIOR OF THE FLOW ENTRAPPED WITHIN NARROW GAPS: “GAP EFFECT” | 135 |
| 4.1 | ABSTRACT | 135 |
| 4.2 | INTRODUCTION | 137 |
| 4.3 | LITERATURE REVIEW | 138 |
| 4.4 | OBJECTIVES | 141 |
| 4.5 | VALIDATION | 143 |
| 4.6 | CASE OF STUDY | 150 |
| 4.7 | RESULTS | 152 |
| 4.7.1 | Numerical convergence | 152 |
| 4.7.2 | Wave reflection | 156 |
| 4.7.3 | Flow in the gap: general behavior | 157 |
| 1.1 | PISTON-TYPE RESONANCE MODE | 167 |
| 4.7.4 | Analysis of resonant periods for piston-type mode | 172 |
| 1.2 | SLOSHING-TYPE RESONANCE MODE | 182 |
| 4.7.5 | Analysis of resonant periods for sloshing-type modes | 188 |
| 4.8 | CONCLUDING REMARKS | 190 |
| 5 | CHAPTER FIVE: MULTIREOLUTION MOVING PARTICLE SEMI-IMPLICIT METHOD BY BORDER MAPPING TECHNIQUE | 193 |
| 5.1 | ABSTRACT | 193 |
| 5.2 | INTRODUCTION | 195 |
| 5.3 | OBJECTIVE | 200 |
| 5.4 | LITERATURE REVIEW | 201 |
| 5.4.1 | Summary of the different multi-resolution techniques | 208 |
| 5.5 | MULTIREOLUTION MPS METHOD BY “BORDER MAPPING” TECHNIQUE | 210 |

| | | |
|----------|---|------------|
| 5.5.1 | Overview..... | 210 |
| 5.5.2 | Simplification of the fine-resolution region..... | 213 |
| 5.5.3 | Refinement of the coarse-resolution region..... | 214 |
| 5.5.4 | Algorithm to keep the resolution: update of the border particles..... | 216 |
| 5.5.5 | Algorithm of the multi-resolution MPS..... | 217 |
| 5.5.6 | Explicit Part..... | 220 |
| 5.5.7 | Implicit calculation of pressure..... | 222 |
| 5.6 | RESULTS..... | 227 |
| 5.6.1 | Concepts on the particle distribution in MPS simulations..... | 227 |
| 5.6.2 | Simplification algorithm..... | 230 |
| 5.6.3 | Refinement algorithm..... | 235 |
| 5.6.4 | Pressure calculation..... | 237 |
| 5.6.5 | Mass conservation..... | 241 |
| 5.6.6 | Processing time..... | 245 |
| 5.7 | CONCLUSION..... | 249 |
| 6 | CHAPTER SIX: CONCLUSION..... | 251 |
| 6.1 | CONCLUDING REMARKS..... | 251 |
| 6.2 | FURTHER WORK AND PROPOSED IMPROVEMENTS..... | 255 |
| 7 | REFERENCES..... | 257 |

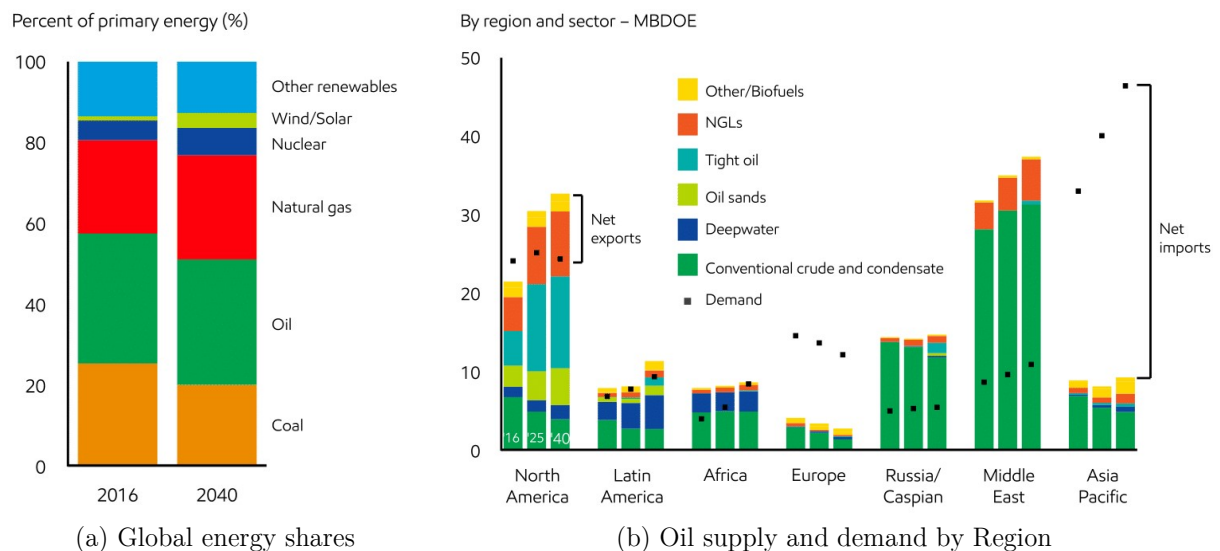
1 CHAPTER ONE: INTRODUCTION

1.1 INTRODUCTION

1.1.1 Background

In the upcoming decades, the global energy demand should increase mainly due to the improvement of the living standards in the developing nations. Simultaneously, aiming to address climate change and reduce the emissions of greenhouse gases, subtle changes in the supply and the demand of primary energy sources are expected. In such context, the share of primary energy sources related to wind, solar, nuclear and natural gas might increase from 2016 to 2040. Nevertheless, as shown in Figure 1.1-a, oil should still be the main primary source of energy by 2040 (ExxonMobil, 2018). From this forecast, oil and natural gas must account for approximately 60% of the primary energy sources.

Figure 1.1 – (a) Global energy demand share and (b) Regional supply of liquid energy sources

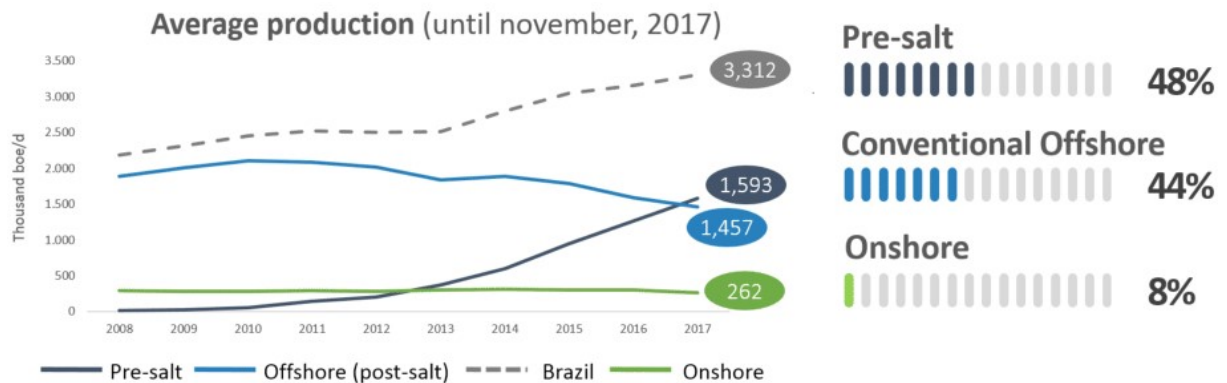


Source: ExxonMobil (2018).

The demand for oil and natural gas usually drives the growth of the naval and offshore industry, which is directly involved in its production and transportation. As presented by Figure 1.1-b, the main importer of oil and gas is the Asia-Pacific region

while the main exporter is the Middle-East. Then, due to the distance between producing and consuming regions, the transport of oil and gas is made by vessels, such as tankers and LNG carriers. Besides, in the case of Africa and Latin-America, a significant portion of the oil and gas production is performed in deep waters (Figure 1.1-b) and ultra-deep waters, by offshore platforms such as semisubmersibles and Floating, Production, Storage and Offloading units (FPSOs). In Brazil, the production in the Pre-Salt layer, a deep water environment, already surpassed the other conventional offshore oil output by 2017 (Figure 1.2).

Figure 1.2 – Track record of Brazilian oil production per environment

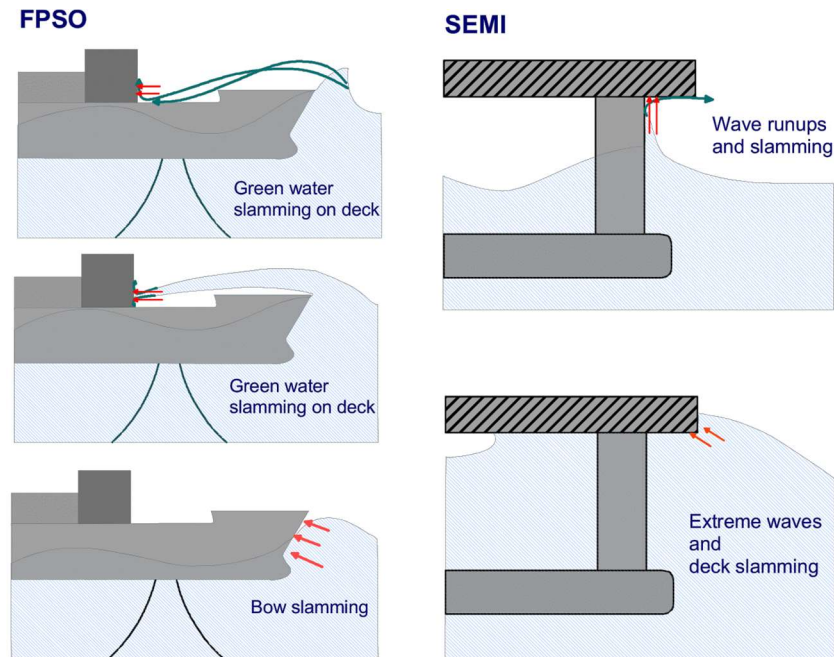


Source: ANP (2018).

1.1.2 Hydrodynamic loads on naval and offshore structures

The floating offshore structures, both sea-going vessels and platforms, are subject to the action of weather agents such as waves, wind and current during its operation. For sake of simplicity, the loads caused by the waves on such structures could be divided into two types: the cyclic slowly varying global loads and the local impulsive loads with short duration associated to violent hydrodynamic impact phenomena. The proper design of offshore structures should consider both types of loads in order to ensure its safe and reliable operation.

Figure 1.3 – Wave impact phenomena on floating offshore structures



Source: SINTEF website (access May/2019).

The bow and stern slamming, the green water, the wave-in-deck impact and the sloshing are examples of violent hydrodynamic impact phenomena that could affect offshore structures, especially in rough seas and weather conditions. Figure 1.3 presents some hydrodynamic phenomena caused by wave impact on offshore floating structures. The bow and stern slamming consist in the violent impact between the bow or the stern of the hull with the fluid free surface when the bow or the stern emerges from the fluid and then re-enter it. The green water, also called shipping water, consists in the water boarding on the deck of floating structures when the sea free surface height exceeds the freeboard of the vessel. The wave-in-deck impact affects floating structures, such as semisubmersibles, in which there is a gap between the sea free surface and the deck of the structures. It happens when the wave height exceeds such gap and wave impact is observed in the bottom of the deck. The sloshing is the violent impact of fluid within partially filled containers, which is related to the formation of resonant waves in the free surface of the fluid inside the tanks. All these phenomena involve violent impulsive

hydrodynamic impact loads with short duration and high-pressure peaks that may damage vessel structures.

1.1.3 Approaches for the investigation of hydrodynamic loads

Three different approaches could be adopted to assess the loads on offshore structures: analytical estimations, experiments and numerical simulations. Each one presents its advantages and respective shortcomings.

In order for a mathematical model to be solved analytically, usually several simplification hypotheses should be adopted. Thus, the results obtained by such approach are usually the least accurate regarding real engineering applications. However, the analytical modeling of the problem provides fast insights about the general behavior of the phenomena regarding its most significant parameters.

On the other hand, experiments in reduced scale models are a common practice in naval engineering that present the most reliable results. It provides a controlled environment in which single aspects of a complex phenomenon could be separated and its effects investigated. On the other hand, this approach is usually time consuming and expensive. It is not very flexible as well, as changes in the experiment setup are usually costly. The measured data is also limited by the number of sensors and scaling effects could impair the results for more complex phenomena.

In such context, a cost effective and flexible approach are the numerical simulations in which approximate solutions of more complex mathematical models could be obtained numerically. The accuracy of the computed results depends only upon the robustness and quality of a given numerical method. Given the steady increase in the computational processing capacity, more complex mathematical models could be numerically solved to reproduce increasingly complex phenomena. In the case a numerical method is adopted to solve the governing equations of a fluid flow, it belongs to the branch of the fluid mechanics known as Computational Fluid Dynamics

(CFD). There are several CFD methods, each presenting its own particular features, which are more suitable for certain types of problems.

For the hydrodynamic loads in floating structures, the linear cyclic global loads due to waves could be accurately predicted by Boundary Element Methods (BEMs). In the most common approach of BEMs for the modeling of seakeeping problems, the flow is considered as potential and the steady state solution of the governing equations in the frequency domain are then calculated. As the governing equations of the fluid flow are solved only for the domain boundaries, it often provides faster computations than the CFD methods that solve them for the entire fluid domain. In the case of nonlinear hydrodynamic phenomena or viscous contributions to the flow become significant, the simplification hypothesis adopted in order to model the flow as potential disregard key aspects of the problems and the BEMs are not a suitable approach.

1.1.4 Application of meshless methods for nonlinear hydrodynamics

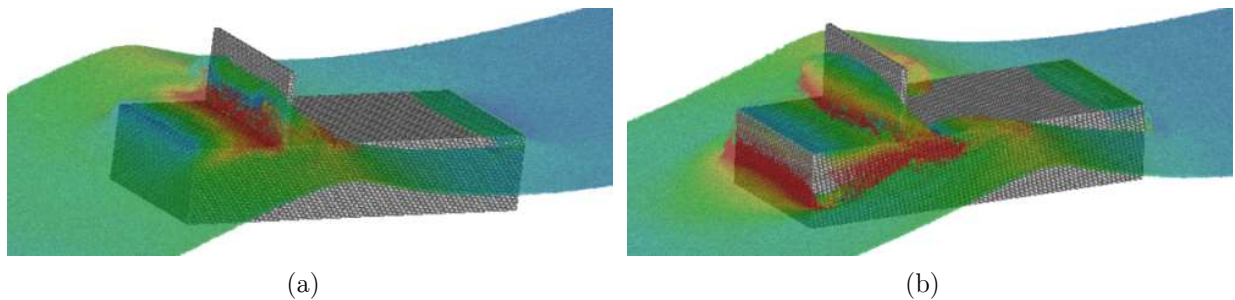
The hydrodynamic impact phenomena have very high Reynolds number so, in other words, the inertial forces prevail over the viscous forces. Moreover, the impulsive loads due to hydrodynamic impact show highly nonlinear and complex behavior. In view of this features, the fully-Lagrangian particle-based CFD methods are suitable techniques for the modeling of such challenging problems and they have been widely adopted for such purpose during the last two decades. In such methods, the fluid domain is discretized in particles that freely move in relation to each other following the flow governing equations, i. e., the topology of the grid continuously change in time. This approach is advantageous to the treatment of hydrodynamic impact problems that involve discontinuities, large free surface deformations, such as fragmentation and coalescing, and complex body geometries. The most common of such methods are the Smoothed Particles Hydrodynamics (SPH), initially proposed by Gingold and Monaghan (1977) to study astrophysical problems and later improved by Monaghan

and Gingold (1983), and the Moving Particles Semi-Implicit (MPS) method, initially proposed by Koshizuka et al. (1995).

Bellezi et al. (2011a) performed two-dimensional MPS simulations of the water entry of bodies with different geometries, including V-shaped wedges with different deadrise angles and a circular section cylinder, both simple cases commonly adopted for the validation of numerical codes for slamming phenomenon. The particle-based numerical results obtained by the authors presented good agreement to the experimental data from Miyagi (2003). Veen and Gourlay (2012) coupled the SPH with a strip theory method in order to study the bow slamming of a vessel. While the strip theory calculated the vessel motions, the SPH was adopted to estimate the impulsive hydrodynamic loads in two-dimensional sections representing each transversal strip of the hull.

Shibata et al. (2012) adopted the MPS method to investigate the effect of the green water phenomenon in the global motion of a vessel under head seas condition with forward speed, which was later deemed as negligible. Bellezi et al. (2013) validated the MPS method to the green water phenomenon by comparing the numerical results to experimental data from Lee et al. (2012) for the pressure measured over the deck of the model. Bellezi et al. (2015)(Figure 1.4) carried out simulations of the green water phenomenon by adopting high resolution particle models, which presented a more accurate pressure calculation with lower numerical noise in the signal.

Figure 1.4 – Snapshots of a MPS simulation of green water phenomenon

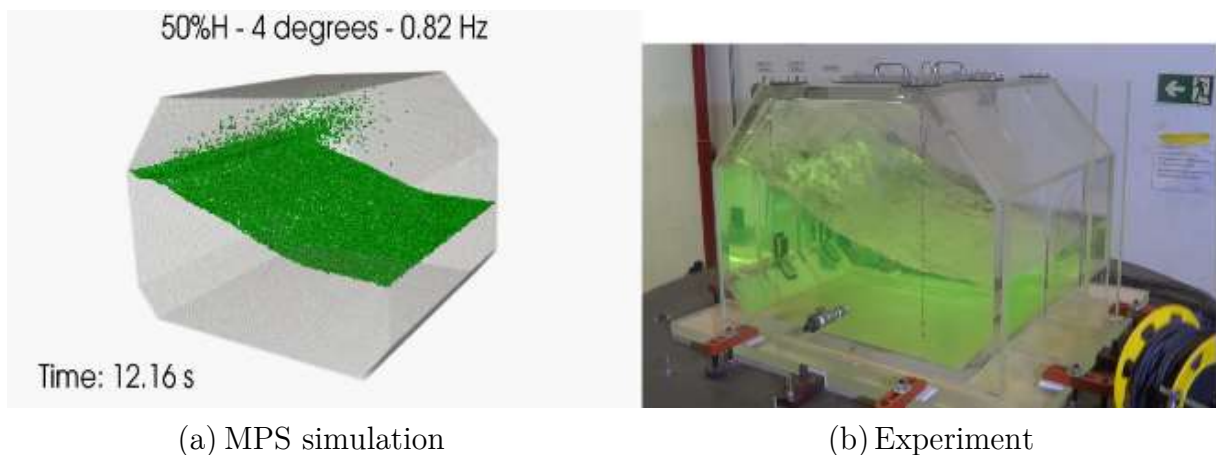


Source: Bellezi et al. (2015).

The wave-in-deck impact phenomenon in a two-dimensional simplified setup was validated for the MPS method by Bellezi et al. (2011b) based on the experimental data from Kendon et al. (2010). The time series of the horizontal and transversal force, from a relatively coarse model, presented significant numerical noise, but the filtered signal which disregards high frequency numerical noise shown close behavior to the experimental data.

Souto-Iglesias et al. (2004) (2006) performed experimental campaigns and numerical SPH simulations of two-dimensional sloshing cases with very low filling levels, which are especially challenging cases because of highly nonlinear free surfaces, such as the formation of travelling waves and wave breaking. Cheng et al. (2015) carried out an experimental campaign and numerical MPS simulations for the sloshing inside a reduced scale prismatic tank based on the geometry of typical membrane-type LNG tank. The computed results for the pressure time series and the dynamic pressure in the frequency domain presented close agreement to the experimental data.

Figure 1.5 – Sloshing in prismatic tank – MPS simulation x experiment



Source: Cheng et al. (2015).

1.1.5 Outline of the Thesis

From the abovementioned works, the particle-based methods were successfully validated and adopted for the investigation of a wide range of nonlinear hydrodynamic phenomena. In such context, the present work is focused on the application and the development of the MPS method to the investigation of nonlinear hydrodynamic problems in naval and offshore engineering. This Thesis comprises three different studies in this context:

The first study is the proposal of an optimized geometry of perforated swash bulkhead aiming to mitigate sloshing within rectangular containers under different filling conditions. Mitigate sloshing is helpful for the safety of the liquid cargo containment systems. It is even more important in the case of the cryogenic containment of LNG carriers and FLNG platforms.

The second study is the investigation of the resonant flow inside narrow gaps between two floating structures. Such kind of phenomenon could be harmful for offloading operations between platforms and shuttle vessels in side-by-side configurations, as the resonant flow could amplify the relative motion between the vessels. Although this resonant flow is mainly a consequence of the slowly varying wave motions, it presents nonlinear nature as the viscosity and the flow separation play a significant role. Thus, it could not be properly modeled by traditional BEM numerical methods, which are the most common technique for seakeeping analysis, without an external damping that should be experimentally calibrated, such as rigid lids.

The third and final study is focused on the development of a multiresolution technique for the MPS method based on a newly proposed border mapping scheme. The main disadvantage of the particle-based methods lies on its computational cost, which increases dramatically as the number of particles of a given numerical model increase. As the original formulation of the MPS adopts a unique resolution for all the particles within the computational domain, in order to use a higher resolution in an

interest region of the domain, the whole domain must be modeled using finer resolution, which makes the processing cost of the simulations unfeasible for some complex cases. Then, a multiresolution scheme that enables to enhance the resolution only in a region while the remaining of the computational domain has a coarser resolution is a very useful improvement to the MPS method towards its practical application to complex engineering problems.

1.2 OBJECTIVES

The present Thesis is composed by three studies, whose focus encompass both basic and applied research in the context of the application and development of the MPS method for nonlinear hydrodynamic problems in naval and offshore engineering.

The first study of the present work is the **investigation of the behavior of the sloshing phenomenon in rectangular tanks equipped with perforated swash bulkheads**. The objective of the first step of this investigation is to provide insights on the effect of the open-area ratio of the perforated bulkhead in the sloshing phenomenon for different conditions. From the results of this investigation, the objective of the next step is the proposal of an optimized geometry of swash bulkhead to better mitigation of sloshing at all the filling levels under motion with frequency in a range comprising the three first sloshing resonant modes. This first study has features of both discovery and invention, as it contributes to add to the knowledge about a physical phenomenon and it proposes a practical engineering solution to a specific problem.

The second study is the **investigation of the resonant flow of fluid trapped within narrow gaps** between two floating structures. The first objective of this investigation is to validate the numerical method and ensure it could reproduce key aspects of the flow. Thereafter, the main objective is to identify the different resonant modes and in which conditions each one occurs by a series of simulations. This study could be better fitted as a fundamental research as it adds to knowledge of the physical phenomenon. Knowledge that could be further applied to develop solutions to mitigate the resonant flow in the gap or to better understand which situations must be avoided for safer offshore operations.

The third study comprises the **development of a multiresolution technique for the MPS method**, which is denominated as “border mapping” technique. The key aspect of the border mapping technique is to generate equivalent particle distributions in the overlapping regions adjacent to the border of the sub-domains with different resolution based on the actual arrangement of the particle in the sub-domain. By considering the multiresolution technique as a kind of coupling between subdomains with different resolutions, the objective of this study is to propose a multiresolution technique characterized by a strong, two-way coupling of the subdomains that properly calculates the pressure and ensure the mass and momentum conservation in the region of the truncated border. The final study best fit the definition of a basic research, in which an improved MPS method-based simulation system is developed.

1.3 TEXT OUTLINE

As previously mentioned, the present thesis is composed by three different studies in the context of nonlinear hydrodynamic phenomena in the field of naval and offshore engineering, by adopting the MPS particle-based method as the numerical technique suitable for such purpose. Hence, the thesis is divided into four chapters:

In the present **Chapter One**, an introduction to the research, its context and outline is presented. Then, the mathematical formulation and several improvements to the original formulation of the MPS method are later introduced in **Chapter Two**.

Chapter Three presents the study of the use of perforated swash bulkheads for the mitigation of sloshing phenomena. This chapter could be divided into three main parts. In the first part, the validation of the particle method for the sloshing in tanks equipped with bulkheads is carried out. In the second part, a comprehensive analysis of the effect of the open-area ratio and its geometric parameters on the bulkhead is carried out in order to obtain better knowledge of the phenomenon. In the second part, the insights obtained previously are used as foundation for the proposal of a relation of the optimal open-area ratio as function of the fluid filling ratio for sloshing mitigation. Three swash bulkhead models based on the optimal relation are then evaluated.

Chapter Four is focused on the investigation of the resonant behavior of flow entrapped within narrow gaps, a phenomenon that affects some naval and offshore operations such as the offloading between floating platforms and shuttle vessels. The contents of this chapter could be divided in four parts. In the first part, a validation analysis and convergence study are performed in order to ensure the adequacy of the - based modeling of the phenomenon. The second part presents the investigations of the gap resonance considering several aspects, such as the distance between the two bodies, the amplitude and frequency of the relative motion between them. From the results,

two types of resonant flow were observed. The third and fourth part of the chapter shows an in-depth analysis of each one of these two resonant modes.

Finally, **Chapter Five** introduces a novel technique for a multiresolution MPS simulation system based on a scheme called “border mapping”. This chapter is divided into three parts. A critical review of the existing multiresolution techniques and its advantages/disadvantages are provided initially. In the second part, the mathematical formulation of the novel technique is introduced. After that, some initial test cases and results are shown in the final part of the chapter.

2 CHAPTER TWO: THEORETICAL FRAMEWORK: THE MOVING PARTICLES SEMI-IMPLICIT (MPS) METHOD

The Moving Particle Semi-Implicit (MPS) is a Computational Fluid Dynamics (CFD) method that was initially proposed by Koshizuka et al. (1995). It is a fully-Lagrangian method for the modeling of incompressible flows in which the continuous fluid domain is discretized into particles. Then, the differential operators of the governing equations are approximated by discrete differential operators in irregular nodes (Isshiki, 2011) derived based on a weight function. The MPS method adopts a two-stage fractional step scheme to couple the velocity and the pressure and solves the Pressure Poisson Equation.

The present work was carried by using the MPS-based numerical simulation system developed by the MPS group of the Numerical Offshore Tank (TPN) laboratory of the University of São Paulo (USP). In the present section, the mathematical formulation of the original version of the MPS method is presented along with the most significant improvements to the method.

2.1 GOVERNING EQUATIONS

The governing equations of the incompressible flow to be solved by the MPS method are the mass conservation equation (eq. 2.1) and the momentum conservation equation (eq. 2.2), both in the Lagrangian formalism. The last term in the right-hand side of the equation 2.2 is related to the viscosity contribution of a Newtonian fluid.

$$\frac{D\rho}{Dt} = -\rho(\nabla \cdot \vec{u}) = 0 \quad (2.1)$$

$$\frac{D\vec{u}}{Dt} = \frac{1}{\rho} \nabla P + \vec{g} + \vartheta \nabla^2 \vec{u} \quad (2.2)$$

where ρ is fluid specific mass, \vec{u} the velocity vector, P the pressure, \vec{g} the gravity acceleration, ϑ the kinematic viscosity and t the time.

2.2 DISCRETE DIFFERENTIAL OPERATORS

In the MPS method, the differential operators of the governing equations are discretized based on a “weight function” (Eq. 2.3), which assign the relative importance for the contribution of the particles within a compact support bounded by a “neighborhood radius” (r_e).

$$w(r) = \begin{cases} \frac{r_e}{r} - 1, & (0 \leq r < r_e) \\ 0, & (r_e \leq r) \end{cases} \quad (2.3)$$

where $r = |\vec{r}_j - \vec{r}_i|$ is the distance between the i -th and the j -th particle.

The compact support of a given particle will be henceforth referred as the particle “neighborhood”. The equation 2.3 tends to infinite if the distance between the i -th and the j -th tends to zero, this feature of the weight function enhances the numerical stability of the particle interaction model (Koshizuka, Tamako., & Oka, 1995).

An important parameter directly calculated from the weight function is the “particle number density” (pnd), given by equation 2.4. As the fluid is incompressible and each particle in which the fluid domain is discretized is assumed to has the same size and same mass, the pnd is directly proportional to the fluid density.

$$[pnd]_i = \sum_{j \neq i} w(|\vec{r}_j - \vec{r}_i|) \quad (2.4)$$

Then, the discrete differential operators are derived based on the weight function and the gradient operator and the Laplacian operator of a scalar quantity ϕ are given by Eq. (2.5) and Eq. (2.6), respectively:

$$[\nabla\phi]_i = \frac{d}{pnd^0} \sum_{j \neq i} \left[\frac{(\phi_j - \phi_i)}{|\vec{r}_j - \vec{r}_i|^2} (\vec{r}_j - \vec{r}_i) w(|\vec{r}_j - \vec{r}_i|) \right] \quad (2.5)$$

$$[\nabla^2\phi]_i = \frac{2d}{pnd^0\delta} \sum_{j \neq i} [(\phi_j - \phi_i)w(|\vec{r}_j - \vec{r}_i|)] \quad (2.6)$$

where pnd^0 is the initial particle number density, which is calculated considering the case of a particle with its neighborhood entirely filled with neighbor particles, d is the number of dimensions of the case, which is 2 for two-dimensional simulations and 3 for three-dimensional ones and, finally, δ is a constant value parameter given by:

$$\delta = \frac{\int_V w(r)r^2 dv}{\int_V w(r)dv} \quad (2.7)$$

The constant δ is also calculated based on a neighborhood fulfilled with neighbor particles that adopt the initial particle distribution. In the case of two-dimensional simulations, the initial particle distribution is usually a square-shaped particle grid with sides of dimension l_0 , which is the initial distance between particles. In the case of three-dimensional simulations, the initial particle distribution is usually based on a cubic particle grid with sides of dimension l_0 .

Koshizuka et al. (1996) obtained stable simulations in the two-dimensional case by adopting a neighbor radius of $r_e = 2.1l_0$ for the gradient operator and $r_e = 4.0l_0$ for the Laplacian in the two-dimensional simulations. For the three dimensional case, a neighborhood radius of $r_e = 2.1l_0$ for both the gradient operator and the Laplacian is suitable.

A fundamental difference between the MPS and the SPH method, which is another widely used fully-Lagrangian CFD method, is the discrete differential operators. In the SPH a “kernel function” is adopted for the interpolation of the values at the i -th particle from the several j -th particles within its compact support, bounded by a “smoothing length”, and the differential operators in the SPH method are obtained from the exact analytical derivative of the kernel function. As a consequence, the SPH

kernel function must be at least of a class C^2 and even higher-order kernel functions are usually adopted in the literature. On the other hand, in the MPS the discrete differential operators are obtained from the weight function in a way that resembles a finite-difference scheme. Therefore, a low-order weight function is perfectly suitable in the case of the MPS method.

2.3 ALGORITHM OF THE INCOMPRESSIBLE FLOW

For the solution of the system of equations obtained from the mass conservation and the momentum conservation equations, the MPS adopts a semi-implicit algorithm in which the velocity and the pressure are coupled based on a two-stage fractional scheme.

- 1) The first step comprises the **explicit part** (Eq. 2.8) in which an intermediate velocity of the particles is calculated by considering the terms in the right-hand side of the momentum conservation equation, except the pressure gradient. The intermediate state of the particles is then obtained from this intermediate velocity (u^*).
- 2) The second step comprises the **implicit part**. The pressure of the particles is calculated implicitly by a Poisson Pressure Equation (PPE) linear system, which is derived from the mass conservation condition and based on the intermediate state of the particles. Then, the correction factor of the intermediate velocity (u') is obtained from the pressure gradient (Eq. 2.9).
- 3) Finally, the final state of the particles (u^{n+1}) is obtained by the update of the intermediate state of the particles (u^*) by the correction factor (u') obtained by the implicit part (Eq. 2.10).

$$u^* = u^n + \Delta t[\vartheta \nabla^2 \vec{u} + \vec{g}] \quad (2.8)$$

$$u' = -\frac{\Delta t}{\rho} \nabla P^{n+1} \quad (2.9)$$

$$u^* + u' = u^{n+1} \quad (2.10)$$

2.4 IMPLICIT CALCULATION OF PRESSURE

One key difference between the MPS method and the SPH method is related to the algorithm for the pressure calculation. The original formulation of the SPH method (Monaghan & Gingold, 1983) calculated explicitly the pressure by an equation of state. Otherwise, the original formulation of the MPS method (1995) calculates the pressure implicitly. The implicit calculation of the pressure enhances the incompressibility of the flow and provide more stable pressure calculations in general. On the other hand, the implicit calculation demands the solution of a linear system, which has a higher computational cost than the explicit estimation.

The density of fluid should be kept constant as consequence of the mass conservation in the incompressible flow. Besides, as each particle is assumed to have the same mass in the MPS method, the particle number density (pnd) is proportional to the density of the fluid. Then, the particle number density of the fluid at the intermediate state (pnd^*) should be corrected by an correction factor pnd' in order to match the initial particle number density (pnd^0).

$$pnd^* + pnd' = pnd^0 \quad (2.11)$$

From the mass conservation condition, the pnd' and the pnd^0 are related to the velocity correction factor u' according to the relation:

$$\frac{1}{\Delta t} \frac{pnd'}{pnd^0} = -\nabla \cdot u' \quad (2.12)$$

Replacing the Eq. 2.9 in the Eq. 2.12, the source term of the PPE is obtained and show in Eq. 2.13. The right-hand side of the Eq. 2.13 is called the particle number density deviation condition of the source term.

$$[\nabla^2 P^{n+1}]_i = -\frac{\rho}{\Delta t^2} \frac{[pnd^*]_i - pnd^0}{pnd^0} \quad (2.13)$$

By replacing the Laplacian model (Eq. 2.6) in the equation of the source term (Eq. 2.13), the linear system of the Poisson's Pressure equation is obtained:

$$\frac{2d}{pnd^0 \delta} \sum_{j \neq i} [(P_j - P_i)w(|\vec{r}_j - \vec{r}_i|)] = -\frac{\rho}{\Delta t^2} \frac{pnd_i^* - pnd^0}{pnd^0} \quad (2.14)$$

$$\sum_{j \neq i} P_j w(|\vec{r}_j - \vec{r}_i|) - \sum_{j \neq i} P_i w(|\vec{r}_j - \vec{r}_i|) = -\frac{\rho \delta}{2d \Delta t^2} (pnd_i^* - pnd^0) \quad (2.15)$$

In relation to this linear system, there are two types of particles:

- (i) the **free surface** particles, henceforth called **Set BC** of particles ($j \in BC$), which are defined as Dirichlet-type boundary conditions of pressure for this linear system ($P_j = P^{atm}$), and
- (ii) the **non free surface** particles, whose pressures are unknown and are later obtained from the solution of the linear system, henceforth called **Set S** of particles ($S = \{j \notin BC\}$).

So, the first term in the left-hand side of the Eq. 2.15 could be partitioned to the form:

$$\sum_{j \neq i} P_j w(|\vec{r}_j - \vec{r}_i|) = \sum_{j \neq i, j \notin BC} P_j w(|\vec{r}_j - \vec{r}_i|) - \sum_{j \neq i, j \in BC} P_j w(|\vec{r}_j - \vec{r}_i|) \quad (2.16)$$

By rearranging the terms of Eq. 2.15 and replacing in it the Eq. 2.16, the linear system is given as follows:

$$\begin{aligned} \sum_{j \neq i, j \notin BC} P_j w(|\vec{r}_j - \vec{r}_i|) - \sum_{j \neq i} P_i w(|\vec{r}_j - \vec{r}_i|) \\ = -\frac{\rho \delta}{2d \Delta t^2} (pnd_i^* - pnd^0) - \sum_{j \neq i, j \in BC} P_j w(|\vec{r}_j - \vec{r}_i|) \end{aligned} \quad (2.17)$$

Moreover, the linear system from Eq. 2.17 can be rewritten in the matrix form $[A] \times \{x\} = [B]$, where $[A]$ is the matrix of coefficients and given by Eq. 2.18, $[B]$ is

the solution vector given by the Eq. 2.19 and $\{x\}$ is the vector containing the variables, which are the pressure of the non free surface particles.

$$[A_{ij}] = \begin{cases} -\sum_{k \neq i} w(|\vec{r}_k - \vec{r}_i|), & i = j \wedge |\vec{r}_k - \vec{r}_i| \leq r_e \\ w(|\vec{r}_j - \vec{r}_i|), & i \neq j \wedge |\vec{r}_j - \vec{r}_i| \leq r_e \\ 0, & i \neq j \wedge |\vec{r}_j - \vec{r}_i| > r_e \end{cases} \quad (2.18)$$

$$[B_i] = -\frac{\rho\delta}{2d\Delta t^2}(pnd_i^* - pnd^0) - \sum_{\substack{k \neq i, k \in S, \\ |\vec{r}_k - \vec{r}_i| \leq r_e}} P_k w(|\vec{r}_k - \vec{r}_i|) \quad (2.19)$$

2.4.1 PPE source term with restricted compressibility

As the particle number density is a function calculated in a compact support and in a discrete domain composed by particles, numerical variations of the pnd may occur while particles enter and leave the compact support. Small variations on the particle number density leads to large variation in the pressure and spurious numerical oscillations were indeed reported in MPS simulations.

In order to mitigate such spurious pressure oscillations, Arai et al. (2013) adopted a smoothing factor to the main diagonal of the matrix of coefficients ($[A]$) of the PPE linear system, called compressibility coefficient (α). Then, the source term with the so-called “restricted compressibility” is obtained as follows:

$$[\nabla^2 P^{n+1}]_i - \alpha \frac{\rho}{\Delta t^2} [P^{n+1}]_i = -k \frac{\rho}{\Delta t^2} \frac{[pnd^*]_i - pnd^0}{pnd^0}, \quad (2.20)$$

where k is a pressure smoothing coefficient attributed to the particle number density deviation condition. Arai et al. (2013) suggests to adopt $\alpha = 10^{-8}$. Meanwhile, Bellezi et al. (2009) concluded that there is an optimized pressure smoothing coefficient k for each combination of resolution (l_0) and time-step (Δt). In a practical sense, both coefficients introduce a small compressibility to the system in a way the spurious pressure oscillation are “absorbed”.

2.4.2 Divergence-free condition for PPE source term

The restricted compressibility approach mitigates the numerical spurious oscillation of the computed pressure and improves the stability of the computations by increasing the diagonal elements of the matrix. However, its behavior is affected by the length scale of the problem. For small length scale problems, the simulations are less stable. On the other hand, in the large length scale problems, the simulations are more stable with effective mitigation of the high frequency numerical spurious numerical oscillations, but the flow becomes compressible so that the low frequency compression waves might be computed. In order to overcome the effect of the length scale, Tanaka and Masunaga (2010) introduced the quasi-compressibility formulation, which consists in an additional divergence-free condition term to PPE source term. The source term from Tanaka & Masunaga (2010) was later rewritten in the form of the equation 2.21 by Lee et al. (2011):

$$[\nabla^2 P^{n+1}]_i = (1 - \gamma) \frac{\rho}{\Delta t} \nabla \cdot \vec{u}_i^* - \gamma \frac{\rho}{\Delta t^2} \frac{[pnd^*]_i - pnd^0}{pnd^0} \quad (2.21)$$

where γ is a numerical parameter that should be adjusted. The first term in the right side of Equation 2.21 is the divergence-free condition and the second term in the right-hand side of Equation 2.21 is the particle number density variation condition.

In this formulation, a larger γ yields large pressure oscillations while a smaller γ turns the flow artificially compressible. Considering such tradeoff, Lee et al. (2011) defined as suitable a coefficient γ in the range between $\gamma = 0.01$ and $\gamma = 0.05$, regardless of the length scale of the problem.

2.4.3 PPE source term with time-scale correction

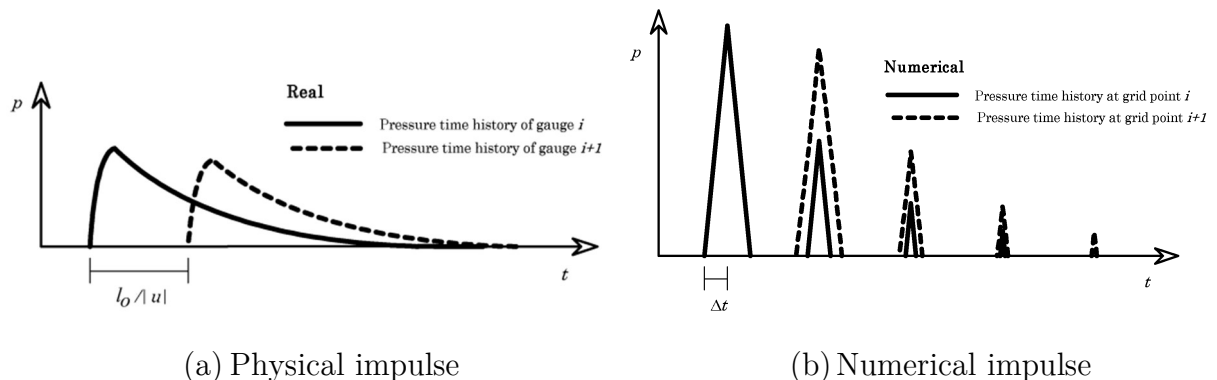
Recently, Cheng et al. (2018) adopted an improved source term to the simulation of wave impact phenomena in floating structures. Although the PPE source term with divergence-free condition (Lee B. H., Park, Kim, & Hwang, 2011) solved the

problem regarding the length scale dependence, the high frequency numerical oscillation is still time-scale dependent because the pressure computed from the particle number density variation condition is amplified by a factor $1/\Delta t^2$. In other words, the amplitude of the spurious pressure oscillation increases as the time-step decrease.

This improved PPE source term is based on the time-scale correction of the particle-level collisions. In particle-level, the collisions among the Lagrangian particles might occur at each time step. Since collision is a time-discontinuous phenomenon, numerically the duration of the collision last Δt (numerical time-step). Nevertheless, then physically the duration of the collision last $\delta t = l_0/c_s$, where c_s is the propagation velocity of the collision front.

Such approach was first proposed by Cheng and Arai (2002) for a Finite Differences Method (FDM) and the concept of such mismatch is illustrated by Figure 2.1. As the momentum conservation is ensured by the governing equation, the numerically calculated impulse and the physical impulse should be equal. Then, the numerical pulses (Figure 2.1-b) of shorter duration must have a higher magnitude than the physical pulses (Figure 2.1-a).

Figure 2.1 – Duration of numerical and physical impulsive phenomenon



Source: Cheng and Arai (2002).

Considering the CFL stability condition for a explicit numerical scheme and the ratio between the magnitude of the numerical collision loads and the physical

collision loads, the relation between the numerical duration and the physical duration of the pulses is given by Equation 2.22:

$$C_r = \frac{c_s \Delta t}{\delta t} \quad (2.22)$$

where C_r is the Courant number for the numerical stability of the explicit calculations. In the MPS particle simulations, the Courant number is usually limited to 0.2.

In this way, a new PPE source term is proposed based on the particle number density deviation condition and the divergence-free condition as follows:

$$[\nabla^2 P^{n+1}]_i = c_s \frac{\rho}{l_0} \nabla \vec{u}_i^* - c_s^2 \frac{\rho}{l_0^2} \frac{[pnd^*]_i - pnd^0}{pnd^0} \quad (2.23)$$

2.5 PRESSURE GRADIENT

2.5.1 Improved gradient model

In order to obtain only repulsive forces between the particles to avoid particle clustering and, as a consequence, improve the numerical instability of the method, Koshizuka et al. (1998) proposed an improved gradient operator in which the pressure related to the i -th particle was replaced by the pressure \widehat{P}_i , which is the minimum pressure considering the i -th particles and all its neighbors:

$$[\nabla P]_i = \frac{d}{pnd^0} \sum_{j \neq i} \left[\frac{(P_j - \widehat{P}_i)}{|\vec{r}_j - \vec{r}_i|^2} (\vec{r}_j - \vec{r}_i) w(|\vec{r}_j - \vec{r}_i|) \right] \quad (2.24)$$

2.5.2 First-order gradient model

Although the problem of the particle clustering can be solved by the gradient model proposed by using Eq. 2.24, it is a numerical approximation of the derivative obtained directly from the weight function with 0-th order accuracy, of which the numerical error is relatively large for non-isotropic particle distributions. The practical outcome is poor conservation of energy and momentum due to numerical damping.

Then, Iribe and Nakaza (2011) proposed an improved gradient model with first-order accuracy based on a Taylor series expansion:

$$[\nabla P]_i = \overrightarrow{C}_i \sum_{j \neq i} \left[\frac{(P_j - \hat{P}_i)}{|\overrightarrow{r}_j - \overrightarrow{r}_i|^2} (\overrightarrow{r}_j - \overrightarrow{r}_i) w(|\overrightarrow{r}_j - \overrightarrow{r}_i|) \right] \quad (2.25)$$

where \overrightarrow{C}_i is a matrix containing coefficients of renormalization that depend only upon the distribution of the particles within the neighborhood of the i -th particle. For two-dimensional cases, \overrightarrow{C}_i is a 2x2 matrix while, for three dimensional problems, \overrightarrow{C}_i is a 3x3 matrix.

$$\overrightarrow{C}_i = \left[\sum_{j \neq i} w(|\overrightarrow{r}_j - \overrightarrow{r}_i|) \left(\frac{\overrightarrow{r}_j - \overrightarrow{r}_i}{|\overrightarrow{r}_j - \overrightarrow{r}_i|} \otimes \frac{(\overrightarrow{r}_j - \overrightarrow{r}_i)^T}{|\overrightarrow{r}_j - \overrightarrow{r}_i|} \right) \right]^{-1} \quad (2.26)$$

From the practical experience of the authors, as a consequence, the numerical convergence of the particle models was achieved for larger values of distance between particles (l_0) than in the case of simulations which adopt the gradient model of Eq. 2.24.

2.6 FREE-SURFACE DETECTION TECHNIQUES

The free surface particles are the Dirichlet-type boundary conditions to the pressure calculation by the linear system of PPE, i. e., $\{P_i = P^{atm} | i \in BC\}$, where P^{atm} is the atmospheric pressure and BC the set of free surface particles. In the case particles within the fluid domain are mistakenly identified as free surface particles, large errors in the pressure calculation might occur. Therefore, an effective technique for the free surface detection is required for consistent pressure calculation.

2.6.1 Original free-surface detection

The original proposal for the free surface detection by Koshizuka et al. (1995) was based only on a particle number density condition. The criterion established a lower threshold as a proportion of the initial particle number density ($\beta \cdot pnd^0$), which a particle must have to not belong to the free surface. The condition is presented below:

$$i \in BC, \quad pnd^* < \beta \cdot pnd^0 \quad (2.27)$$

Koshizuka and Oka (1996) performed a parameter analysis and achieved that $0.8 \leq \beta \leq 0.99$ is a suitable range for a proper free surface detection. In their next works, $\beta = 0.97$ was often adopted.

2.6.2 Free-surface detection by number of neighbor particles

However, the original algorithm (Eq. 2.27) was very sensitive for small variations in the particle number density and often particles within the fluid were wrongly identified as free surface particles. Such error contributed to an increase in the spurious numerical oscillations of the pressure calculated. In order to avoid that, Lee et al. (2010) introduced an additional criterion based on the number of particles within the neighborhood of a given particle (Eq. 2.28). Then, besides of a lower threshold for the particle number density, a lower threshold based on the initial number of neighbor particles ($\gamma \cdot N^0$) was also adopted:

$$i \in BC, \quad \begin{cases} pnd^* < \beta \cdot pnd^0 \\ N^* < \gamma \cdot N^0 \end{cases} \quad (2.28)$$

where N^* is the number of neighbor particles after the explicit part of a given particle, N^0 is the initial number of neighbor particles expected for a fully submerged particle and γ is the threshold coefficient. Lee et al. (2010) maintained $\beta = 0.97$ for the two-dimensional cases and indicated $\beta = 0.98$ for three-dimensional cases. Meanwhile, $\gamma = 0.85$ was suggested for the particle number criterion.

2.6.3 Free-surface detection by neighbor particle centroid deviation (NPCD)

The free surface detection technique based the number of particle criterion (Eq. 2.28) successfully avoided the misdetection of free surface particle within the fluid domain. However, the criterion was so conservative that usually a thick layer of free surface particles was often detected. As a layer of free surface particles with width

about only one particle is better, Tsukamoto et al. (2016) proposed an improved free surface detection algorithm named “neighborhood particle centroid deviation” (NPCD) technique.

Besides the particle number density criterion, a criterion based on the location of the centroid of the particle distribution within the compact support was introduced (Eq. 2.29). A free surface particle in which the neighborhood is only partially filled usually presents a large value for centroid deviation while fully submerged particles shows small deviations.

$$i \in BC \quad \begin{cases} pnd^* < \beta \cdot pnd^0 \\ \sigma > \varepsilon \cdot l_0 \end{cases} \quad (2.29)$$

where σ is the centroid deviation, calculated according to the Eq. 2.30, and ε is the cut parameter of the centroid deviation criterion.

$$\sigma_i = \frac{\sqrt{|\sum_{i \neq j} x_{ij} w_{ij}|^2 + |\sum_{i \neq j} y_{ij} w_{ij}|^2 + |\sum_{i \neq j} z_{ij} w_{ij}|^2}}{\sum_{i \neq j} w_{ij}} \quad (2.30)$$

where $w_{ij} = w(|\vec{r}_j - \vec{r}_i|)$, $x_{ij} = x_j - x_i$, $y_{ij} = y_j - y_i$ and $z_{ij} = z_j - z_i$.

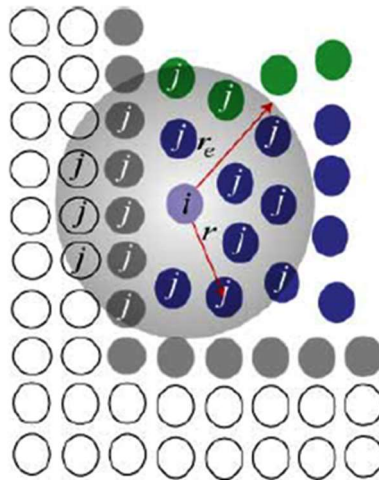
Tsukamoto et al. (2016) adopted as the most accurate thresholds $\beta = 0.97$ for the two-dimensional cases and $\beta = 0.98$ for three-dimensional cases in the case of the particle number density criterion. Besides, they defined $\varepsilon = 0.2$ as the most suitable value for both two-dimensional and three-dimensional cases.

The NPCD technique avoid the misdetection of free surface particles in the interior of the fluid domain and provide a fine layer of free surface particles. Moreover, the algorithm introduced minimal additional computational cost. Hence, the NPCD technique was adopted for all the MPS simulations of the present work.

2.7 RIGID SOLID BOUNDARY CONDITION

The solids are modeled as particles as well in the MPS method. The solid particles are Dirichlet-type boundary conditions for the velocity and position. As the velocity and position of the particle are previously known, its values are attributed in the explicit part of the algorithm. There are two types of solid particles in the MPS method: the wall solid particles and the dummy solid particles. In Figure 2.2, the wall solid particles are the grey particles while the dummy solid particles are the white ones.

Figure 2.2 – Sketch of the neighborhood of a fluid particle



Source: Tsukamoto (2006)

The wall solid particles belong to the first layer of solid particles that have direct contact to fluid particles (the blue and green particles in Figure 2.2). Then, adjacent layers of dummy solid particles are added opposite to the wetted side of the wall solid particles in order to completely fill the truncated neighborhood of the wall solid particles. The number of adjacent layers of dummy solid particles is defined in order to fulfill the solid particle neighborhood, thus based on the neighborhood radius adopted by the simulation. As the solid bodies are modeled only as rigid bodies in the present study, the dummy particles follow the motion of the wall solid particles associated to them.

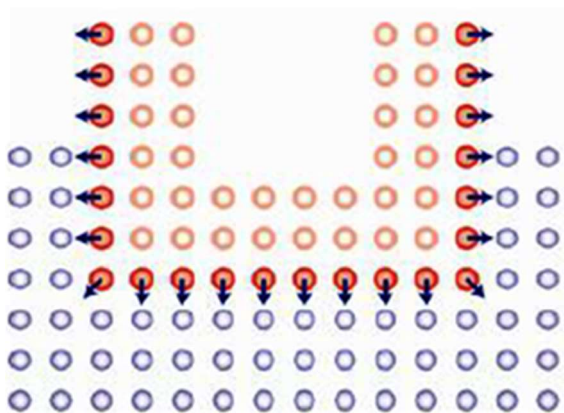
In the MPS simulation system of the present work, three types of rigid solids could be modelled:

- 1) The **fixed solid**, in which the velocity is imposed as zero,
- 2) The **imposed motion solid**, also called forced solid, in which a non-zero velocity is attributed and
- 3) The **floating solid**, in which the motion is attributed based on the external forces acting on the body, including the pressure due to the fluid.

2.7.1 Floating body

Sueyoshi and Naito (2002) first proposed a formulation for the floating solid to the MPS method. The velocity and position of the floating solid are calculated in the explicit part of the algorithm. Its position and velocity are obtained from the motion equation of the rigid solid after the calculation of the external forces acting on the floating body. An example of a two-dimensional floating solid is depicted by Figure 2.3, in which the fluid particles are blue, the solid wall particles are red-filled and the dummy solid particles are white-filled.

Figure 2.3 – Sketch of the modeling of the free solid



Source: Tsukamoto (2011).

The physical properties of the body, such as its mass, center of gravity and moment of inertia, and the external forces and linear momentum acting on the body are required in order to solve the motion equation of the solid. The physical properties of the floating body are defined as input data in the present approach. Meanwhile, the external forces should be calculated.

Only the gravity and the forces from the fluid are considered as external forces acting on the floating body. The force and linear momentum due to the solid are calculated from the summation of the individual contributions of the pressure acting on the wall solid particles, as presented by the Eq. 2.31 and the Eq. 2.32, respectively.

$$\vec{F} = \sum (-P_i S_i \vec{n}_i) \quad (2.31)$$

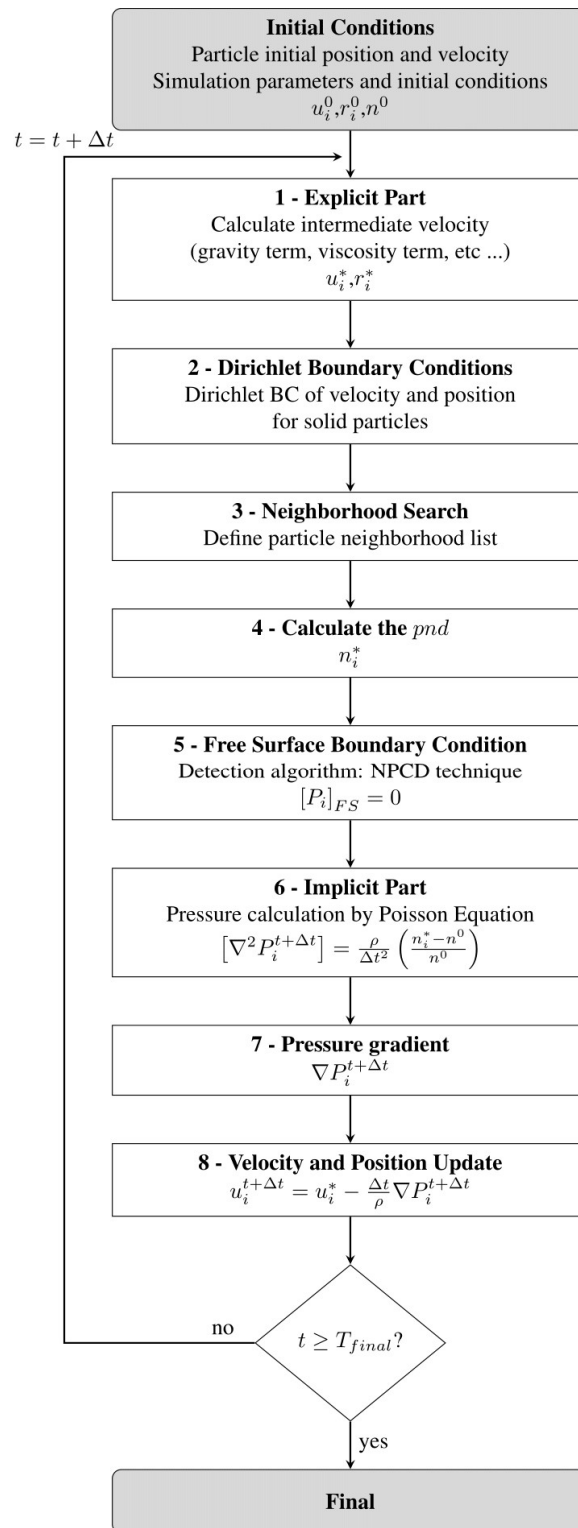
$$\vec{M} = \sum (\vec{r}_i \times \vec{n}_i) \quad (2.32)$$

where \vec{F} is the external force from the pressure integration, \vec{M} the linear momentum from the pressure integration, \vec{n}_i the vector normal to the surface of the solid related to the i -th wall solid particle, which could be defined as input data or calculated during the initialization of the simulation, S_i is the projected area for each particle and \vec{r}_i the vector with the relative position of the i -th wall solid particle to the center of gravity of the floating body. The projected area of a single particle is usually defined as $S_i = l_0$ for two-dimensional problems and $S_i = l_0^2$ for three-dimensional problems.

2.8 ALGORITHM OF THE METHOD

The algorithm of the method is illustrated by the flowchart of Figure 2.4.

Figure 2.4 – Flowchart of the MPS method algorithm



Source: figure from the author.

3 CHAPTER THREE: SLOSHING MITIGATION BY PERFORATED SWASH BULKHEAD WITH OPTIMIZED GEOMETRY

3.1 ABSTRACT

The sloshing is a highly nonlinear problem that has different behaviors for different filling levels. Hence, most of the previously proposed techniques to mitigate sloshing, such as baffles, are effective for a small range of filling levels or involve floating devices, which are very difficult to install in practical applications. In such context, the first study of the present Thesis consists in the proposal of a perforated swash bulkhead with optimized geometry to mitigate the sloshing in rectangular tanks. It suppresses the sloshing at any filling level for the frequency range encompassing the three first resonance modes. Summarizing, it is a very effective technique that is also simple and very easy to install. The first step of the study comprises the investigation of the effects of the bulkhead open-area ratio in the sloshing flow based on a comprehensive parameter analysis. Then, a function of the optimized open-area ratio as function of the filling ratio is proposed. Three different swash bulkhead models with optimized geometry are evaluated and have been proven to successfully mitigate the sloshing. The findings of this study were published as a journal article (Bellezi et al., 2019).

3.2 INTRODUCTION

The liquid containment in partial filling condition and under forced motion is present in a wide range of situations, from tuned liquid dampers (TLD) on buildings to offshore oil platforms. When it is excited by motions close to the tank-fluid system lowest resonant modes, an extremely violent flow, known as sloshing, may occur. In TLDs, the geometry of the tanks and the fluid filling level are set in order to the resonance frequency of the tank match that of the structural vibration of the building. As the action of wind or earthquakes makes the building vibrate, the motion of the fluid within the TLD, out of phase with the structural vibration, suppress the motion of the building and improves its comfort and safety. To introduce a damping in the tank-fluid mechanical system, perforated screens are a suitable technique with relatively simple implementation, but complex nonlinear behavior. A deeper understanding about the effects of perforated screen on the fluid motion is important to the design of TLDs, thus several recent efforts were focused on the modelling of the sloshing in TLDs with perforated screens (Tait, El Damatty, Isyumov, & Siddique, 2005), (Love & Tait, 2010), (Molin & Remy, Experimental and numerical study of the sloshing motion in a rectangular tank with a perforated screen, 2013), among others. Simulations of the coupled dynamic of main structures and the TLDs and the assessment of optimized system performance were performed by Kaneko and Ishikawa (1999) and Tait, Isyumov and El Damatty (2008).

In liquid storage and transportation systems, such as oil platforms, shuttle oil tankers, LNG carriers and floating liquified natural gas (FLNG) platforms, the occurrence of sloshing is dangerous and highly undesirable since it could result in damage of the tank inner structures and may affect the motion of the vessel while coupled with the loads due waves, wind and current. While the sloshing in TLDs usually occurs in a short frequency range close to the building structural vibration mode, a much wider range of frequencies associated to winds, waves and current, must

be evaluated in transportation systems and offshore industry. Thus, classification societies usually define very strict rules for the operation of such naval structures, as operations under filling levels between 10% and 70% must be avoided (Lloyd's Register, 2012).

Within this context, the control or mitigation of the sloshing is an important issue to the design of buildings and naval and offshore structures in order to increase the safety of the operations or even enlarging their operation envelopes. One common approach consists on the placement of internal structures within the tanks such as baffles or columns. Other technique consists upon the compartmentalization of tanks by using non-watertight bulkheads, such as wire-screens, slat-screens and perforated swash bulkheads, which are considered more efficient than baffles or columns for sloshing mitigation (Faltinsen & Timokha, 2009).

3.3 LITERATURE REVIEW

In the 70's, focusing on the design of very large crude oil carriers (VLCCs), Akita (1967) and Sawayanagi and Matsumoto (1977a), (1977b) and (1978) carried out experimental studies and confirmed the effectiveness of the swash bulkheads. Regarding the flow through perforated bulkheads, Laws and Livesey (1978) observed that the pressure loss caused by the perforations could be modelled as quadratic regarding the flow velocity through the porous bulkhead. Tait, El Damatty, Isyumov and Siddique (2005) concluded that the phenomenon is highly nonlinear when under large motions that often occurs in practical applications. More recently, Firoozkoohi (2013) performed an extensive set of experiments for a two-dimensional setup of a tank equipped with a slat-screen bulkhead under harmonic sway motion considering solidity ratios (S_n) (the ratio between the watertight area of the bulkhead and the tank cross-section area) above 40% and filling ratios of $h/L = 0.4$ and 0.12 , where h is the filling level and L is the length of the tank.

On the other hand, analytical and semi-analytical models were proposed as well. Firoozkoohi and Faltinsen (2010), Faltinsen, Firoozkoohi and Timokha (2011a) (2011b) modelled the problem by a potential flow through a multimodal description. The tank was divided into two compartments separated by a porous bulkhead that allows the flow between them. The blockage coefficient of the flow on the bulkhead is estimated by accounting for the correct geometry of slots and slats. For a tank with $h/L = 0.4$, the analytical results agree qualitatively with experimental data for small motions but it is unable to predict accurately both the free surface elevation on resonance conditions and the frequency of the compartmented resonant mode. Molin and Remy (2013) also adopted the potential flow theory and modelled the bulkhead as a porous boundary with quadratic pressure loss. Only one perforated bulkhead with open-area ratio ($\Phi = 1 - S_n$) of 18% was evaluated considering different excitation motion amplitudes in a tank with $h/L = 0.4$. The results show good agreement with the

experiments for small amplitude excitation, but discrepancies occur for larger amplitude motions as the nonlinearities of the phenomena become more significant. Despite the analytical approaches can provide valuable insights regarding the general behaviour of the sloshing flow on tanks with bulkheads, the accuracy of their results is limited by the simplification hypotheses of the flow as potential, such as the linearized free surface hypothesis. Furthermore, the pressure drop coefficient used to reproduce the effect of the bulkhead usually must be estimated experimentally.

In the last decades, numerical modelling and simulations to investigate the effects of the perforated bulkheads on sloshing were reported. Maravani and Hamed (2010) developed a simulation system based on finite-difference scheme on a staggered grid and Volume-of-fluid (VOF) method for free-surface tracking. A two-dimensional rectangular tank with a slat screen and with shallow water depth was simulated. The results show very good agreement with experimental results for the force on the tank under relatively small excitation motions. Firoozkooni, Faltinsen and Arslan (2015) used the open-source finite volume simulation system OpenFOAM to simulate a two-dimensional rectangular tank with finite water depth ($h/L = 0.4$). The numerical results presented good agreement with experiments of tanks under small amplitude motions even for the higher resonant frequencies. Xue et al. (2013) performed numerical simulations and experiments of a tank divided by a perforated bottom mounted baffle with one square-shaped hole. The numerical method adopted was based on a finite difference method (FDM), the free surface algorithm was based on the volume-of-fluid (VOF) technique and the turbulence was modelled by large eddy simulation (LES), and, from the free surface elevation data, the authors concluded that the perforated baffle provided better sloshing mitigation for low frequency motion, i. e., the first mode. Xue et al (2017) later performed experiments of several different vertical baffle configurations, including a perforated baffle and a watertight baffle, and provided dynamic pressure measurements for a wide range of frequencies in probes located both

at the tank wall and at the bulkheads. Yu et al. (2019) performed experiments of slat-screen bulkheads by evaluating different open-area ratios, different slot sizes, and different number of bulkheads within the tank for the highly nonlinear shallow liquid conditions. As a result, the authors identified, among the several combinations of the three parameters, the best ones to mitigate sloshing at shallow water.

Recently, due to their flexibility and effectiveness in modelling highly nonlinear interaction between structures with complex geometry and flows with large free surface deformation, fragmentation and merging, numerical approach based on Lagrangian meshless particle-based method have been adopted to investigate the effects of the baffles and internal structures on sloshing. Tsukamoto et al. (2011) simulated the sloshing phenomenon on a two-dimensional rectangular tank equipped with an elastically-linked baffle by using the Moving Particle Semi-implicit (MPS) method (Koshizuka & Oka, 1996). Chen et al. (2016) used the MPS method to assess the effectiveness of bottom mounted baffles and ring-shaped baffles to suppress sloshing. Specifically concerning sloshing in tanks with perforated bulkheads, Cheng et al. (2016) adopted the MPS method to investigate numerically the effects of the opening-area ratios of the bulkhead. The results show a gradual transition of the sloshing behaviour from that of clean tank to a tank with a watertight bulkhead as the open-area ratio of the perforated bulkhead decreases. Also, a high open-area ratio is better to mitigate the sloshing on the second mode while a low open-area ratio is better to the first mode. However, no further discussion on how those behaviours can effectively be used to control or mitigate sloshing were provided.

3.4 OBJECTIVES

Since the sloshing inside tanks with perforated bulkheads is an extremely nonlinear phenomena that may depend on many parameters other than the open-area ratio of the bulkhead, additional objectives of the present works are:

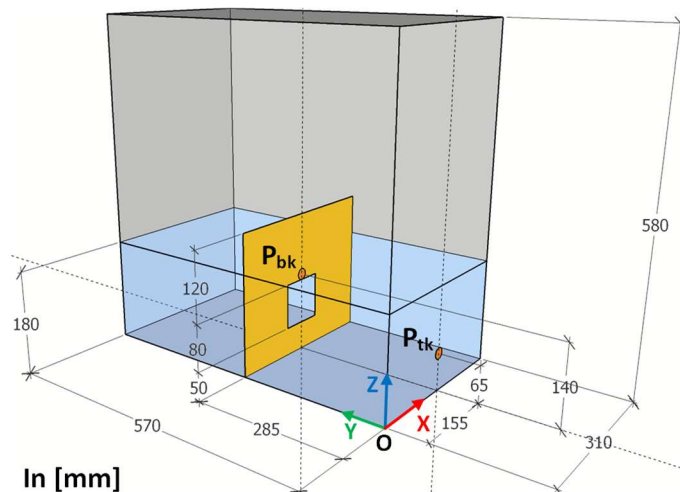
- a) To carry out a numerical investigation on the possible influence of other parameters such as shape and arrangements of the perforations, as well as a wider range of open area ratios and the nonlinearities due to excitation amplitude;
- b) To determine the optimal geometry of perforated bulkheads that is effective for the sloshing mitigation.

For this purpose, a series of simulations were carried out considering a box shaped tank with several geometries of the perforated bulkheads, a wide range of excitation frequency, two excitation amplitudes and three filling levels from shallow to high filling level. After that, the relation between the sloshing responses and the parameters were established. Based on the results, optimized parameter ranges that mitigate the sloshing loads and the formulation for the optimal distribution of the perforations that minimizes sloshing responses in all filling levels were obtained. Finally, three models of perforated bulkheads with optimized geometries capable to mitigate the sloshing in a wide range of filling levels and excitation frequencies encompassing the three lowest resonant modes were proposed and evaluated to confirm the effectiveness of the proposed formulation. In this way, the mechanisms of the sloshing flow through the perforated bulkhead and the optimized solutions for sloshing mitigation are provided.

3.5 VALIDATION

The first step of the study is the validation of the MPS-based simulation system for the simulation of the sloshing phenomenon in tanks with perforated bulkheads. For this purpose, the experimental results of Xue et al (2017) were used as reference. The experiments are based on a rectangular tank, equipped with several different types of vertical baffles for sloshing mitigation, under harmonic lateral excitation for a wide range of frequencies. Among the different tank configurations, three of them are of particular interest for this work: the tank without baffle, the tank with a watertight baffle and the tank with a perforated baffle. The configuration, main dimensions and the location of two pressure probes of the tank with perforated baffle are presented in Figure 3.1. The thickness of the baffle is 6 mm and the perforated baffle has one square hole with side of 8 cm. For the tank with watertight baffle and the clean tank, the basic dimensions and the locations of the pressure probes are the same.

Figure 3.1– Main dimensions and the positions of the pressure probes of the validation case with perforated baffle (based on Xue et al (2017))



Source: figure from the author.

The natural frequency of the first mode of sloshing for the tank without baffle is $\omega_1 = 6.403 \frac{rad}{s}$. Numerical simulations of the harmonic linear motion in Y direction in

the range of frequencies from $0.5\omega_1$ to $1.4\omega_1$ and amplitude of $A = 0.01m$ were performed for the three different tank configurations.

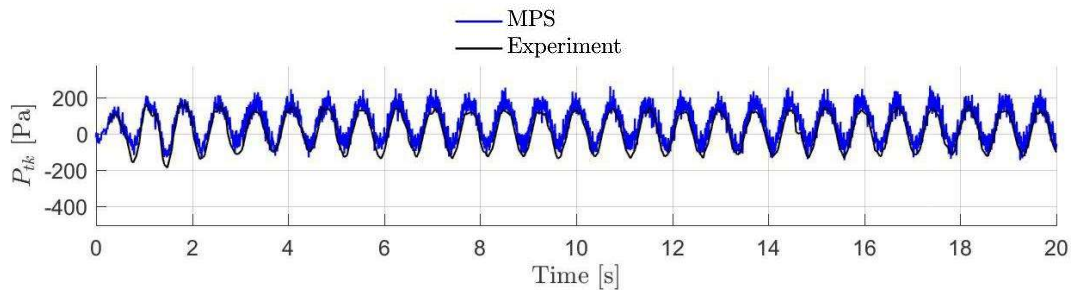
Regarding sloshing flow through perforated bulkheads, two aspects must be considered to define the resolution of the particle-based model: the flow past perforated plates and the sloshing itself. Notwithstanding, the flow through perforated plates consists on the computational bottleneck for such problem (Cheng, Bellezi, Amaro Junior, Arai, & Okada, 2016). Amaro Junior et al. (2015) studied a problem with very similar features: the performance of perforated breakwaters by using the MPS method. In the study, the convergence for the flow past circular holes was achieved by using a resolution of $D/l_0 = 10$, where D is the diameter of the holes and l_0 is the distance between particles of the numerical model. Fonfach, Manderbacka and Neves (2016) investigated the sloshing in a compartmented tank with a single-hole bulkhead by two-dimensional MPS simulations and achieved the numerical convergence with an even lower resolution of $D/l_0 \geq 5$. Furthermore, the numerical results from Fonfach, Manderbacka and Neves (2016) were validated against experimental data and presented good agreement, even for the complex cases in which the highly nonlinear phenomenon of wave breaking was dominant.

In the simulations carried out for the validation of the numerical method, the resolution adopted was $l_0 = 5 \text{ mm}$, i.e., $L_h/l_0 = 8$, where L_h is the side of the square hole of the tank with perforated baffle, the time step is $\Delta t = 5 \times 10^{-3} s$ and pressure relaxation coefficient of $k = 0.045$. The simulations were carried out for 30 cycles of the harmonic sway motion.

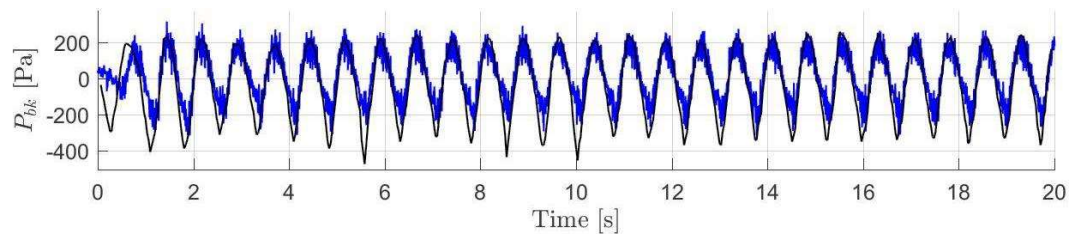
In the Figure 3.2 the time series of the pressure registered by the two probes are presented for the case of the tank with perforated baffle, under excitation with frequency of $\omega = 1.32\omega_1$ and amplitude of $A = 0.01m$. The raw pressure signal obtained numerically shows a sinusoidal profile with amplitude and phase closely related to that measured in the experiment. So, the numerical results presented good

agreement with experimental data for both the pressure probes P_{tk} and P_{bk} . The high frequency oscillations of the computed pressure are typical of particle-based simulations, and the results obtained here show oscillation magnitudes significantly lower than those of the physical low frequency dynamic pressure variations, so good agreement between the computed and the measured results was obtained.

Figure 3.2 – Pressure time series for the tank with perforated baffle– $\omega = 1.32\omega_1$, $A = 0.01m$ – computed results and experimental data (Xue, Zheng, Lin, & Yuan, 2017)



(a) Probe P_{tk} of the tank with perforated baffle



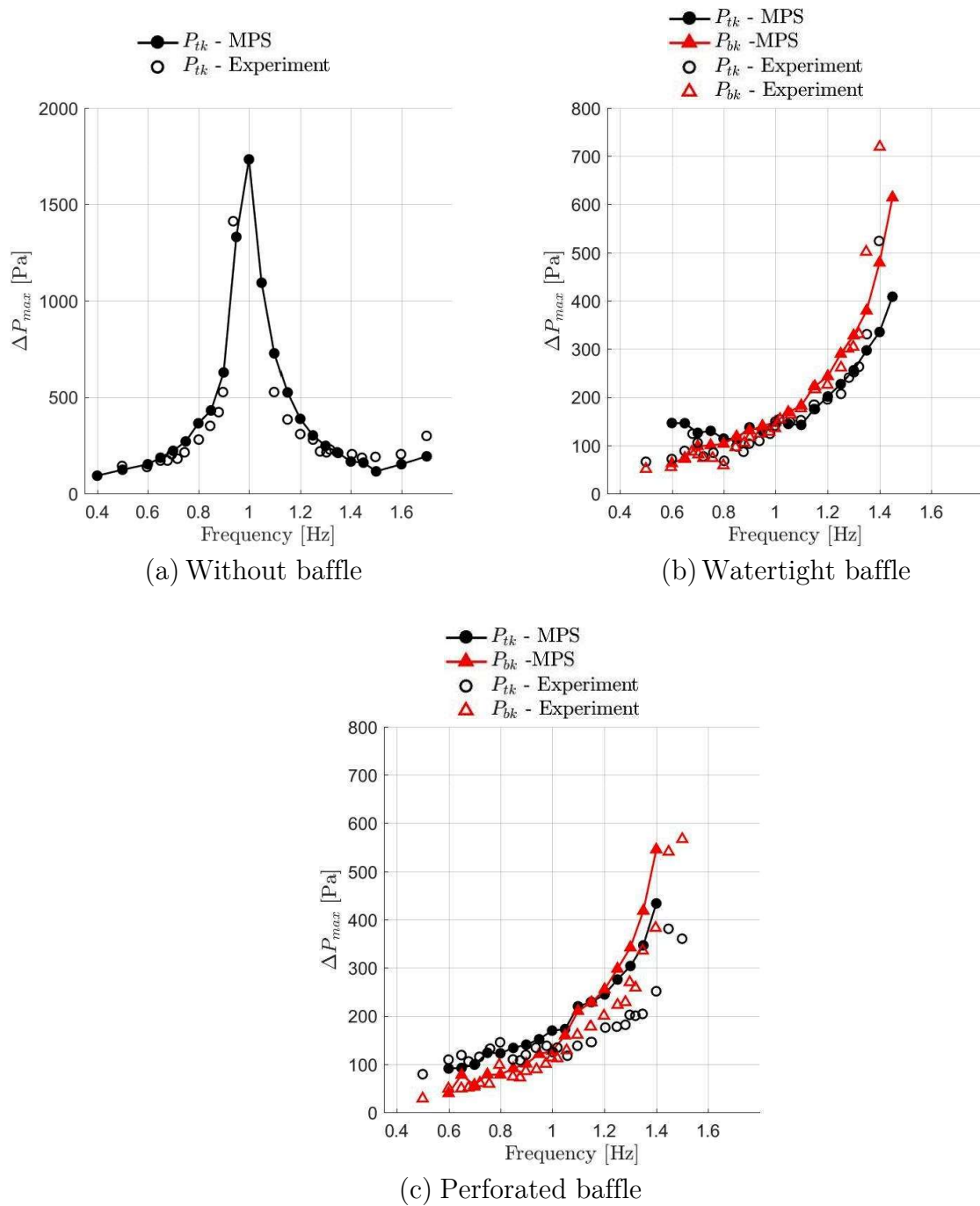
(b) Probe P_{bk} of the tank with perforated baffle

Source: figure from the author.

The maximum dynamic pressure as a function of the excitation frequency is presented in Figure 3.3 for the three tank configurations. In order to estimate the maximum dynamic pressure of the MPS results, only the last 10 cycles of the harmonic sway motion were accounted for. For the tank without baffle (Figure 3.3-a), only the pressure probe P_{tk} , located in the tank wall, is considered and shown in the figure. For the tanks with watertight baffle (Figure 3.3-b) and with perforated baffles (Figure 3.3-c), in addition to the pressure on the probe P_{tk} , the pressure of the probe P_{bk} , which is

located in the baffle and just above the position of the square-shaped perforation, are also presented.

Figure 3.3 – Maximum dynamic pressure as a function of motion frequency: computed results and experimental data (Xue, Zheng, Lin, & Yuan, 2017)



Source: figure from the author.

In the Figure 3.3-a, the experimental data was not provided in the range from $0.98\omega_1$ to $1.06\omega_1$ due to water spillage out of the tank (Xue, Zheng, Lin, & Yuan, 2017). Regardless the lack of experimental data in the most violent resonant frequencies, the numerical results for the dynamic pressure are very close to the experimental data for the remaining frequency range.

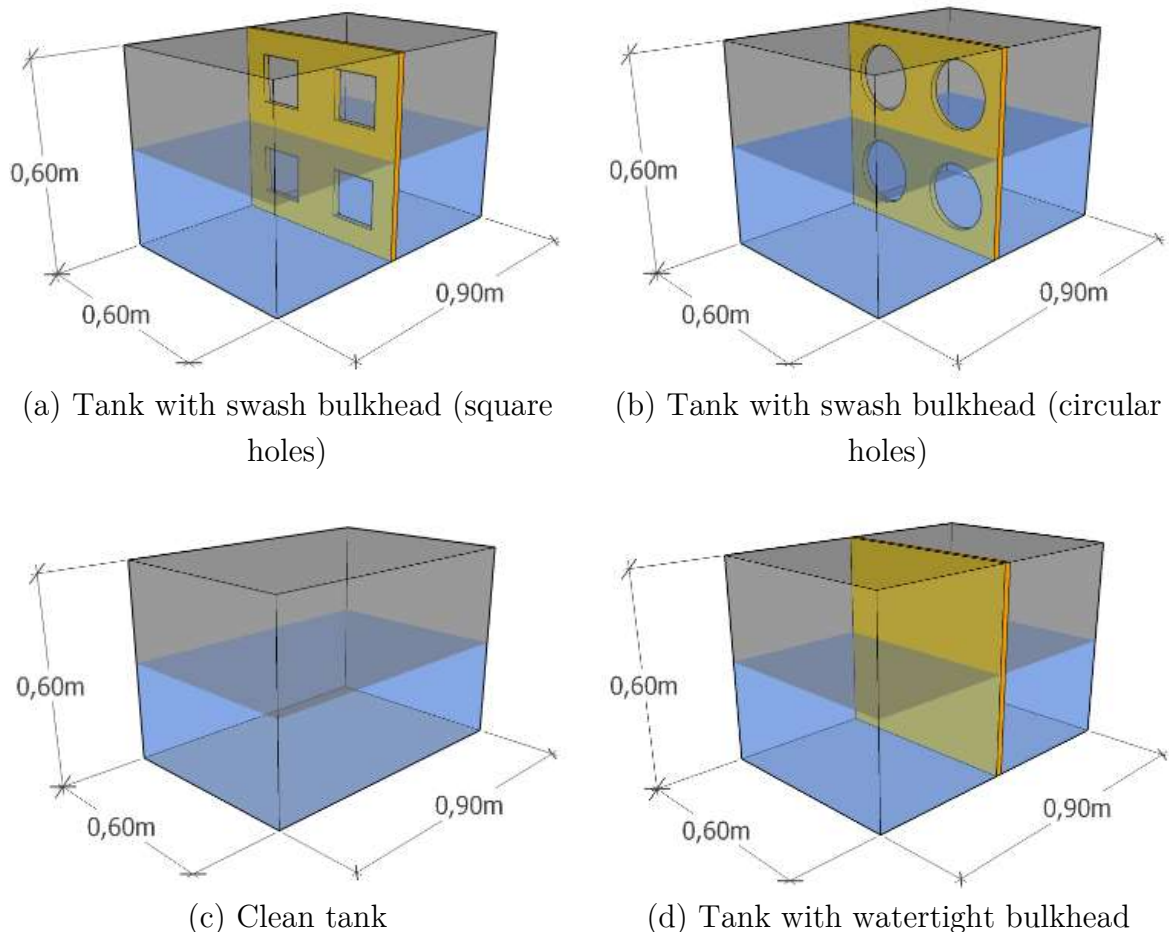
In the case of the tank with the watertight baffle (Figure 3.3-b), the numerical results are in good agreement with the experimental data as well. In the experiments, the maximum dynamic pressure at the probe P_{bk} is slightly higher than that for the probe P_{tk} for frequencies higher than $0.85\omega_1$. Such behavior is also observed in the numerical simulations and the dynamic pressure sharply increases for frequencies above $1.2\omega_1$ in both results. However, the measured maximum dynamic pressure is slightly higher than the numerical one for frequencies higher than $1.3\omega_1$. For these frequencies, a “beating” in the pressure signal (Xue, Zheng, Lin, & Yuan, 2017) was reported in the experiments but it was not observed in the computed results. The beating indeed increases the maximum dynamic pressure. Also, the tank geometries with the baffles are in such a way that the tanks are divided in two parts with width to length ratio of 1.1, which is within the range where complex modes due to the amplification of the perturbations in transverse direction, such as swirling, might occur. Nevertheless, swirling was not observed in the numerical simulations.

Finally and most important, the numerical and experimental results presented good agreement for the tank with the perforated baffle (Figure 3.3-c). The maximum dynamic pressure at the probe P_{bk} becomes higher than that for the probe P_{tk} as the frequency is higher than $1.1\omega_1$ for both the simulation and the experiment. Hence, in general, the numerical results obtained by using the MPS-based numerical simulation system presented good agreement with the experimental data presented by Xue et al (2017).

3.6 CASE OF STUDY

In the present study, the basic geometry of the tanks is a box with length L of 0.9 meters and width W and height H of 0.6 meters, as presented by Figure 3.4. A perforated bulkhead is placed in the mid length of the tank in the longitudinal direction. Two different geometries of the holes were considered: circular and square holes (Figure 3.4-a and Figure 3.4-b, respectively). Cases with a tank without bulkhead (Figure 3.4-c) and with a watertight bulkhead (Figure 3.4-d) were simulated as well.

Figure 3.4 – Configuration and main dimension of the tank models

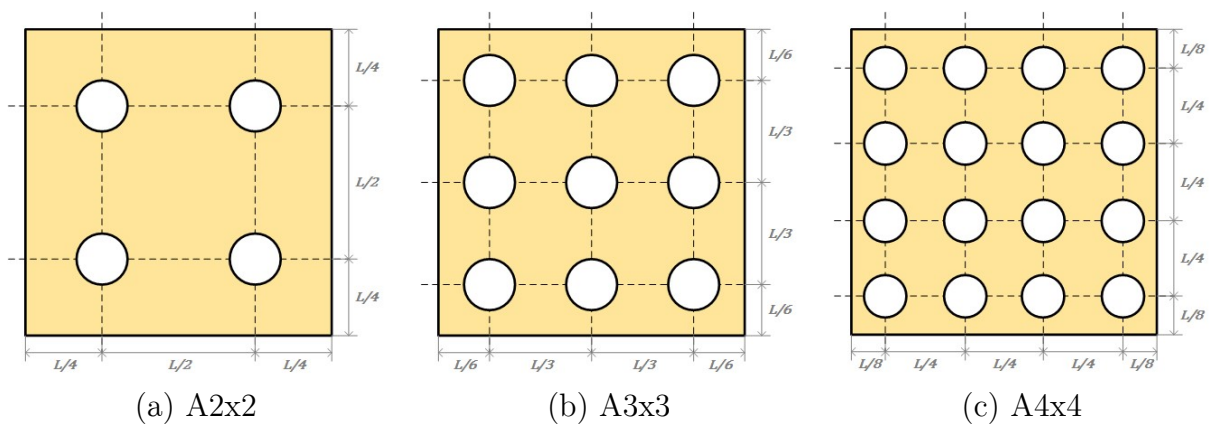


Source: figure from the author.

Several different layouts of perforated bulkheads were taken into account to determine the effect of the overall open area ratio (ϕ_o) of the bulkheads and the distribution of the holes on the sloshing. The different arrangements of the holes

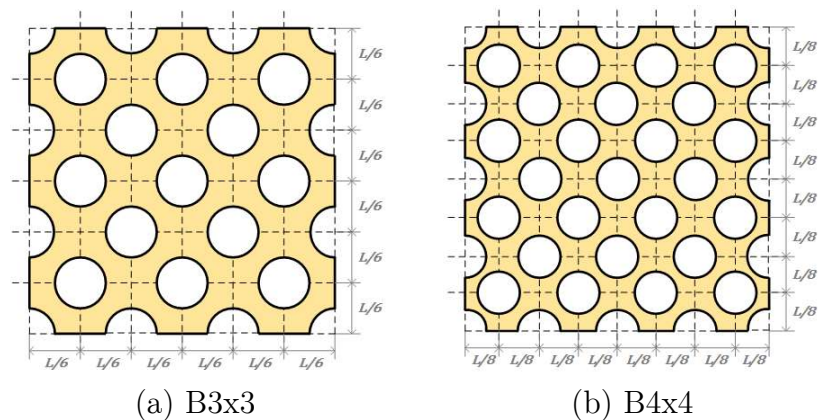
adopted herein could be divided into three basic layouts. The layout “A” is presented by Figure 3.5 and consists in a cluster of holes distributed along N rows and N columns, with $N = \{2,3,4\}$. To obtain bulkheads with larger overall open area ratio, in the layout “B” (Figure 3.6), additional holes were inserted between each row and columns of the layout “A”. Finally, the layout “C” (Figure 3.7) consist on N columns of 4 holes, with $N = \{1,2,3\}$.

Figure 3.5 – Swash bulkhead perforation arrangement – Model A



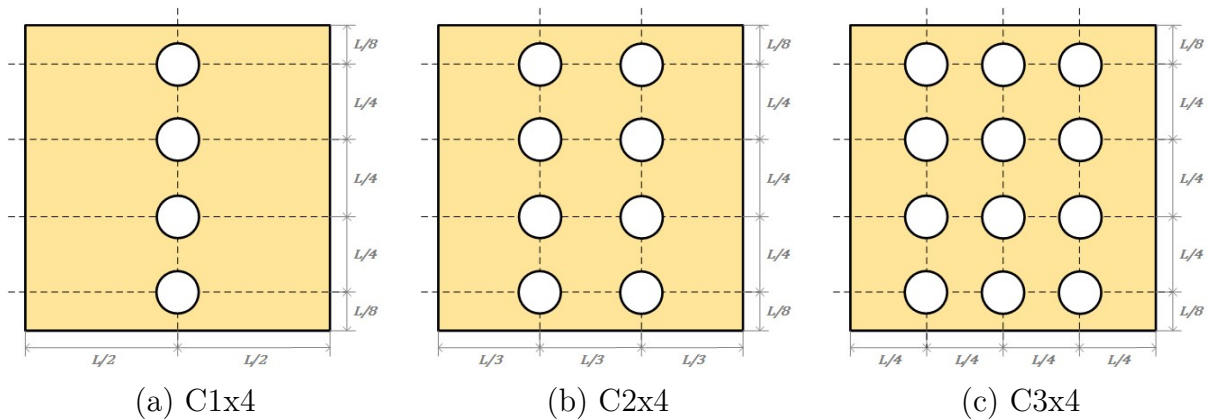
Source: figure from the author.

Figure 3.6 – Swash bulkhead perforation arrangement – Model B



Source: figure from the author.

Figure 3.7 – Swash bulkhead perforation arrangement – Model C



Source: figure from the author.

The sloshing behavior is highly related to the filling level, among other aspects. So, the analysis was carried out considering three different filling levels: h/H of 25% ($h/L = 0.167$), 50% ($h/L = 0.33$) and 75% ($h/L = 0.50$), where h is the liquid height. The three filling levels will be henceforth defined as “low”, “intermediate” and “high” filling levels, respectively.

For some arrangements, different hole sizes and hole geometries were adopted as well. The complete list of the perforated bulkheads evaluated in the present work and their respective overall open area ratio (ϕ_o) and submerged open area ratios (ϕ_s) for the three filling levels, both calculated by considering the bulkhead discretized in particles of $l_0 = 10$ mm, are presented by Table 3.1 (circular holes) and Table 3.2 (square shaped holes). Besides the concept of overall open area ratio of the bulkheads, it is interesting to introduce two additional parameters:

- a) **Local open-area ratio** at the fluid level (ϕ_l), which is the open area ratio measured locally considering an infinitesimal strip associated to the still filling level h .
- b) **Submerged open-area ratio** (ϕ_s), which is the ratio between the open area and the total cross section area of the submerged portion of the bulkhead, between the bottom of the tank and a given filling level h .

Table 3.1 – Bulkhead with circular holes dimensions and open-area ratio

| Case | Radius (r) [cm] | Submerged open area ratio (ϕ_s)[%] | | | Overall open area ratio (ϕ_o) $h/L = 0.67$ |
|------------|------------------------|---|--------------|-------------|--|
| | | $h/L = 0.167$ | $h/L = 0.33$ | $h/L = 0.5$ | |
| A2x2-C-P11 | 5.64 | 11.1 | 11.1 | 11.1 | 11.1 |
| A2x2-C-P25 | 8.46 | 25.0 | 25.0 | 25.0 | 25.0 |
| A2x2-C-P44 | 11.28 | 44.4 | 44.4 | 44.4 | 44.4 |
| A2x2-C-P69 | 14.10 | 69.4 | 69.4 | 69.4 | 69.4 |
| A3x3-C-P25 | 5.64 | 32.5 | 25.0 | 22.5 | 25.0 |
| A3x3-C-P56 | 8.46 | 63.9 | 56.2 | 53.6 | 56.2 |
| A4x4-C-P44 | 5.64 | 44.4 | 44.4 | 44.4 | 44.4 |
| B3x3-C-P50 | 5.64 | 49.4 | 50.5 | 50.1 | 50.0 |
| B3x3-C-P96 | 8.46 | 94.9 | 95.5 | 94.4 | 95.5 |
| B4x4-C-P86 | 5.64 | 85.7 | 85.7 | 85.7 | 85.7 |
| C1x4-C-P11 | 5.64 | 11.1 | 11.1 | 11.1 | 11.1 |
| C2x4-C-P22 | 5.64 | 22.2 | 22.2 | 22.2 | 22.2 |
| C3x4-C-P33 | 5.64 | 33.3 | 33.3 | 33.3 | 33.3 |

Table 3.2 – Bulkhead with square holes – dimensions and open-area ratio

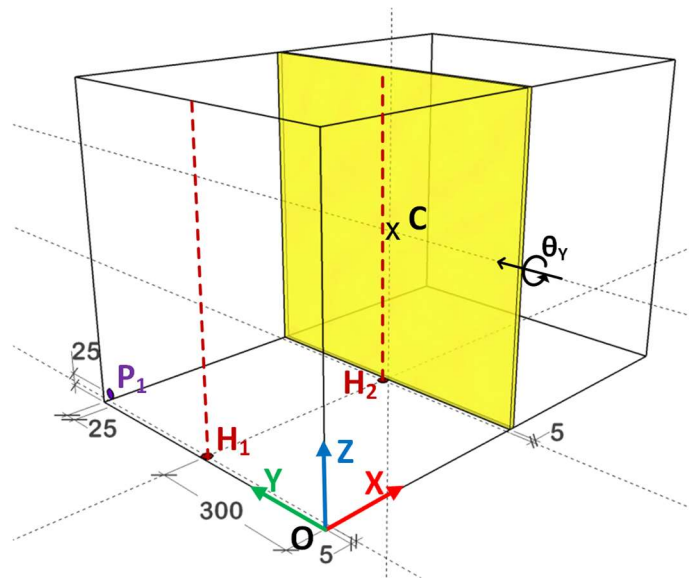
| Case | Side (L) [cm] | Submerged open area ratio (ϕ_s)[%] | | | Overall open area ratio (ϕ_o) $h/L = 0.67$ |
|------------|----------------------|---|--------------|--------------|--|
| | | $h/L = 0.167$ | $h/L = 0.33$ | $h/L = 0.50$ | |
| A2x2-S-P11 | 10 | 11.1 | 11.1 | 11.1 | 11.1 |
| A2x2-S-P25 | 15 | 25.0 | 25.0 | 25.0 | 25.0 |
| A2x2-S-P44 | 20 | 44.4 | 44.4 | 44.4 | 44.4 |
| A2x2-S-P69 | 25 | 69.4 | 69.4 | 69.4 | 69.4 |
| A3x3-S-P25 | 10 | 33.3 | 25.0 | 22.2 | 25.0 |
| A3x3-S-P56 | 15 | 62.5 | 56.3 | 54.2 | 56.3 |
| A4x4-S-P44 | 10 | 44.4 | 44.4 | 44.4 | 44.4 |

The nomenclature of each layout consists in three parts separated by hyphens: the first part defines the layout of the holes (according to Figure 3.5 to Figure 3.7); the second part defines the shape of the holes (**C**ircular or **S**quare) and the third part defines the overall open area ratio of the perforated swash bulkhead. The tank without bulkhead is called herein as “Model P100” or “clean” tank (equivalent to a tank with

overall open area ratio of 100%), and the tank with watertight bulkhead is called “Model P0” or “compartmented” tank (equivalent to a tank with overall open area ratio of 0%).

Figure 3.8 presents the locations of the pressure and wave probes. In each simulation, a harmonic pitch excitation was imposed to the tank around the axis Y , where C is located in the geometric center of the rectangular tank. Except specifically stated, the amplitude of the excitation is $\theta_0 = 6^\circ$. Besides the harmonic pitch motion, additional simulations with harmonic surge motion were carried out as well, for two different amplitudes of motion of 1% and 2% of the tank length.

**Figure 3.8 – Numerical tank: center of rotation and location of the probes
(dimensions in mm)**



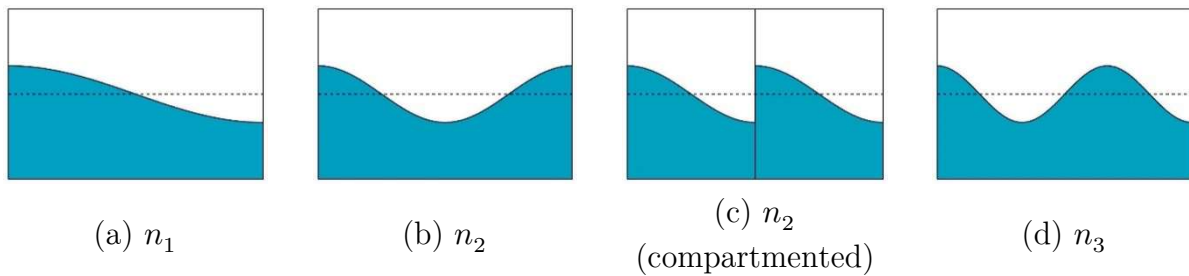
Source: figure from the author.

The free surface elevation was measured by two wave probes located in the longitudinal center plane of the tank ($y = 0.3\text{m}$). The H_1 wave probe is placed 5 mm from the tank left wall and the H_2 wave probe is located 5 mm to the left from the bulkhead. The pressure was measured by the pressure probe P_1 , located on the tank left wall, 25 mm from the bottom of the tank and 25 mm from the rear wall of the tank.

Simulations considering frequencies ranging from 0.5 Hz to 1.75 Hz were performed for each filling level and tank model, with an interval of 0.025 Hz between successive frequencies.

The frequency range adopted in this analysis covers the first three lowest sloshing resonant modes, which are sketched in Figure 3.9. In the present study, the “first mode” (n_1) consists on a stationary wave with wavelength $L/\lambda = \frac{1}{2}$ and is defined as the non-compartmented first antisymmetric resonant mode (Figure 3.9-a); the “second mode” (n_2) consists on a stationary wave with $L/\lambda = 1$ and could be both the first symmetric mode for the clean tank (Figure 3.9-b) and the first antisymmetric mode of the compartmented tank (Figure 3.9-c); the “third mode” (n_3) consists on the stationary wave with $L/\lambda = \frac{3}{2}$ and is the second antisymmetric mode of the clean tank (Figure 3.9-d). The resonant periods and frequencies for each mode in each filling level can be estimated analytically from the wave dispersion relation of potential Airy waves and the estimated values are given in Table 3.3.

Figure 3.9 – Typical sloshing resonant modes



Source: figure from the author.

Table 3.3 – Filling levels and analytical natural frequencies

| Filling level [mm] ($\frac{h}{L}$) | T_{n1} [s] (f_{n1} [Hz]) | T_{n2} [s] (f_{n2} [Hz]) | T_{n3} [s] (f_{n3} [Hz]) |
|---|----------------------------------|----------------------------------|----------------------------------|
| 150 (0.167) | 1.5493 (0.6455) | 0.8594 (1.1636) | 0.6474 (1.5446) |
| 300 (0.33) | 1.2154 (0.8228) | 0.7710 (1.2971) | 0.6212 (1.6098) |
| 450 (0.50) | 1.1214 (0.8918) | 0.7608 (1.3144) | 0.6201 (1.6127) |

A distance between particles of $l_0 = 10$ millimeters was adopted in the present work in order to obtain $D/l_0 \geq 10$ for circular holes with $D \geq 11.2$ cm and $L_S/l_0 \geq 10$ for square holes with $L_S \geq 10$ cm, where L_S is the side of the square hole. For such resolution, a time step of 0.5 milliseconds and a relaxation coefficient for the PPE of $k = 0.05$ were suitable numerical simulation parameters.

Given the large number of simulations and aiming to reduce the processing time, a MPS-based simulation system with hybrid parallelization by domain decomposition developed by Fernandes et al. (2015) was used in the present analysis. The hybrid parallelization consists on both shared memory and distributed memory frameworks, which allows the use of multiple processors per cluster node and multiple nodes of a computer cluster, respectively. Such simulation system enables a more efficient use of the computational resources given its homogeneous load balancing and supra-linear scalability (Fernandes, Cheng, Favero, & Nishimoto, 2015). The hardware used to perform the simulations is the computational Cluster of the Numerical Offshore Tank laboratory (TPN) of the University of São Paulo (USP). The Cluster has 48 nodes, each one contains 20 cores of AMD Shanghai processors with 2.66 GHz and 128GB of shared memory. By using only one node for each simulation, the processing times for a 40 seconds simulation range from between 4.0 hours (low filling level) and 12.5 hours (high filling level).

3.7 RESULTS

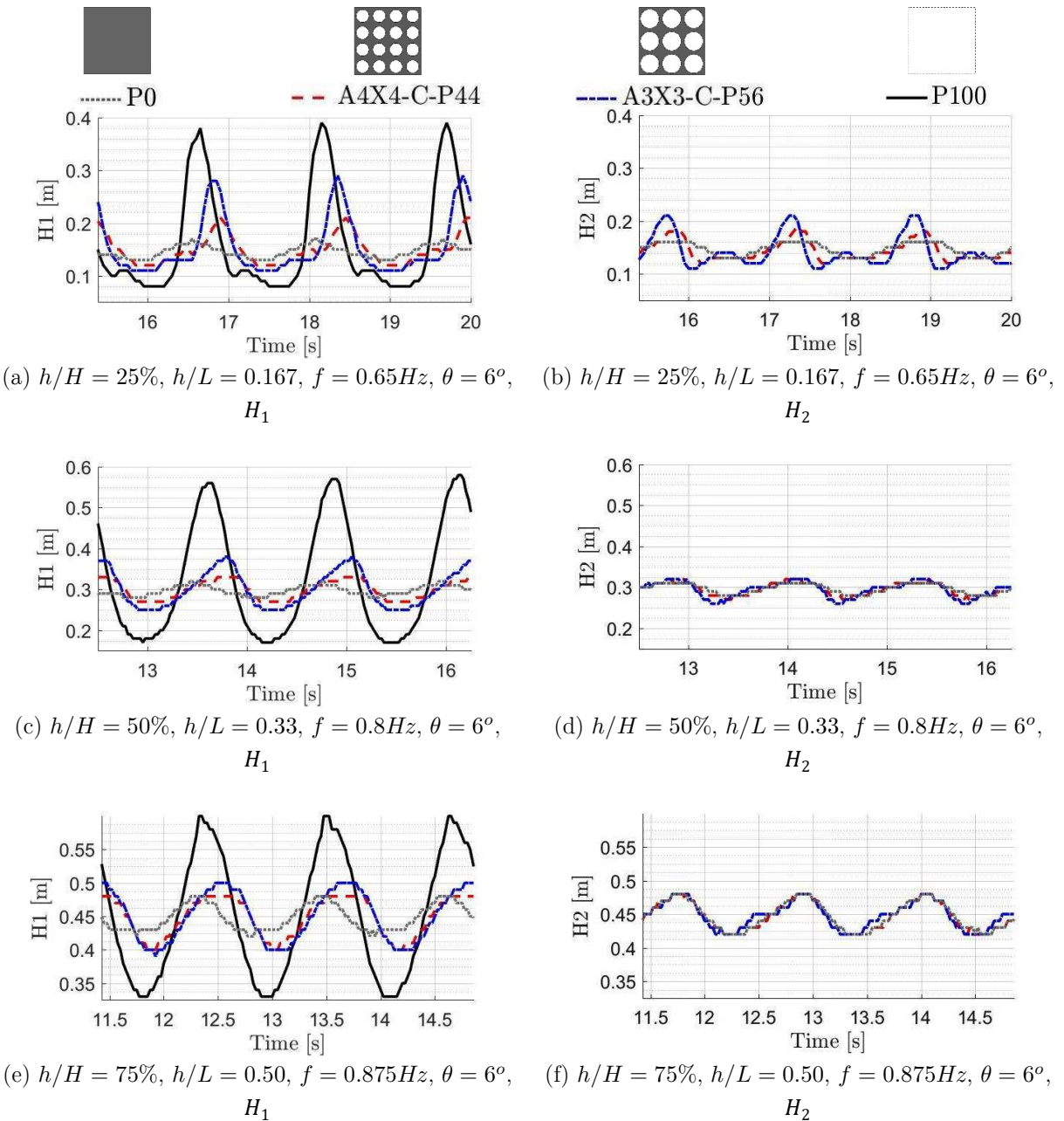
3.7.1 Effect of the open-area ratio: General Behavior

In Cheng et al. (2016) the investigations are limited to perforated bulkhead with the A2x2 layout (Figure 3.5-a) and a range of open area ratio was verified by changing the size of the circular holes. As a result, insights about the phenomenon were obtained. In the present study, a wide variety of parameters, which includes perforated bulkheads with different hole arrangements, hole geometries, number of holes and its size, were considered to study a broader range of the flow aspects.

The focus of the present section is to relate the overall effects of perforated swash bulkhead geometrical parameters on the sloshing mitigation. At first, simulations using four tank configurations were carried out considering excitation amplitude of 6 degrees and excitation frequencies close to the first antisymmetric resonant mode of the clean tank (n_1) for three filling ratios, 0.167, 0.33 and 0.50. The tanks are: Model P0 (compartmented tank), A4x4-C-P44, A3x3-C-P56 and Model P100 (clean tank). In Figure 3.10, the graphs of the left and right columns show, respectively, the time series of the free surface height at the wave probes H1, close to the tank wall, and H2, close to the bulkhead. The three rows of Fig. 8 are associated to the three filling levels.

According to the computed results, in general, the largest free surface displacements were observed for the clean tank in all the three filling levels. As the open area ratio of the perforated bulkhead decreases, the maximum free surface height on the left wall (H1) is increasingly mitigated for all the filling levels (Figure 3.10-a,c,e). However, the computed free surface heights on the bulkhead left wall (H2) show that the mitigation occurs for the low filling level (Figure 3.10-b) while, for the intermediate and high filling levels, the effects of the open area ratio is almost negligible (Figure 3.10-d,f).

Figure 3.10 - Time series of free surface height on (left) tank left wall (H_1) and (right) bulkhead left wall (H_2): first mode of sloshing motion (n_1)



Source: figure from the author.

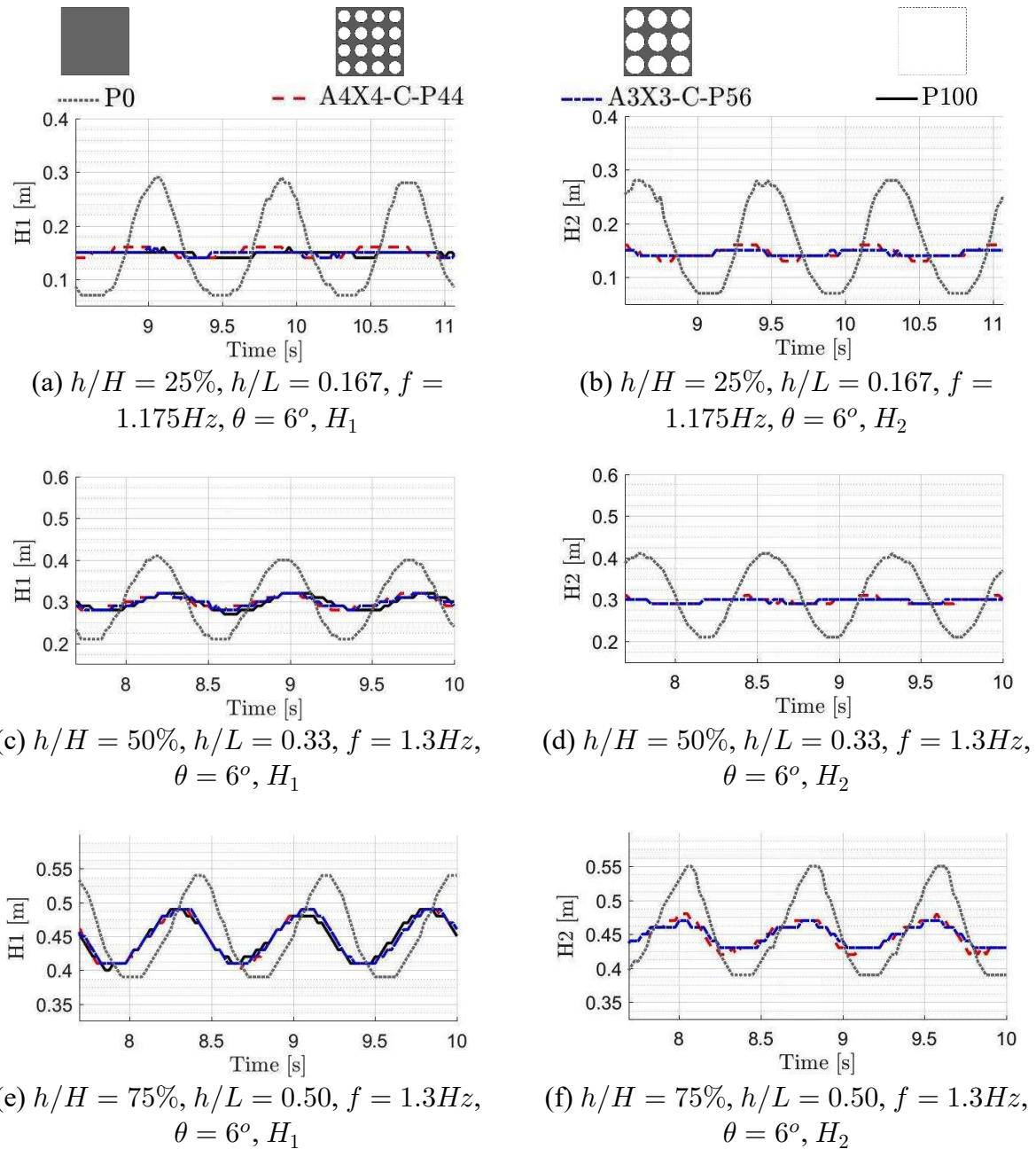
Such result regarding H_2 could be explained by the sloshing behavior in low filling levels, in which a travelling wave is formed in the clean tank, and the wave amplitude is reduced by damping and/or shift of the resonant frequency provoked by the decreasing open area ratio of the bulkhead. On the other hand, for the intermediate and high filling levels, the sloshing consists on a stationary wave and the small free

surface elevation observed in the bulkhead wall is because the knot of the stationary wave is located exactly in the longitudinal center of the tank.

The second analysis is concerned to the responses of the tanks excited in the frequencies close to the first symmetric resonant mode of the clean tank and the first antisymmetric mode of the compartmented tank (n_2) for each filling level. Figure 3.11 shows the time series of the free surface height at the tank (H_1) and bulkhead (H_2) left walls for such cases. For all the filling levels the largest free surface motion is observed for the tank with watertight bulkhead. On the other hand, under the excitations, almost no difference can be observed among the free surface height at H_1 and H_2 of the clean tank and the tanks with perforated bulkhead. Moreover, the perforated bulkhead provided large mitigation of the free surface heights in low and intermediate filling levels.

From the time series of the free surface height on the tank left wall (H_1), an average double amplitude of its elevation, simply denominated as “free surface elevation” henceforth, can be obtained by subtracting the average value of the minimum free surface heights from the average value of the maximum free surface heights in every cycle, except for the first 10 cycles of the tank harmonic motion, which were considered as transient ones and were neglected in the computation of the average values.

Figure 3.11 – Time series of free surface height on (left) tank left wall (H_1) and (right) bulkhead left wall (H_2): second mode sloshing motion (n_2)

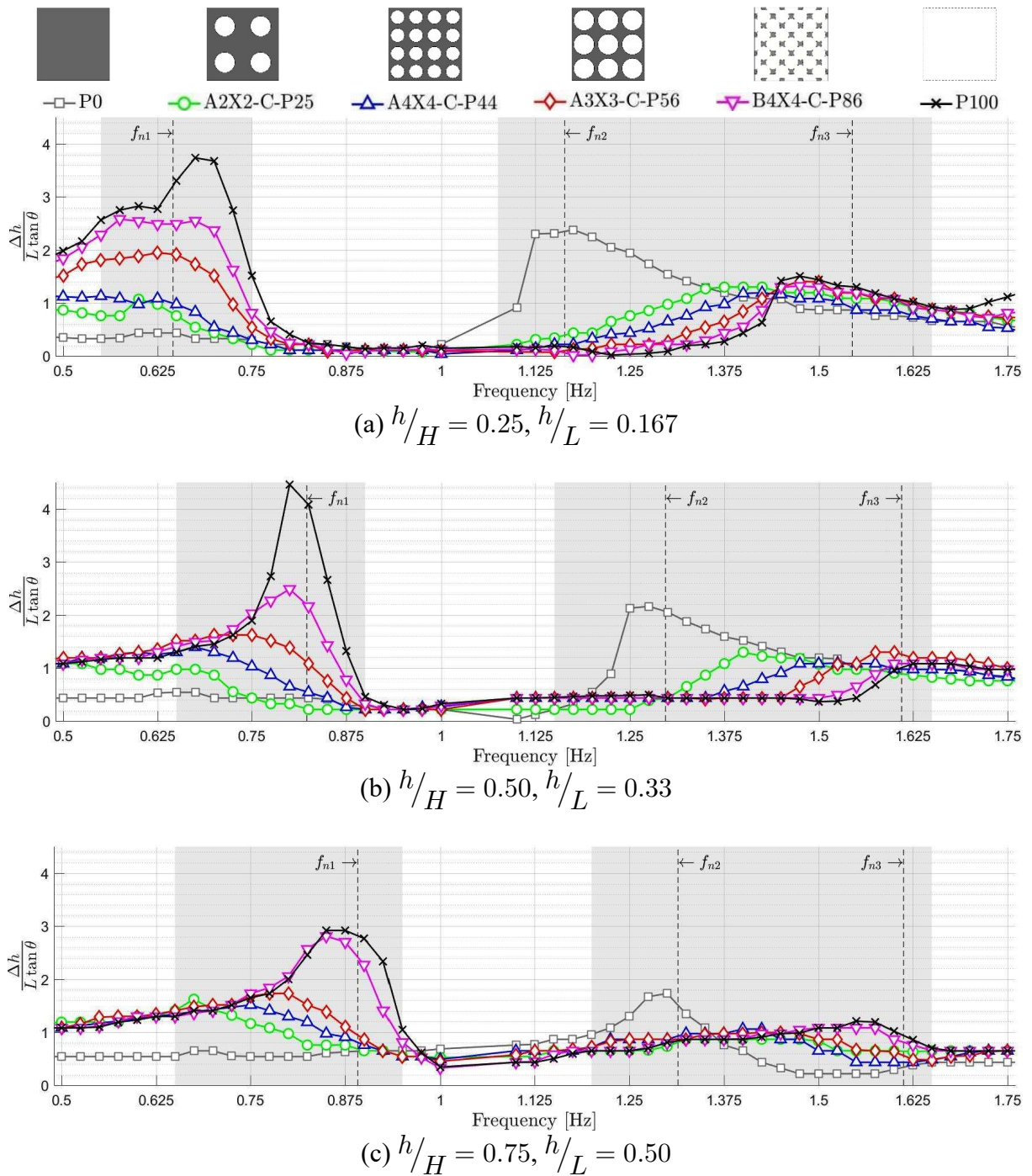


Source: figure from the author.

Figure 3.12 shows the computed free surface elevation in H_1 as function of excitation frequency considering the three filling levels for the clean tank, the tank with watertight bulkhead and tanks with perforated bulkheads with open area ratios ranging from 22% to 75%. The vertical axis is made dimensionless dividing the free surface

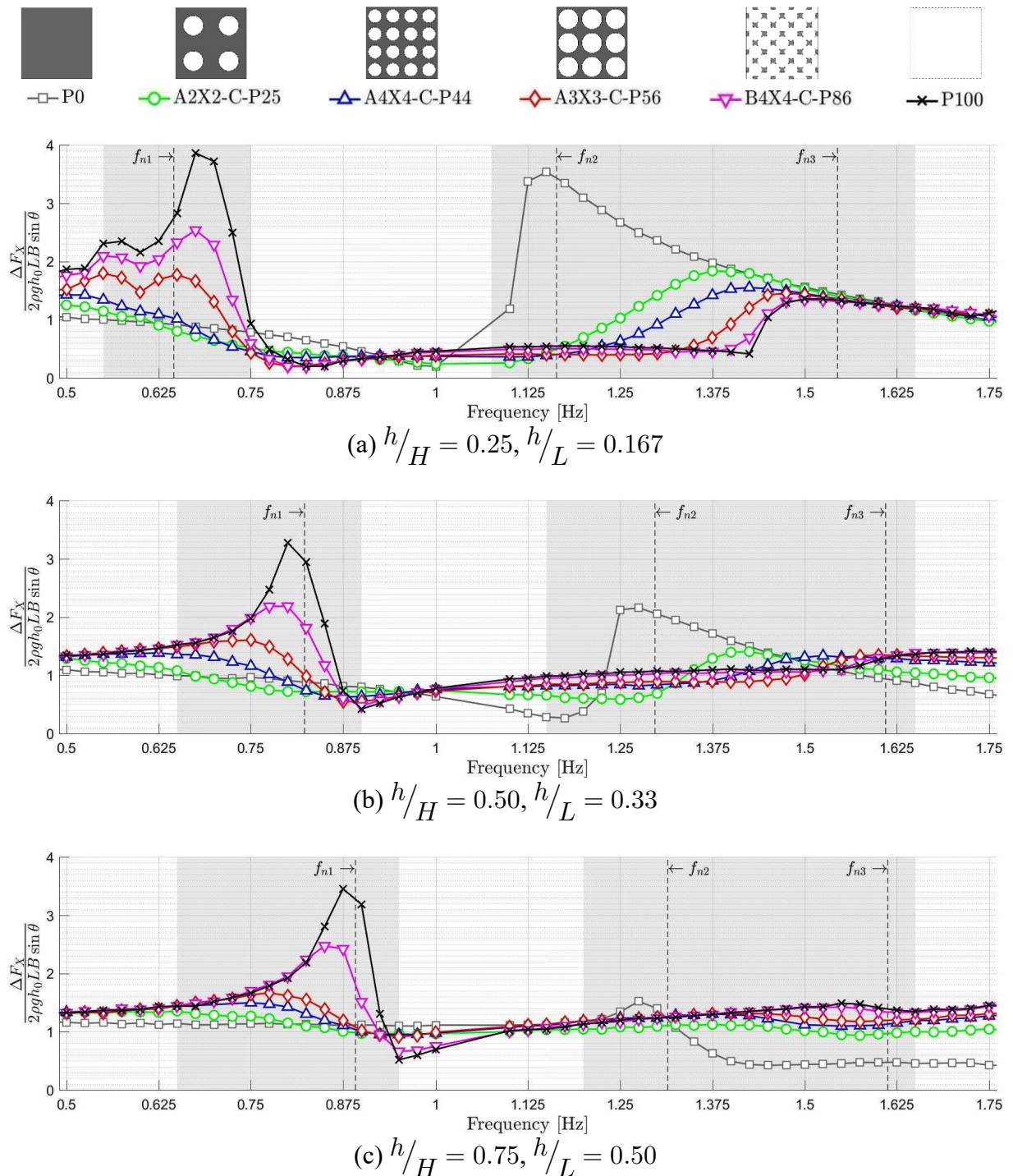
elevation by the hydrostatic variation due to the pitch motion of the clean tank ($\Delta h' = h_{max} - h_{min} = L \tan \theta_0$).

Figure 3.12 – Dimensionless amplitude of free surface elevation in the tank wall (H_1) in the frequency domain, pitch motion, $\theta = 6^\circ$



Source: figure from the author.

Figure 3.13 - Dimensionless longitudinal dynamic force in the frequency domain, pitch motion, $\theta = 6^\circ$

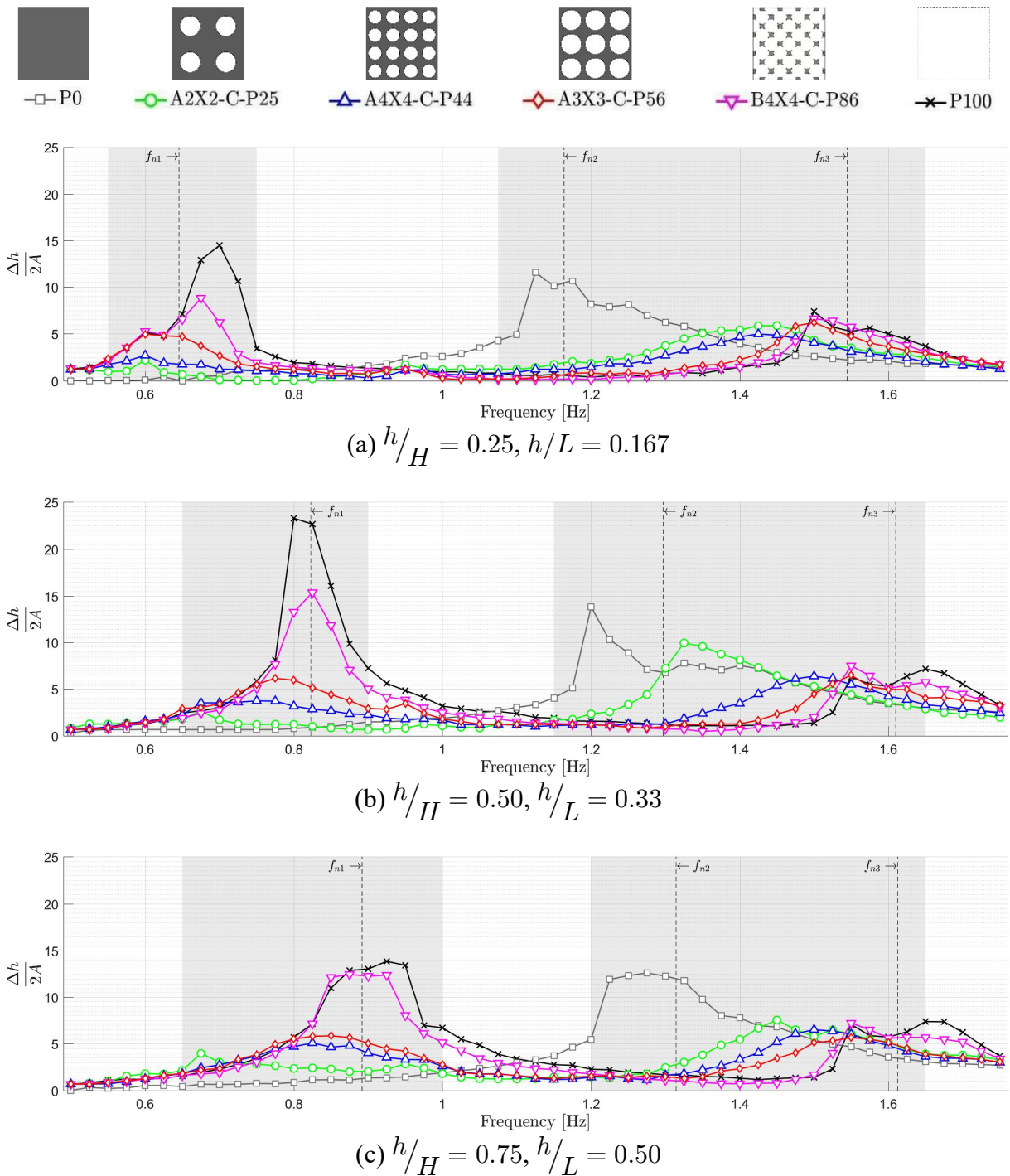


Source: figure from the author.

By considering a local coordinate system attached to the tank that follows its pitch motion, the dynamic longitudinal force is calculated as the average value of the difference between the maximum and minimum longitudinal force at each cycle of

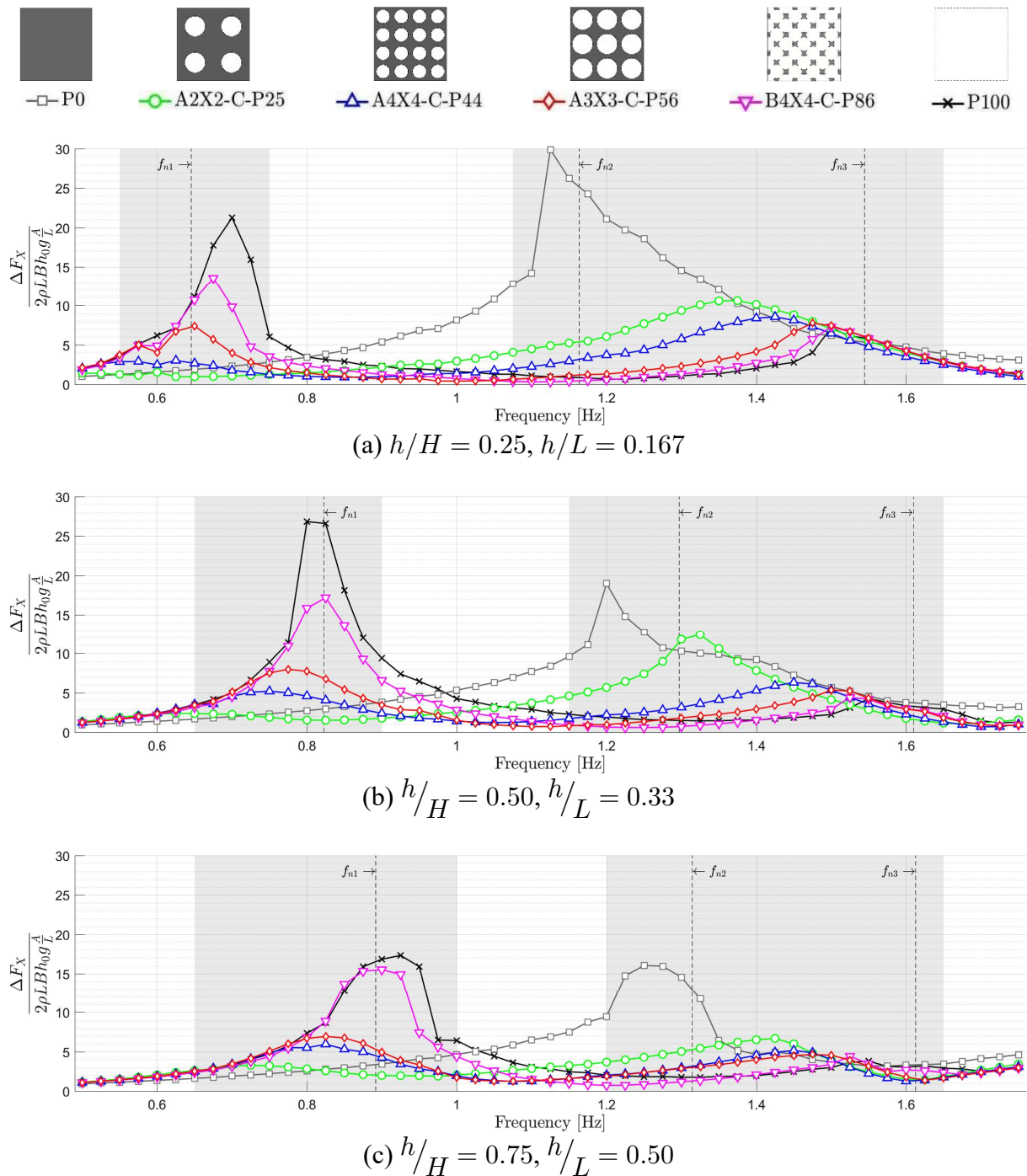
harmonic motion. Figure 3.13 shows the dimensionless longitudinal dynamic force in the frequency domain obtained using the variation of hydrostatic force due to the maximum and minimum pitch inclinations of the clean tank ($\Delta F_X' = 2\rho gh_0 LB \sin \theta_0$).

Figure 3.14 - Dimensionless amplitude of free surface elevation in the tank wall (H_1) in the frequency domain, surge motion, $A = 1\% \times L$



Source: figure from the author.

Figure 3.15 - Dimensionless longitudinal dynamic force in the frequency domain, surge motion, $A = 1\% \times L$



Source: figure from the author.

Figure 3.14 presents the dimensionless amplitude of the free surface elevation in tank wall as function of the motion frequency for the case with imposed harmonic surge motion with amplitude of 1% of the tank length. The free surface height

measured at the probe H1 is made dimensionless by dividing it by double the amplitude of the harmonic motion ($\Delta H/(2A)$). Figure 3.15 shows the dimensionless longitudinal dynamic force as function of the motion frequency for harmonic surge motion with amplitude of 1% the tank length. The dimensionless longitudinal dynamic force is the ratio between the computed longitudinal dynamic force and the force factor $2\rho gBLh_0(A/L)$.

The frequency domain considered in this study can be divided in two parts to simplify the discussion of the results, which are illustrated by the two gray-shaded areas in each graph. The frequencies of the three resonant modes of the clean tank (f_{n_1} , f_{n_2} and f_{n_3}), calculated analytically from the linear potential Airy wave theory (Table 3.3), are presented by the vertical dashed lines. The first part corresponds to the excitation frequencies between 0.5 Hz and 1.0 Hz and it is related to the first mode (n_1) associated the three filling levels. For the low frequencies, the clean tank and the tanks with perforated bulkheads show essentially hydrostatic behavior and the dimensionless responses tends to one. As the frequency approaches the first mode (n_1), larger free surface elevations were computed as the open area ratio of the perforated bulkhead increases. Moreover, the frequencies associated to the maximum free surface elevation increase as the open area ratio of the bulkhead increases.

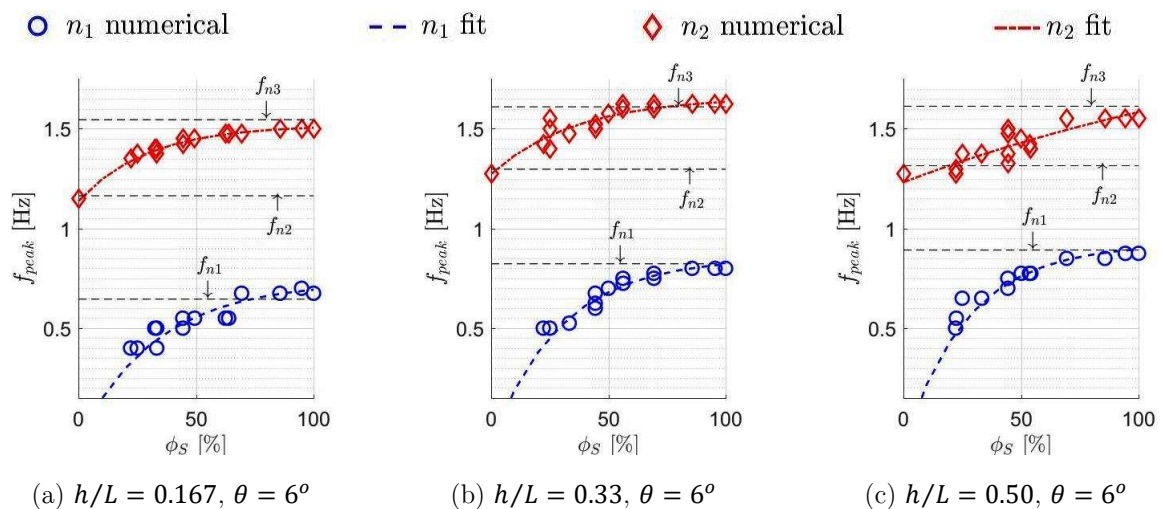
The second part consists of the frequencies range from 1.0 Hz to 1.75 Hz for the three filling levels. Peaks were computed for the tank with watertight bulkhead close to 1.125Hz, 1.25 Hz and 1.3 Hz for the filling ratios of 0.167, 0.33 and 0.50, respectively, and are related to the first antisymmetric mode of the compartmented tank or the second mode (n_2). In addition to this, in a higher frequency range but with lower magnitude, peaks related to the third mode (n_3) were computed for the clean tank. For the tanks with perforated bulkheads, one peak could be identified in the frequency range between the resonant modes n_2 and n_3 as well. In such cases, the general behavior of the tank with perforated bulkheads tends to resemble the behavior

of the clean tank as the open area ratio of the bulkhead increases and, therefore, presenting lower peaks at a higher frequency.

In general, for the tanks with perforated bulkheads, the behavior of the dynamic longitudinal force diagrams shows the same tendencies presented by the free surface elevation diagrams. For the clean tank, in all the three filling levels, large amplifications ranging from 3.5 to 4 times the quasi-static response were obtained at the first resonant mode (n_1). On the other hand, for the tank with watertight bulkhead at second mode (n_2), the dynamic component of the force reduces remarkably as the filling level increases. In such cases, while the amplification of the dynamic force is around 3.5 times the quasi-static one for the low filling level, the amplification for the high filling level is about only 1.5 times the quasi-static response. For the high filling level, between 1.0 Hz and 1.75 Hz (Figure 3.13-c), the difference between the clean tank and the tanks with perforated bulkheads is almost negligible regarding the longitudinal dynamic force.

In Figure 3.16, the resonant frequencies in the two regions of the frequency domain in relation to the perforated bulkhead open area ratio are presented.

Figure 3.16 – Frequency of the first (n_1) and the second resonant peak (n_2) as a function of submerged open area ratio



Source: figure from the author.

The general behavior is very similar for the three filling levels. The resonant frequency increases monotonically as the submerged open area ratio of the bulkhead increases. The increase rate is higher for low submerged open area ratios and, for submerged open area ratio above 50%, the frequency of the peaks tends towards an asymptotic behavior. In the curve for the first mode, the asymptote is the frequency of the first antisymmetric mode (f_{n1}) for the clean tank. In the curve for the second mode, the resonant peak for zero open area ratio is the frequency of the second mode of the clean tank (f_{n2}) and tends to the frequency of the third mode of the clean tank (f_{n3}) as the open area ratio approaches 100%. The numerical data presented a good correlation with the dashed lines, which are regressions curves obtained by adopting an exponential curve in the form $f(\Phi) = C_1 - C_2e^{-C_3\Phi}$, where C_1 , C_2 and C_3 are positive constant values.

In conclusion, as the open area ratio of the bulkhead decreases, there is a gradual change of the sloshing behavior from that resembling the response of a clean tank to that of a tank with watertight bulkhead. Thus, aiming to reduce the amplification of the fluid motion within the tank, the results obtained herein intuitively show that perforated bulkheads of low open area ratio present better results for frequencies close the first resonant mode (n_1), while tanks with perforated bulkheads with high open area ratios presented better results for frequencies close to the second resonant mode (n_2).

3.7.2 Effects of excitation amplitude

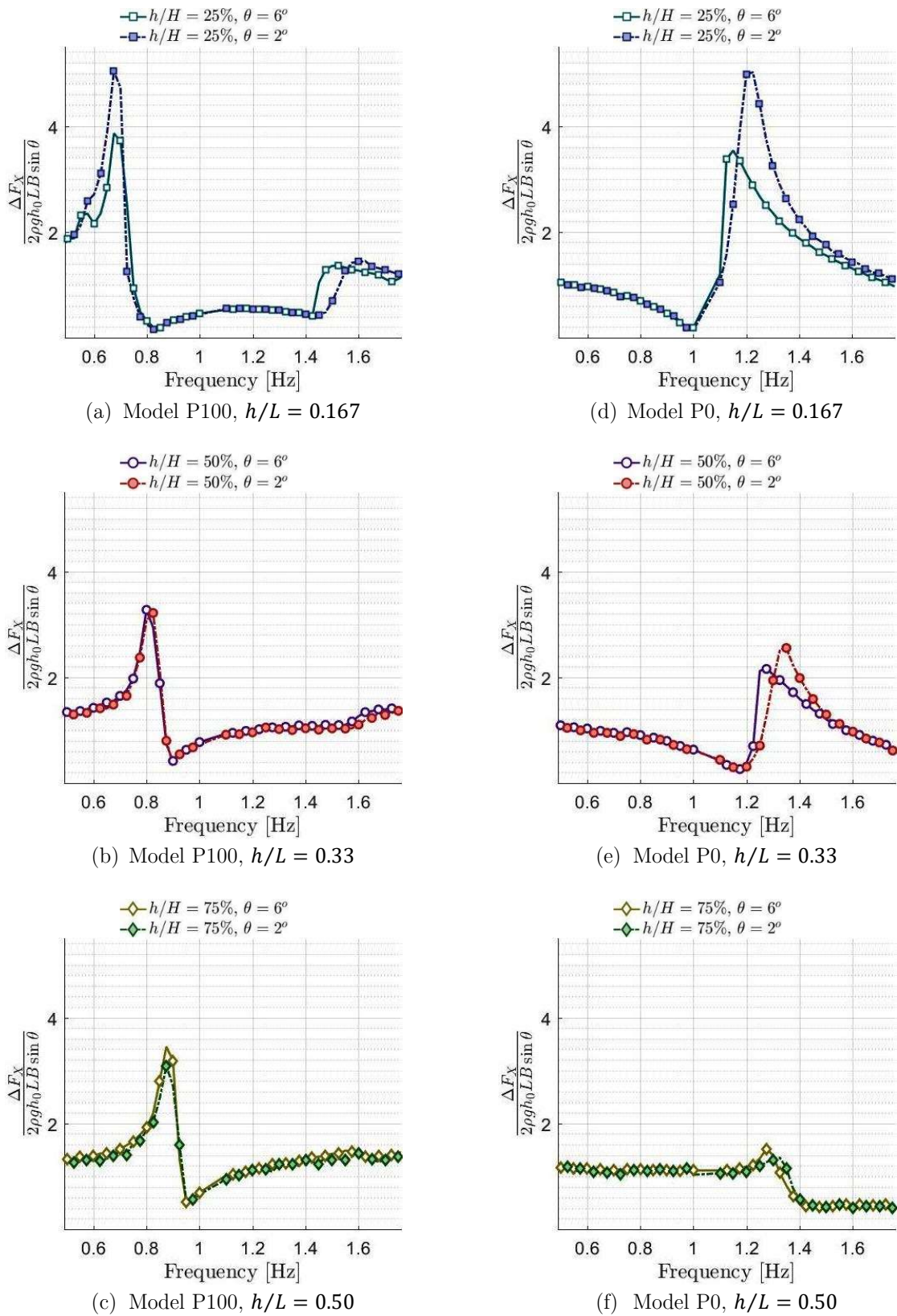
In order to verify the effects of the harmonic motion pitch amplitude on the sloshing responses of the tanks with perforated bulkheads, cases with pitch harmonic motion with a smaller amplitude of 2 degrees were simulated for the clean tank, the tank with watertight bulkhead and the tanks with perforated bulkhead with layout "A". Figure 3.17-a,b,c show the diagrams in the frequency domain of the dimensionless dynamic longitudinal force for the clean tank, Figure 3.17-d,e,f for the tank with

watertight bulkhead, Figure 3.18-a,b,c for tank with perforated bulkhead with higher open area ratio of 68% and Figure 3.18-d,e,f for the tank with perforated bulkhead with a small open area ratio of 10%.

Besides, in order to show the effects of the amplitude of the surge motion of the sloshing behavior, additional simulations with a larger amplitude of 2% of the tank length were performed as well for the models with layout “A” and “B”. For the comparison of the results with different surge amplitudes, Figure 3.19-a,b,c shows the dimensionless dynamic longitudinal force for the clean tank, Figure 3.19-d,e,f shows the longitudinal dynamic force, Figure 3.20-a,b,c shows the dimensionless longitudinal dynamic force for the tank with a high open-area bulkhead (A2x2-P-69) and Figure 3.20-d,e,f shows the longitudinal dynamic force for the tank with a relatively low open-area ratio of 10% (A2x2-C-P11).

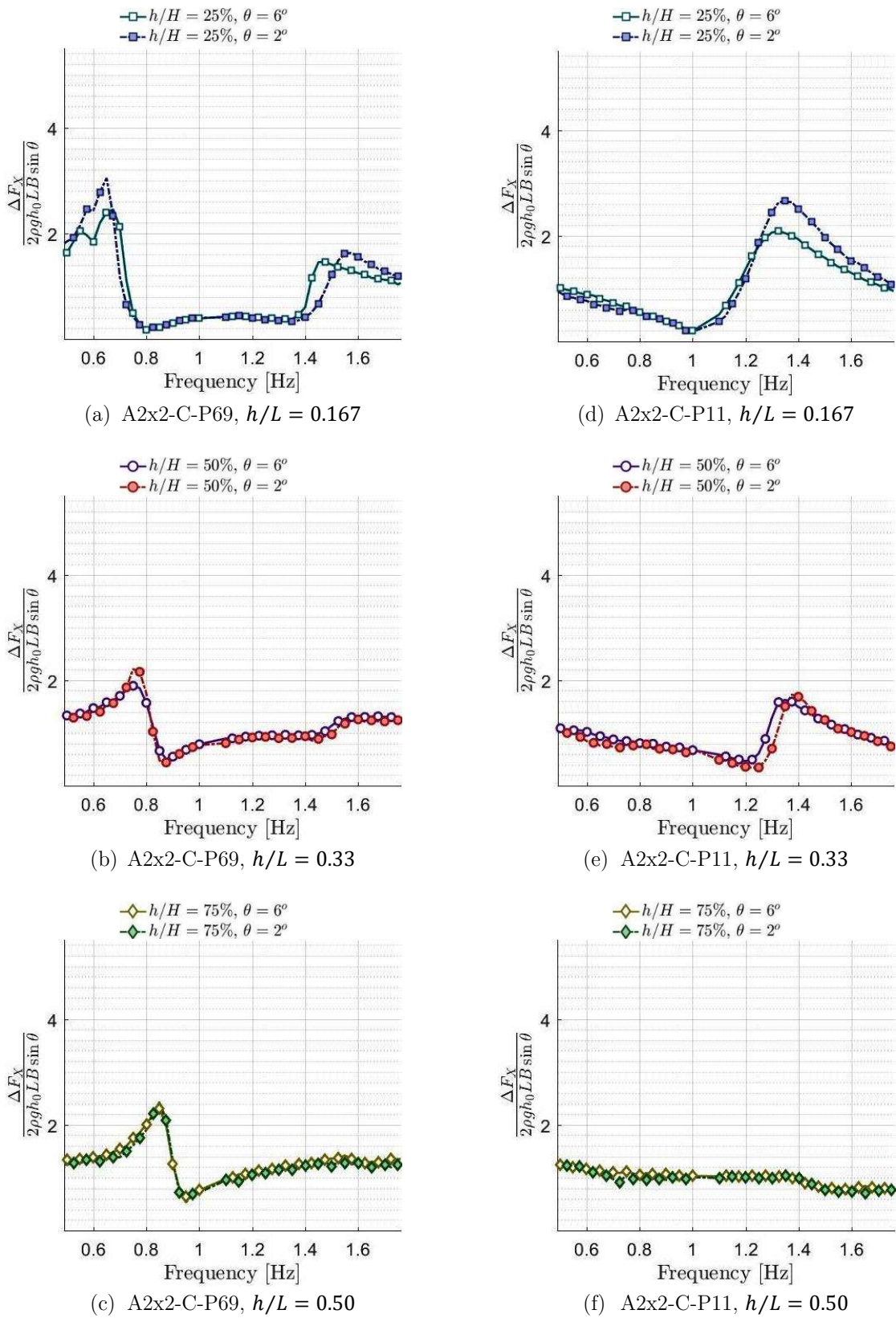
In Figure 3.17-a, for the clean tank with a low filling level, some differences were observed in the two resonant modes. In the first mode (n_1), strong nonlinear effect is observed. The response amplification in the resonance of the case with larger amplitude motion is due the damping caused by nonlinear free surface effects such as the wave breaking of the travelling wave. For the intermediate and high filling levels, the difference is relatively small, showing a nearly linear response. In Figure 3.17-e,f, for the tank with watertight bulkhead, the peak response amplification due to the small amplitude excitation is larger in the second mode (n_2) and occur at a slightly higher frequency.

Figure 3.17 – Dimensionless longitudinal dynamic force as a function of the excitation frequency, pitch motion – Model P0 and Model P100



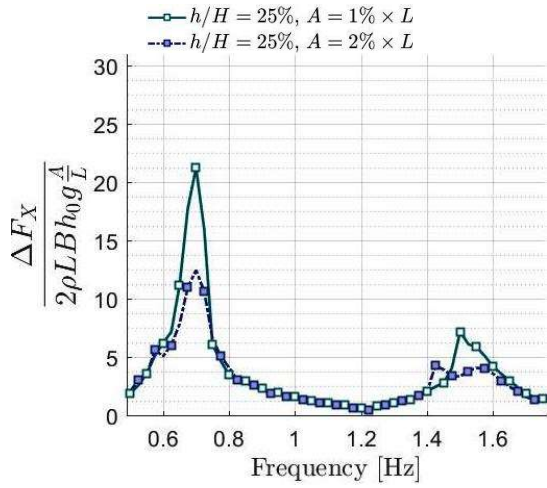
Source: figure from the author.

Figure 3.18 – Dimensionless longitudinal dynamic force as a function of the excitation frequency, pitch motion – A2x2-C-P11 and A2x2-C-P69

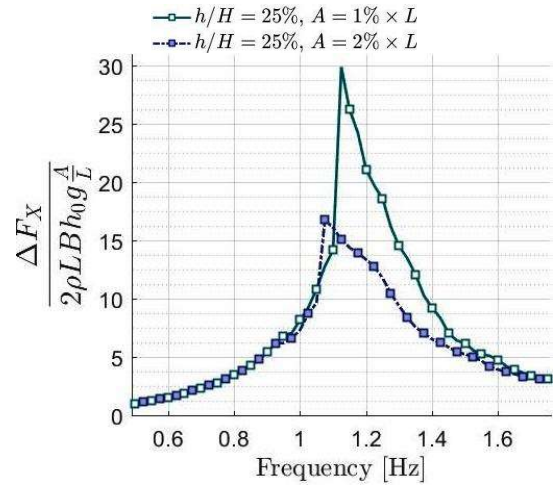


Source: figure from the author.

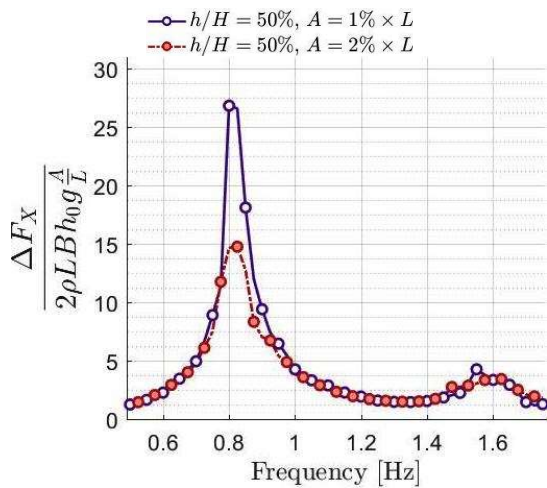
Figure 3.19 – Dimensionless longitudinal dynamic force as a function of the excitation frequency, surge motion – Model P0 and Model P100



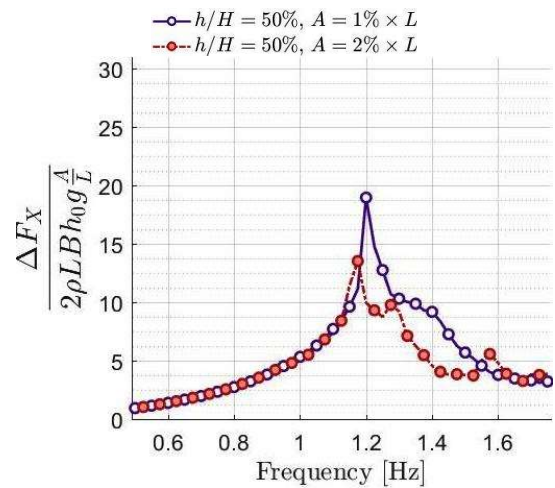
(a) Model P100, $h/L = 0.167$



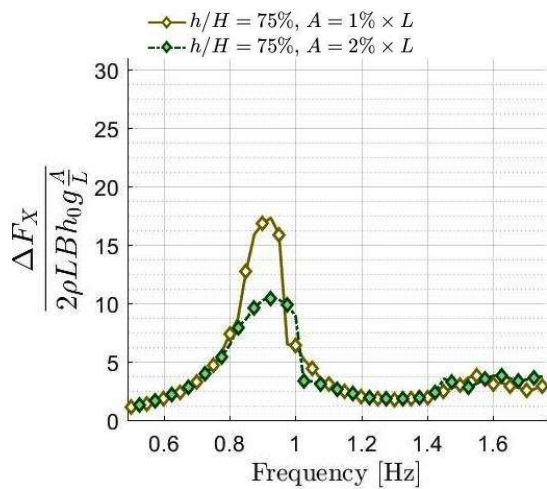
(d) Model P0, $h/L = 0.167$



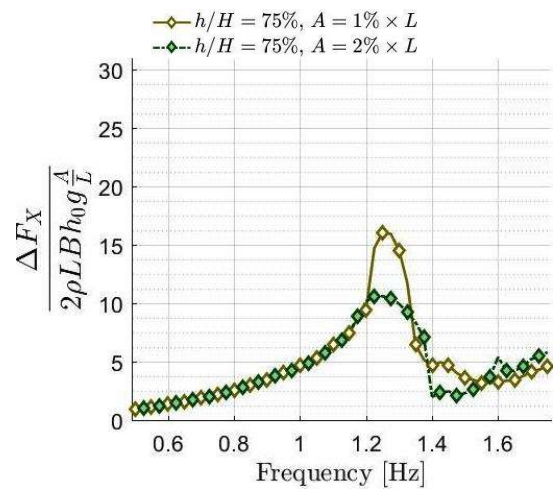
(b) Model P100, $h/L = 0.33$



(e) Model P0, $h/L = 0.33$



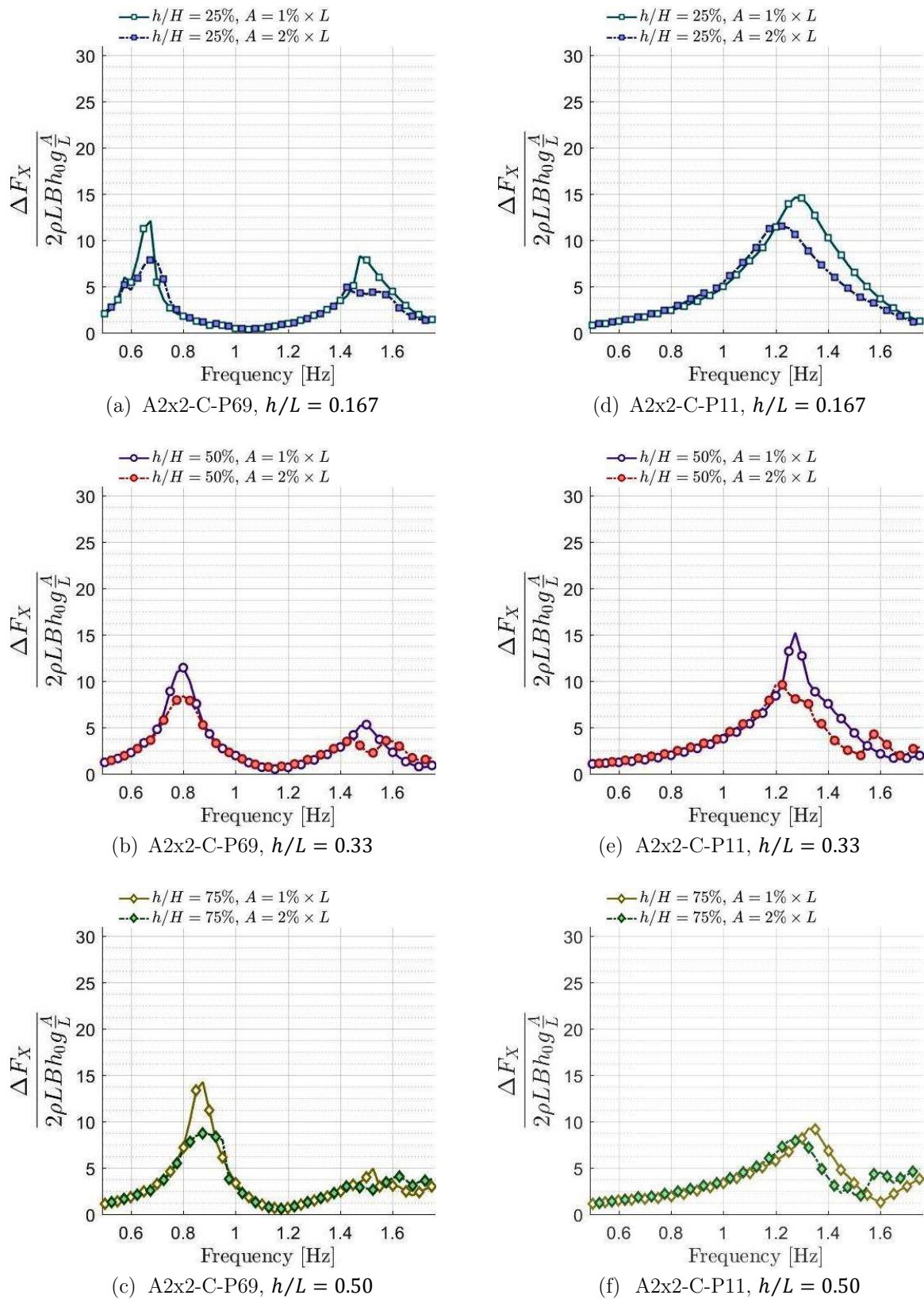
(c) Model P100, $h/L = 0.50$



(f) Model P0, $h/L = 0.50$

Source: figure from the author.

Figure 3.20 – Dimensionless longitudinal dynamic force as a function of the excitation frequency, surge motion – A2x2-C-P11 and A2x2-C-P69



Source: figure from the author.

The tank with perforated bulkhead of low open area ratio of 10% (Figure 3.18-d,e,f) has a behavior that resembles the tank with the watertight bulkhead, but its resonant peaks in the second mode (n_2) present significant lower magnitudes than that observed for the tank with watertight bulkhead. Similarly, the behavior of the tank with perforated bulkhead of high open area ratio of 68% (Figure 3.18-a,b,c) resembles that of the clean tank, but it has significantly lower response amplifications at the first resonant mode (n_1). For both tanks with perforated bulkheads, the effects of the excitation amplitude are small for the low and the intermediate filling levels, but they are almost negligible for the high filling level. In general, larger amplitudes of motion introduce additional damping due to free surface nonlinear phenomena. As such, it results in lower peaks of the dimensionless longitudinal dynamic force and slightly shifts the frequency of the resonance peak to a lower value. Notwithstanding such difference, the general behavior of the sloshing regarding the effects of open-area ratio is kept.

3.7.3 Effects of the geometry of the holes

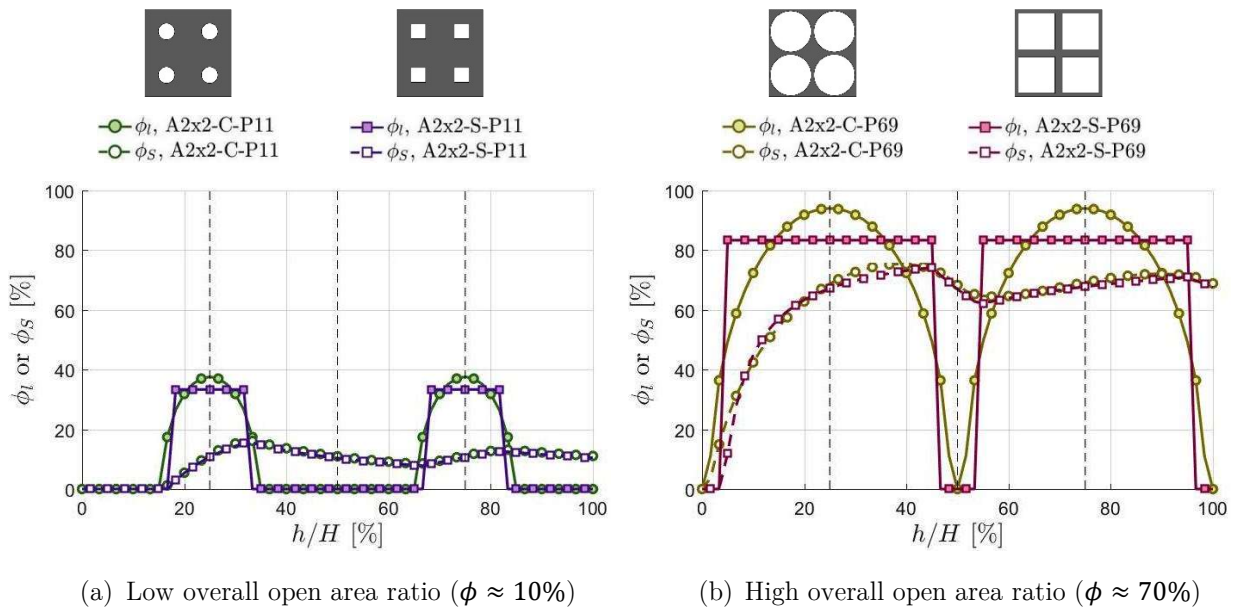
The investigation on the effect of the hole geometry on the sloshing was carried out taking into account circular and square-shaped holes with the arrangement of Model A bulkheads. The size of the circles and squares were adjusted in order to obtain “equivalent bulkheads” with almost the same overall open area ratios. The small discrepancies of the overall open area ratios are negligible considering the particle model resolution.

As initial analysis on the geometry of the bulkheads, the local open area ratio at the fluid level and the submerged open area ratio are considered. Figure 3.21 shows the distribution of the open area ratios in two sets of equivalent bulkheads as a function of filling ratio $\frac{h}{H}$. In Figure 3.21-a, the distributions for the low overall open area ratio bulkhead models (around 10%) A2x2-C-P11 and A2x2-S-P11 are presented.

In Figure 3.21-b, the distributions for the high overall open area ratio bulkhead models (around 70%) A2x2-C-P69 and A2x2-S-P69 are provided.

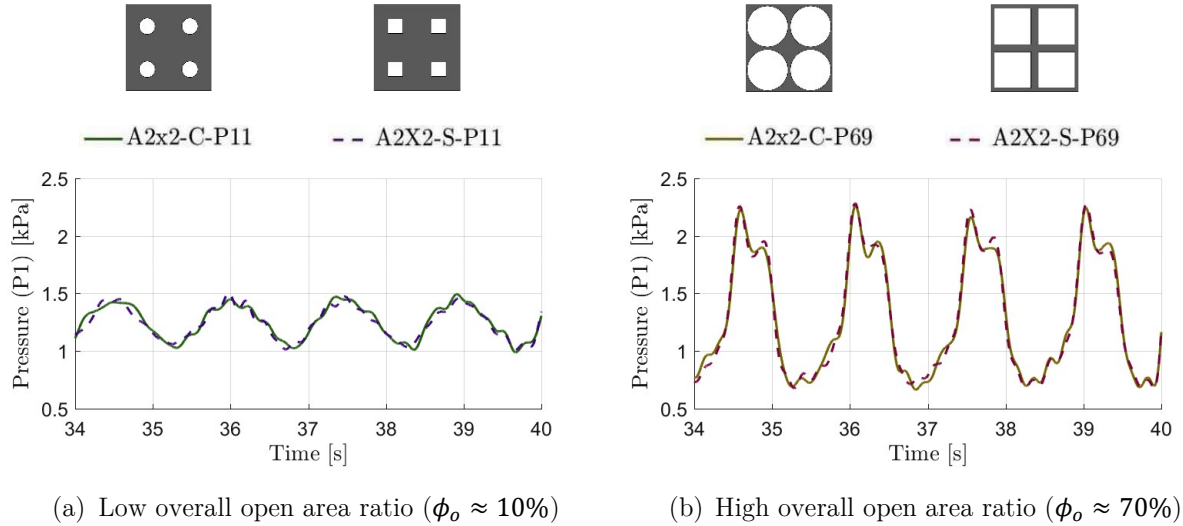
The different profiles of the open area distribution for circular holes and for square holes are shown by the curves of the local open area at the fluid level (ϕ_l). For the two sets of models (Figure 3.21-a,b), the local open area at the fluid level of 25% and 75% are slightly higher for the models with circular holes than the ones with square-shaped holes. Nevertheless, despite the small differences in the local open area ratios, the submerged open area ratio is very similar between equivalent bulkheads for the three filling levels.

Figure 3.21 – Open area ratios as a function of filling level – comparison considering circular and square shaped holes



Source: figure from the author.

Figure 3.22 – Time series of pressure at probe P1 (filtered) – first mode (n_1): $h/H = 25\%$, $f = 0.675\text{Hz}$, $\theta = 6^\circ$ – comparison considering circular and square shaped holes



Source: figure from the author.

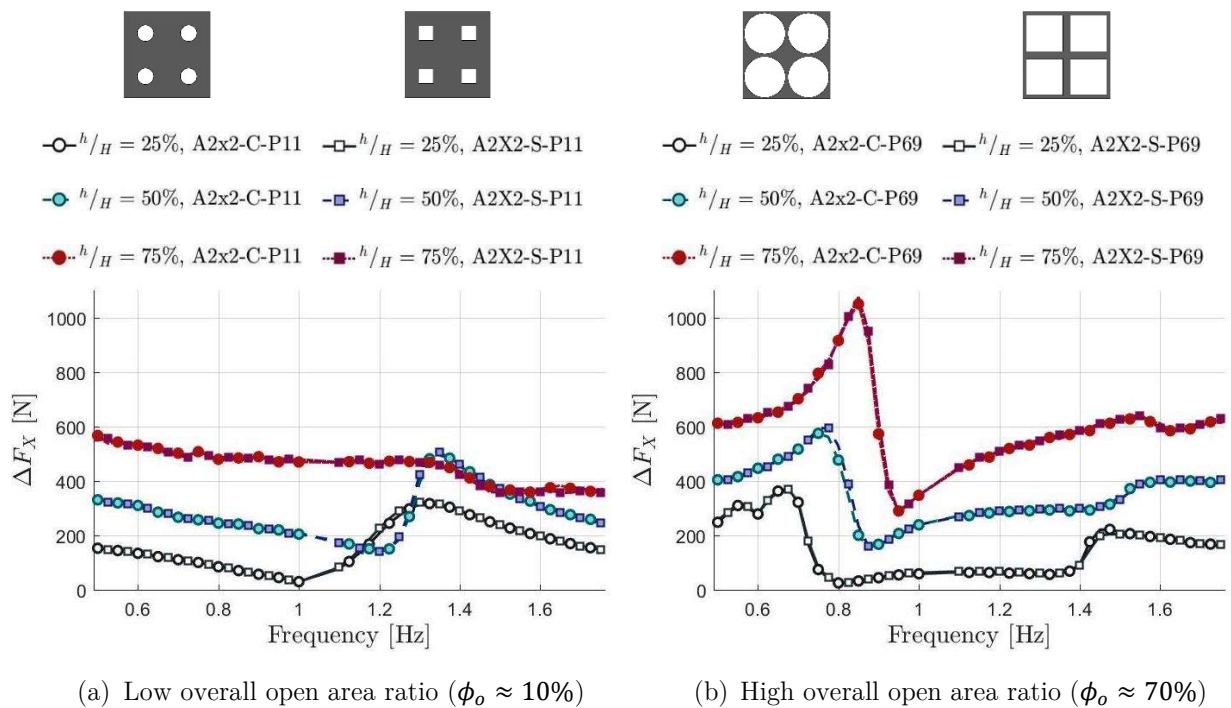
Figure 3.22 shows the time series of the computed pressure at probe P1 in the first resonant mode (n_1) of the sloshing. The raw pressure time series obtained from the particle simulations were filtered by a low-pass filter with threshold of 20 Hz in order to provide a clear view of the main harmonics and spurious numerical noise. As expected from the results shown in the previous section, for high overall open area ratio bulkheads, the sloshing is more violent in the first mode as higher pressures were measured for them (Figure 3.22-b) than for those with lower open area ratios (Figure 3.22-a).

The pressure time series in Figure 3.22-b shows two peaks at each cycle. The first peak, with higher magnitude, is related to the impact of the travelling wave on the tank wall. After the impact, the fluid flows upwards along the right wall until reaching a maximum height, which is followed by the collapse of the water column that generates the second peak, of smaller magnitude. This hydrodynamic behavior is not observed for the low open area ratio bulkheads (Figure 3.22-a) in which a quasi-sinusoidal curve profile is obtained. Moreover, the difference between the pressure time

series for the bulkheads with circular and square-shaped hole is almost negligible in both Figure 3.22-a and Figure 3.22-b.

To provide a clear picture of the difference in response between the circular and square-shaped bulkheads, Figure 3.23 shows the longitudinal dynamic force in the frequency domain covering the sloshing first three resonant modes, for the two sets of equivalent bulkheads and for the three filling levels.

Figure 3.23 – Longitudinal dynamic force as function of the frequency, $\theta = 6^\circ$ – comparison considering circular and square shaped



Source: figure from the author.

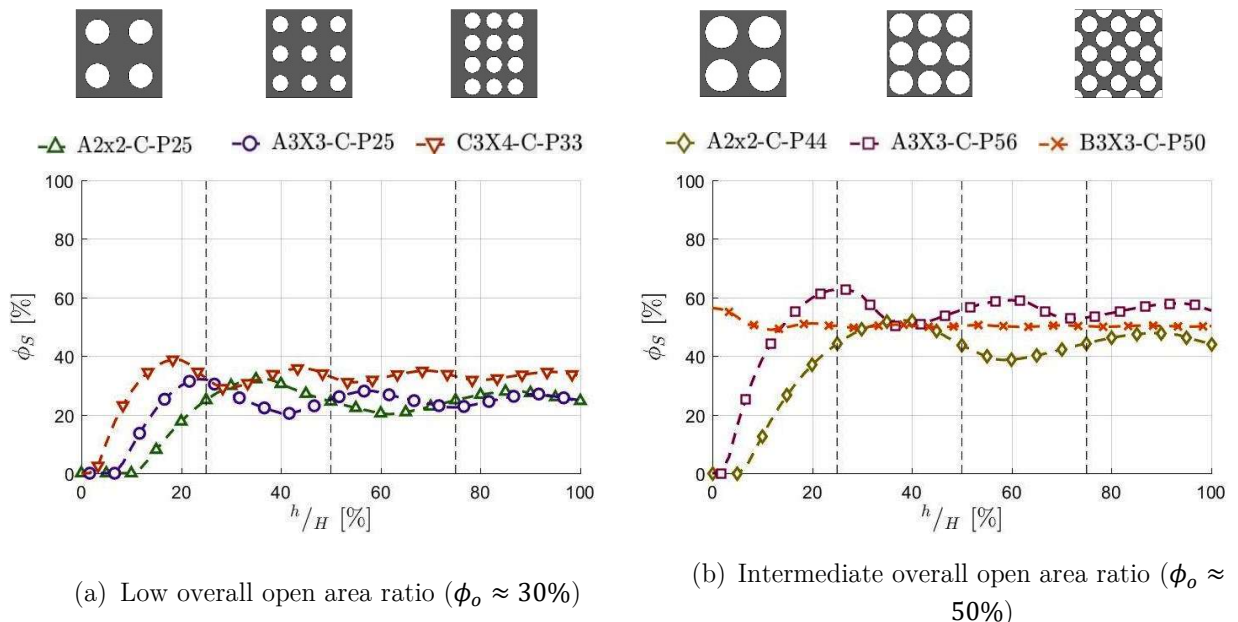
In Figure 3.23-a, for the bulkheads with low open area ratio, a resonant flow could be identified only in the second mode (n_2) for the low and intermediate filling level. In this case, no first mode resonance was observed for the three filling levels. On the other hand, in Figure 3.23-b, for the high open area ratio bulkheads, there is a clear first resonant mode for the three filling levels and the third resonant mode (n_3) appears between 1.4 Hz and 1.5 Hz for the low filling level. Furthermore, in both graphs, the difference between the square-shaped holes and the circular holes for the equivalent

bulkheads is negligible. Therefore, the shape of the hole has no effect on the sloshing behaviors of the perforated swash bulkheads.

3.7.4 Effects of the arrangement of the holes

In the previous section, models of perforated bulkheads with the same arrangement of the holes but different hole shapes were analyzed. In such cases, the “equivalent bulkheads” were obtained using same numbers of square-shaped and circular holes with the same arrangements and similar open area ratio. In this section, “equivalent bulkhead” models with different arrangements are considered, i.e., with a variety of number of circular with different dimensions and distributions, but with similar overall open area ratio. Figure 3.24 shows the submerged open area ratio as function of the filling level for two sets of three “equivalent bulkheads”.

Figure 3.24 – Open area ratios as a function of filling ratio – comparison considering different hole arrangements



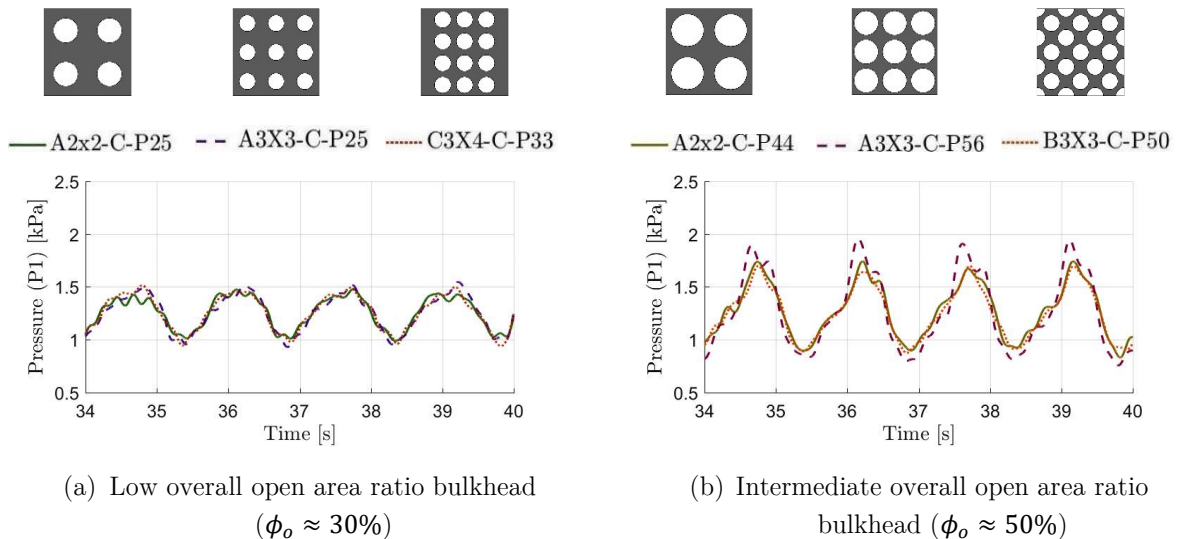
Source: figure from the author.

Figure 3.24-a gives the submerged open area ratios of A2x2-C-P25, A3x3-C-P25 and C3x4-C-P33 models, whose overall open area around 30% (low overall open area

ratio models). Meanwhile, Figure 3.24-b provides the submerged open area ratios of the models A2x2-C-P44, A3x3-C-P56 and B3x3-C-P50, whose overall open area ratio are close to 50% (intermediate overall open area ratio models).

Figure 3.25 presents the pressure time series at probe P1 computed in the first resonant mode (n_1) in the low filling level for the two sets of equivalent bulkheads. Figure 3.25-a and Figure 3.25-b, show the time series for the low and intermediated overall open area ratios, respectively.

Figure 3.25 – Time series of pressure at probe P1 (filtered) – first mode (n_1): $h/H = 25\%$, $f = 0.675Hz$, $\theta = 6^\circ$ – comparison considering different hole arrangements



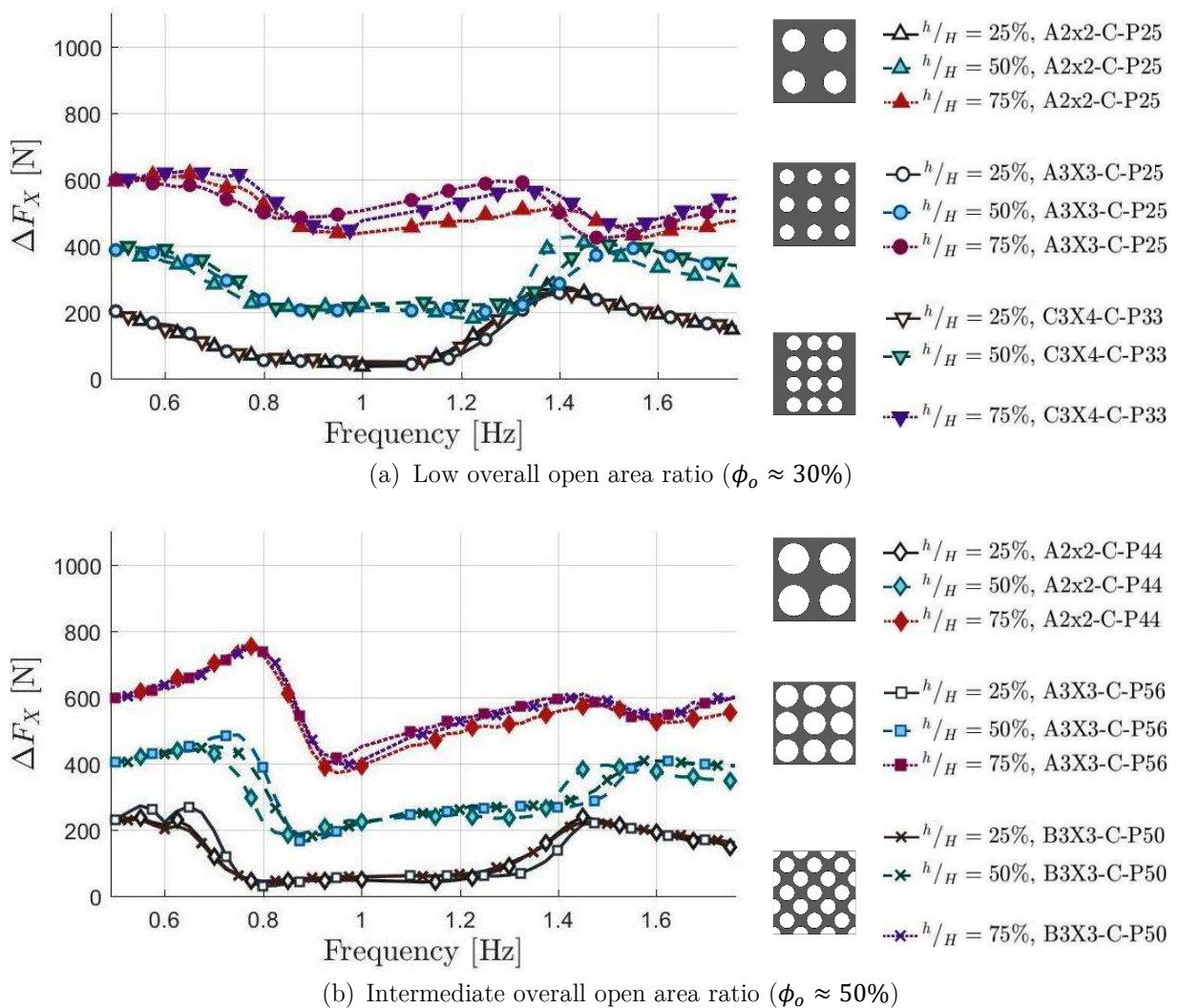
Source: figure from the author.

The low overall open area ratio bulkheads (Figure 3.25-a) show very similar behavior, and the pressure histories are quasi-sinusoidal. For the three equivalent models with intermediate overall open area ratio bulkheads (Figure 3.25-b), the magnitude of pressure variation is similar. The submerged open area ratio of the model A3x3-C-P56 below 25% filling is slightly higher than those of the other two models. As a consequence, it has a pressure peak slightly higher than that computed for the other equivalent bulkheads. For this model, a second pressure peak due the collapse of the

fluid column, similar to that occurred in the high overall open area ratio bulkheads (Figure 3.25-b), was also computed.

The graphs of the longitudinal dynamic force as function of excitation frequency for the two sets of equivalent bulkheads are presented in Figure 3.26. The longitudinal dynamic forces for the low and intermediate overall open area ratio bulkheads are given in Figure 3.26-a and Figure 3.26-b, respectively.

Figure 3.26 – Longitudinal dynamic force as function of excitation frequency, $\theta = 6^\circ$ – comparison considering different hole arrangements



Source: figure from the author.

At any filling level evaluated herein, the computed longitudinal dynamic force for the equivalent bulkheads, which have almost same overall open area ratio, are very

similar, despite the large difference in number, size and arrangements of the holes. The general behavior of the longitudinal dynamic force is very close between model A2x2-C-P44 and B3x3-C-P50 (Figure 3.26-b), and small differences occurs only in the vicinity of the resonant frequencies.

In the bulkhead with a larger number of holes (B3x3-C-P50) the fluid flows through a larger amount of edges than in the models with a smaller number of holes (A2x2-C-P44) and nonlinear effects such viscous damping, flow separation and vortex shedding must be more significant. The expected outcome is a larger damping on the resonance region for such models with smaller but more numerous holes. However, such tendency was not identified in our results. Notwithstanding, despite the different number and size of the holes, the models with slightly higher open areas show higher longitudinal dynamics forces at the first resonant mode. On the other hand, the models with slightly lower open areas presented higher longitudinal forces at the second resonant mode.

3.7.5 Discussion of the damping effects of the perforated bulkheads

Vertical baffles and bulkheads are extensively used to mitigate the sloshing. They affect the flow in different ways such as by restraining the flow and intensifying viscous damping through flow separation and vortex formation. While the first is related to changes in the added mass of the mechanical system, the second is related to its damping. Thus, it is interesting and useful the better understanding on the contribution of each one of these aspects regarding sloshing mitigation by perforated bulkheads.

In previous section, as square holes have about 12% more perimeter of sharp edges than circular holes with equivalent area, it is expected higher formation of vortices in the bulkheads with square holes and, as consequence, a slightly more damped flow. However, in general, the difference was negligible. Similar results were observed for the effect of the arrangement of the holes and its number. In general,

regardless the number, size and arrangement of the holes, bulkheads with similar open-area ratio presented very close results for sloshing mitigation (Figure 3.26). Such results indicate that the vortex formation has a relatively smaller contribution to the damping by perforated baffles if compared to the effects due to the flow restriction.

In the first and third sloshing resonant modes, as the velocities normal to the bulkheads near the free surface are larger than near the bottom of the tank, the bulkhead which provides more restriction to the flow close to the free surface is expected to be more effective for sloshing mitigation. In order to verify this hypothesis, bulkheads with equivalent submerged open-area ratio, but with nonuniform distribution of the local open-area ratio along the tank depth, i.e., with different local open-area ratios near the free surface and close to the tank bottom, can be considered. Such is the case of Yu et al (2019) experiments, which used slat-screen bulkheads with three different open-area ratios and, for each one, two different sizes of slots. The results show that for equivalent open-area ratios, the cases using large slots, with the slot height about a third of the depth and placed very close to the free surface, the amplitudes of free surface motion is higher for the first and third modes than the cases using small slots. As a result, the experiments corroborated the hypothesis.

In order to estimate the effects of the open-area ratio of the perforated bulkhead on the added mass and the damping of the system, we will adopt the approach used by Molin and Remy (2013), in which the longitudinal force acting on the tank wall and the bulkhead wall could be written as:

$$F_X = i \cdot 2\rho A\omega^2 Lh(C_{a11} + i \cdot C_{b11})e^{-i\omega t} \quad (3.1)$$

where F_X is the longitudinal force, $\omega = 2\pi f$ is the frequency in radians of the harmonic motion, $C_{a,11}$ is the added mass coefficient for the surge motion and $C_{b,11}$ is the damping coefficient of the surge motion. Besides, the longitudinal force (F_X) could be also a function of the amplitude of the longitudinal force $\overline{F_X}$ and its phase θ , as stated by the equation 3.2:

$$F_X = \overline{F_X} e^{-i(\omega t + \theta)} \quad (3.2)$$

Based on the computed results for the longitudinal force, the steady-state amplitude and phase associated to the main harmonic could be obtained by a Fast Fourier Transform (FFT). With such data, the surge added mass coefficient and the surge damping coefficient could be estimated by the equation 3.3 and the equation 3.4, respectively.

$$C_{a11} = \frac{\overline{F_X} \cos \theta}{2\rho A \omega^2 L H} \quad (3.3)$$

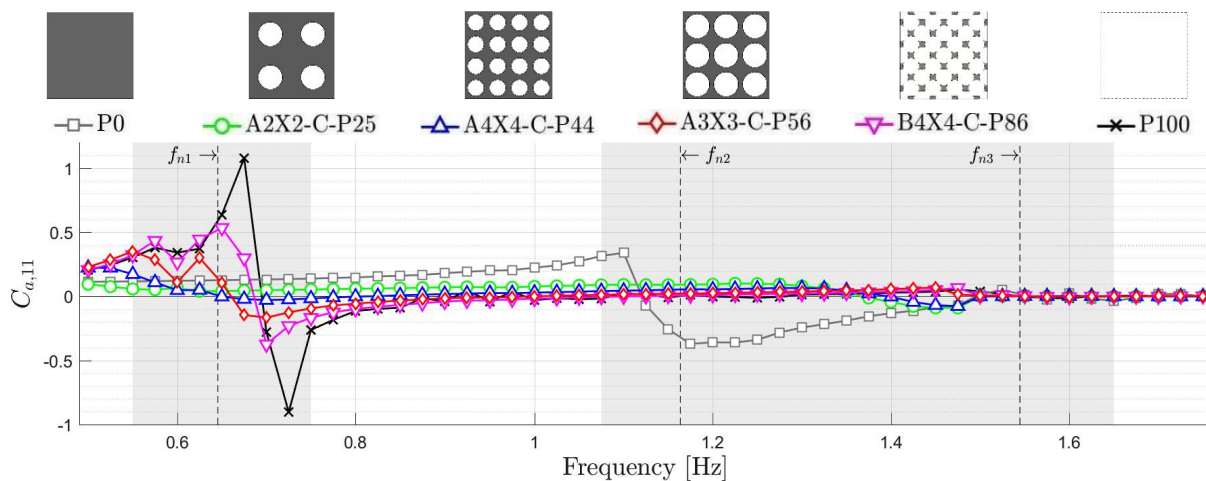
$$C_{b11} = \frac{\overline{F_X} \sin \theta}{2\rho A \omega^2 L H} \quad (3.4)$$

Figure 3.27 shows the graphs in the frequency domain of the surge added mass coefficient for the different models of swash bulkhead and for the three filling levels. Figure 3.28 shows the graphs in the frequency domain of the surge damping coefficient for different models of swash bulkheads and for the three filling levels. The graphs from Figure 3.27 and Figure 3.28 were obtained from data of the simulations with harmonic surge motion with amplitude of 1% of the tank length.

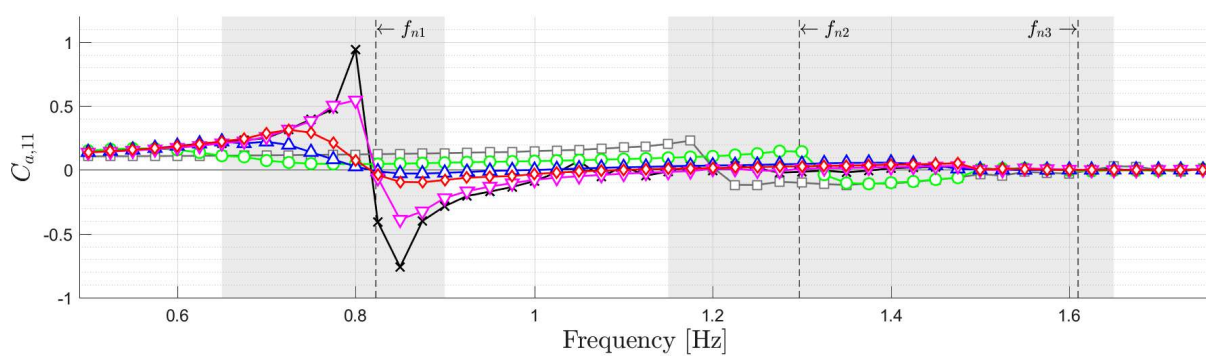
As stated by Molin and Remy (2013), the added mass coefficient opposes the surge acceleration and the damping coefficient opposes the surge velocity. In other words, the added mass coefficient quantifies the inertial contribution of the hydrodynamic component of the flow in the longitudinal direction. So, large added mass coefficients are related to large accelerations of the fluid within the tank in the longitudinal direction. Figure 3.27 shows that, in general, bulkheads with large open-area ratios have large added mass coefficients for frequencies close to the first non-compartmented anti-symmetric mode (f_1). Meanwhile, bulkheads with small open-area ratios have large added mass coefficients for frequencies close to the first compartmented anti-symmetric mode (f_2). It is related to the restriction of the flow in the center of the tank due to the perforated bulkhead and its relation to the standing wave pattern associated to each one of these two resonance modes. The first non-

compartmented anti-symmetric mode have large longitudinal velocities in the center of the tank, in which the knot of the standing wave must be placed. Hence, the higher the open-area ratio of the bulkhead, the better to intensify this mode.

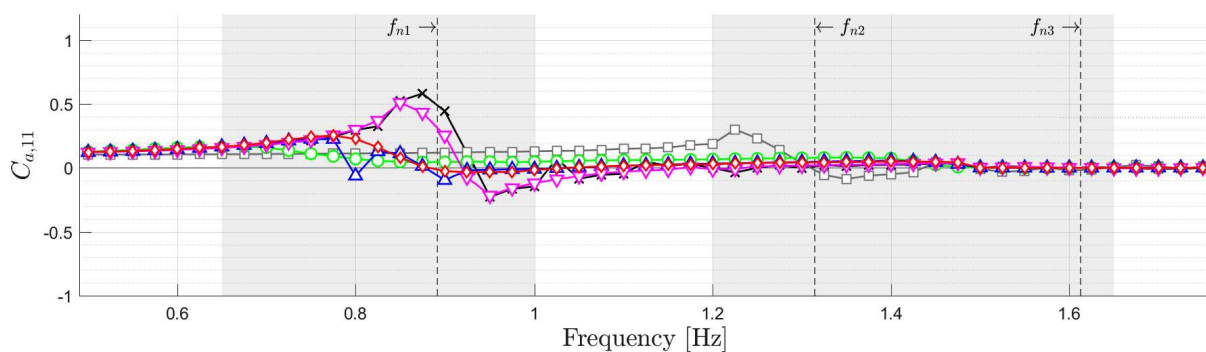
Figure 3.27 – Surge added mass coefficient ($C_{a,11}$) in the frequency domain, surge motion, $A = 1\% \times L$



(a) $h/H = 0.25, h/L = 0.167$



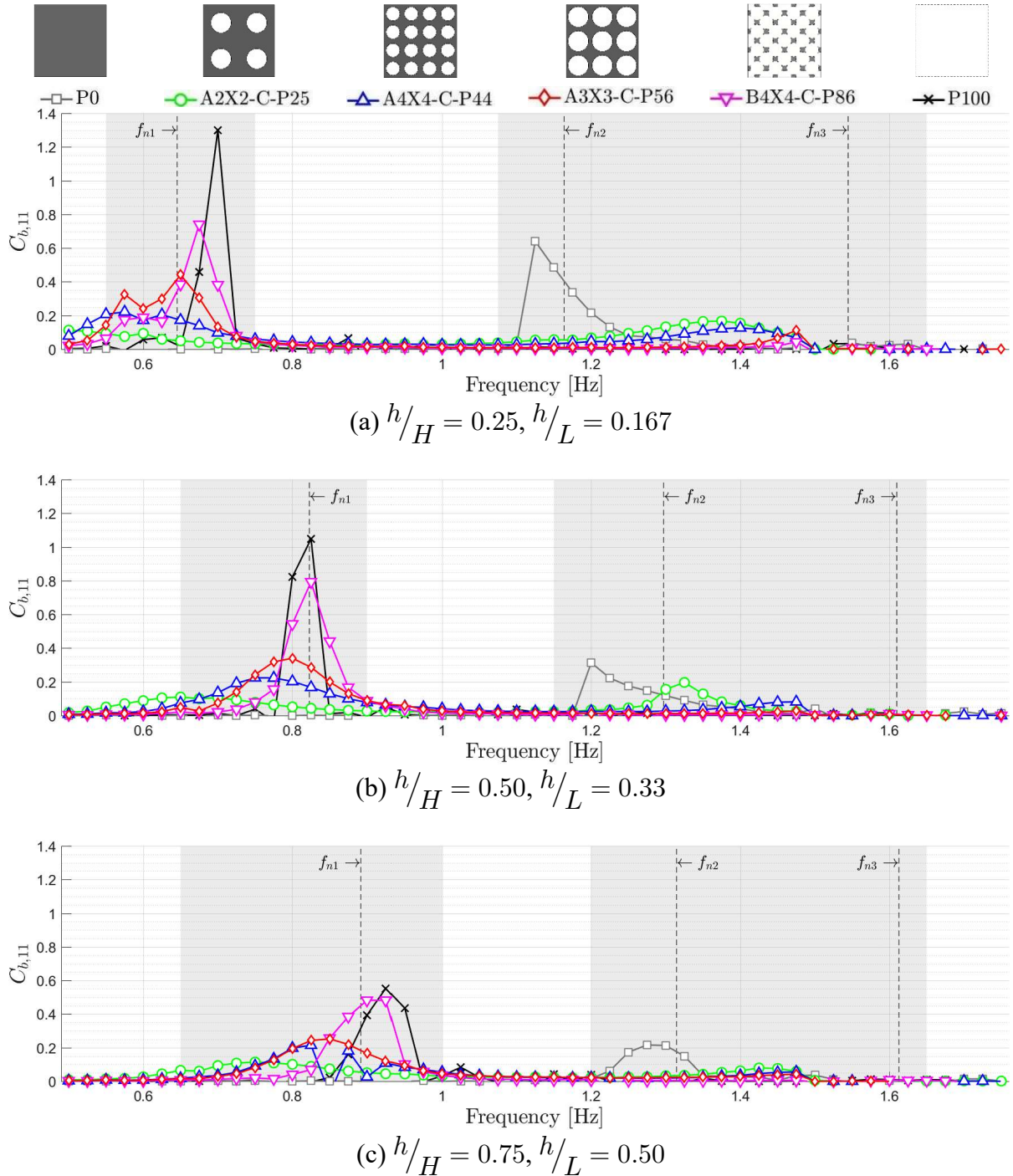
(b) $h/H = 0.50, h/L = 0.33$



(c) $h/H = 0.75, h/L = 0.50$

Source: figure from the author.

Figure 3.28 – Surge damping coefficient ($C_{b,11}$) in the frequency domain, surge motion, $A = 1\% \times L$



Source: figure from the author.

In the case of the first compartmented anti-symmetric mode, one standing wave is created in each compartment of the tank and the velocity of the flow in the longitudinal direction at the center of the tank should be close to zero. Therefore, the

lower the open-area ratio of the perforated bulkhead, the better to intensify the first compartmented anti-symmetric mode.

Larger accelerations of the fluid within the tank in the longitudinal direction yields larger velocities in the flow as well. So, the damping coefficient is strongly related to the added mass coefficient. For frequencies in the vicinity of that of the first non-compartmented anti-symmetric mode (f_1), very large damping coefficients were obtained for bulkheads with large open-area ratios as consequence of nonlinear phenomena of wave breaking in the free surface. On the other hand, large damping coefficients for frequencies close to that of the first compartmented anti-symmetric mode (f_2) were computed for bulkheads with small open-area ratios, as wave breaking and other nonlinear phenomena that introduce significant damping were observed in the simulations.

Both the added mass coefficients and the damping coefficients are larger in the case of the filling ratio of 0.167 (Figure 3.27-a and Figure 3.28) than for higher filling levels. It is related to the sloshing pattern typical of the low filling levels, in which a travelling wave is created in the free surface, which has significant more longitudinal acceleration and velocity than the standing wave usually created for higher filling levels.

It is important to emphasize particular aspects of the bulkheads evaluated in the present work. First, the distribution of the holes was proposed in order to be the most homogeneous and symmetrical as possible to avoid non-uniform open-area distribution along the depth. Second, the largest holes are only 6 times larger than the smallest holes. Third, even the smallest holes studied are large enough in order to avoid that very complex phenomena become predominant in the flow, such as capillarity in the jet flow through the holes, viscous damping and sub-particle scale effects of the turbulence.

Then, for the range of open-area ratios and considering the abovementioned features of the bulkheads, the results obtained in the previous sections and from other

works in literature strongly indicate that the restriction of the flow is the most fundamental contribution provided by perforated bulkheads, and other vertical baffles in general, to sloshing mitigation. Such aspect is strongly affected by the relation between the distribution of the open-area ratio in vertical direction as the flow velocity amid the tank decreases with the depth. Thus, the focus of the following sections is the investigation of the relation between open-area ratio and the tank depth in order to develop a perforated bulkhead with an optimized open-area distribution for sloshing suppression.

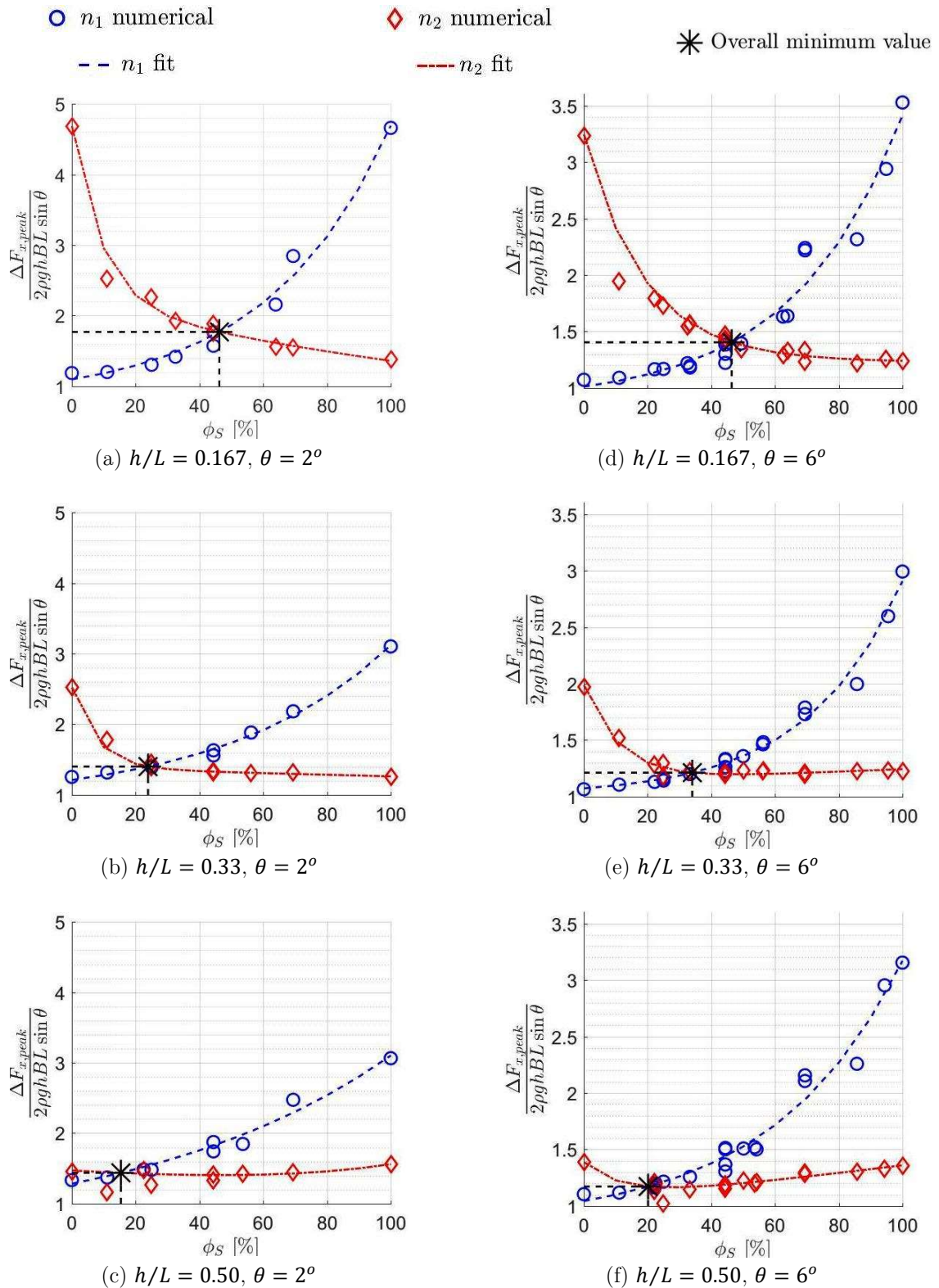
3.8 OPTIMUM OPEN AREA RATIO OF SWASH BULKHEAD FOR SLOSHING MITIGATION

According to the diagrams in the frequency domain of the free surface elevation (Figure 3.12) and the dynamic longitudinal force (Figure 3.13), the open area ratio of the swash perforated bulkhead affects both the magnitude of the peak resonant response and the frequency at which it occurs. So, based on the division of the frequency domain into two parts: first part comprising the first resonant mode (n_1), from 0.5 Hz to 1.0 Hz, and second part, containing the second resonant mode (n_2) and the third resonant mode (n_3), from 1.0 Hz to 1.75 Hz, the magnitude and frequency of the peak of the curves were identified for each case and each filling level.

Considering the computed dynamic longitudinal force, Figure 3.29 provides the magnitudes of the response amplification of the first and second resonant peaks as functions of the open area ratio of the bulkhead. Besides, in Figure 3.30, the magnitude of the free surface elevation amplifications of the resonance peaks in relation to the open area ratio of the bulkhead is presented. In both groups of diagrams, the results for the three filling levels and the two pitch excitation motion amplitudes are shown.

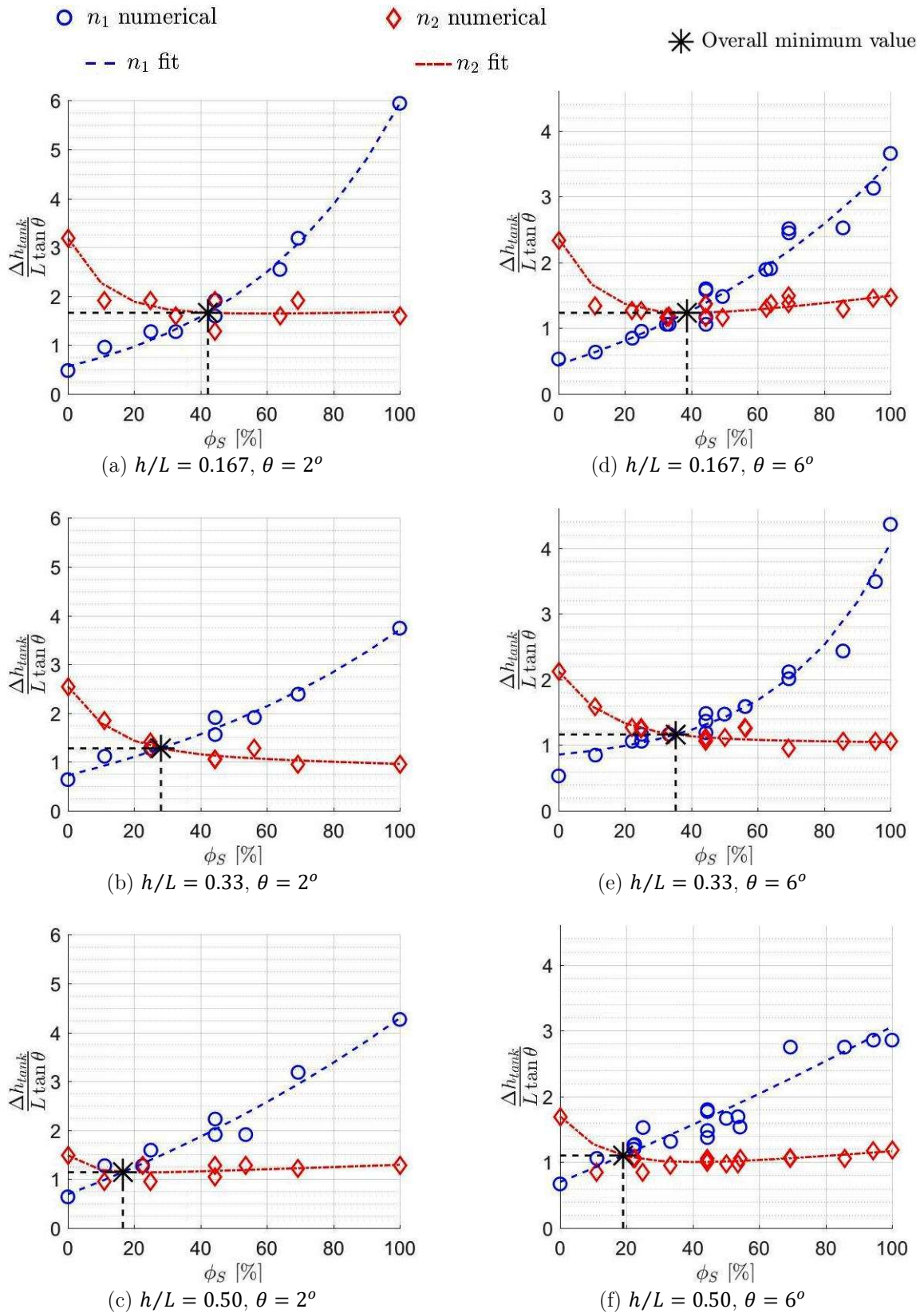
The graphs with the magnitude of the peaks of the dimensionless dynamic longitudinal force for the cases with surge harmonic motion are presented by Figure 3.30. The graphs with the magnitude of the peaks for the dimensionless free surface amplitude in the case of surge harmonic motion are presented by Figure 3.31. Six graphs are shown by each Figure 3.30 and Figure 3.31, as the combination of the two surge harmonic motion amplitudes and the three different filling levels.

Figure 3.29 – Dimensionless longitudinal dynamic force of the first (n_1) and second resonant peak (n_2) as functions the open area ratio, pitch motion



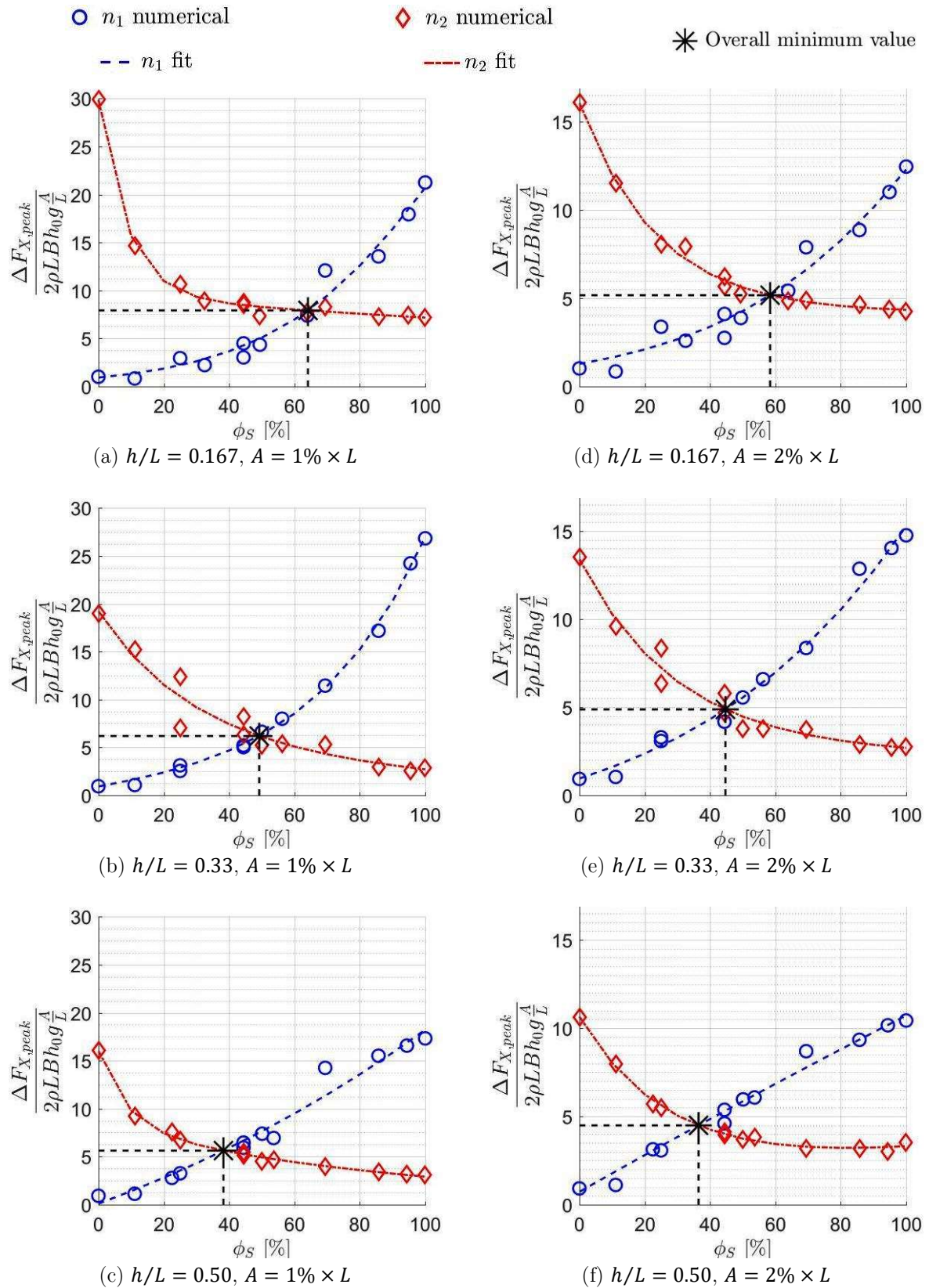
Source: figure from the author.

Figure 3.30 – Dimensionless free surface elevation of the first (n_1) and second resonant peak (n_2) as functions of the open area ratio, pitch motion



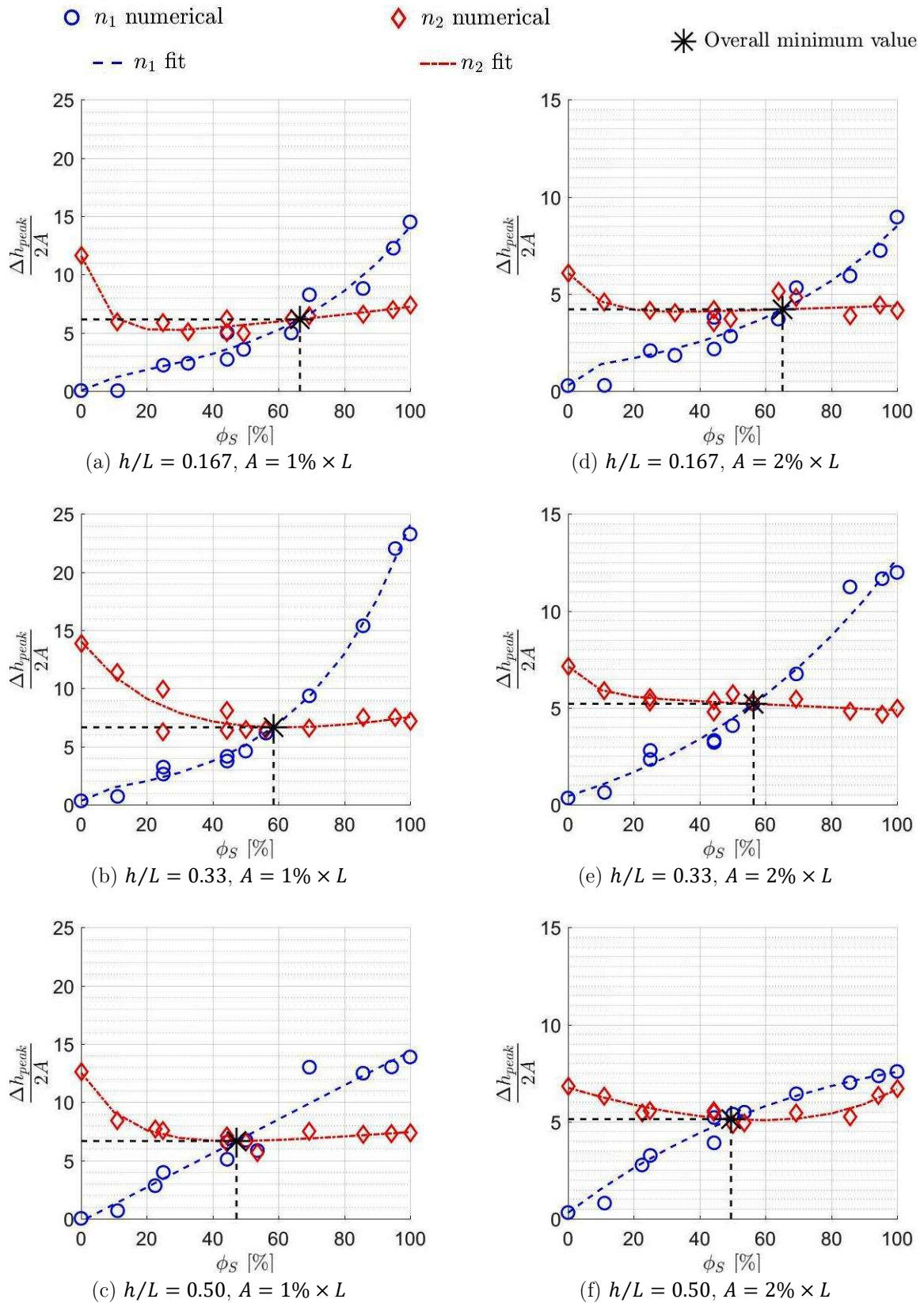
Source: figure from the author.

Figure 3.31 – Dimensionless longitudinal dynamic force of the first (n_1) and second resonant peak (n_2) as functions the open area ratio, surge motion



Source: figure from the author.

Figure 3.32 – Dimensionless free surface elevation of the first (n_1) and second resonant peak (n_2) as functions of the open area ratio, surge motion



Source: figure from the author.

In Figure 3.29, Figure 3.30, Figure 3.31 and Figure 3.32, regarding the first resonant peaks, the amplification magnitude increases monotonically as the open area ratio of the bulkhead increases. The increase rate becomes larger as the submerged open area ratio increases. Concerning the second resonant peaks, the opposite behavior is obtained: the magnitude of the amplification is reduced monotonically as the submerged open area ratio increases, and the decrease rate is larger for small submerged open area ratios. Similar to the approximate formulation for the frequency of the resonant peak, the computed results of response amplification as a function of submerged open area ratio were approximated by exponential curves, which are shown in the graphs by dashed lines, with correlation factor above 95% for all the cases.

Focusing on the sloshing mitigation in the entire frequency domain, the results indicate a clear tradeoff in relation of the submerged open area ratio of the perforated bulkhead. While by reducing the submerged open area ratio of the perforated bulkhead the sloshing is mitigated in the first resonant mode (n_1), the sloshing is increased in the second mode (n_2 , compartmented). On the other hand, by increasing the submerged open area ratio of the perforated bulkhead, the sloshing is mitigated in the second resonant mode (n_2 , compartmented) but increased in the first resonant mode (n_1).

Notwithstanding, the two exponential curves in each diagram intersects each other at an “optimal” point in which the overall minimum value for the amplification at the resonance for a given filling level occurs. From this point, the so-called “optimum open area ratio” for a given filling level can be obtained. It is interesting to observe that the magnitude of the amplification at the optimum open area ratio is lower than two times the quasi-static free surface elevation or the hydrostatic variation of longitudinal force for all the filling levels. Moreover, it exceeds 1.5 times only for the low filling level. Thus, the “optimum open-area ratio” is one that results in the lowest overall peak magnitudes of longitudinal force and free surface elevations in the entire frequency range comprising the lowest three resonant modes of sloshing. Summarizing,

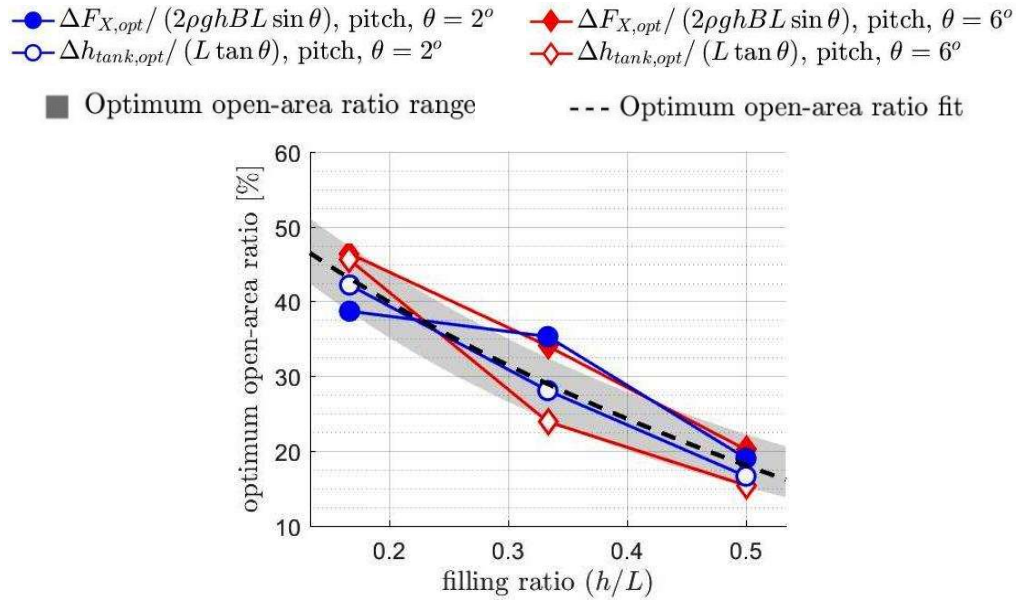
in the context of the present work, considering the liquid storage and transportation containments, the smaller the liquid motion is, the better. In the context of TLDs (Kaneko & Ishikawa, 1999) (Tait, Isyumov, & El Damatty, Performance of Tuned Liquid Dampers, 2008), a different concept of “optimum open-area ratio” must be adopted because some level of fluid oscillation is required to make TLD functioning as a dynamic damper and transfer energy from the tank to the main structural system. In such case, a more complex balance between damping and inertia must be achieved whilst only the damping is the prevalent feature in the present analysis.

The results obtained in this analysis are consistent with Firoozkoohi and Faltinsen (2010). The authors studied the case of a two-dimensional rectangular tank equipped with a slat-screen only for the filling ratio of $h/L = 0.4$. For very small motion amplitudes, an optimized solidity ratio of $S_n \approx 90\%$ was obtained, which is equivalent of an open area ratio of approximately $\phi = 10\%$. The optimum open-area ratio calculated by the present study for the filling ratio of $h/L = 0.5$ for the motion amplitude of $\theta = 2^\circ$ is around 15%.

The results of Figure 3.29, Figure 3.30, Figure 3.31 and Figure 3.32 indicate that the optimum open area ratios decrease as the filling level increases. Figure 3.33 shows the optimum open area ratios as a function of filling ratio h/L for the cases with harmonic pitch motion. From the data of the surge harmonic motion, Figure 3.34 shows the optimum open area ratio as function of the filling ratio.

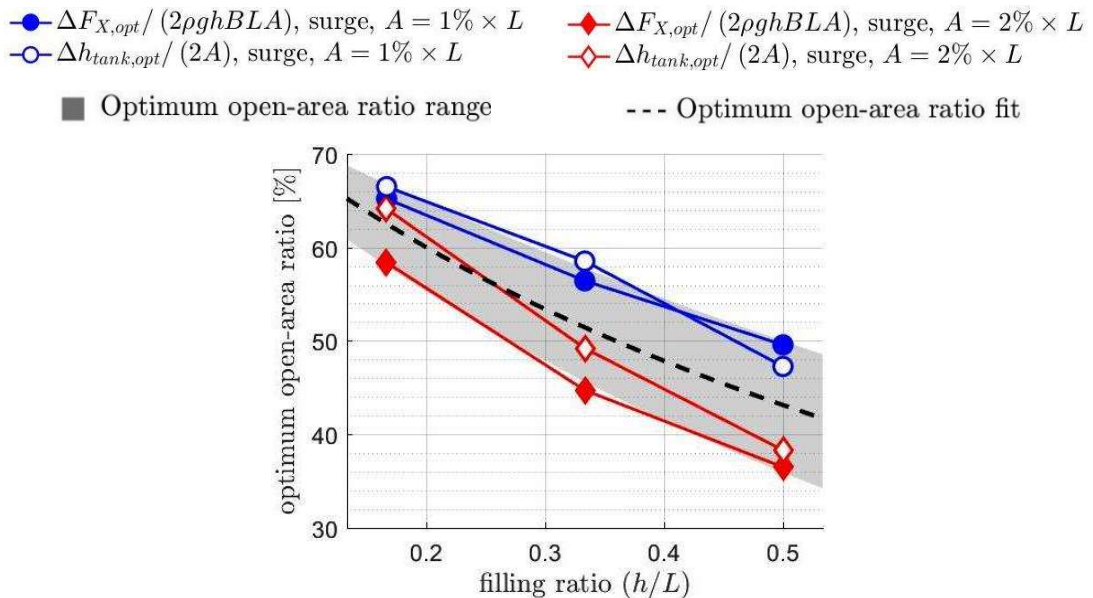
Regardless of small differences, the curves associated to free surface elevation and the curves of the dynamic longitudinal forces show similar behavior and could be approximated by exponential curves. In order to encompass the optimum open area ratio obtained from the four curves, a lower and an upper envelope obtained from the curves is defined as an “optimum open-area ratio range” as a function of the filling level and shown in Figure 3.33, for the pitch motion, and in Figure 3.34, for the surge motion, as a shaded area.

Figure 3.33 – Optimum open area ratios for sloshing mitigation as a function of the filling ratio h/L , pitch motion



Source: figure from the author.

Figure 3.34 – Optimum open area ratios for sloshing mitigation as a function of the filling ratio h/L , surge motion



Source: figure from the author.

The optimum open-area ratio follows a similar pattern regardless of the kind of motion, it has a logarithm-like profile as it decreases monotonically and the decrease

rate of the curve decreases as the fillig ratio increase. However, for an equivalent filling ratio, the optimum open-area ratio for the surge motion is around 20% higher than the optimum open-area ration for the pitch motion. Further investigation is required in order to understand such phenomenon.

Furthermore, as the logarithmic decay curve trends towards an asymptote, a constant optimum area ratio might be achieved as the filling ratio trends towards infinite for deep liquid condition. Considering that the deep liquid condition occurs for filling ratios larger than 1.0, additional simulations with tanks with a higher ceiling and a higher filling level are required in order to define such constant.

Using the average value of the upper and the lower limits of the optimum open area ratio range, the regression curve of “optimum open area ratio”, which is shown as a dashed line in Figure 3.33 and Figure 3.34, is obtained by adopting the exponential equation provided in equation 3.5. As a result, the empirical formula for the optimum open area ratio is obtained as function of the dimensionless filling ratio (h/L). For the case of the pitch harmonic motion, the coefficients are $C_1 = 65.3$ and $C_2 = 2.5$. For the case of the surge harmonic motion, the coefficients are are $C_1 = 75.4$ and $C_2 = 1.2$.

$$\phi_{opt} = C_1 e^{-C_2(\frac{h}{L})} \quad (3.5)$$

The fitted relation of eq. 12 is suitable for tanks with rectangular shape in the filling ratios from 0.167 to 0.5, as the relation was interpolated from the results obtained in this interval. Notwithstanding, the extrapolation for higher filling ratios ($h/L > 0.5$) is deemed as suitable as well because it has a logarithmic profile that leads to a constant value as the filling ratio increases. Likewise, although the lower limit for the deep liquid condition is defined as $h/L \gtrsim 1.0$ (Faltinsen & Timokha, Sloshing, 2009), for the case in which $h/L > 0.5$ the effect of tank bottom on the flow is already small.

3.9 TEST CASE: SWASH BULKHEADS WITH OPTIMUM OPEN AREA RATIO

The previous section was focused on the investigation of the sloshing mitigation due to perforated swash bulkheads. The models adopted for that purpose were based on several holes distributed in different arrangements along a bulkhead in the longitudinal center of the tank. For sake of simplicity, arrangements considering uniform distribution of the perforations were adopted so that the open area ratio is almost independent to the filling levels. Nevertheless, the results of section 3.8 show that an optimum open area ratio could be defined as function of the ratio between the filling ratio (h/L). As a further step on the investigation of the effects of the perforated bulkheads on the sloshing mitigation, the focus of the present section is to apply the insights obtained by the previous results in order to propose and evaluate the models of perforated bulkheads with an open area ratio distribution within the “optimum open area ratio range” for all the filling levels and, thus, being capable of mitigate the sloshing in the entire frequency range comprising the three first resonant modes of sloshing motions. In this section, the investigation is focused only on the pitch motion.

3.9.1 Models

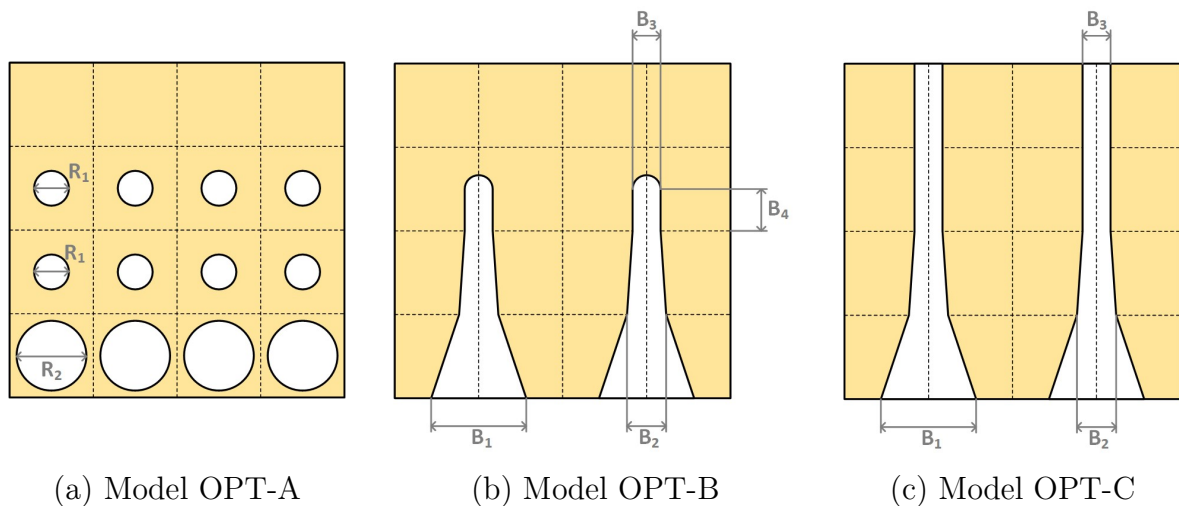
Figure 3.35 presents the three proposed layouts of swash bulkheads whose open area ratio is within the “optimum open area ratio range” for all the filling levels.

The model “OPT-A” was proposed following the same concept of the previous section, with distribution of the holes in the bulkhead based on the amplitude modulation. The holes are circular and the radius of the holes in lower row are $R_2 = 8.46cm$ and the radius of the holes in intermediate and top rows are $R_1 = 5.24cm$, with the dimension of the smaller holes limited by the convergence criteria of the numerical model of $D/l_0 \geq 10$. Despite not analyzed herein due to much higher computation cost

required, alternative hole distribution geometries for the bulkhead can also be generated using larger amounts of smaller holes based on frequency modulation.

The model “OPT-B” was proposed based on the idea of vertical strips with variable width in order to make the open area ratio fits within the “optimum open area ratio range”. In the present study, only two strips were used to model the bulkhead OPT-B due the restriction imposed by the numerical model convergence criteria of $\Delta l/l_0 \geq 10$ that must be matched in the narrowest part of the strip, where Δl is the minimum linear dimension of the hole. In the Figure 3.35-b,c, the main dimensions are $B_1 = 18cm$, $B_2 = 12cm$, $B_3 = 10cm$ and $B_4 = 7.5cm$. Both models OPT-A and OPT-B show a watertight section above the 0.50 filling ratio because the previous analyzes were restricted for filling levels below that. So, a model “OPT-C”, which follows the same concept of OPT-B, was proposed with the strip opening reaching the top of the bulkhead.

Figure 3.35 – Geometry of the models of bulkheads with optimum open area ratio

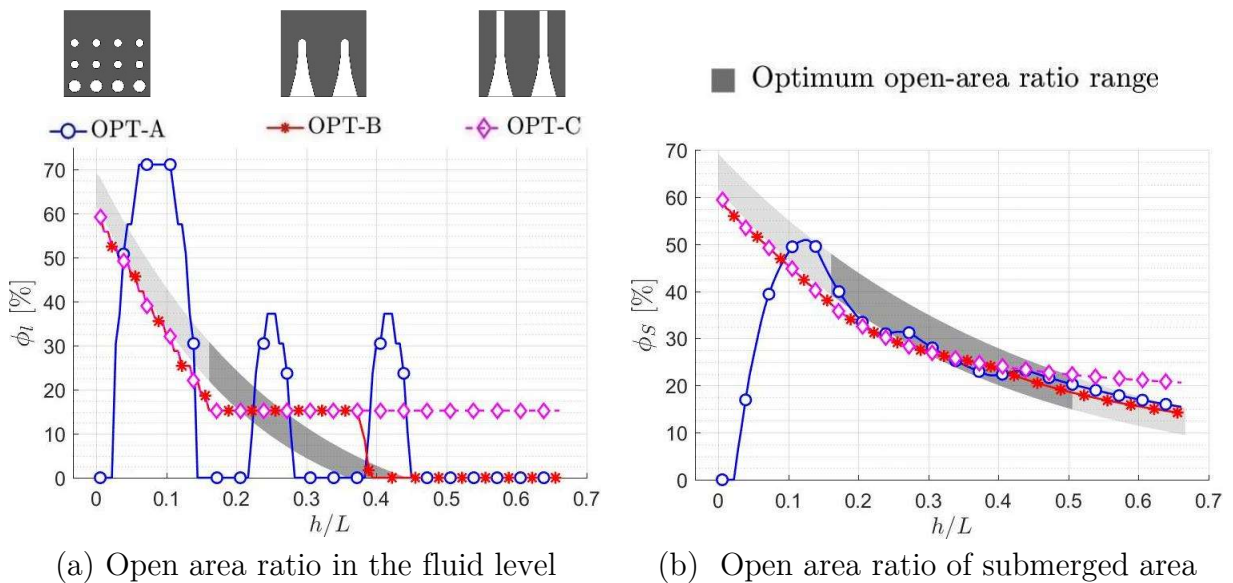


Source: figure from the author.

Figure 3.36-a shows the local open area ratio in liquid levels for the three proposed bulkhead models. Figure 3.36-b illustrates the open area ratio of submerged bulkheads of the three proposed models as a function of the filling level. The open area

ratio of submerged area bulkheads consists on the ratio between the total area of the openings below the still water level and the total area of the bulkhead below such level. The “optimum open area ratio range” is indicated by the gray region on the graphs. The dark grey area is between the filling ratios from 0.167 to 0.50 evaluated previously, while the light gray areas were defined by the extrapolation of the tendency for higher and lower filling levels. The open area ratio of the submerged area of all the three proposed bulkhead models fits inside the “optimum open-area ratio range” between 0.167 and 0.50.

Figure 3.36 – Relation between open area ratio distribution of the optimized swash bulkheads and the filling level



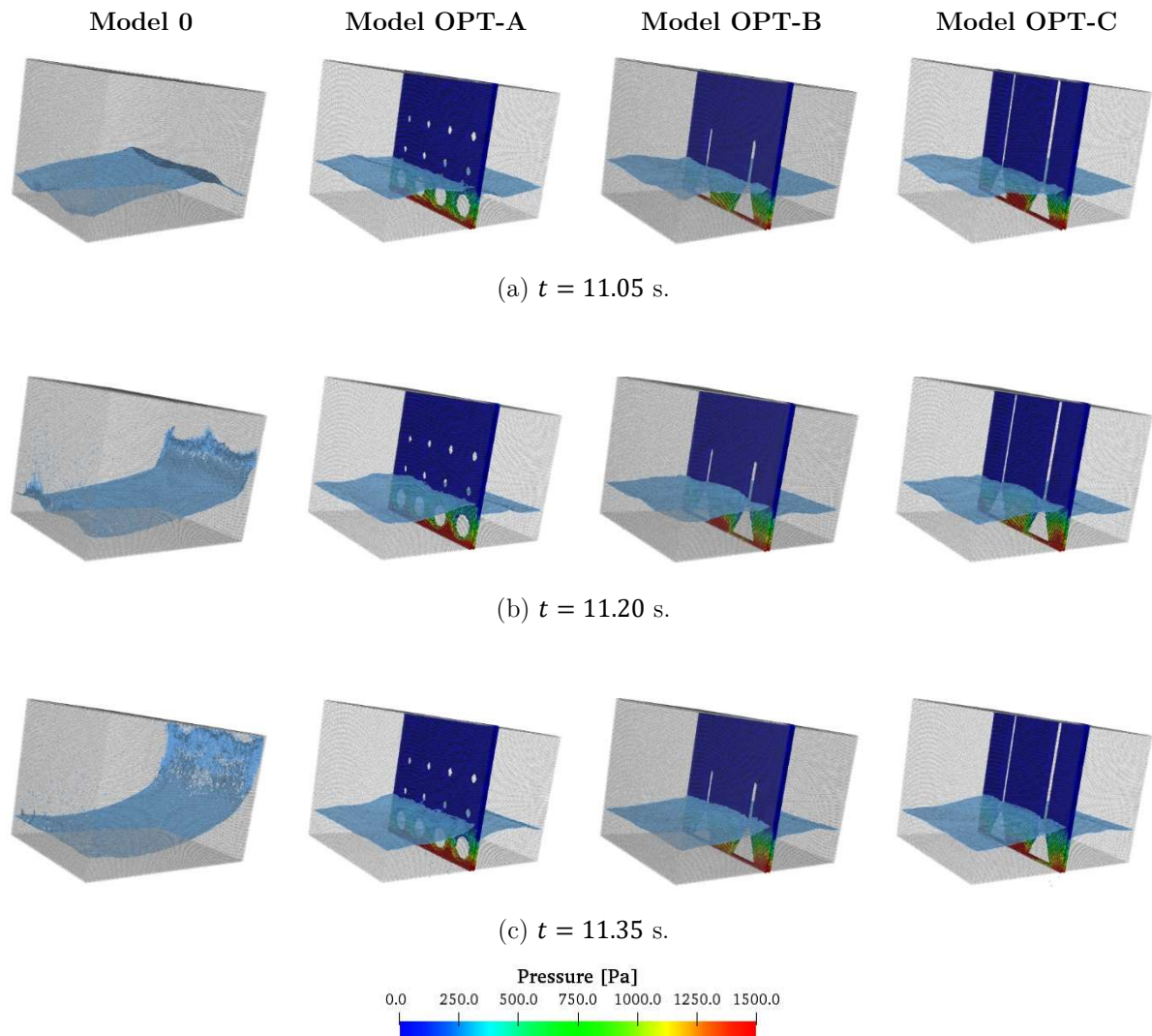
Source: figure from the author.

3.9.2 Results

Figure 3.37 provides snapshots of the particle simulation in the first mode (n_1) at the low filling level, for the clean tank and the three tanks with optimized swash bulkhead geometries. In the time frame presented by the snapshots, violent impact of the travelling wave on the side walls occurs in the clean tank while relatively calm fluid

motions, with only very small free surface displacements were computed for the three tanks with optimized perforated bulkheads.

Figure 3.37 – Snapshots of particle simulation – $h/L = 0.167$, non-compartmented first mode (n_1)

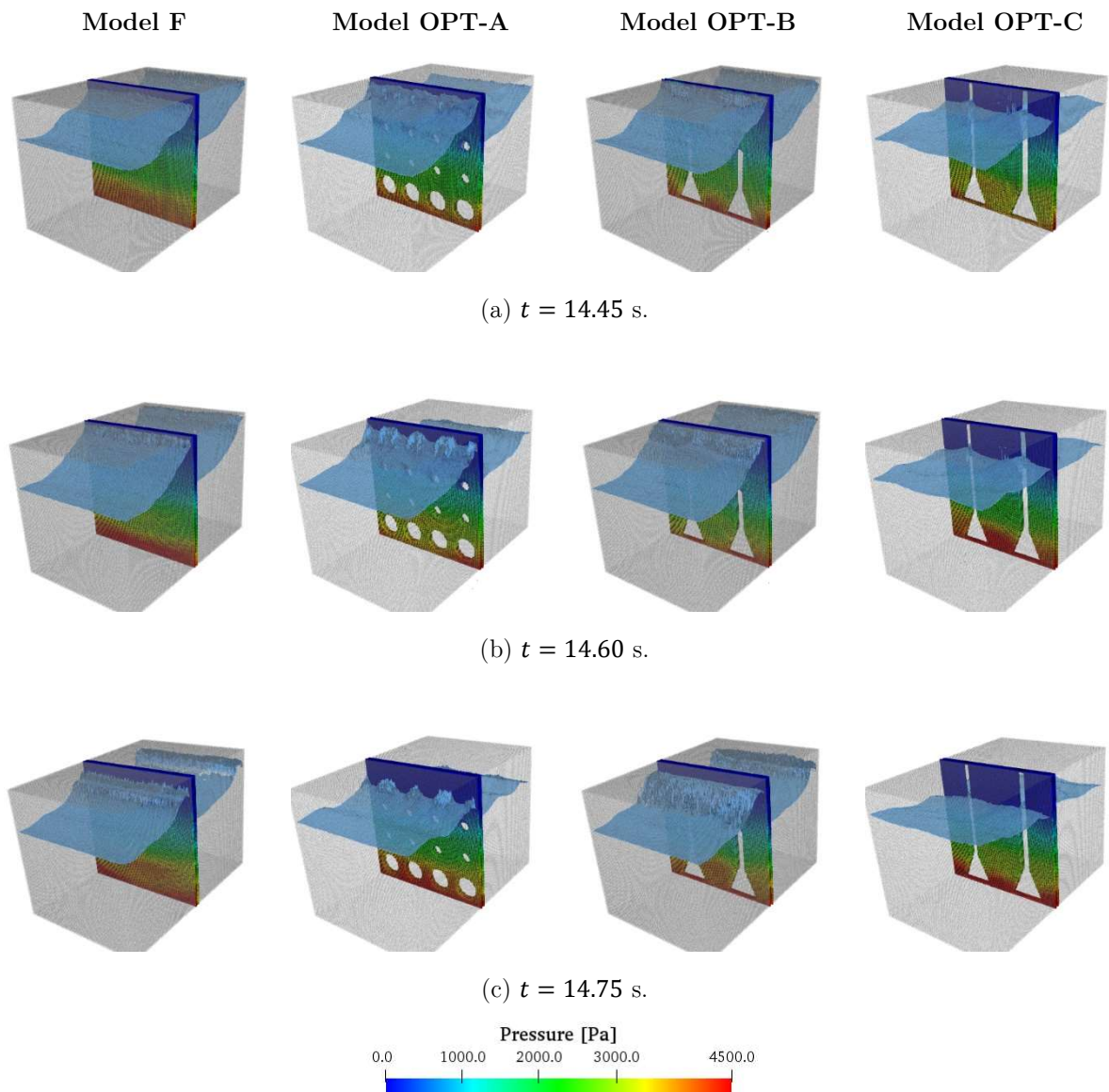


Source: figure from the author.

Figure 3.38 shows snapshots of the particle simulation for the tank with watertight bulkhead and other three tanks with optimized swash bulkhead in the second mode (n_2) for the high filling level. The free surface reaches tank ceiling for watertight bulkhead and both OPT-A and OPT-B models. The impact on the ceiling is violent enough to generate splash in the tank with watertight bulkhead and the OPT-B

swash bulkhead model (Figure 3.38-c). The jet flow through the circular holes cause the highly nonlinear free surface profile observed in the second frame for the OPT-A model (Figure 3.38-b). Finally, only the OPT-C model presented small free surface displacements for the high filling level at the second mode (n_2).

Figure 3.38 – Snapshots of particle simulation – $h/L = 0.5$, compartmented second mode (n_2)



Source: figure from the author.

The graphs of the dimensionless free surface elevation and the dimensionless dynamic longitudinal force in the frequency domain are given in Figure 3.39 and Figure

3.40, respectively. The results were obtained considering harmonic pitch excitation of 6 degrees amplitude. In the graphs, the responses obtained by using the proposed optimized bulkheads were compared to the responses of the clean tank and the tank with watertight bulkhead. The model OPT-C was simulated only for the high filling level because its behavior for the low and intermediate filling levels is assumed as equivalent to those of the OPT-B bulkhead.

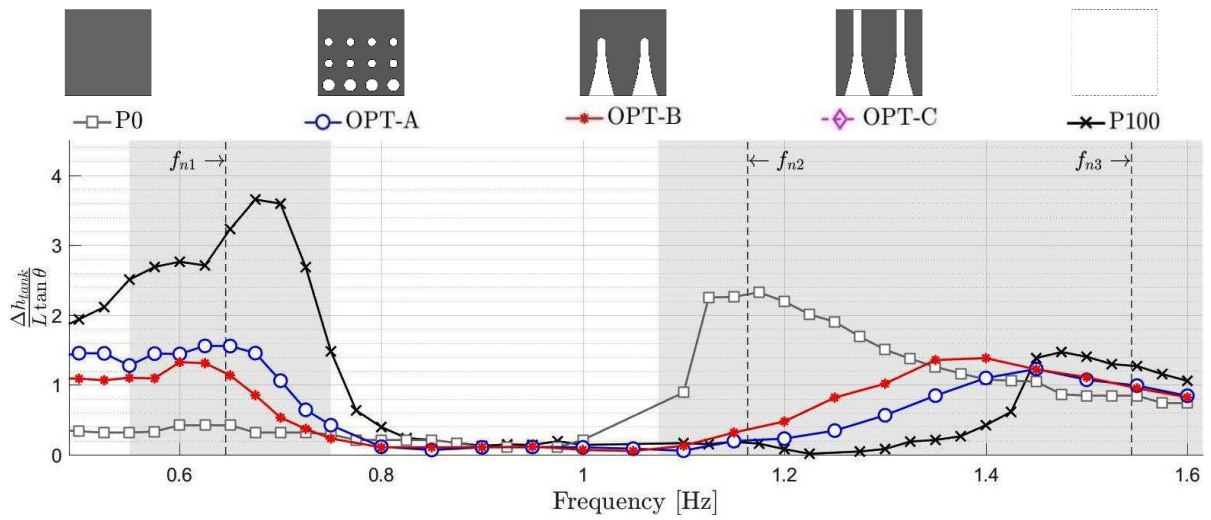
For the low and the intermediate filling levels, all the proposed models presented remarkably sloshing mitigation in the range of frequencies close to the two resonant modes (n_1 and n_2), with amplifications of the free surface elevation not exceeding 1.5 times the hydrostatic free surface displacement, as shown in Figure 3.39-a and Figure 3.39-b.

Nevertheless, for the high filling level (Figure 3.39-c), all the proposed models lead to excellent sloshing mitigation in the first mode (n_1), while slightly larger free surface elevation amplifications occurs in the second mode (n_2) for the models OPT-A (2 times) and OPT-B (2.5 times) in relation to the tank with watertight bulkhead (1.8 times). Only the model OPT-C is capable of mitigating the sloshing also in the high filling condition at the second resonant mode (n_2 , compartmented), with free surface elevation amplification less than 1.5 times the quasi-hydrostatic free surface displacement. In addition to these results, resonant frequencies of the first resonant mode (n_1) in the models with optimized swash bulkhead geometries are lower than the clean tank.

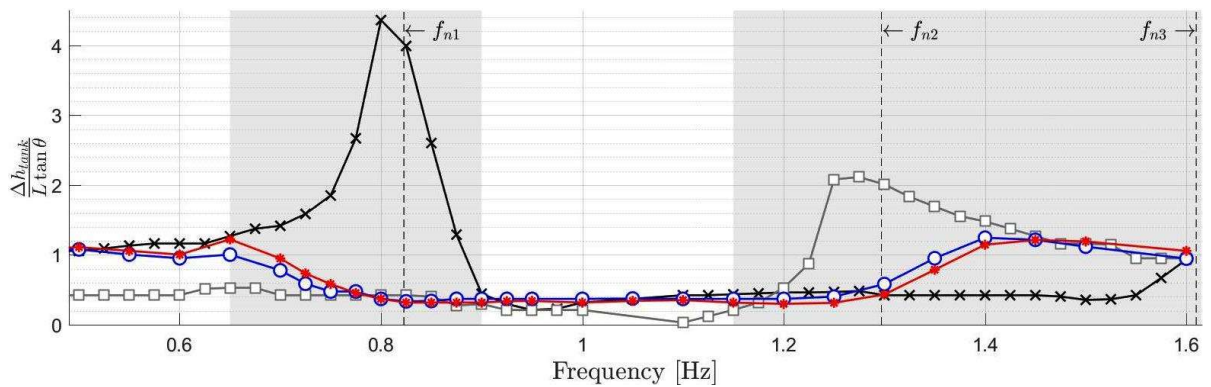
Such results observed for high filling levels indicate that the open area ratio above the still water level has also an important effect on the flow due to the runup a watertight bulkhead might cause. Hence, the extrapolation of the “optimum open-area ratio” to filling ratios above 0.5 is suggested in order to achieve better sloshing mitigation in high filling levels. Since both bulkheads OPT-A and OPT-B are watertight just above the height of 75%, the flow behavior resembled those of the

watertight bulkhead at high filling levels, with large fluid motions at the second resonant mode (n_2).

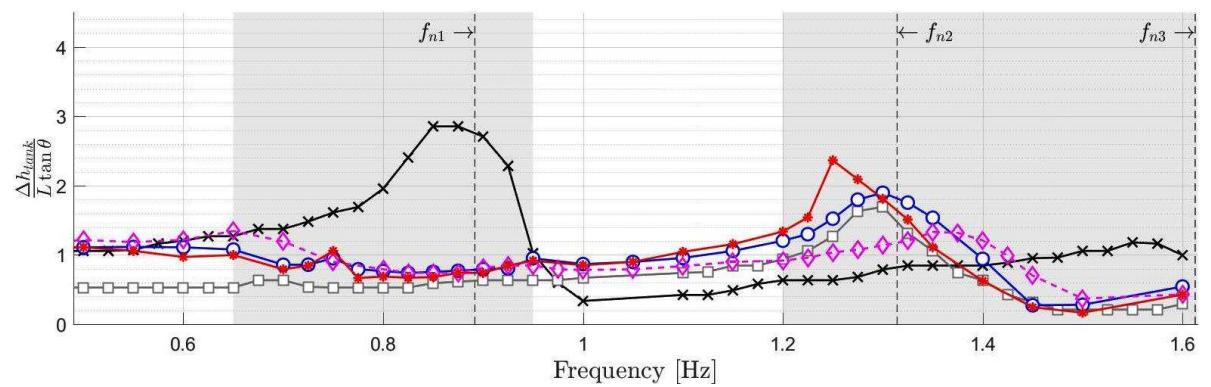
Figure 3.39 – Optimized swash bulkheads: dimensionless free surface elevation in frequency domain



(a) $h/H = 0.25, h/L = 0.167$



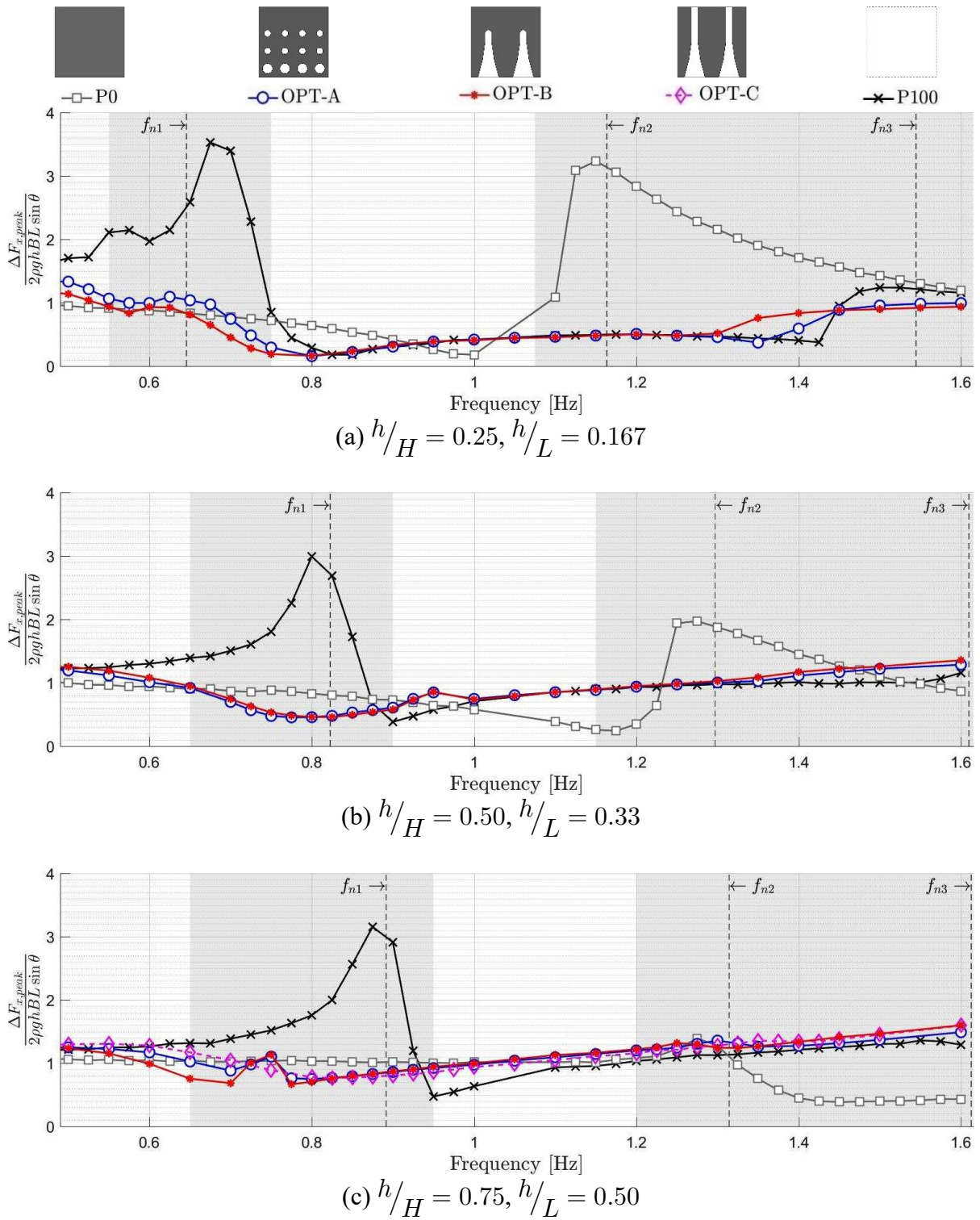
(b) $h/H = 0.50, h/L = 0.33$



(c) $h/H = 0.75, h/L = 0.50$

Source: figure from the author.

Figure 3.40 – Diagram of the dimensionless longitudinal dynamic force in the tank in the frequency domain: optimized



Source: figure from the author.

In conclusion, an optimized model of watertight bulkhead was obtained in the model OPT-C, which reduces the amplification of both free surface elevation and

dynamic longitudinal force to less than 1.5 times for all the evaluated filling levels in the entire frequency range comprising the first three sloshing modes of a rectangular tank. As mentioned above, other bulkhead models with different perforation geometries, such as small holes distributed based on frequency modulation, which follow the “optimum open area ratio range” can also be considered in order to achieve a similar performance on sloshing mitigation.

3.9.3 Full scale test case

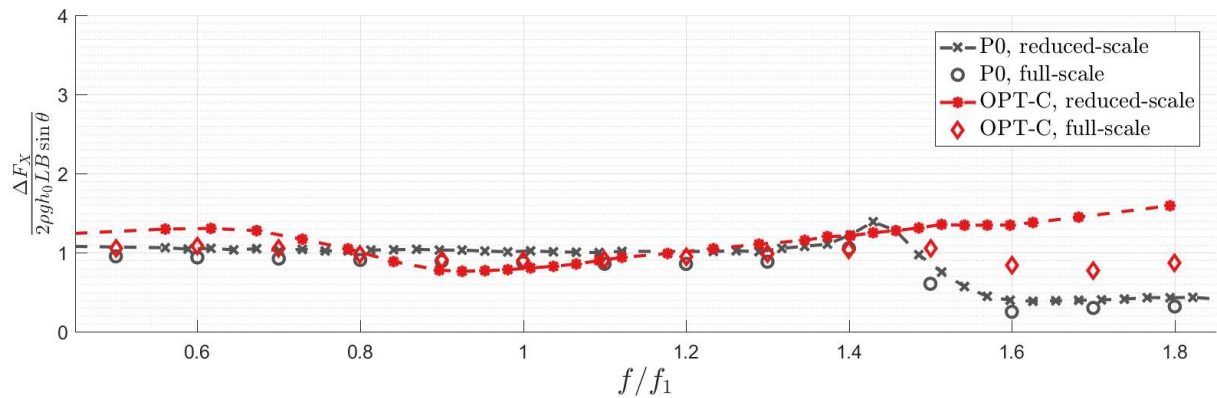
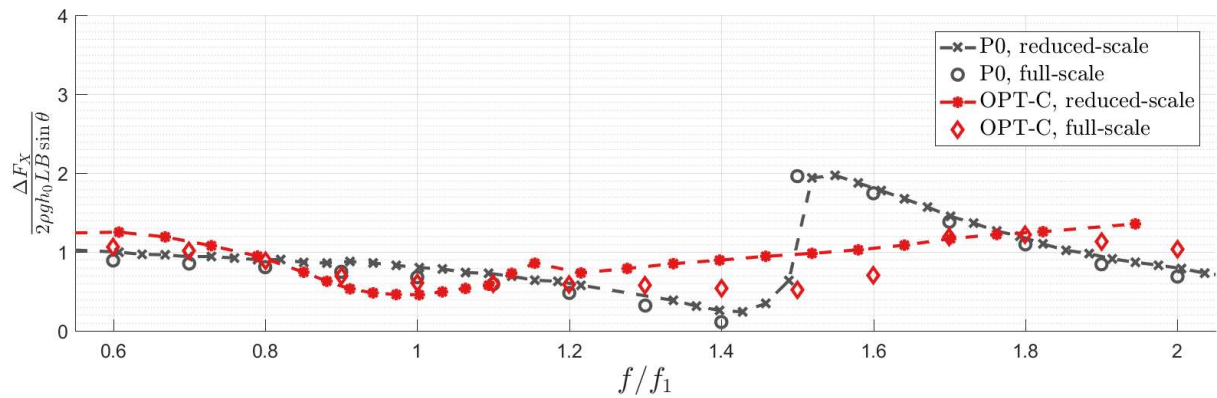
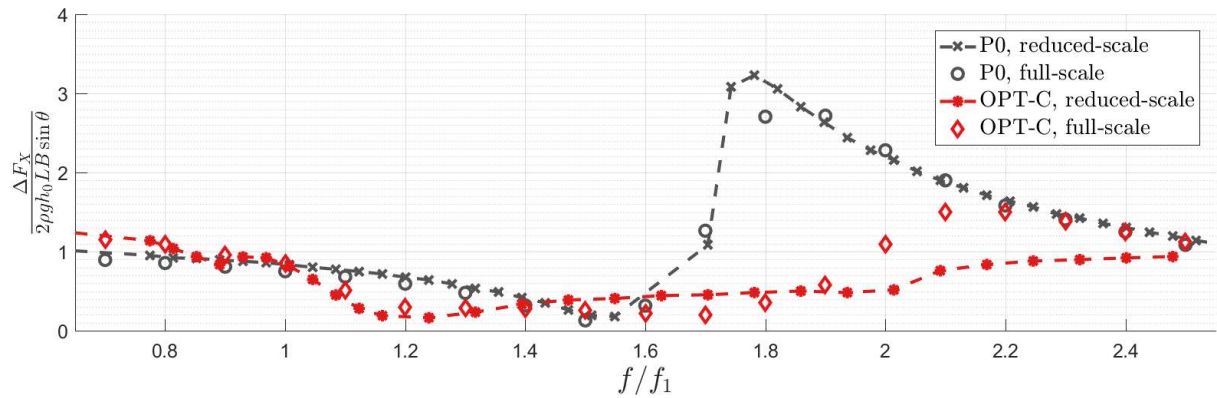
As recommend by the International Towing Tank Conference (2017), the sloshing pressure obtained from reduced scale models can be scaled to full scale by adopting the Froude scaling (Karimi, Brosset, Ghidaglia, & Kaminski, 2014), except for some specific situations, such as local impacts close to the free surface, in which complex phenomena like air trapping might occur and scaling laws concerning compressibility of the liquid and the gas must also be taken into account (Karimi, Brosset, Ghidaglia, & Kaminski, 2014).

Since the focus of the sloshing mitigation by the perforated swash bulkheads is the restriction to the global sloshing flow, the contribution of the local hydrodynamic impact phenomenon might be negligible. However, as the perforated bulkheads introduce additional complexity to the sloshing phenomenon, it is relevant to verify the validity of the Froude scaling in order to extend the obtained optimized open-area ratio to full-scale naval and offshore structures. For this purpose, the dimensions of a typical Suezmax tanker are considered. The cargo tanks of the vessel are around 40 m width and they are divided into two compartments by a watertight bulkhead at its longitudinal center plane. Based on these dimensions and considering a rectangular shaped tank, the relation between the full-scale model and the reduced-scale model adopted in the present work is 1:45. Then, in order to investigate the scaling effects, numerical simulations with full-scale models of the tank with watertight bulkhead (Model P0) and the tank with optimized perforated bulkhead OPT-C were carried out.

Figure 3.41 presents the results for the dimensionless dynamic longitudinal force of the full-scale cases (1:1) and the corresponding results previously obtained using the reduced-scale models (1:45). The harmonic excitation motion has amplitude of 6 degrees and the dimensionless motion frequencies in Figure 3.41 are defined in relation to the analytical estimation of the first non-compartmented mode.

In Figure 3.41, the dimensionless longitudinal dynamic force of the full-scale OPT-C model is slightly larger than that calculated for the reduced scale model for $f/f_1 > 2.0$ at the filling ratio $h/L = 0.167$ (Figure 3.41-a). The opposite is observed for $f/f_1 > 1.6$ at the filling ratio $h/L = 0.5$ (Figure 3.41-c). Besides that, the general behavior presented good agreement between the different scales for both models and the Froude scaling worked relatively well. Hence, both the proposed optimized geometry of swash bulkhead and the relation of the optimized open-area ratio as function of the filling ratio (Eq. 2.1) could be applied to full-scale conditions. Moreover, these results provide further evidence that the nonlinear viscous damping such as skin friction and vortex generation introduce only secondary contributions to the effect of the perforated baffle, otherwise larger discrepancies between the reduced-scale and the full-scale simulation might be expected. Furthermore, the sloshing commonly has very high Reynolds number, so the inertial forces prevail over the viscous forces.

Figure 3.41 – Diagram of the dimensionless longitudinal dynamic force in the tank in the frequency domain – analysis of scaling effects



Source: figure from the author.

3.10 CONCLUSIONS

The focus of the present study is to investigate the effectiveness of perforated swash bulkheads as a technique to mitigate the sloshing in tanks. For sake of simplicity, the basic setup adopted herein was a reduced scale model of a clean rectangular tank and its variants equipped with perforated and watertight bulkheads. As the investigation approach, considering its flexibility and effectiveness, numerical simulations based on a fully Lagrangian particle method, which is capable to model phenomena involving large free surface nonlinearities, was adopted. The work was divided into two main parts. The first part of the study consisted on a basic investigation of the effect of the perforated bulkheads on the sloshing by performing a comprehensive evaluation of several parameters as bulkhead open area ratio, filling level, pitch motion frequency and amplitude. As a result, the relation between the optimal open area ratio for sloshing mitigation and filling level was obtained. Then, in the second part of the study, the optimized relation was applied to generate some proposals of optimal geometries for the perforated bulkhead capable of mitigate the sloshing for a wide range of filling levels and frequencies that resembles the typical operational conditions of offshore structures.

The main conclusions of the study are:

- a) Among the geometrical parameters of the perforated bulkheads, the sloshing is essentially affected by the open area ratio and its local distribution along the depth; and the effects of the shape, size, number and arrangements of the perforations are almost negligible. Moreover, the fundamental aspect of the sloshing mitigation by perforated bulkhead is related to its capacity to restrain the flow, and other aspects, such as viscous damping by flow separation and vortex formation, have relatively smaller contributions.

- b) The reduction of the excitation amplitude θ , considering $\theta \leq 6^\circ$, affects essentially the amplitude of the sloshing responses in the vicinity of the resonant peaks and slightly changes its frequency.
- c) In the non-compartmented first antisymmetric mode (n_1), the most violent flows occur for the clean tank and perforated bulkheads with low open area ratio ratios are more effective to mitigate the sloshing.
- d) In the compartmented second mode (n_2), the most violent flows occur in the tank with watertight bulkhead and perforated bulkhead with high open area ratio ratios are more effective to mitigate the sloshing.
- e) As the open area ratio of the bulkhead increases, the flow becomes more violent in the first mode (n_1) but is mitigated in the second mode (n_2). As the open area ratio of the bulkhead decreases, the flow is mitigated in the first mode (n_1) but becomes more violent in the second mode (n_2). The relation between the open area ratio and the magnitude of the free surface elevation amplification and longitudinal dynamic force amplification could be approximated by an exponential form.
- f) The frequency of the resonant modes is affected by the open area ratio of the bulkhead as well. As the open area ratio of the bulkhead increases the sloshing motion associated to the first mode becomes more evident, and the frequency of the first mode increases asymptotically to the first mode of the clean tank (f_{n1}) for $\phi_s \rightarrow 100\%$. The frequency of the second mode also increases gradually as the open area ratio of the bulkhead increase, starting from the frequency of the second mode of the clean tank (f_{n2}) for $\phi_s \rightarrow 0\%$, it increases asymptotically to the third mode of the clean tank (f_{n3}) when $\phi_s \rightarrow 100\%$. The relations between frequency of the resonant modes and open area ratio follows an exponential curve.

- g) Given such tradeoff, an “optimum open area ratio” could be defined for each filling level in order to obtain the minimum overall sloshing for the frequency range covering the three lowest resonant modes and a wide range of filling levels, from shallow to high filling conditions. The “optimum open area ratio” decreases as the filling level of the tank increases and its value can be approximated by an exponential function.
- h) Besides the simulation of the sloshing under pitch motion, the simulation of cases with imposed harmonic surge motion was carried out as well. The general behavior and its relation to the bulkhead open-area ratio are very similar. However, the “optimum open-area ratio” for a given filling ratio is about 20% higher for the case with surge motion than the case with pitch motion. Further study is required to explain such difference.
- i) The relation between optimal open area ratio and filling ratio were used to create three geometries for the perforated bulkheads, which have their performance evaluated. The amplification of the free surface elevation and longitudinal dynamic force, even in the resonant conditions, were below 1.5 times the response of quasi-static condition, showing the effectiveness of the relation.
- j) Due to its ability to mitigate runup provoked by the bulkhead in high filling conditions, the OPT-C design, with vertical opening reaching the ceiling presented excellent performance on sloshing mitigation in all the frequency range for all the filling levels.
- k) As a reference, amplifications of free surface elevation of 4.5 times might occur in the clean tank for filling level of 25% ($h/L = 0.167$) and amplification on the longitudinal dynamic force of 3.5 times might occur in the tank with watertight bulkhead for filling level of 75% ($h/L = 0.5$).

The results of the present work are consistent with findings by previous works in the literature. Notwithstanding, the comprehensive analysis of the problem carried out by the present work provided valuable insights regarding a broader range of aspects and parameters related to the phenomenon. In a practical sense, the optimum open-area ratio relation proposed herein provides bases for the design of many other perforated swash bulkhead as well as tank geometries, with practical application to the offshore industry. For the proper design of TLDs using perforated bulkheads to mitigate the sloshing, the concepts of the optimum open area ratio, the variation of the resonant period of the first mode with respect to the open area ratio of the bulkhead and the damping in the first resonant mode are useful information. Finally, as the excitations in real conditions might be more complex than the ones considered in the present study, for the development of optimized design focusing a specific condition, further investigation is recommended.

4 CHAPTER FOUR: INVESTIGATION OF THE RESONANT BEHAVIOR OF THE FLOW ENTRAPPED WITHIN NARROW GAPS: “GAP EFFECT”

4.1 ABSTRACT

In the second study of this Thesis, the resonance within narrow gaps between naval and offshore structures is investigated by MPS simulations. The first step of the study consists on a parameter analysis of a simplified two-dimensional model of a barge with imposed harmonic sway motion. The effects of the dimension of the gap, the motion frequency and motion amplitude were investigated. Two different resonant modes were observed in the gap from the particle-based simulations: the piston-mode and the sloshing-mode. In the frequency range of the piston-type resonance, two peaks were observed in the frequency domain. The behavior of the second peak resembles a syphon U-tube flow and it was not previously reported in the literature. An analogy to two simple mechanical systems, with 1 DOF and 2 DOF, respectively, was proposed in order to explain these two piston-type resonant flows. In this study, the MPS was adopted in order to model significant nonlinear aspects of the flow that are not properly modeled by mesh-based methods, such as the flow separation in the edges of the hull.

4.2 INTRODUCTION

The resonant flow inside a narrow gap is a concern for several naval and offshore operations, such as the flow inside moonpools, the flow in the gap between a quay and a berthed vessel and the flow in-between two vessels operating in side-by-side arrangement. In this kind of flow, a large portion of the energy is trapped inside the narrow gap and the resonant flow situations are often related to very large fluid motions that could severely impair the operation of the floating structures.

Through the moonpools, which are vertical openings placed in a hull and often adopted in drilling ships and some Floating, Production, Storage and Offloading units (FPSOs), are placed mooring lines, pipelines and hoses. The resonant flow of the fluid inside the moonpool could induce large vessel motion and high loads on the mooring lines, pipelines and hoses that pass through the moonpool. Other situation is the berthing of a vessel to a quay or an offshore terminal. The large motions of the fluid inside the narrow gap between the ship and the harbor could enlarge the motion of the vessels. Large motions of the ship hamper the offloading operations carried out at the terminal and could result in collision in most critical situations.

Another subject, which is receiving increasing attention nowadays, is the side-by-side offloading operation in open sea. The context is the exploration of oil and, more recently, LNG in deep waters. Instead of a tandem arrangement, the side-by-side one is more effective because it allows offloading from a floating production unit to several tanks of a shuttle vessel simultaneously. However, the downtime of side-by-side operations is usually longer because such operations are more sensitive to the weather conditions. Thus, the prediction of dangerous operational conditions, such as the resonant flow within the gap, is a key issue.

4.3 LITERATURE REVIEW

The flow within narrow gaps has been extensively studied by naval and offshore engineering for, at least, the last three decades given its broad application to the industry. The phenomenon was previously studied by adopting analytical approximations, experiments, empirical formulae and numerical simulations based on several different methods. Nevertheless, the topic is far from exhausted due its highly complex nature.

Analytical and quasi-analytical approaches based on potential linear theory were adopted by Molin (2001) and Faltinsen et al. (2007) in order to estimate the resonant modes and its frequencies for the case of the flow inside a moonpool. Both authors modeled two-dimensionally the moonpool as a gap between a vertical wall and a square-shaped barge. The vertical wall resembles the symmetry-plane of a moonpool. Molin (2001) introduced a very useful simplified analytical formulation to estimate the frequency of the resonant modes by solving the stationary eigenvalue problem. An infinite water depth and a barge with beam much larger than moonpool width are simplifications assumed by this formulation. Faltinsen et al. (2007) solved the boundary value problem by linearized potential theory using a domain decomposition approach and considered finite water depth and barge beams of similar magnitude of the moonpool width.

Maisondieu et al. (2001) performed free oscillation tests by using a quasi-two-dimensional experimental setup based on the simplified model proposed by Molin (2001). The free oscillation tests are performed by inserting a removable lid over the narrow gap and displacing the free surface within it by depressing the air inside the compartment. The study is focused only on the piston-like resonance mode and the results obtained from the experiments are used to estimate the natural frequencies and provide considerations about the damping in the resonance.

Several numerical analyzes of the flow inside narrow gaps were carried out as well. The most widespread approach is the diffraction-radiation model based on Boundary Element Methods (BEM). These methods are generally formulated based on linearized potential theory and present good results to problems of seakeeping and response of floating structures under ocean waves. However, despite the reduced computational cost required by BEM method in relation to Navier-Stokes CFD solvers, several simplifications are adopted in order to model the problem by using the potential theory. These simplifications usually affect the accuracy of the results mainly in the most critical and challenging situations of flow resonance.

Newman and Sclavounos (1988) carried out frequency domain simulations of a catamaran under waves by using a BEM method. The frequency domain response diagrams presented sharp spikes, with some of them of numerical character. As it is well reported in the literature that the linear potential methods overestimate several times the piston-mode resonant flow, a large number of ensuing works addressed such shortcoming. Huijmans et al. (2001) introduced a zero flux condition in vertical direction to the boundary conditions of the free surface in the gap; a technique called “rigid lid” method. This proposal was able to reduce the amplitude of the flow in piston-mode resonance and was widely used in following works. However, the “rigid lid” has no physical relation and the damping factor of each resonant mode must be calibrated by experiments.

The damping in the flow within gaps could be generated by different phenomena such as skin friction on the hull, flow separation, nonlinearities in the free surface and vortices formation and shredding. Kristiansen and Faltinsen (2010) concluded that the flow separation and the vortex formation in lower edges are the most significant components of the damping observed in piston-mode resonance. Feng and Bai (2015) studied cases involving waves with larger amplitudes and larger wave steepness by using nonlinear BEM simulations with a remeshing technique. They observed a very

slight shift in the resonance period for such cases and concluded that the free surface nonlinearities could be also a significant aspect of the damping.

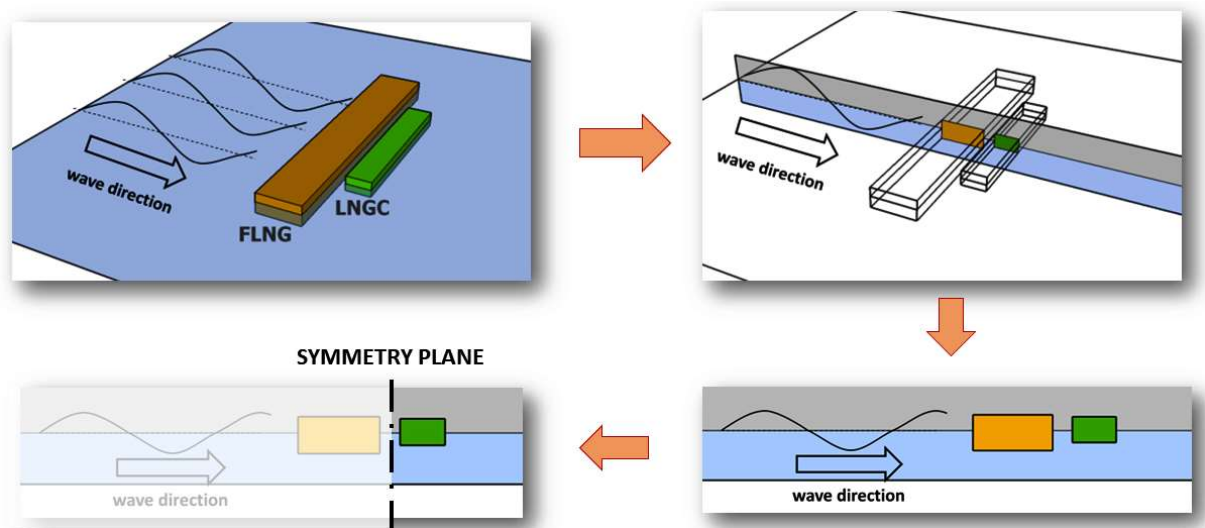
The complex nature of the damping on piston-mode resonant flow impose important challenges to the modelling of this phenomenon by BEM, the widespread numerical technique to study seakeeping. Within this context, the fully Lagrangian particle-based method are capable to account highly nonlinear aspects of the flow, such as large free-surface deformation, vortex formation due complex hull and bilge geometries and motion of structures. The Moving Particle Semi-implicit or Moving Particle Simulation (MPS) method, originally proposed by Koshizuka et al. (1995), is adopted in the present study to investigate large amplitude fluid motions inside narrow gaps.

The MPS method solves the governing equations for the incompressible flow and the fluid is represented by moving particles. The particle method easily deals with phenomena involving large free surface displacements and large body motions, which are important aspects of the resonant flow in the gap. Tsukamoto et al. (2011) used the MPS method to simulate the sloshing inside tanks with an elastically linked suppression device and Bellezi et al. (2013) (2015) used the method to study the green water in offshore structures in rough seas. Both phenomena are highly nonlinear and present very large free surface displacements and body motions. The most important drawback regarding the CFD methods is the high computational cost.

4.4 OBJECTIVES

The present study is divided into two parts. The first part consists in the validation of the numerical code regarding the problem of piston-mode flow. The free oscillation tests made by Maisondieu et al. (2001) were reproduced by a particle simulation. The frequency of the computed free surface elevation signal and the amplitude of its first peaks were compared to the experimental results and analytical estimations.

Figure 4.1 – Sketch of the two-dimensional modeling of the problem



Source: figure from the author.

In the second part, nonlinear aspects of the flow inside a narrow gap are investigated numerically through a numerical tank. One of the ends of the tank is a vertical wall, and a square shaped barge is located close to it. Another end of the tank consists of a beach to dissipate the wave energy passively. As the aspect ratio between the length and the width of the narrow gap is often very large in practical applications, focusing on the transversal mode of the resonant flow, the problem is modelled as a two-dimensional one in the present work. The sketch presented in Figure 4.1 depicts how the three-dimensional problem of the narrow gap between two floating structures

during a side-by-side offloading operation could be simplified into a two-dimensional case. Although our study is focused, in fact, on the width of the narrow gap of the three-dimensional case, the distance between the body and the symmetry plane, or the tank wall as it will be modeled herein, will be referred as the “length of the gap” from now on, as it is in the longitudinal direction of the two-dimensional model. Only the radiation problem is analyzed as the flow is generated by imposing sway motion to the barge.

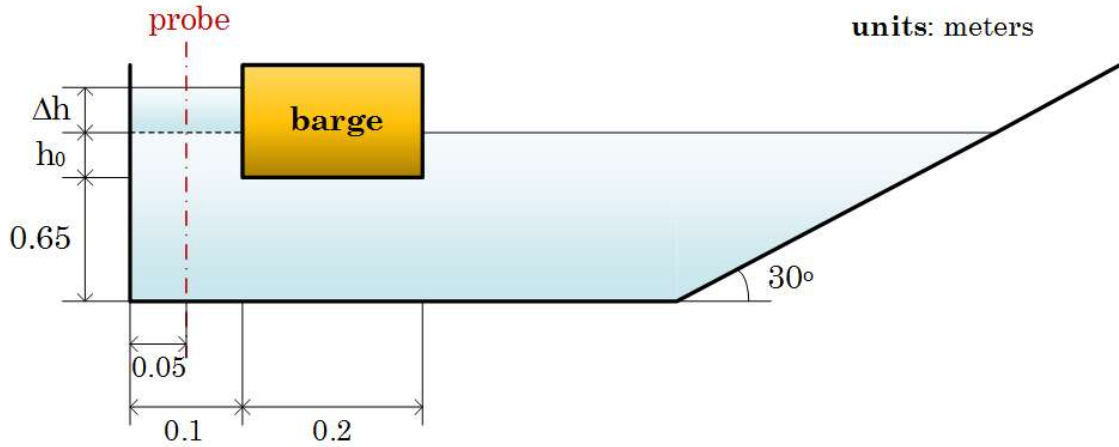
The analysis of the results is divided into three sections. The first section presents the general behavior of the flow in the gap and its relation to three parameters: length of the gap, period and amplitude of the sway motion. In the second section, the piston-like resonance is investigated in detail. Finally, in the third section of the results, the analysis is carried out considering the sloshing-type resonant modes.

4.5 VALIDATION

The first analysis carried out in the present work is the validation of the particle-based numerical method for the flow inside a narrow gap. The simulation system based on MPS method was previously validated for hydrodynamic phenomena such as sloshing (Tsukamoto, Cheng, & Nishimoto, 2011), green water (Bellezi, Cheng, & Nishimoto, 2013) and dam break (Bellezi, Cheng, & Nishimoto, 2013). Both sloshing and the flow inside the gap show similarities and could be defined as flows inside “trapping structures”. However, sloshing is a flow entirely confined inside a tank whilst the flow inside the gap communicates with external flow. This difference is particularly significant in the case of the piston-like vertical resonant motion of the fluid inside the gap. Hence, the validation analysis carried out in this work is focused on the piston-type vertical resonant flow. Besides, numerical results from simulations adopting the 0-th order gradient model (Koshizuka & Oka, 1996) and the 1-st order gradient model (Iribe & Nakaza, 2011) to calculate the pressure gradient are provided and the effect of the gradient model are discussed.

The configuration and main dimensions of the numerical towing tank are presented by Figure 4.2. The two-dimensional setup adopted herein is based on the experimental setting used by Maisondieu et al. (2001). The validation is carried out by a free oscillation test. The free surface level inside the gap between a square-shaped barge and the tank left wall is displaced a height Δh from the still water level by placing a rigid lid over the gap and decompressing the compartment. Then, the rigid lid is removed and the system is allowed to oscillate freely. The experimental basin is 13 meters long and it is equipped with a beach at its end in order to avoid the reflection of the waves. The data of the free surface elevation is acquired by a wave probe located at the center of the gap.

Figure 4.2 – Dimensions of the validation model

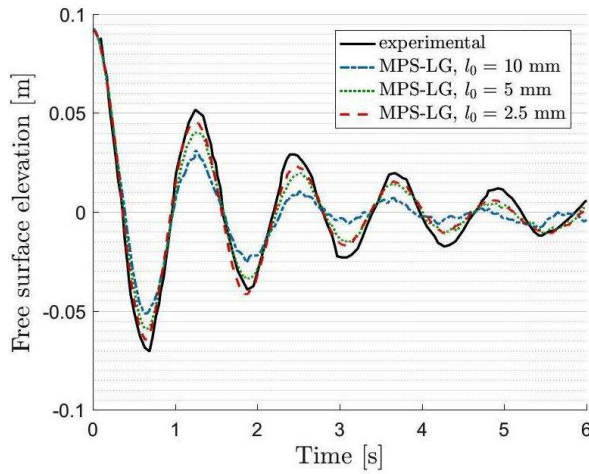


Source: figure from the author, adapted from Maisondieu et al. (2001).

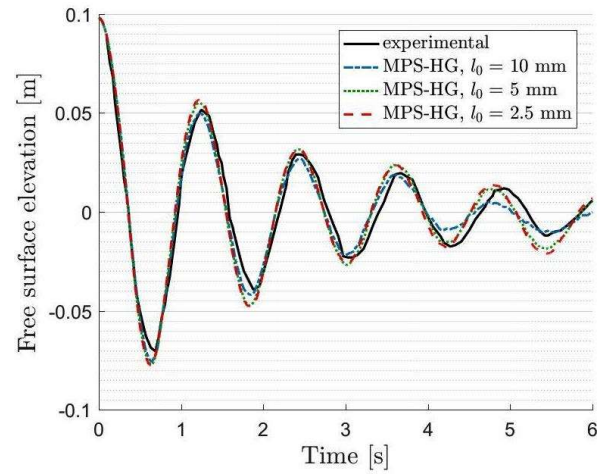
Maisondieu et al. (2001) performed tests for two different values of free surface initial displacement (Δh): 5 cm and 10 cm, combined with three different values of the barge draft (h_0): 10 cm, 15 cm and 20 cm, resulting in six test cases. Besides the validation of the numerical method, a convergence analysis is carried out as well. Particle models with resolutions of 10 mm ($L_{gap}/l_0 = 10$), 5 mm ($L_{gap}/l_0 = 20$) and 2.5 mm ($L_{gap}/l_0 = 40$) were considered.

Figure 4.3 compares the experimental data extracted from Maisondieu et al. (2001) to the time series obtained from the particle simulations for the case with draft of 20 cm. Figure 4.4 shows the time series of the free surface elevation and the FFT of the signal for the case with draft of 15 cm and free surface initial displacement of 10 cm. In both cases, the results in the left-hand side were obtained using the 0-th order gradient model (MPS-LG, **L**ow-order **G**radient) while the results in the right-hand side were obtained using the 1-st order gradient model (MPS-HG, **H**igh-order **G**radient).

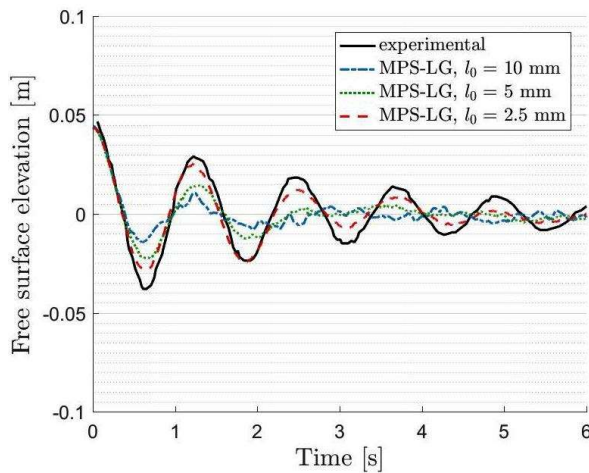
Figure 4.3 – Time series of free surface elevation at wave probe: $h_0 = 20\text{cm}$
(experimental data from Maisondieu et al. (2001))



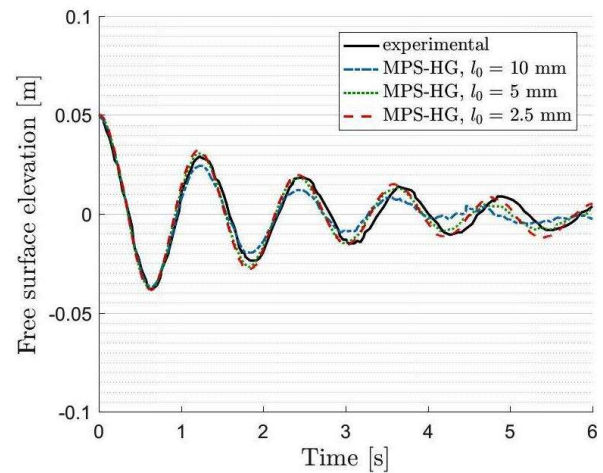
(a) $\Delta h = 10\text{cm}$, 0-th order gradient model



(c) $\Delta h = 10\text{cm}$, 1-st order gradient model



(b) $\Delta h = 5\text{cm}$, 0-th order gradient model



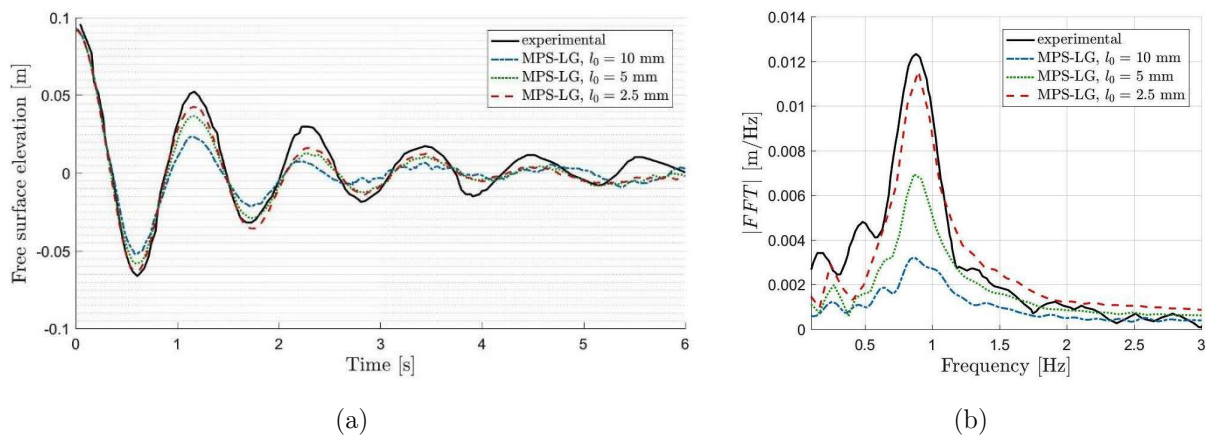
(d) $\Delta h = 5\text{cm}$, 1-st order gradient model

Source: figure from the author.

In the case of Figure 4.3-a and Figure 4.3-c, obtained with the 0-th order gradient model, the computed results oscillate at a frequency very close to the experimental time series, even for the coarser resolution evaluated herein. Nevertheless, only the model with resolution of $l_0 = 2.5\text{ mm}$ shows a decay in the amplitude of the oscillation with similar magnitude of that from the experiment. The two other coarser resolutions show a larger decay than the experiment. Hence, as the resolution increases, the amplitude of the computed time series tends to fit better with the experimental

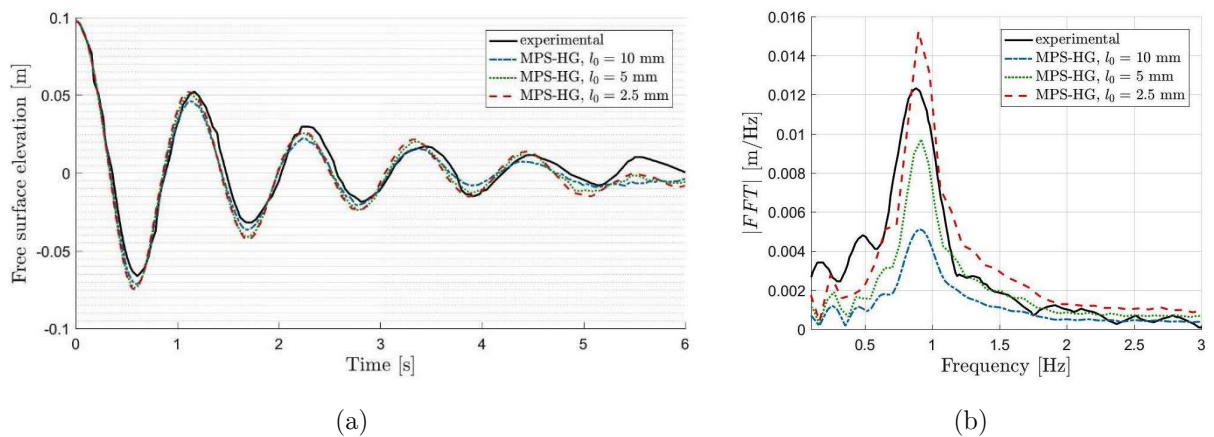
results. For the simulations with the 0-th order gradient model, a suitable convergence was achieved only for the resolution of 2.5 mm, which is equivalent to a resolution ratio of $L_{gap}/l_0 = 40$.

Figure 4.4 – (a) Time series of the free surface elevation at probe and (b) FFT of the free surface elevation: $h_0 = 15\text{cm}$, $\Delta h = 10\text{cm}$ (experimental data from Maisondieu et al. (2001)), 0-th order gradient model



Source: figure from the author.

Figure 4.5 – (a) Time series of the free surface elevation at probe and (b) FFT of the free surface elevation: $h_0 = 15\text{cm}$, $\Delta h = 10\text{cm}$ (experimental data from Maisondieu et al. (2001)), 1-st order gradient model



Source: figure from the author.

Meanwhile, the computed results presented by Figure 4.3-b and Figure 4.3-d, obtained with the 1-st order gradient model, indicate that the convergence was achieved even for the coarsest resolution evaluated herein ($L_{gap}/l_0 = 10$), as both the oscillation frequency and the decay rate of the numerical results show good agreement to the experimental data for the three resolutions.

For the case with $h_0 = 15 \text{ cm}$ and $\Delta h = 10 \text{ cm}$, Figure 4.4 and Figure 4.5 show the time series of the free surface oscillation at the right-hand side and the FFT of the signal at the right-hand side as computed by using the 0-th order gradient model and the 1-st order gradient model, respectively. In general, the same behavior previously shown by Figure 4.3 is obtained. The FFTs show good agreement between the numerical and the experimental results for the frequency of the oscillation, regardless the resolution. On the other hand, the time series show that the numerical convergence is achieved for coarser resolutions in the case of 1-st order gradient simulations.

Such difference is explained by the fact that the 1-st order gradient model provides a more accurate calculation of the pressure gradient for irregular and non-isotropic particle distributions and for fluid particles close to the solid boundaries. The error of the calculation of such situations by using the 0-th order gradient model introduce additional numerical damping in the simulation. So, for phenomena like flow separation and formation of vortices, which are expected in the lower edges of the barge, this numerical damping becomes non-negligible and a much higher resolution should be adopted in order to reduce its magnitude.

In general, one of the key advantages of the particle method is to easily deal with large free surface displacements. However, for the cases involving small free surface displacements, numerical damping becomes non-negligible in comparison to the overall energy of the flow. This is the reason behind the numerical results fitting very well in the initial cycles with large amplitude, almost overlapping the experimental

curves, and becoming gradually more different for the last cycles, when the computed free surface elevations vanish slightly faster. Notwithstanding, since the upcoming analysis are based on the flow generated by a barge with relatively large imposed motion, the small numerical damping observed will not be an issue for the main study of this work.

Table 4.1 – Oscillation frequency of the free oscillation test – numerical, analytical and experimental data – (MPS, 0-th order gradient model).

| Model draught (h_0) [cm] | Initial height (Δh) [cm] | Experimental [Hz] | Analytical [Hz] | MPS Simulation | | |
|---------------------------------|---------------------------------------|----------------------|--------------------|-----------------|----------------|------------------|
| | | | | l_0 = 10mm | l_0 = 5mm | l_0 = 2.5mm |
| 20 | 5 | 0.808 | 0.8461 | 0.7227 | 0.8473 | 0.8397 |
| 15 | 5 | 0.8749 | 0.9145 | 0.8164 | 0.8779 | 0.8905 |
| 10 | 5 | 0.9675 | 1.0028 | 1.1289 | 0.9695 | 0.9927 |
| 20 | 10 | 0.808 | 0.8461 | 0.8477 | 0.8244 | 0.8321 |
| 15 | 10 | 0.8749 | 0.9145 | 0.8594 | 0.8779 | 0.8905 |
| 10 | 10 | 0.9675 | 1.0028 | 0.9961 | 0.9924 | 0.9927 |

Table 4.2 – Oscillation frequency of the free oscillation test – numerical, analytical and experimental data – (MPS, 1-st order gradient model).

| Model draught (h_0) [cm] | Initial height (Δh) [cm] | Experimental [Hz] | Analytical [Hz] | MPS Simulation | | |
|---------------------------------|---------------------------------------|----------------------|--------------------|-----------------|----------------|------------------|
| | | | | l_0 = 10mm | l_0 = 5mm | l_0 = 2.5mm |
| 20 | 5 | 0.808 | 0.8461 | 0.8594 | 0.8397 | 0.8467 |
| 15 | 5 | 0.8749 | 0.9145 | 0.9180 | 0.9160 | 0.9197 |
| 10 | 5 | 0.9675 | 1.0028 | 0.9766 | 1.0000 | 1.0073 |
| 20 | 10 | 0.808 | 0.8461 | 0.8360 | 0.8397 | 0.8467 |
| 15 | 10 | 0.8749 | 0.9145 | 0.9102 | 0.9160 | 0.9197 |
| 10 | 10 | 0.9675 | 1.0028 | 0.9961 | 1.0000 | 0.9908 |

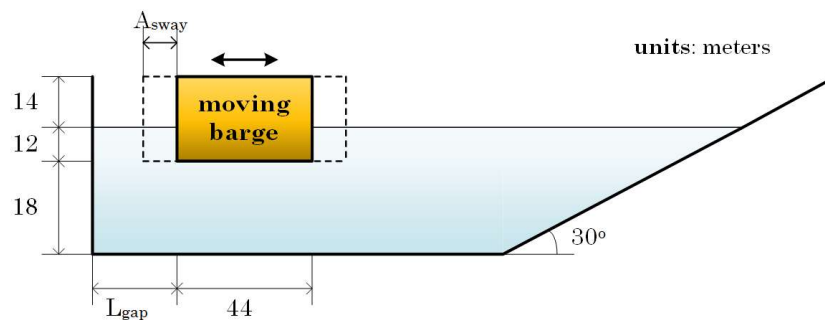
Finally, the oscillation frequencies obtained by the FFT of the MPS-based numerical simulations are compared to the frequencies obtained from the FFT of the experimental data and the analytical estimation of Molin (2001) in Table 4.1, for the numerical results obtained with the 0-th order gradient model, and in Table 4.2, for the numerical results obtained with the 1-st order gradient model. Both the experimental data and the analytical estimation were extracted from Maisondieu et al. (2001).

In general, the analytical estimation is in good agreement with the experimental result, although slightly overestimating the resonant frequency as consequence of the linear assumption and by disregarding important sources of damping. The numerical results obtained by the particle simulations presented good agreement to the experimental measurements as well. Besides, the 1-st order model provides numerical convergence for coarser resolutions than the 0-th order gradient model.

4.6 CASE OF STUDY

The second part of the investigation consists in a parametric analysis of the flow in the gap related to the length of the gap and the frequency. Focusing only on transversal resonance modes, the two-dimensional approach is suitable for the analysis proposed in the present work. Figure 4.6 shows the configuration of the cases and the main parameters used in the analysis.

Figure 4.6 – Dimensions of the numerical model of the parameter analysis



Source: figure from the author.

The numerical model adopted herein is adapted from the two-dimensional setup of Maisondieu et al. (2001) for the free oscillation tests and first proposed by Molin (2001). The tank is composed by a vertical fixed wall in the left and a slope beach in the right. A square shaped barge is positioned close to the left wall. An oscillating sway motion is imposed to the barge. The sway motion was adopted instead of the heave or roll motions because the former is capable to generate larger waves from smaller barge motions than the two latter, as pointed out by the linear wavemaker theory (Dean & Dalrymple, 1991). The physical slope beach is adopted in order to absorb the waves radiated by the right side of the barge. The damping by the slope beach is almost entirely obtained by wave breaking, which occurs as the wave travels through the beach and its depth decreases and it is very effective to absorb long waves.

The analysis is carried out considering three parameters. The length of the gap ranges from 10 meters to 60 meters, with interval of 2 meters. The sinusoidal oscillating sway motion is performed for periods from 5 seconds to 20 seconds, with interval of 0.25 seconds between consecutive periods. Three different amplitudes of the sway motion were taken into account: 0.55 m ($A_{sway} = 0.025 \times B$), 0.875 m ($A_{sway} = 0.0375 \times B$) and 1.1 m ($A_{sway} = 0.05 \times B$); where B is the barge breadth. The main dimensions of the square shaped barge are defined considering typical dimensions of shuttle vessels such as LNG carriers and oil tankers. The periods of the sway motions from 5 to 20 seconds were chosen in order to cover typical wave periods of Basins where oil and gas operations are performed. Long simulations of 35 cycles of sway harmonic motion were carried out in order to extract the significant parameters of the steady state. From the results obtained in the previous section, only simulations with the 1-st order gradient model were performed.

4.7 RESULTS

4.7.1 Numerical convergence

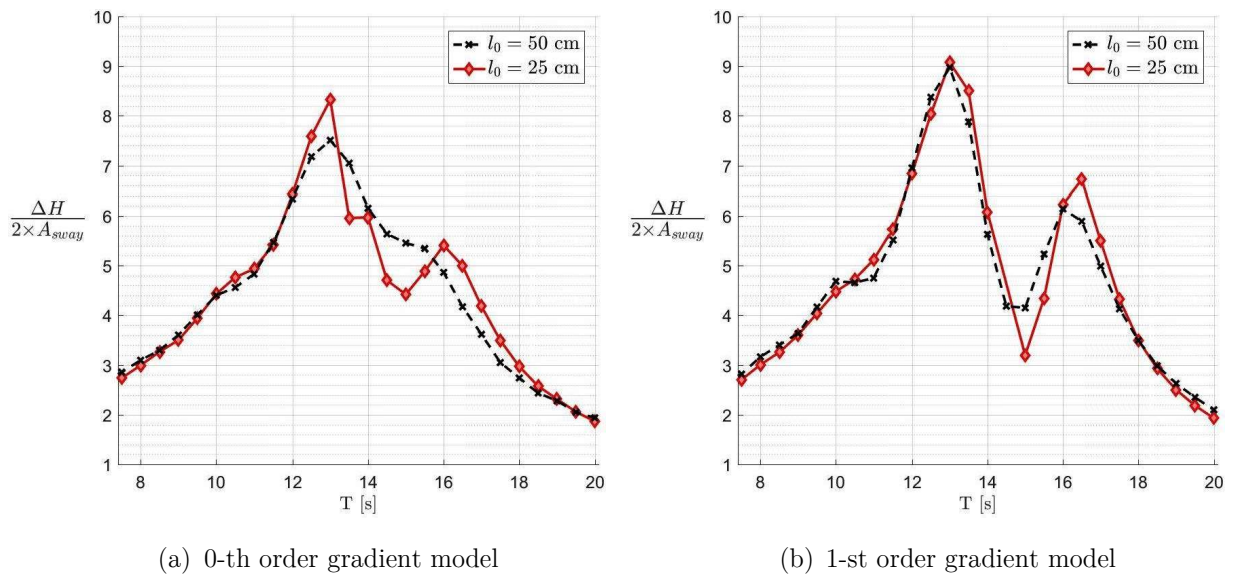
Although a convergence analysis was carried out previously during the validation of the numerical method, the case with the harmonic sway motion might introduce substantially larger fluid motions than those from the initial disturbances of the free oscillation tests. Thus, an additional convergence analysis should be performed for the parameter study. Hence, it is carried out by considering the case with the narrowest gap and the largest sway motion amplitude, i. e., $L_{gap} = 10$ m and $A_{sway} = 0.05 \times B$.

Figure 4.7-a shows the dimensionless amplitude of the free surface elevation in the barge left wall as function of the sway motion period for the resolutions of 50 cm and 25 cm for the 0-th order gradient model simulations. Figure 4.7-b shows the dimensionless amplitude of the free surface elevation in the barge left wall as function of the sway motion period for the resolutions of 50 cm and 25 cm for 1-st order gradient model simulations. The dimensionless amplitude of the free surface elevation is the ratio between the average free surface elevation height and double the amplitude of the sway motion. The average free surface elevation height is the average value of the difference between the free surface elevation at its maximum and at its minimum during one cycle of harmonic sway motion. Only the last 10 cycles of motion were considered for the calculation of the average free surface height.

The results from Figure 4.7 show agreement with those obtained on the validation section as the simulation with the 1-st order gradient model seems to be closer to reach the numerical convergence than the simulations with the 0-th order gradient model. The curve of the dimensionless amplitude of the free surface elevation has two local maximum values in the period range between 8 and 20 seconds. In the case of Figure 4.7-a, the two peaks are clear only for the finer resolution of 25 cm. In the case of Figure 4.7-b, the two peaks appear for both resolutions and the convergence

was achieved for the peak at 13 seconds but not yet for the peak at 16.5 seconds. Therefore, from now on, only simulations adopting the 1-st order gradient model are performed.

Figure 4.7 – Dimensionless free surface elevation height in relation to sway period: convergence analysis – $L_{gap} = 10m$, $A_{sway} = 0.05 \times B$.

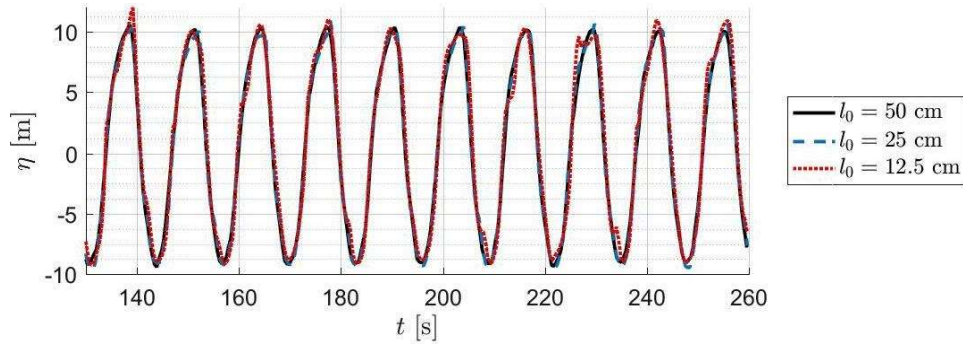


Source: figure from the author.

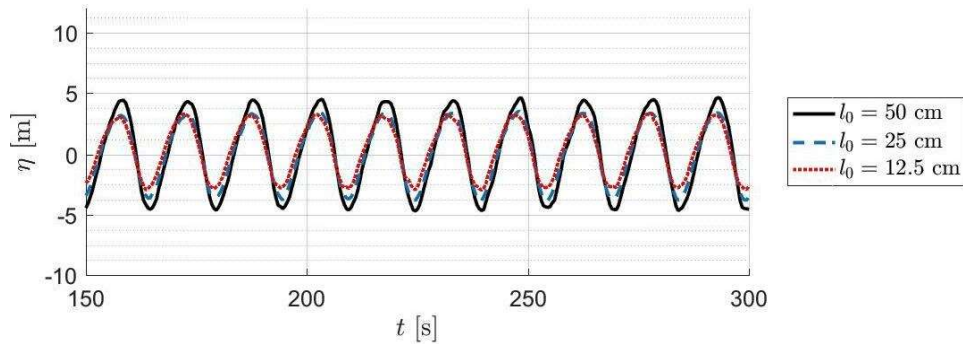
The most critical conditions to the convergence of the numerical model might be the two local maximum values and the local minimum between them for the amplitude of the free surface elevation. Then, for this three sway motion conditions (periods of 13.0, 15.0 and 16.5 seconds) additional simulations with the resolution of 12.5 cm were made to ensure the numerical convergence was reached. Figure 4.8 shows the timeseries of the free surface elevation at the barge left wall for the three different resolutions.

Figure 4.8 – Time series of the free surface elevation: convergence analysis -

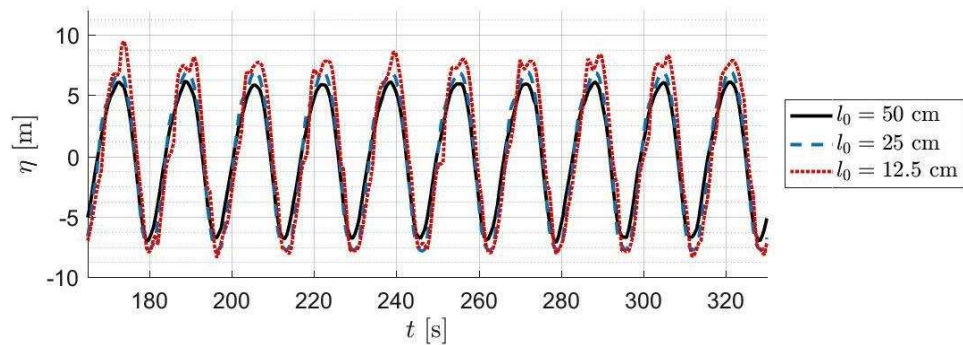
$L_{gap} = 10m$, $A_{sway} = 0.05 \times B$, 1-st order gradient model.



(a) $T = 13.0s$



(b) $T = 15.0s$



(c) $T = 16.5s$

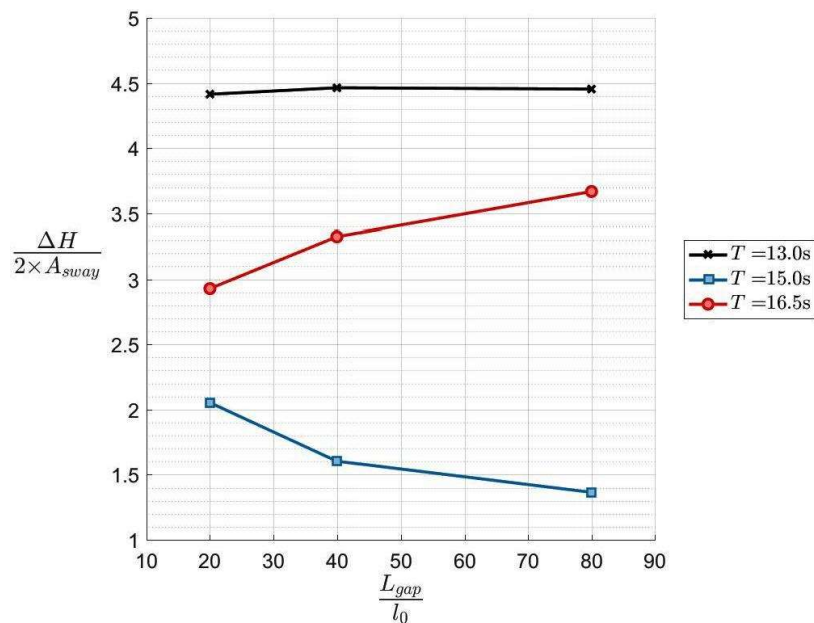
Source: figure from the author.

For Figure 4.8-a, the numerical convergence was achieved for the resolution of 50 cm as the three curves almost overlap each other. For Figure 4.8-b, the convergence was achieved at the resolution of 25 cm because only the result for the resolution of 50 cm is slightly different. Finally, the convergence was obtained for the resolution of 25 cm in Figure 4.8-c. The small difference between the curves from the resolutions of 25 cm and 12.5 cm for the period of 16.5 seconds does not lie in the main harmonic of the

oscillation but in very small nonlinear contributions related to fluid fragmentation and runup in the side of barge.

In order to make clear that the numerical results are converging, Figure 4.13 shows the dimensionless amplitude of the free surface elevation as function of the resolution ratio for the three afore-mentioned conditions. For the first maximum in the period domain, the curve remains flat as the converge was already achieved. For the local minimum in the period domain, the amplitude decreases as the resolution ratio increase. Notwithstanding, the dimensionless amplitude decreases only from 1.6 to 1.4 by doubling the resolution. For the second local maximum in the frequency domain, the magnitude of the peak increases as the resolution ratio increase. By doubling the resolution ratio from 40 to 80, the dimensionless amplitude increases only from 3.3 to 3.6. Summarizing, a suitable numerical convergence was achieved as by doubling the resolution, the change in the results are in the order of only 10%.

Figure 4.9 – Dimensionless free surface height as function of the particle resolution - $L_{gap} = 10m$, $A_{sway} = 0.05 \times B$, 1-st order gradient model.



Source: figure from the author.

Hence, the numerical towing tank of the ensuing parameter analysis is modeled by using a distance between particles of 0.25 meters, i. e., a resolution ratio of $L_{gap}/l_0 = 40$ for the case with the narrowest gap. This resolution results in models with approximately 1×10^5 particles overall. A time step of 2.5 milliseconds is adopted to achieve numerical stability of simulations and satisfy the Courant-Friedrichs-Lewy condition. For the simulation of 35 cycles of harmonic motion, it is usually required between 20 minutes and 1 hour of processing time. The hardware consists in the computational Cluster of the Numerical Offshore Tank laboratory (TPN) of the University of São Paulo (USP). This Cluster comprises 48 nodes; each one contains 20 cores of Shanghai 2.66Ghz AMD processors with 128GB of RAM shared memory. The MPS based numerical simulation system uses OpenMP library in order to use shared memory and being capable of taking advantage of the 20 cores of each node.

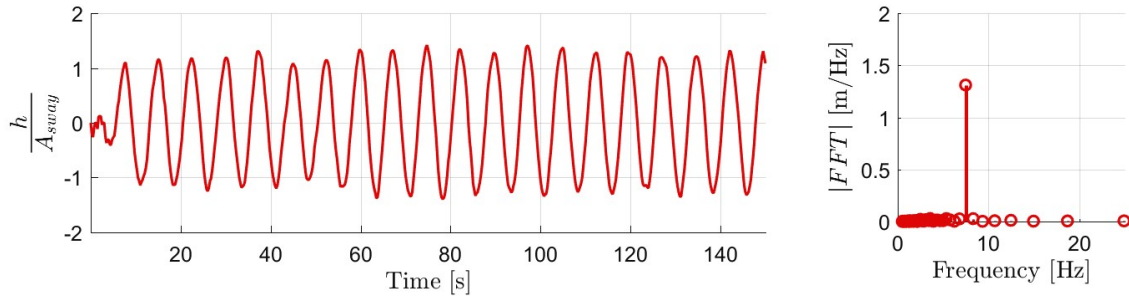
4.7.2 Wave reflection

Both sides of the moving barge act as a piston-type wavemaker due its sway motion. While the wave reflection on the left wall of the numerical tank is required in order to assess the resonant flow inside the gap, the wave reflection on the opposite side of the tank must be avoided to not affect the flow inside the gap. In this way, a 30° slope-shaped beach is placed in the right side of the tank to physically suppress the long waves (Figure 4.6).

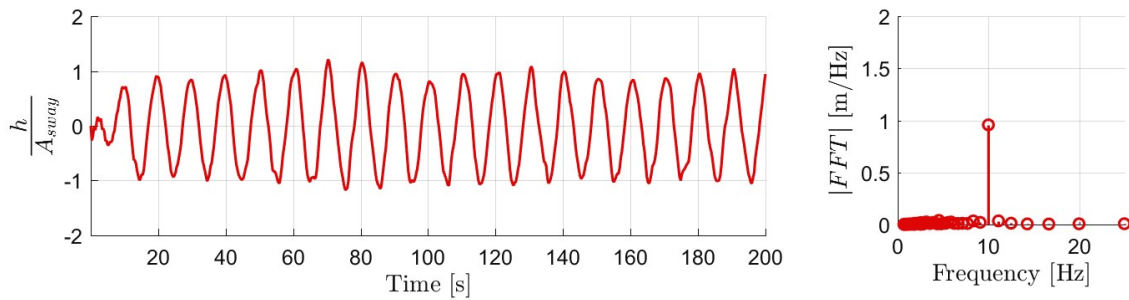
The Figure 4.10 shows the time series of the free surface elevation in the right side of the barge for three wave periods ($T = \{7.5 \text{ s}; 10.0 \text{ s}; 15.0 \text{ s}\}$) and for a large number of cycles of the motion. These results provide strong evidence that the wave reflection on the right side of the tank was avoided because typical signals of wave reflection were not observed, such as changes in the amplitude of the wave or “wave beating”.

Figure 4.10 – Time series of free surface elevation in the barge right wall (left) and its FFT (right) for 32 cycles of sway motion – $L_{gap} = 50m$,

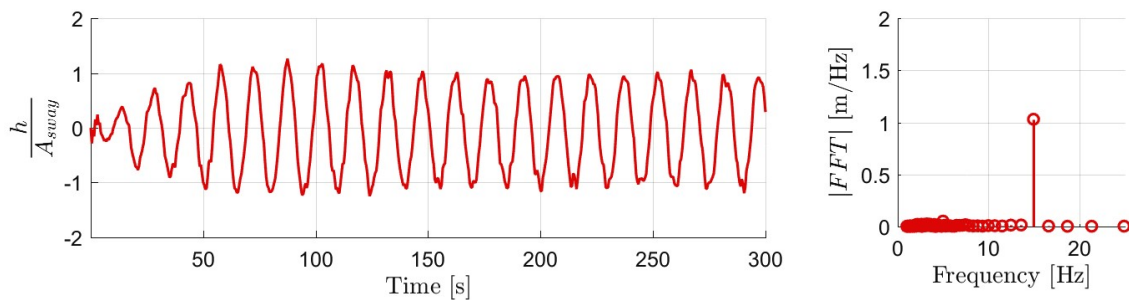
$$A_{sway} = 0.05 \times B$$



(a) $T = 7.5s$



(d) $T = 10.0s$



(e) $T = 15.0s$

Source: figure from the author.

4.7.3 Flow in the gap: general behavior

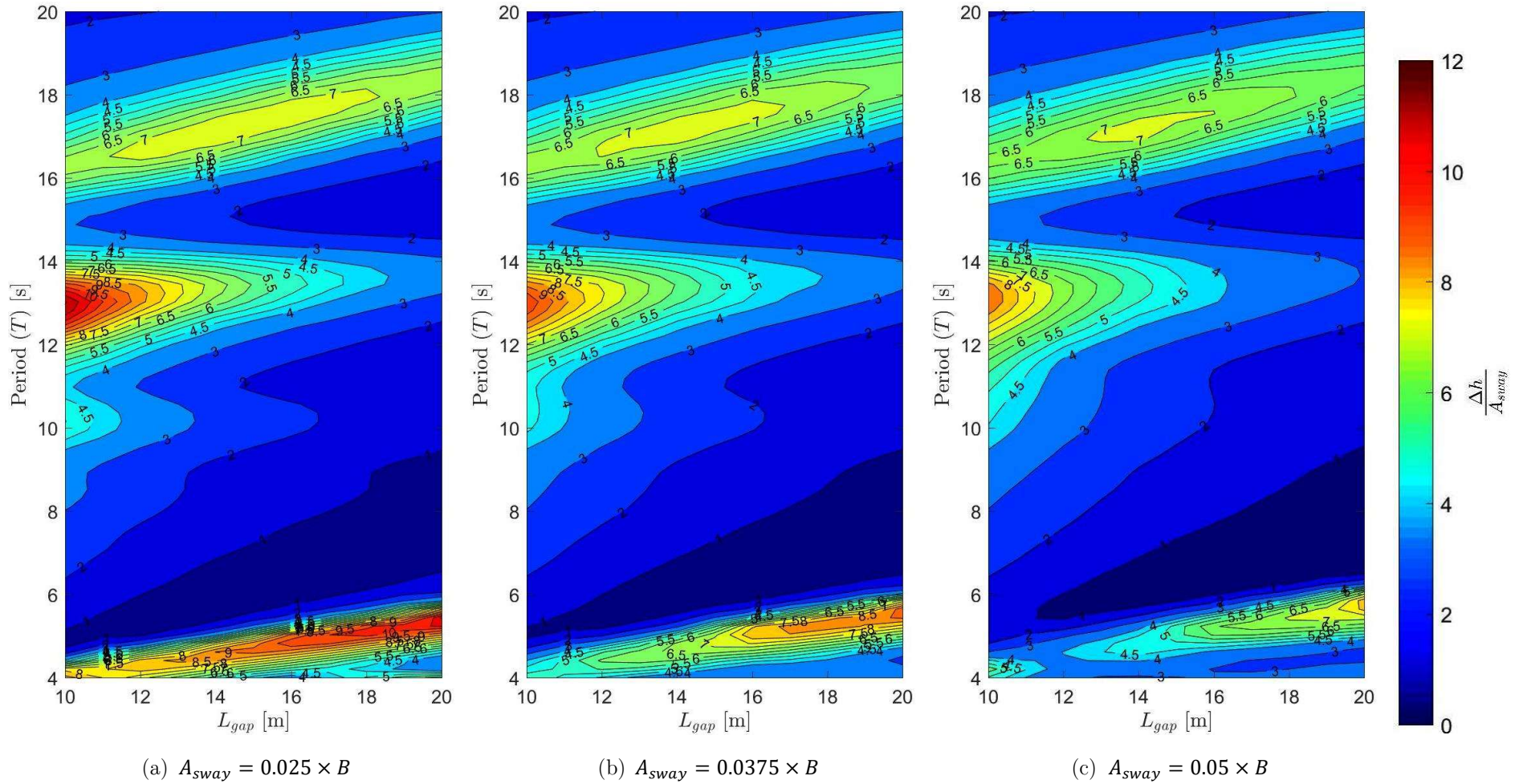
The computed flow in the gap is analyzed based on the free surface elevation registered by several wave probes located along the entire extension of the gap, placed 1 meter from each other. Another wave probe is placed on the barge left wall and

follows its motion. The double amplitude of the free surface elevation signal, which will be further referred as “wave height” in this work, is calculated by the difference between the maximum and minimum value of each cycle of the barge harmonic motion. Then, the average wave height is calculated for each simulation. The first seven cycles of sway motion were disregarded because they are considered as the transient part of the simulation. The seven-cycle threshold adopted herein was defined based on the general behavior of the numerical results since they reached the steady-state response after 6 or 7 cycles.

Figure 4.11 shows the wave height in relation to the length of the gap and the period of the sway motion by contour maps in which the color scale indicates the average double amplitude of the free surface elevation, henceforth also referred as free surface height. Three contour maps are presented, each one is related to one of the sway motion amplitudes. These diagrams allow to understand the behavior of gap flow for a wide range of sway motion periods and length of the gap combinations. Although simulation for cases with the length of the gap up to 60 meter were performed, the Figure 4.11 shows only the results for gaps below 20 meters, which present a ore interesting behavior.

From the contour diagrams three resonance situations could be observed, each related to one of the three local maximum values of average wave height. The first resonant condition occurs for gap widths smaller than 15 meters under motion between 10 and 15 seconds. This resonant condition of the partially entrapped flow inside the gap is known as piston-type resonant flow, also called pumping mode or Helmholtz mode.

Figure 4.11 – Contour map of the dimensionless wave height as function of the length of the gap and the sway period



Source: figure from the author.

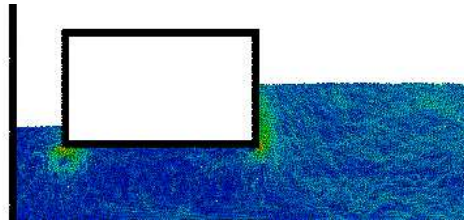
Figure 4.12 presents snapshots for the case with the largest sway motion, gap width of 10 meters and motion period of 13 seconds, exactly within the range of the piston mode resonance. Five instants that comprise half period of the barge motion, from the minimum free surface elevation to its maximum, are presented. In Figure 4.13 the envelope of the free surface is shown as shaded area in the back of the curves representing the instantaneous free surface profile of the five instants presented in Figure 4.12. Both figures show that, in the piston-like resonant flow, the free surface within the gap assumes a horizontal profile that moves up and down during the motion cycle. The snapshots show regions of high velocity in the flow around lower edges of the barge hull for the instants between the maximum and minimum free surface elevations inside the gap.

In the contour diagrams, for the region related to the piston-type resonance, significant differences could be observed between the diagram of the smallest sway motion amplitude (Figure 4.11-a) and the diagram of the largest sway motion amplitude (Figure 4.11-c), which suggest the non-linearity of the problem.

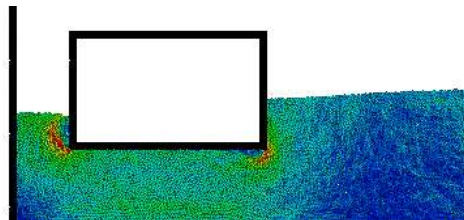
Besides, a second resonance condition is shown by the contour plot for periods between 15.5 seconds and 18.5 seconds. The behavior of the flow in this region is very similar to the region previously presented. The profile of the free surface is flat and it moves upwards and downwards. As the period of the sway motion increases, the natural period associated to this resonance mode increases almost linearly.

Figure 4.12 – Snapshots of the particle simulation – $L_{gap} = 10m$, $T = 13.0s$,

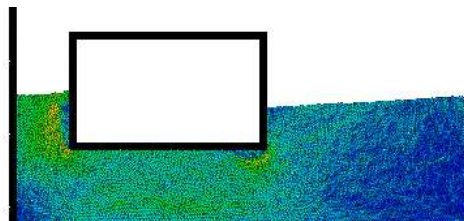
$$A_{sway} = 0.05 \times B$$



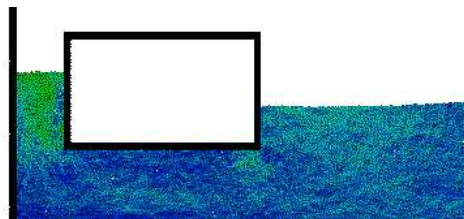
(a) $t = 104.3s$



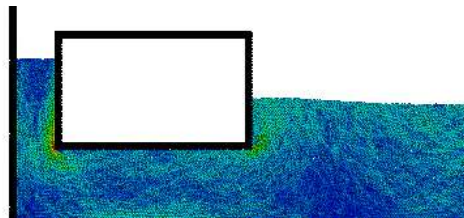
(b) $t = 106.5s$



(c) $t = 108.1s$



(d) $t = 109.8s$

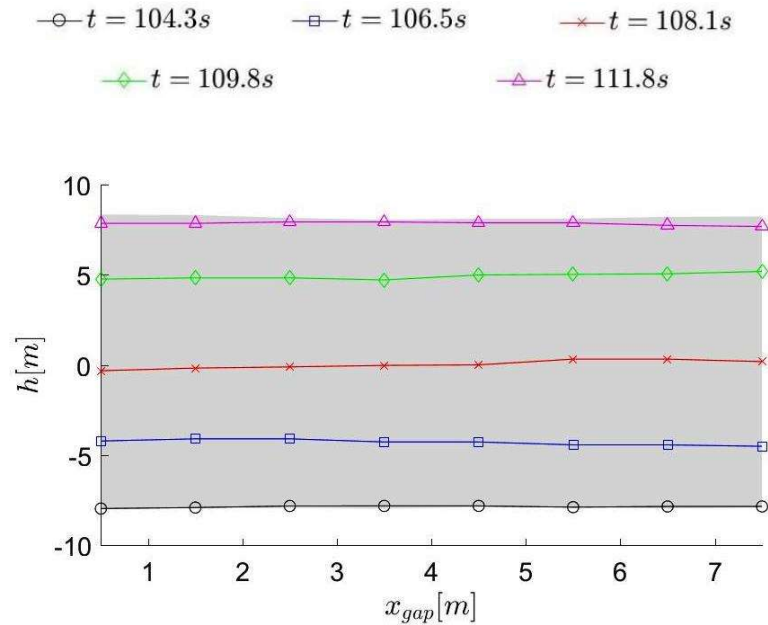


(e) $t = 111.8s$

Source: figure from the author.

Figure 4.13 – Free surface profile and envelope – $L_{gap} = 10m$, $T = 13.0s$,

$$A_{sway} = 0.05 \times B$$



Source: figure from the author.

Considering the range of motion periods evaluated in the present work, the third resonant condition is observed in a wider range of lengths of the gap, from 15 meters to 60 meters, but for lower motion periods, below 10 seconds. Figure 4.14 present snapshots for the case with the largest sway motion, length of the gap of 60 meters and motion period of 9 seconds, which is within the range of parameters of the second resonant motion. Figure 4.14 shows five instants of half period of the barge motion, from the minimum free surface elevation in the barge left wall to its maximum.

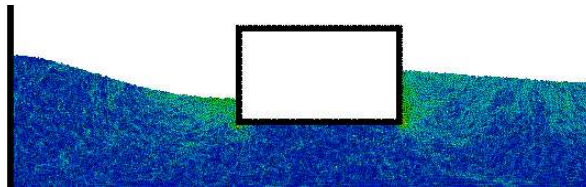
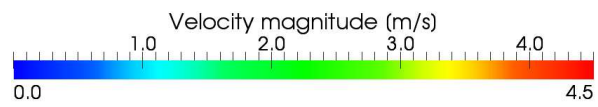
Figure 4.16 provides the envelope of the flow as shaded area in the back of the curves representing the instantaneous free surface profile of the five instants presented by Figure 4.14. This condition is related to the first anti-symmetric sloshing-type resonant flow in the gap. In this condition, a stationary wave is created inside the gap and the free surface assumes a quasi-sinusoidal profile of a half wavelength. When the free surface reaches its maximum elevation in the tank left wall, it is in its minimum in the barge left wall at the same time, and vice-versa.

Finally, there is other resonant situation, which is not shown in the range of sway period and length of the gap of Figure 4.11, that occurs for lengths of the gap larger than 35 meters and for shots motion periods below 7 seconds. Figure 4.16 present snapshots for the case with the largest sway motion, length of the gap of 60 meters and motion period of 6.25 seconds. As shown in Figure 4.14, five instants within half period of the barge motion are provided in Figure 4.16, from the minimum free surface elevation in the barge left wall to its maximum. The Figure 4.17 presents the envelope of the flow by a shaded area in the background of the curves representing the instantaneous free surface profile of the five instants presented in Figure 4.15. This condition is related to the first symmetric sloshing-type resonant condition. A stationary wave is created within the gap as well, but with a quasi-sinusoidal profile of one wavelength instead. When the free surface elevation is at its maximum in the tank left wall, its maximum value is also observed in the barge left wall. The minimum value of free surface elevation is also observed simultaneously in the barge and the tank left walls.

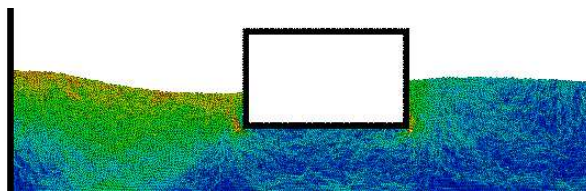
For the two sloshing-type resonant modes, the snapshots show higher velocity magnitudes in the free surface. However, high velocities were not computed in the vicinity of the lower corners of the hull. In the contour plots of Figure 4.11, the responses in the regions of both sloshing-type resonances are similar independently of the amplitude of the sway motion. This behavior suggests a small influence of nonlinear phenomena on the sloshing-type resonant flows. For the piston-type mode, the maximum free surface height decreases steeply as the length of the gap increases.

Figure 4.14 – Snapshots of the particle simulation – $L_{gap} = 60m$, $T = 9.0s$,

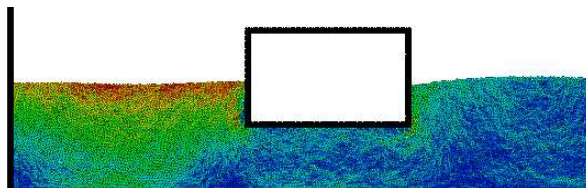
$$A_{sway} = 0.05 \times B$$



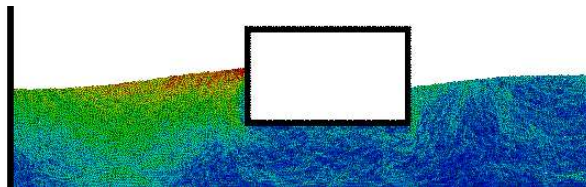
(a) $t = 62.8s$



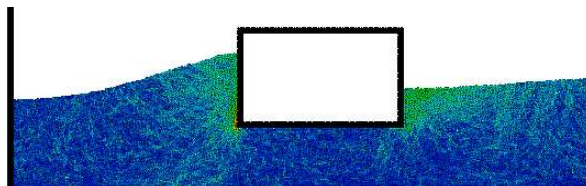
(b) $t = 64.2s$



(c) $t = 65.1s$



(d) $t = 65.8s$

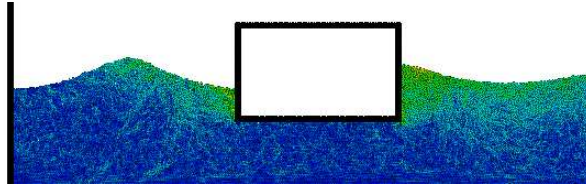


(e) $t = 67.4s$

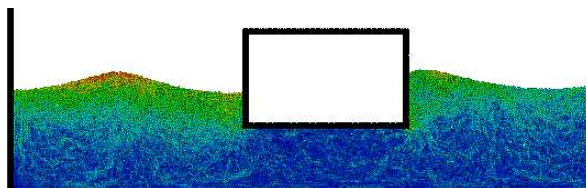
Source: figure from the author.

Figure 4.15 – Snapshots of the particle simulation – $L_{gap} = 60m$, $T = 6.25s$,

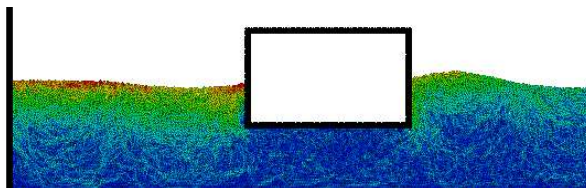
$$A_{sway} = 0.05 \times B$$



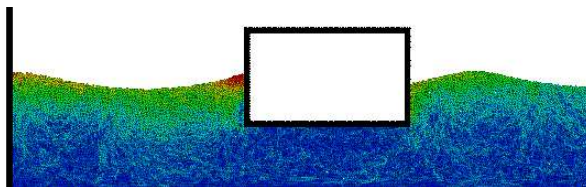
(a) $t = 43.5s$



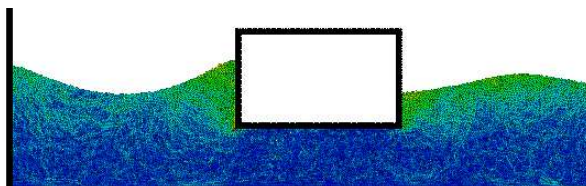
(b) $t = 44.5s$



(c) $t = 45.2s$



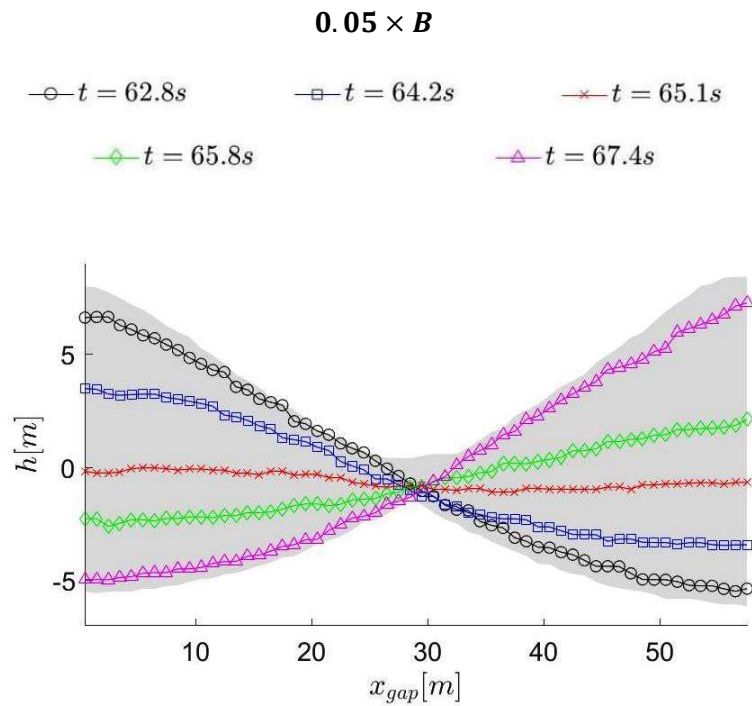
(d) $t = 45.7s$



(e) $t = 47.0s$

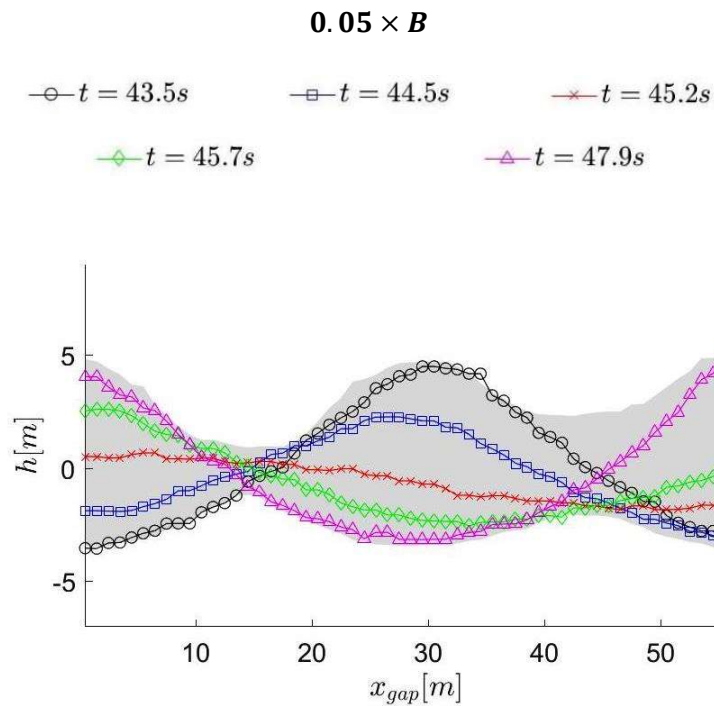
Source: figure from the author.

Figure 4.16 – Free surface profile and envelope – $L_{gap} = 60m$, $T = 9.0s$, $A_{sway} =$



Source: figure from the author.

Figure 4.17 – Free surface profile and envelope – $L_{gap} = 60m$, $T = 6.25s$, $A_{sway} =$



Source: figure from the author.

1.1 PISTON-TYPE RESONANCE MODE

The following analysis of the piston-type resonant mode is focused only on the gaps with length below 20 meters. Figure 4.18 shows graphs of the dimensionless free surface height as function of the period of the sway motion. Such diagram consists on “slices” of constant gap width obtained from the contour maps. Each graph is related to a sway amplitude.

In the range of periods between 9 seconds and 12 seconds, three local maximum values were obtained, one close to 10.5 seconds, other to 13.0 seconds and the third one between 16 and 19 seconds. The flow in these three different regions shows a flat free surface profile that moves up and down between the barge and the left wall of the tank. So, these three resonant conditions might be called piston-mode resonance.

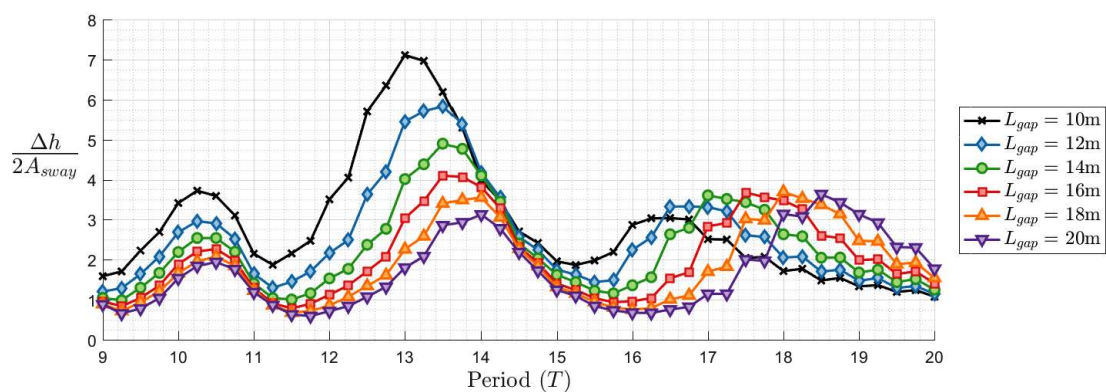
In the case of the first local maximum, which was computed between 9 seconds and 11 seconds, its magnitude decreases as the length of the gap increase and its period tends to slightly increase as the length of the gap increase, very slowly. For the gap with 10 meters, the first peak has magnitude of the dimensionless free surface height around 4.0 in Figure 4.18-a while it is around 3.0 in Figure 4.18-c. So, it seems to be related to non-linear phenomena as its amplitude decrease as the amplitude of the sway motion increase.

In general, the larger magnitudes of the free surface height were computed in the period range between 12 and 15 seconds. As previously observed in the contour maps of Figure 4.11, the decrease of the magnitude of free surface height is very steep as the length of the gap increases. Moreover, the resonant period increases as the length of the gap increase. Finally, it is also related to non-linear phenomena, as the magnitude of the peak decreases as the amplitude of the sway motion increase.

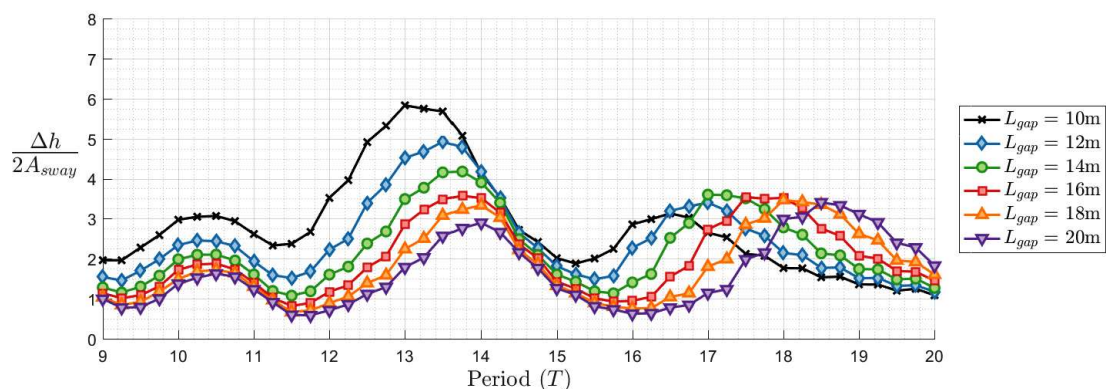
Finally, the third local maximum occurs for periods between 16 seconds and 19 seconds and it has a behavior different from the previous two local maxima. The peak period substantially increases as the length of the gap increase. From the contour plots

of Figure 4.11, this increase is almost linear. Despite presenting very close peak magnitude in gaps between 10 meters and 20 meters, the magnitude of the peak seems to achieve its maximum for gaps with length between 14 meters and 16 meters.

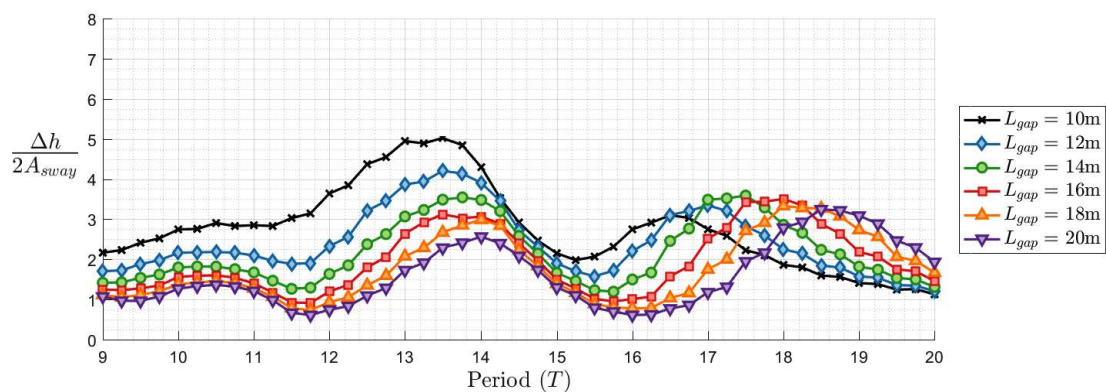
Figure 4.18 – Dimensionless free surface elevation height in relation to sway period: piston mode flow.



(a) $A_{sway} = 0.025 \times B$



(b) $A_{sway} = 0.0375 \times B$

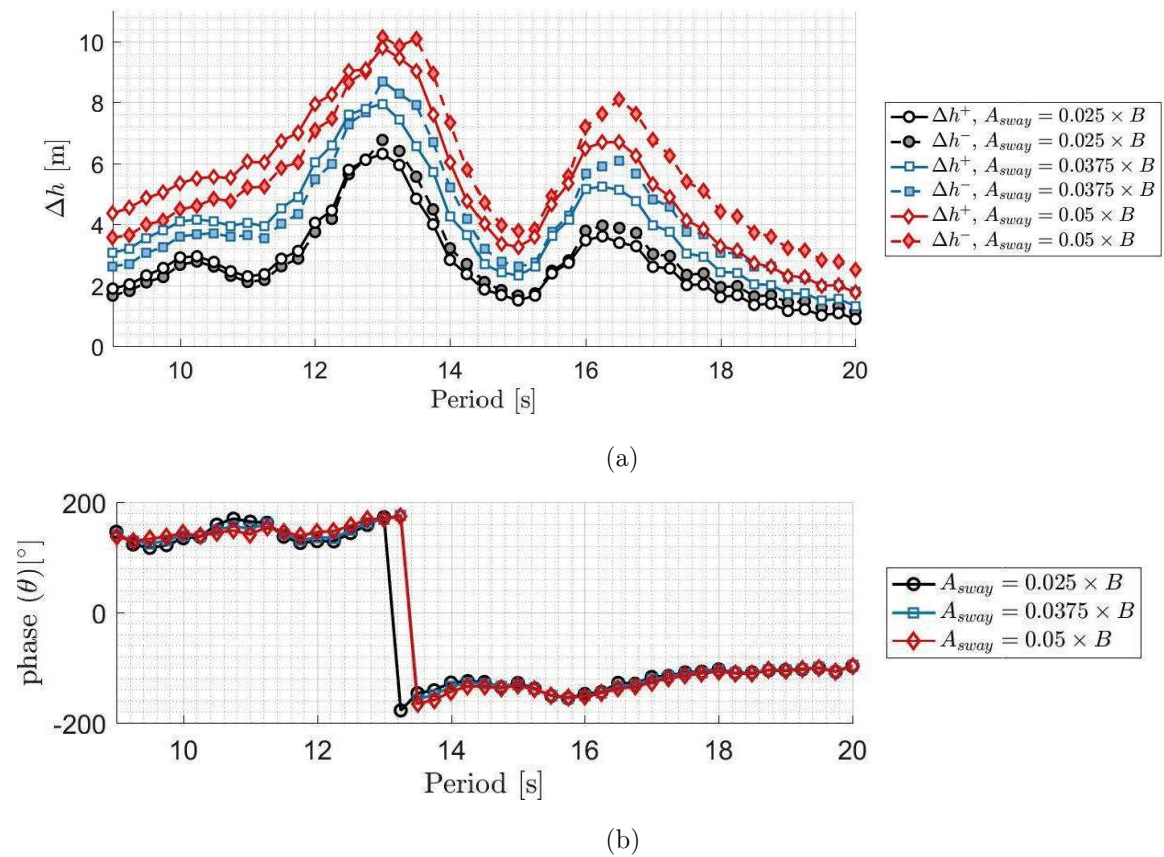


(c) $A_{sway} = 0.05 \times B$

Source: figure from the author.

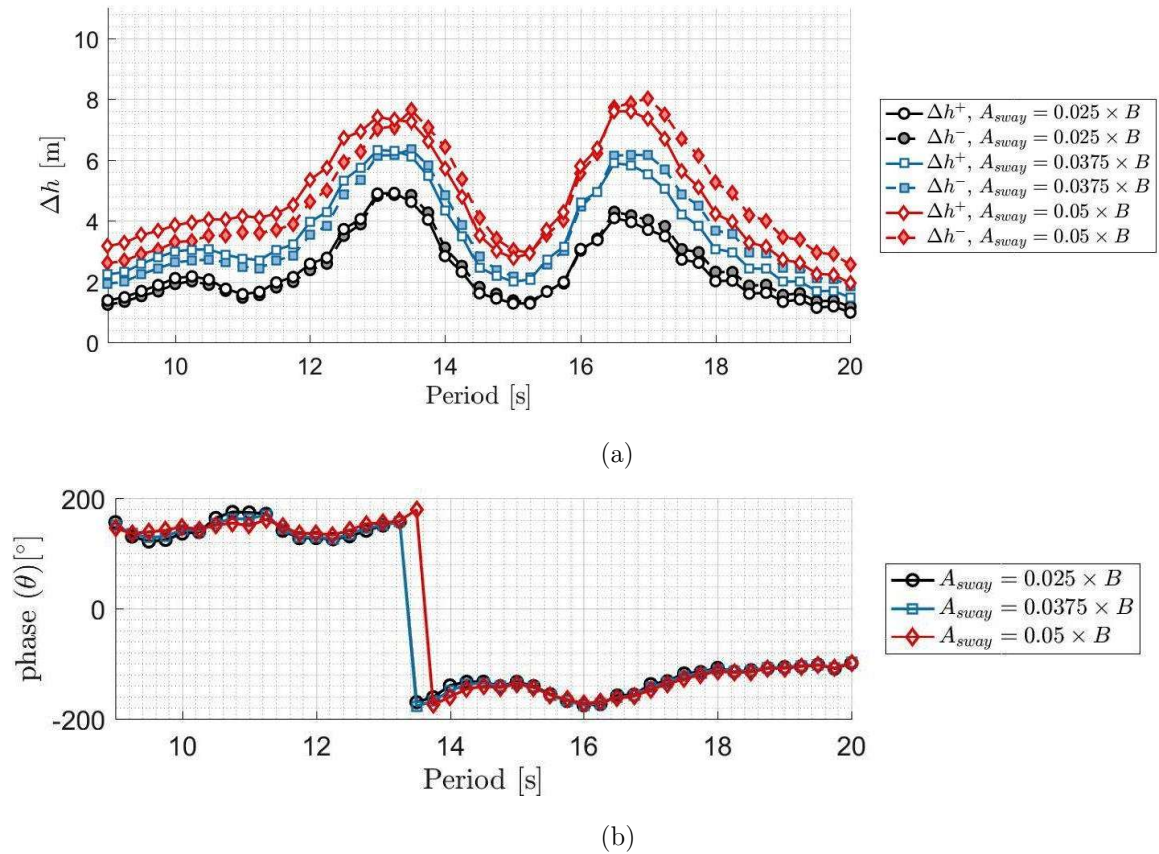
Additional details associated to the gaps with length of 10, 12 and 14 meters are provided in Figure 4.19, Figure 4.20 and Figure 4.21, respectively. Each figure comprises two graphs. The first graph, at the top, has two curves for each sway amplitude, one for the amplitude of the free surface elevation above the still water level (Δh^+) and other to the amplitude below the still water level (Δh^-). The second graph, at the bottom of each figure, shows the phase of main harmonic of the free surface elevation. The phase is obtained from the FFT of the quasi-sinusoidal free surface elevation time series.

Figure 4.19 – (a) Amplitude of the crest (Δh^+) and the trough (Δh^-) of the free surface elevation and (b) phase of free surface elevation at barge wall as function of the sway period – $L = 10m$.



Source: figure from the author.

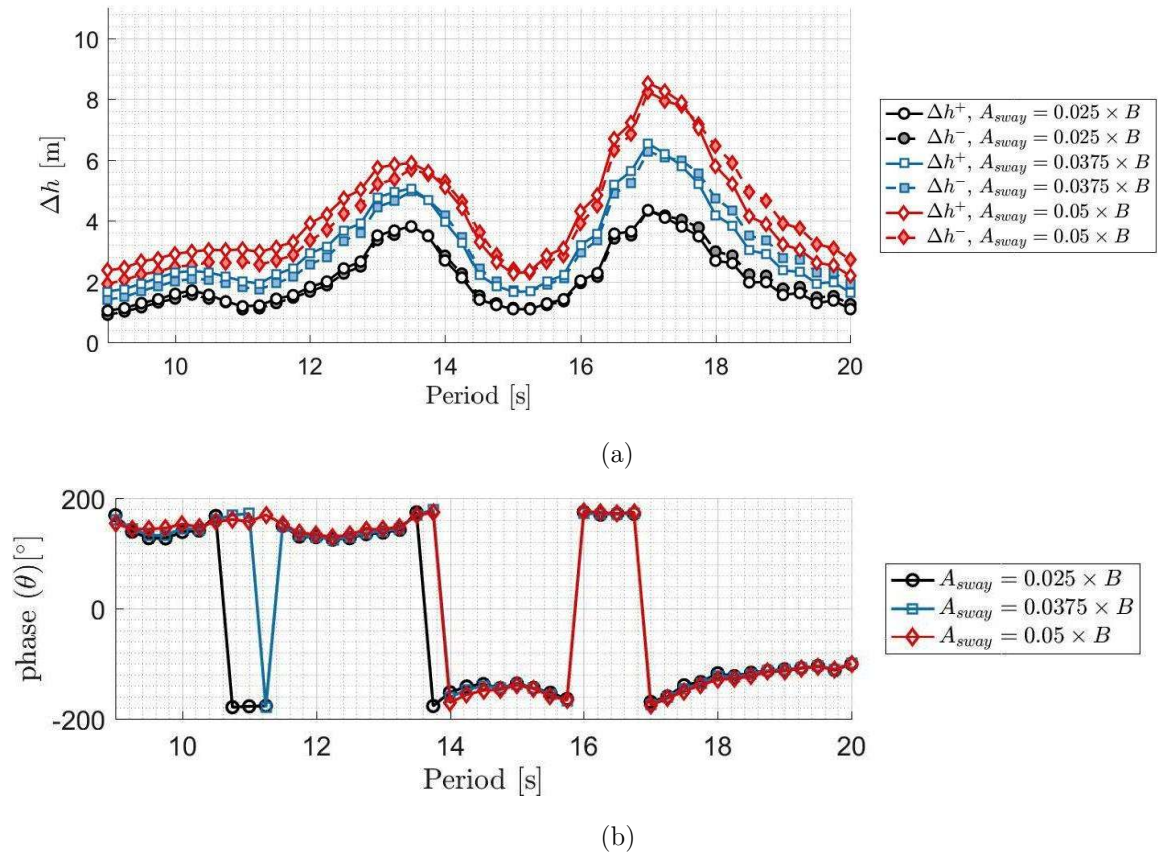
Figure 4.20 – (a) Amplitude of the crest (Δh^+) and the trough (Δh^-) of the free surface elevation and (b) phase of free surface elevation at barge wall as function of the sway period – $L = 12m$.



Source: figure from the author.

The graphs of the amplitude above and below still water level aims to highlight the nonlinear behavior of the piston-mode resonance. In linear phenomena, a quasi-sinusoidal curve is usually obtained, in which the amplitude of the peaks is the same or very close to that of the trough ($\Delta h^+ \cong \Delta h^-$). However, for nonlinear phenomena like the resonant flow in narrows gaps, these amplitudes might differ. In addition, the graphs with the phase of the main harmonic of the oscillation aim to indicate the exact resonance period because a phase shift from +180 degrees to -180 degrees occurs for the resonance peaks (local maxima) and a phase shift from -180 to +180 degrees occurs for the minimum values.

Figure 4.21 – (a) Amplitude of the crest (Δh^+) and the trough (Δh^-) of the free surface elevation and (b) phase of free surface elevation at barge wall as function of the sway period – $L = 14m$.



Source: figure from the author.

In general, for the first local maximum close to 10 seconds, the amplitude of the free surface elevation above the still water level is substantially larger than the amplitude below the still water level. In the case of the other two local maxima, the first one close to 14 seconds and the second one close to 17 seconds, the amplitude above the water level is larger than the amplitude below the still water level for periods shorter than the period in which the peak occurs. For periods longer than that of the peak, the amplitude below the still water level is larger than the amplitude above the still water level. Such behavior is explained by the relative phase between the elevation of the free surface and the harmonic sway motion of the barge. The amplitudes have a trend to become larger in the case the barge is moving closer to the tank left wall. So,

for periods shorter than the period of the peak, the water columns in the gap is flowing upwards while the barge is moving closer to the tank wall. On the other hand, for periods longer than the period of the peak, the water column is moving downward as the barge moves closer to the tank left wall.

Furthermore, in the case of the gap with length of 10 meters (Figure 4.19), the peak at 13 seconds is higher than the peak at 16.5 seconds. Meanwhile, the opposite happens in the case of the gap with length of 16 meters (Figure 4.21), as the peak at 17 seconds is significantly higher than the peak at 13.5 seconds. For the gap with length of 12 meters (Figure 4.20), the magnitude of both peaks is similar. Nevertheless, the peak at 13.5 seconds is slightly higher for the smallest sway amplitude and the peak at 17 seconds is slightly higher for the largest sway amplitude in Figure 4.20. This behavior is consequence of the steep decrease of the wave height and its nonlinear features for the peak around 13 seconds.

The graphs with the phase of the free surface elevation presented by Figure 4.19-b, Figure 4.20-b and Figure 4.21-b show that the resonance period is slightly shifted towards a longer period as the amplitude of the sway motion increase in the case of the peak close to 13 seconds. This small shift for a longer period might be explained by the damping caused by nonlinear phenomena. On the other hand, the period of the phase shift is the same for the three sway amplitudes in the case of the peak close to 17 seconds in Figure 4.21. This behavior is in agreement with the result obtained by Feng and Bai (2015), which they denoted as a “stiff/soft spring” or Duffing-like behavior, based on the nomenclature adopted by Faltinsen et al. (2007).

4.7.4 Analysis of resonant periods for piston-type mode

In the present section, the numerical results obtained for the resonant piston-mode are compared to analytical estimations found in literature. Although three local maxima were computed in the period range between 9 seconds and 20 seconds, the local maximum that occurs for the shorter period has much lower magnitude than the

other two. Hence, the present analysis is focused on the other two local maxima. Herein, the physical meaning of these two free surface height peaks is addressed. Molin (2001) modelled the problem of a moonpool for the two-dimensional and the three-dimensional cases. For sake of simplicity, we will focus only in the two-dimensional case herein. The setup adopted by Molin (2001) was similar to that presented by Figure 4.2; but it considered the left wall of the tank as a symmetry plane, such as in Figure 4.1, in order to depict a moonpool with length $2 \times L_g$ placed within a hull with breadth of $2 \times (L_g + B)$.

In this formulation, Molin (2001) first assumes a barge with infinite beam to formulate the boundary value problem (BVP). Infinite water depth was assumed as well. In the next step, the potential of two symmetrical sinks is introduced to approximate the effect of the outer flow. The sinks are placed somehow arbitrarily far enough of the gap. Then, the resonant period is obtained by solving the eigenvalue problem. The relation found by Molin (2001) is:

$$T_{Molin(2001)} = 2\pi \sqrt{\frac{h}{g} + \frac{2L_g}{g\pi} \left[\frac{3}{2} + \ln \left(\frac{6(B + L_g)}{4L_g} \right) \right]}, \quad (4.1)$$

where h is the barge draft, L_g the length of the gap, and B the beam of the barge.

Molin et al. (2002) modelled the flow through a rigid ice-sheet. It is a case that resembles closely the transversal flow within the gap due to the high value of the gap length-width ratio, which could be approximated by a channel with infinite length. The previously proposed analytical estimation (Molin, 2001) was improved by replacing the Neumann boundary conditions using Dirichlet boundaries.

$$T_{Molin(2002)} = \sqrt{\frac{2\pi}{g\lambda_n} \left(\frac{J_{n0} + \tanh(\lambda_n h)}{1 + J_{n0} \tanh(\lambda_n h)} \right)}, \quad (4.2)$$

where:

$$J_{n0}(r) = \frac{2}{nr\pi^2} \left(\int_0^1 \frac{r^2}{u^2 \sqrt{u^2 + r^2}} \left[1 + 2u + (u - 1) \cos(n\pi u) - \frac{3}{n\pi} \sin(n\pi u) \right] du - \frac{1}{\sin \theta_0} + 1 + 2r \ln \left[\frac{1 + \cos \theta_0}{1 - \cos \theta_0} \right] \right), \quad (4.3)$$

where $\theta_0 = \tan^{-1}(1/r)$ and $\lambda_n = n\pi/L_g$. For the piston-type resonant flow n must be 0.

Besides the modelling of the problem by a BVP, the piston-mode vertical resonant flow in the gap could also be depicted by a mechanical system of one degree-of-freedom (DOF). This approach was first adopted by Aalbers (1984) to model the problem of the resonance within a moonpool due to the hull vertical motion and later used also by Maisondieu et al. (2001). The piston-type flow could be described by a single DOF due its flat free surface profile. Then, the mechanical system is modelled by approximations of the inertial, restoring and damping terms. Special attention was given to the damping term, which was divided into two parts. The first part is linear and related to the potential damping (B_{lin}). The second part is nonlinear and assumed as quadratic (B_{qdr}). The physical meaning of the second part could be related to the effect of the flow separation at the lower corner of the hull and vortex formation. The nonlinear damping term must usually be calibrated experimentally. With the appropriate approximations for the inertial ($m + m_a$) and restoring terms (K), the undamped natural frequency of the mechanical system obtained by Maisondieu et al. (2001) turns out to be the Molin (2001) estimation.

$$(m + m_a)\ddot{y} + B_{lin}\dot{y} + B_{qdr}|\dot{y}|\dot{y} + Ky = 0 \quad , \quad (4.4)$$

where,

$$m = \rho L h L_g, \quad (4.5)$$

$$m_a = \frac{2L_g^2 L}{\pi} \left[\frac{3}{2} + \ln \left(\frac{6(B + L_g)}{4L_g} \right) \right] \quad (4.6)$$

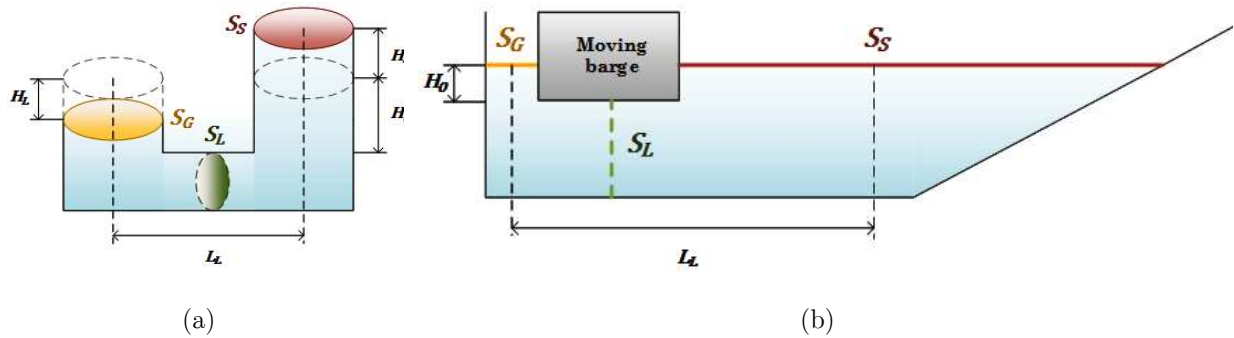
$$B_{lin} = \frac{1}{2} \rho L_g L C_D \quad (4.7)$$

$$K = \rho g L_g L \quad (4.8)$$

where L is the length of the gap considering the three-dimensional case and C_D is a drag coefficient supposed to be constant.

The previous analytical approximations consider the contribution of the outer flow as a secondary one. However, the numerical results previously obtained suggest that this contribution could be significant, mainly for large sway motions of the barge. Hence, in the present work, an analogy between the gap flow and the syphon U-tube flow is proposed aiming to account for the effect of the fluid mass transfer below the barge as result of the difference of free surface height between the two sides of the barge. Such resemblance is illustrated by Figure 4.22.

Figure 4.22 – Layout and coordinates of (a) the U-tube mechanical model and (b) the equivalent model for the piston-flow in the gap



Source: figure from the author.

Tkachenko et al. (2015) modeled the syphon U-tube mechanical system from the Lagrangian function of the system, which was derived to obtain the system motion equation. The kinetic energy terms of the Lagrangian function were estimated based on three generalized coordinates: the free surface displacement on both sides of the tube and the fluid flow in the connection region. A system of only one DOF is obtained based on the assumption of incompressible flow, and relations between the three generalized coordinates were obtained. As a result, the motion equation assumes the form given by equation 4.9.

$$2\ddot{y} \left[y(1 - \sigma_{SG}) + 1 + \frac{L_L}{\sigma_{LS}(1 + \sigma_{SG})} \right] + \dot{y}^2(1 - \sigma_{SG}) + 2y = 0 \quad (4.9)$$

where $\sigma_{SG} = S_S/S_G$ and $\sigma_{LS} = S_L/S_S$. After some algebraic manipulation, the resonant period of the system could be defined as:

$$T_{u-tube} = 4\sqrt{\frac{H_0}{g}(1 - \sigma_{SG})(y_0 + q)}E\left(\frac{\pi}{2}, k\right) \quad (4.10)$$

where E is the elliptic integral of second type, y_0 is the initial free surface displacement and:

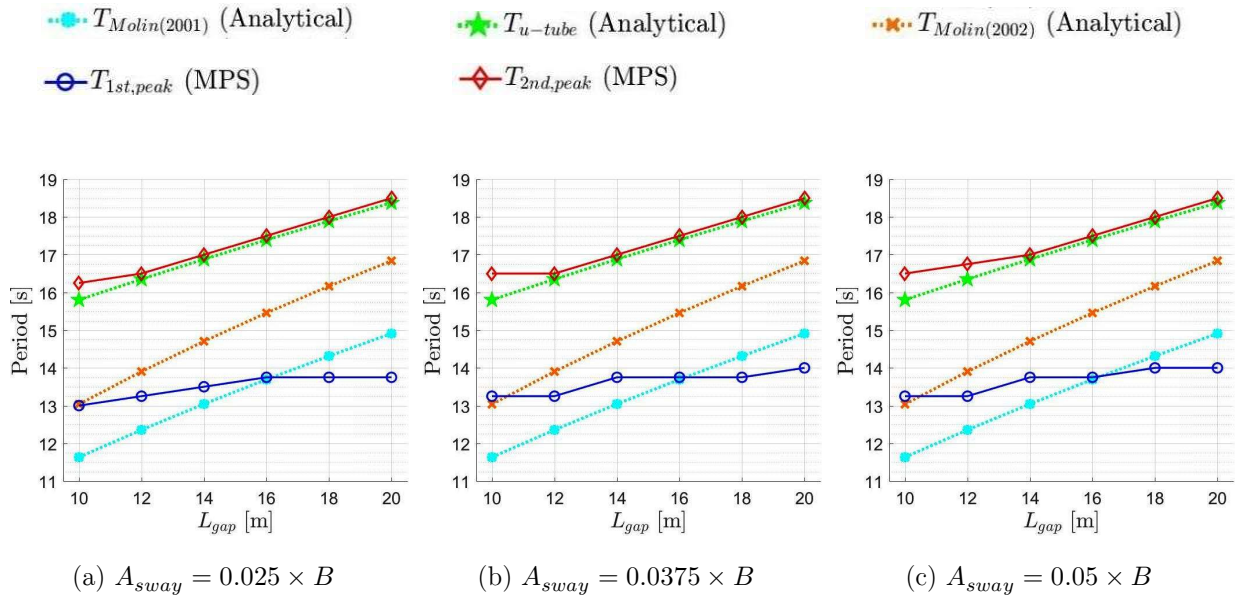
$$q = \frac{1}{1 - \sigma_{SG}} + \frac{1}{\sigma_{LS}(1 - \sigma_{SG}^2)} \quad , \quad (4.11)$$

$$k = \sqrt{\frac{2y_0}{y_0 + q}} \quad . \quad (4.12)$$

An important feature of the motion equation of the syphon U-tube is that the mechanical system is linear only if the free surface area on both sides of the barge are equal ($S_S = S_G$, thus $\sigma_{SG} = 1$). In such case, the inertial component of the motion equation becomes linear and the quadratic first time derivative of the free surface elevation term (\dot{y}^2) vanishes. However, the analogy with the piston-like flow consists in a case in which the free surface area of the outer flow tends to infinite ($\sigma_{SG} = 0$). So, the approximation of the system by a syphon U-tube is intrinsic nonlinear, even disregarding the effects of flow separation and vortex formation in the lower edges of the hull.

Figure 4.23 compares the periods obtained by the analytical estimations for the piston-mode resonance and the periods obtained from the numerical results. The analytical estimations consist on Molin (2001), Molin et al. (2002) and the U-tube formulae (Tkachenko, Kazachkov, Lykah, Minakova, & Syrkin, 2015). Two numerical results are presented: the periods of the first peak ($T_{1st,peak}$) and the period of the second peak ($T_{2nd,peak}$), which could be obtained directly from free surface elevation response (Figure 4.18).

Figure 4.23 – Period of free surface elevation peaks: analytical and numerical estimations



Source: figure from the author.

From Figure 4.23, some relation between the numerical results and the analytical estimations could be established. First, the period of the first peak of the free surface elevation is usually close to the analytically estimated period by Molin (2001) (Eq. Figure 4.23). Second, the period of the second peak of the free surface elevation is close to the analytical estimation of the resonance for the syphon U-tube flow (equation 4.10).

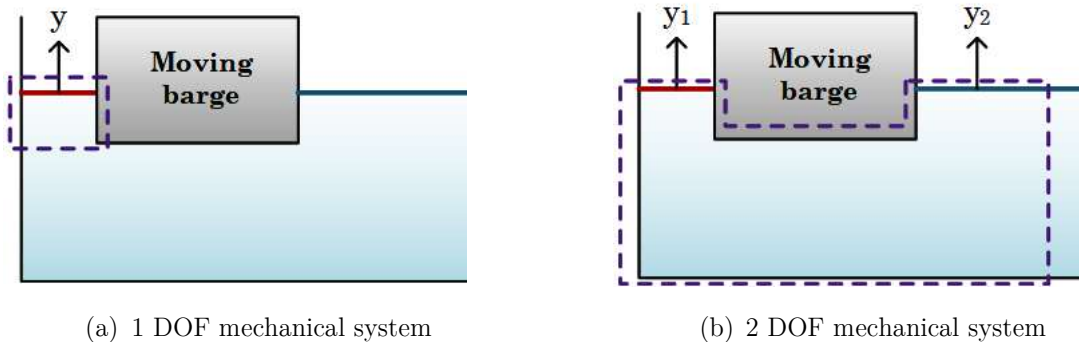
As an explanation, when the gap is large and under large motion amplitude, the analytical estimation proposed by Molin (2001), based on the assumption of a barge of infinite beam, underestimates the effect of the outer flow. On the other hand, the modelling of the U-tube flow is proposed exactly to account for the situation where the flow in both sides of the barge are strongly related.

Therefore, the relations pointed above between the numerical results and the results from the simplified analytical formulations suggest that the piston-type resonant flow presents two distinct physical behaviors depending on the sway motion amplitude and the length of the gap for this case with a relatively shallow water depth. The

effects of the water depth should be further investigated as the other investigation in literature did not reported the U-tube type flow but were carried out for much deeper basins in general.

The first behavior was usually more pronounced for gaps smaller than 14 meters under the smaller sway amplitudes. In this case, the piston-type flow behaves as a single degree-of-freedom mechanical system that considers the free surface elevation in the gap as the generalized coordinate. It comprises only the region within the gap and the influence of the outer flow could be neglected, as depicted by the sketch of Figure 4.24-a. On the other hand, the second behavior resemble a syphon U-tube flow, which could be depicted as a two degree-of-freedom mechanical system with two generalize coordinates: the free surface elevation at the gap and the free surface elevation in the right side of the barge, as depicted by the sketch of Figure 4.24-b. In such cases, the flow on both sides of the barge strongly affect each other.

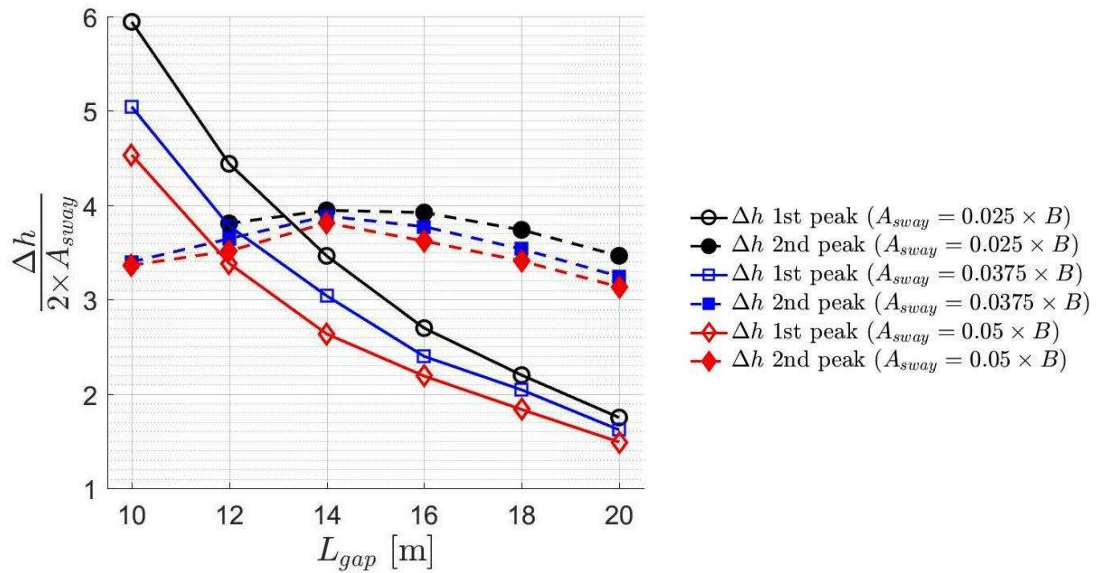
Figure 4.24 – Sketch of the simplified mechanical models.



Source: figure from the author.

Figure 4.25 shows the dimensionless magnitude of the first and the second peaks of the free surface elevation as function of the length of the gap. The magnitudes of the first peak for the three sway motion amplitudes are presented by the solid lines. The magnitude of the second peak is presented by the dashed lines for the three sway motions.

Figure 4.25 – Diagram of the magnitude of the two free surface height peaks in relation to the width of the gap



Source: figure from the author.

The dimensionless amplitude of the first peak decreases as the amplitude of the sway motion increase, which indicates strong nonlinear effects. The solid lines are monotonic and decrease steeply, but their decreasing rate slows down as the length of the gap increases. Such curves also could be approximated by a logarithmic decay function towards a constant asymptotic value. This behavior is consistent with the modeling of the moving barge by a piston-type wavemaker. The wavemaker's transfer function (equation 4.13) could be obtained by the solution of the steady state BVP by linear potential theory (Dean & Dalrymple, 1991) and is composed by exponential functions (hyperbolic sines and cosines). As the period of the wave radiated by the wavemaker increases, its wavelength also increases and, as consequence, the amplitude decreases logarithmically.

$$\frac{H}{S} = 2 \frac{\cosh(2kh - 1)}{\sinh(2kh) + 2kh}, \quad (4.13)$$

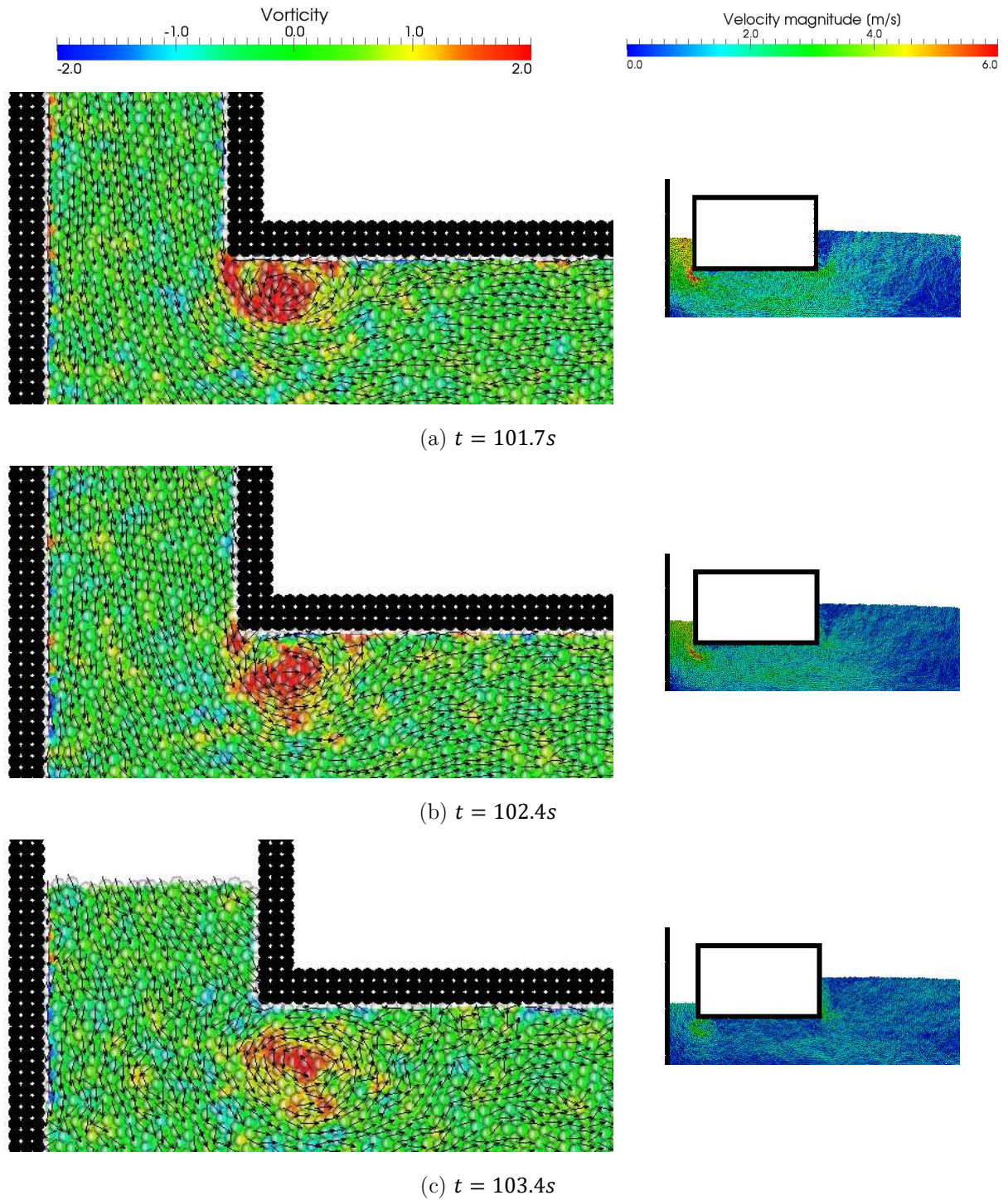
where H is the height, i. e., double amplitude of the radiated wave and S is the stroke amplitude of the harmonic motion of the piston-type wavemaker.

Regarding the second peaks, different sway motion amplitudes also lead to non-overlapping dashed lines, which indicates a phenomenon affected by the amplitude of the motion, thus, nonlinear as well. This is quite consistent result because the syphon U-tube flow motion equation (equation 4.9), which is associated to the second peak, is nonlinear as well. As previously shown in Figure 4.18, the magnitude of the U-tube type resonance peak reaches a maximum for gaps of 14 meters in this case.

The nonlinearities of the piston-type resonant flow were observed for several previous works in literature and were generally related with additional damping introduced by phenomena such as flow separation in the lower edges of the hull and vortex formation (Kristiansen & Faltinsen, 2010). The results of the present section and its comparison to the syphon U-tube case suggests that the mass transfer below the hull, as consequence of the difference between the free surface elevation in the two sides of the barge, could be a reason of such nonlinearities as well.

Figure 4.26 shows snapshots for the case with the shortest gap and under the largest sway motion moving at the period of the first amplitude peak, and highlights the flow around the lower edge of the barge between the left wall and the bottom at the instant when the downward motion of the flow inside the gaps is reaching its lowest point. The color scale of the snapshots at the left column indicates the magnitude of the local flow vorticity and the color scale of the snapshots at the right column indicates the magnitude of the local flow velocity. The direction of the flow is indicated by the arrows. Both the flow separation and the formation of a vortex could be clearly identified in the snapshots. As the velocity of the flow around the edge decreases, the vorticity of the vortex is also reduced until it vanishes.

Figure 4.26 – Snapshots of the vortex in the lower edge of the barge: vorticity and flow direction (left column) free surface profile and velocity magnitude (right column) – $L_{gap} = 10m$, $T = 13.0s$, $A_{sway} = 0.05 \times B$



Source: figure from the author.

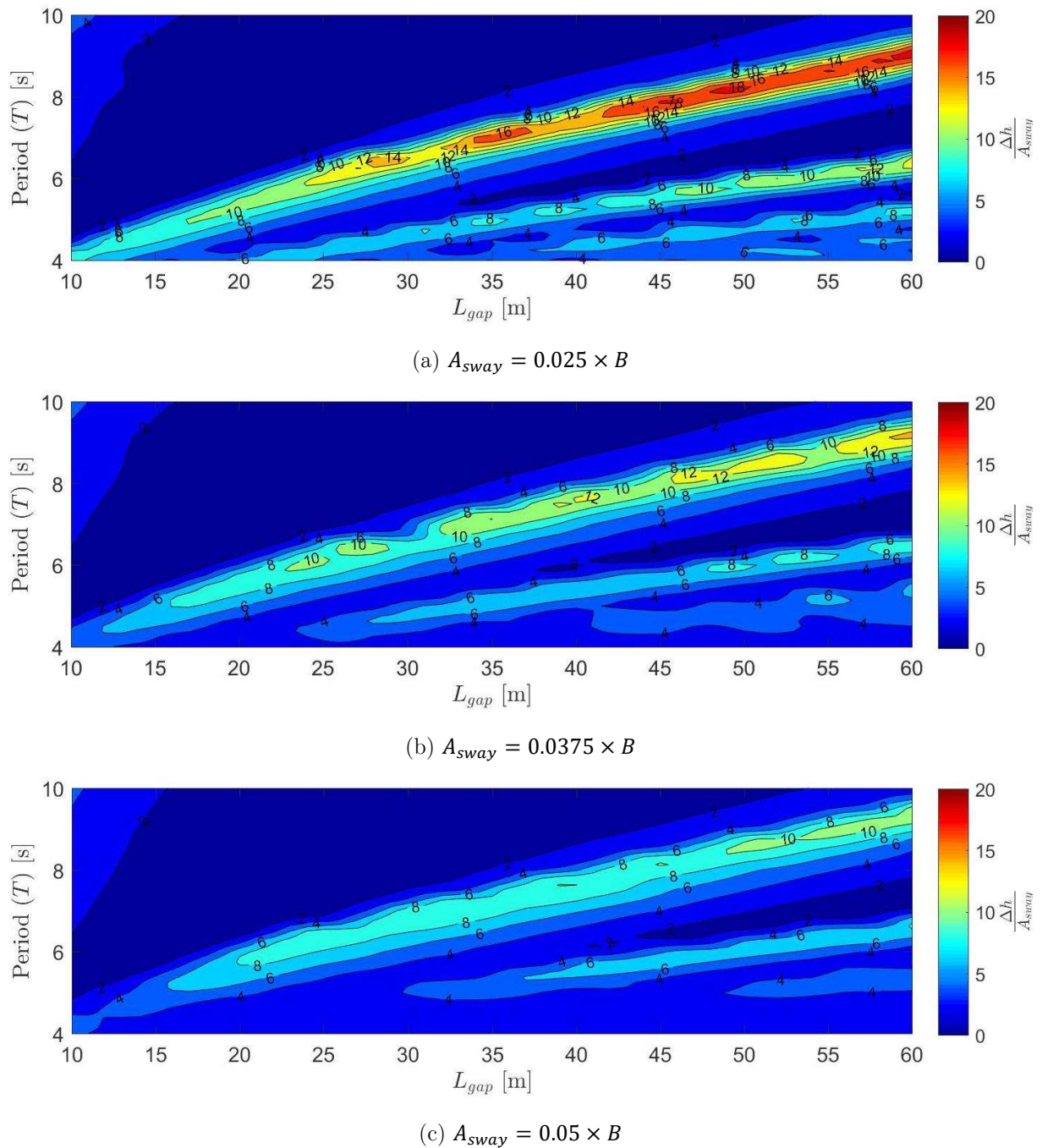
1.2 SLOSHING-TYPE RESONANCE MODE

The other type of local maximum of the free surface elevation observed in the contour maps of Figure 4.11 is related to the case of the sloshing-type resonance. The sloshing modes occur when a stationary wave is created within the gap and the length of the gap matches a multiple of half of its wavelength ($L_{gap} = \frac{n\lambda}{2}$). Two sloshing modes were identified in the range of length of the gap and sway motion periods considered in the present study. One is the first antisymmetric mode ($n = 1$) and the other is the first symmetric mode ($n = 2$), both cases occur for sway motions with periods shorter than 10 seconds and length of the gap up to 60 meters. Between these two sloshing modes, a local minimum of the free surface elevation is also observed. It is also related to the formation of a stationary wave. However, in such case, the left wall of the barge is located just on the node of the sinusoidal free surface profile of the stationary wave.

Figure 4.27 shows the contour maps of the dimensionless free surface amplitude as function of the period of sway motion and the length of the gap for the conditions in which the sloshing-type resonant flow occurs. The period range is between 4 seconds and 10 seconds and the length of the gap goes from 10 meters until 60 meters. The three contour maps from Figure 4.27-a to Figure 4.27-c shows the results for the three sway motion amplitudes.

In general, three “stripes” in the diagonal of the contour maps with local maxima of the dimensionless amplitude of the free surface elevation could be observed. The larger “stripe” related to the longer periods is associated to the first anti-symmetric sloshing resonant mode. The “stripe” in the middle is related to the first symmetric sloshing mode. Finally, the third “stripe” at very short periods is related to the second anti-symmetric sloshing resonant mode. From Figure 4.27-a to Figure 4.27-c, the magnitude of the local maxima has a large decrease, which indicates, as expected, that the sloshing phenomenon is highly nonlinear.

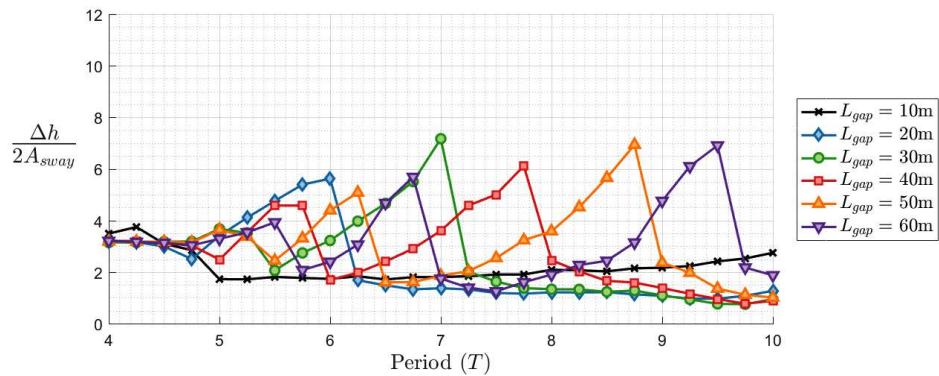
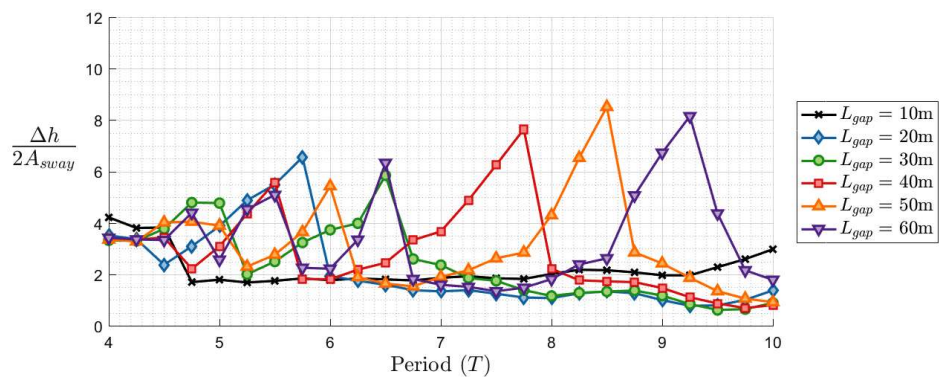
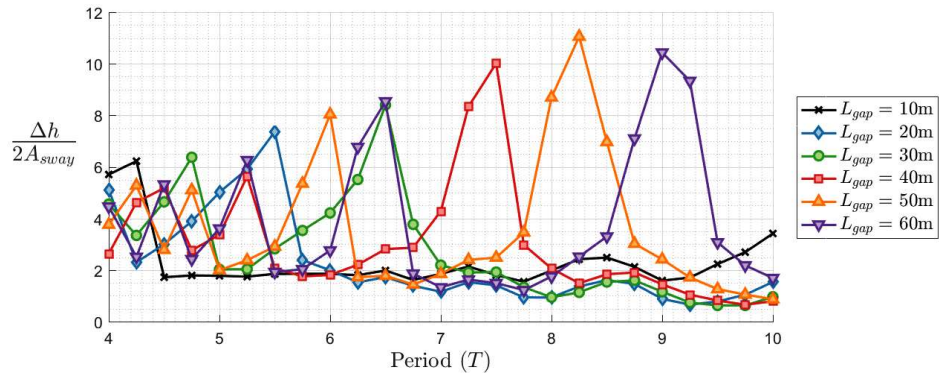
Figure 4.27 – Contour map of the dimensionless wave height as function of the length of the gap and the sway period – sloshing-type resonance.



Source: figure from the author.

Figure 4.28 presents the diagram in the period domain of the dimensionless free surface elevation amplitude in the range of sway motion periods between 4 and 10 seconds. The local maximum values observed in such diagrams are related to the sloshing-type resonance.

Figure 4.28 – Dimensionless free surface elevation in relation to sway period:
sloshing mode.



Source: figure from the author.

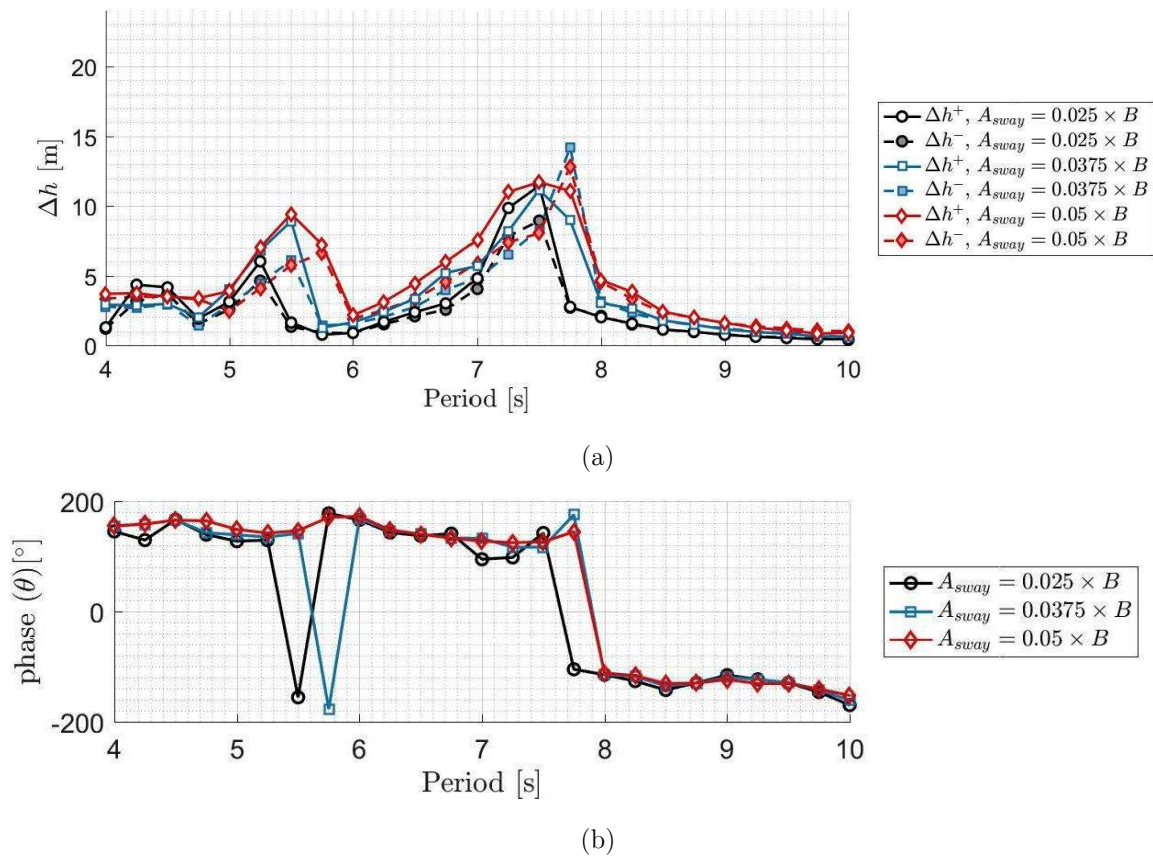
For the six values of gap length presented in Figure 4.28, the respective first anti-symmetric sloshing resonance is associated to the highest peak of the free surface elevation of each curve. For the three gaps equal or larger than 40 meters, a second local maximum, which is related to the first symmetric sloshing mode, can also be

observed. Finally, for the gaps with length over 50 meters, a third small local maximum related to the second sloshing anti-symmetric mode occurs. Considering the relevant range of gap dimensions, the period of the sloshing resonant modes is much shorter than that of the piston type mode.

As the amplitude of the sway motion increases, the period of the sloshing-type resonance peak increases very slightly. This trend is more visible for short gaps below 40 meters. On the other hand, the magnitude of the peak of the dimensionless free surface amplitude is much larger for small sway motion (Figure 4.28-a) than that obtained in the case of large sway motions (Figure 4.28-c), mainly due to additional damping from highly nonlinear phenomena such as wave breaking, wave runup along the barge wall and so on.

In the sloshing modes, the time series of the free surface elevation on the barge left wall presents a quasi-sinusoidal profile. Assuming such behavior, the amplitudes and phase of the dominant frequency as function of the sway period are presented by Figure 4.29, Figure 4.30, and Figure 4.31 for gaps with length of 40, 50 and 60 meters, respectively. Two curves are presented for each sway amplitude in the graphs at the top, one related to the free surface elevation amplitude above the still water level (Δh^+) and the other to the amplitude below the still water level (Δh^-). The graph in the period domain of the phase of the dominant frequency is presented by the graphs and the bottom in order to indicate the resonant period by the phase shift.

Figure 4.29 – (a) Amplitude of the crest (Δh^+) and the trough (Δh^-) of the free surface elevation and (b) phase of free surface elevation at barge wall as function of the sway period – $L = 40m$.

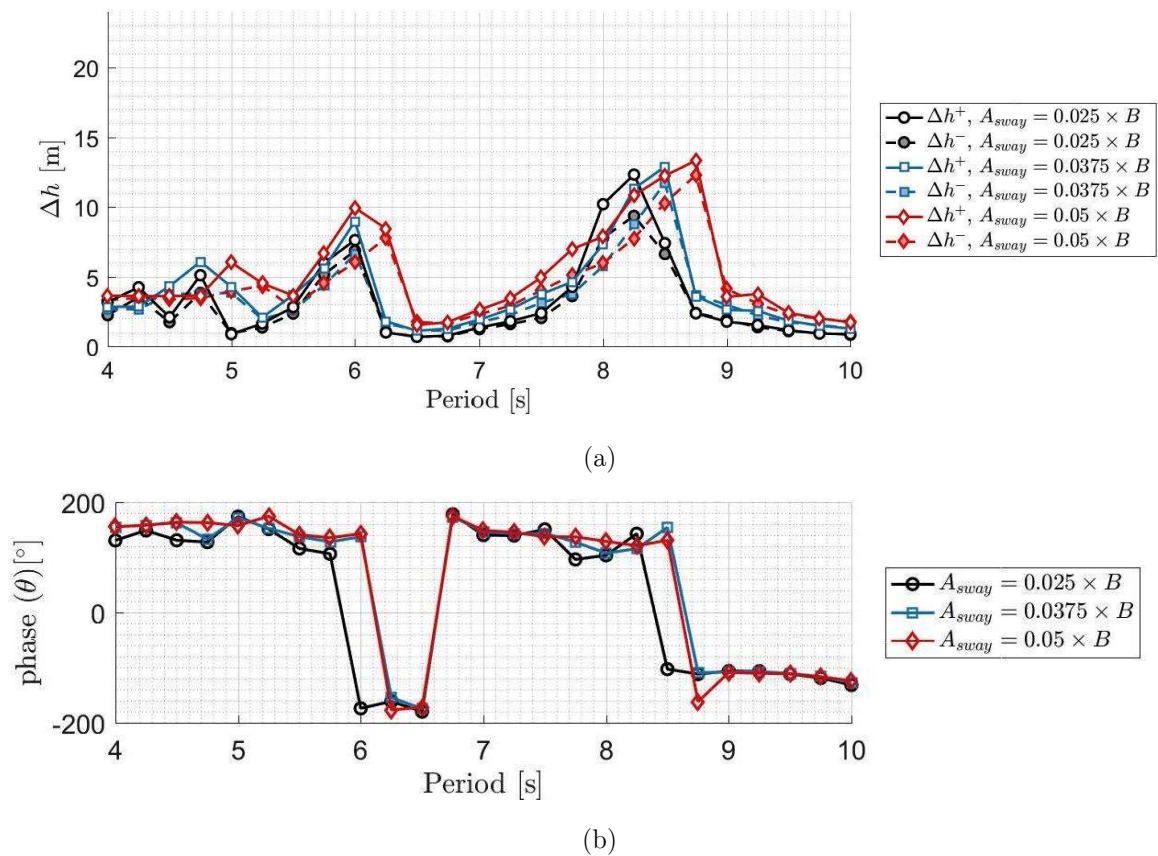


Source: figure from the author.

The amplitude of the free surface elevation above the still water level is higher than the amplitude below the still water level for the vicinity of the sloshing-type resonance period range, as observed from the diagrams of Figure 4.29-a, Figure 4.30-a, and Figure 4.31-a. In this case, the maximum free surface elevation is at the barge wall as it moves closer to tank left wall. Besides, wave runup in the left side of the barge was observed in the simulation, which also contributed to the amplitude of the free surface elevation above the level becoming larger than the amplitude of the free surface elevation below the still water level. On the other hand, both amplitudes are almost equal in the local minimum between the two resonance peaks related to the case in which is created a stationary wave and the barge left wall is placed exactly in its node.

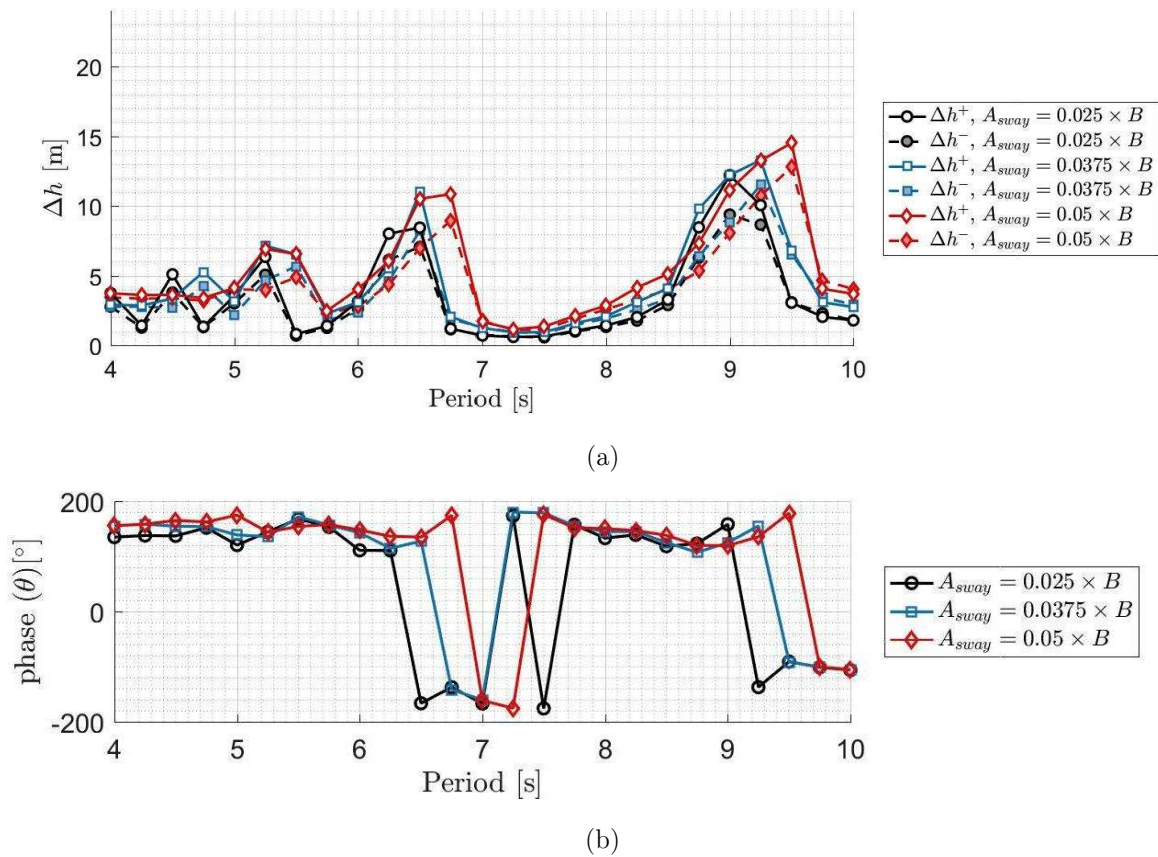
From Figure 4.29-b, Figure 4.30-b and Figure 4.31-b, the period of the phase shift of the resonance peaks is slightly longer for the sway amplitude of 5% of B than for the amplitude of 2.5% of B due to nonlinear free surface conditions typical of the sloshing phenomenon. On the other hand, the periods of the phase shift associated to the minimum free surface elevation are the same for the three sway amplitudes.

Figure 4.30 – (a) Amplitude of the crest (Δh^+) and the trough (Δh^-) of the free surface elevation and (b) phase of free surface elevation at barge wall as function of the sway period – $L = 50m$.



Source: figure from the author.

Figure 4.31 – (a) Amplitude of the crest (Δh^+) and the trough (Δh^-) of the free surface elevation and (b) phase of free surface elevation at barge wall as function of the sway period – $L = 60m$.



Source: figure from the author.

4.7.5 Analysis of resonant periods for sloshing-type modes

An analytical estimation of the period of the n -th mode of sloshing-type resonant flow could be obtained by replacing the wavelength on the wave dispersion relation by the n -th multiple of half the width of the gap ($L_{gap} = \frac{n\lambda}{2}$). Herein, the dispersion relation for finite depth from Airy linear potential theory is adopted.

$$T_{sls,n} = \frac{2\sqrt{\pi L_{gap}}}{\sqrt{ng \tanh\left(\frac{n\pi h}{L_{gap}}\right)}}, \quad (4.14)$$

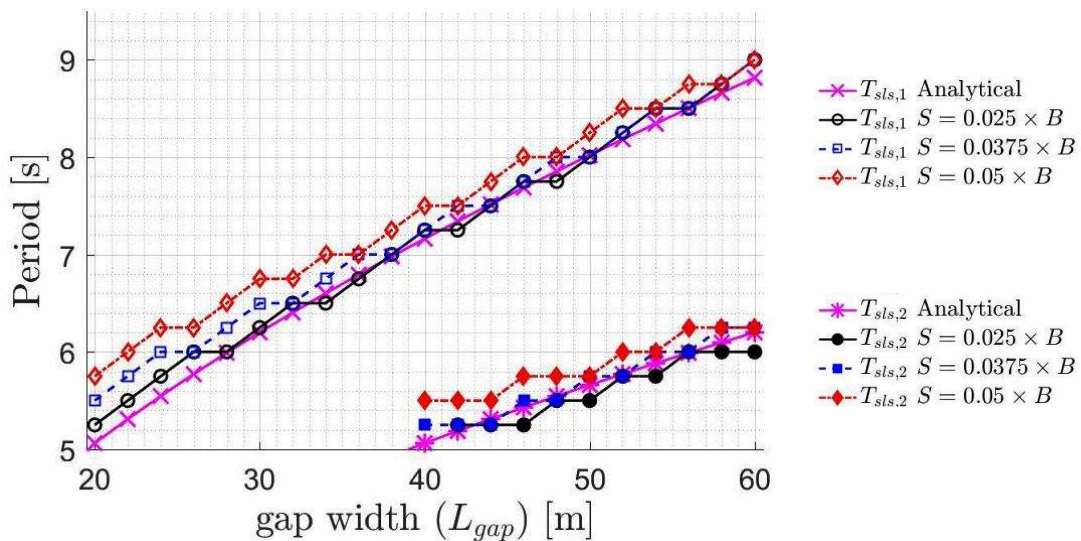
Figure 4.32 compares the periods of the sloshing resonant flow from the numerical simulations to the resonant periods of sloshing estimated analytically based

on equation 4.14. The periods from the numerical simulations were obtained from the local maximum values at the free surface height diagrams.

The sloshing resonance period for the smallest sway motion showed very close agreement to the analytical estimation for the two sloshing modes. In this case, the differences between numerical and analytical results were often smaller than the increment of sway period of 0.25 seconds between simulation cases. Notwithstanding, as the sway motion amplitude increases, the sloshing resonant period tends to slightly shift. Such trend is more evident for the shorter gaps, i. e., when the ratio between the sway motion amplitude and the width of the gap becomes larger, showing the effects of the nonlinearities regarding the resonant period.

Figure 4.32 – Diagrams of the resonant period for sloshing modes:

Analytical estimation and numerical results



Source: figure from the author.

4.8 CONCLUDING REMARKS

The fluid flow trapped inside narrow gaps is an important phenomenon to be addressed during the design of offshore and naval structures and in the planning of offshore operations. As the flow within the gap show significant nonlinear aspects in resonant conditions, a fully nonlinear particle-based method was adopted in the present work to investigate the resonant flow trapped inside narrow gaps. For the sake of simplicity, the analysis carried out herein was focused only on the transversal resonant conditions based on a two-dimensional setup. The particle simulations were performed in real scale numerical models for different values of length of the gap and sway motion amplitudes and periods.

First, the results of validation for the piston-type resonance presented good agreement with the experimental data from Maisondieu et al. (2001). After that, analysis regarding the piston-type resonance and the sloshing-type resonance flow are carried out. As a result, significant nonlinear features were identified for the piston-type resonant flow and the results were verified using analytical approaches in order to understand the system behavior:

- a) Two large peak values of the free surface elevation could be observed for the piston-type resonant flow, each one is related to a distinct flow type.
- b) The flow associated to the first peak, which has shorter period, could be depicted by a mechanical system composed only by fluid column inside the gap with the free surface initially displaced. In this case, the effect of the outer flow can be neglected. The flow shows almost linear behavior as the sway amplitude increases. The magnitude of the peak decreases monotonically as the width of the gap increases assuming a logarithmic decay profile. These results agree well with the ones obtained by modeling the moving barge as a piston-type wavemaker with infinite breadth.

- c) The flow associated to the second peak, with longer period, could be depicted by a syphon U-tube mechanical system. It is the case in which the flow within the gap is strongly affected by the outer flow. The phase lag between the free surface elevation on both sides of the barge intensifies the flow below the hull. Even disregarding nonlinear features such as flow separation and vortex formation, such kind of flow is intrinsic nonlinear. The magnitude of the peak almost constant in the range of lengths of the gap evaluated herein, but it has a small decreasing rate as the length of the gap increases from 14 meters.
- d) In general, the period of these two peaks slightly increases as the sway motion amplitude increases. Also, for the cases analyzed, the length of the gap of 14 m is a turning point: the first peak is higher than the second one for gaps smaller than 14 m, the opposite is observed for gaps larger than 14 meters.
- e) Two modes of sloshing-type resonant flow could be observed in the range of sway motion period considered herein. The resonance periods slightly increase as the sway motion increase. The nonlinearities observed in the simulations could be related to the large free surface displacements and the flow below the hull.

The rules for practical applications to naval and offshore engineering, such as offloading operations on side-by-side arrangements, usually consider only the period related to the first peak observed for the piston-type resonance. Such approach could be enough for deep waters and ships under small waves. However, for shallow water environments or under large ship motions, a second nonlinear resonant piston-type flow may occur in longer periods. In these conditions, which must be considered in the delimitation of the operation envelop in order to perform a safer operation. Finally, a syphon U-tube mechanical system can be used as a simple technique for the modeling the phenomenon associated to the second peak of piston mode resonance.

Even for the simplified two-dimensional modeling of the problem, it involves a large number of different parameters. In this analysis, the investigation was focused mostly

on the effects of the wave period and the length of the gap to the resonant flow in narrow gaps. Therefore, a single tank depth and a single geometry of barge, with a single draft and beam, was investigated. The depth of the tank seems to have a large effect on the results obtained herein as it is relatively small compared to other works in literature. Further investigation might be performed in order to consider the effects of the other parameters not addressed in depth herein, such as the draft of the barge and the depth of tank. Moreover, the present study was focused only on the radiation problem as the wave was generated solely by the motion of the barge. Novel cases of study might be proposed in order to add complexity to the problem and turn it close to the real cases of interest in the naval and offshore industry.

5 CHAPTER FIVE: MULTIREOLUTION MOVING PARTICLE SEMI-IMPLICIT METHOD BY BORDER MAPPING TECHNIQUE

5.1 ABSTRACT

In the third study of this thesis, a multiresolution technique called “border mapping” is proposed for the MPS method. The border mapping technique aims to obtain an “equivalent particle distribution” in the truncated boundary between two sub-domains with different resolutions and it is divided into two steps: the refinement of the coarse region of the border and the simplification of the fine region of the border. The main aspect of the proposed approach is to use the actual irregular particle distribution in the border region, which enhances the numerical stability. The preliminary tests of the proposed technique were promising, as the pressure was correctly calculated, the mass of the system was conserved and the computational cost could be substantially reduced in relation to a single-resolution simulation.

5.2 INTRODUCTION

The Moving Particle Semi-Implicit (MPS) method is a fully-Lagrangian Computational Fluid Dynamics (CFD) method for the modelling of the incompressible flow. The MPS and other particle-based numerical methods easily deal with phenomena involving large free-surface deformations, fragmentation and merging. Besides, these methods are very flexible and suitable for the modeling of phenomena with complex geometry, fluid-structure interaction, multi-bodies, multi-liquid, multi-phase and multi-physics, as each particle carry its own physical properties. Hence, the particle methods are numerical techniques better suited to the modeling of the impulsive local hydrodynamic loads in naval and offshore structures than the traditional mesh-based methods.

However, the MPS method has an important shortcoming: it is a very computer intensive technique. In general, its computational cost is significantly higher than traditional mesh-based numerical methods. The processing time is expected to increase dramatically when the number of particles of the numerical model increases. As numerical models with a larger number of particles are expected for the modelling of more complex and detailed engineering problems, the computational cost becomes an important issue towards the feasibility of the MPS as a practical engineering tool. In such context, two parts of the algorithm of the MPS method have the highest computational costs: the search of each particles neighborhood and the solution of the linear system of the Pressure Poisson Equation (PPE) in the implicit part.

The particle-based method owes its flexibility, in part, to the fact that the particles are distributed in an unstructured particle-grid and allowed to freely move in relation to each other according to the conservation equations. This feature allows the method to easily model complex geometries and large free surface deformations. As a consequence, the set of neighbor particles within the compact support of each particle continuously change in time and its update should be carried out at each time step. In

such regard, the processing time required for the update of the neighbor particle list is proportional to N^2 in the two-dimensional case, where N is the total number of particles of the numerical model. Koshizuka et al. (1998) proposed an optimized algorithm that required the neighbor search to be performed only once for several time-steps. The processing time for the neighbor search decreased to the order of $N^{1.5}$. The neighbor search procedure was further improved by introducing a division of the computational domain in cells. Then, the search of neighbor particles is performed by considering only the particles within cells close to the particle instead of the entire computational domain. By using this technique, the processing cost of the neighbor search increases an order N^1 , i. e., linearly, as the number of particles increase.

The other computer intensive step of the MPS algorithm is the calculation of the pressure by the solution of a linear system of Pressure Poisson Equation. One key aspect that differs the MPS method to the Smoothed Particles Hydrodynamics (SPH) method is the calculation of the pressure. While the MPS calculates it implicitly by solving the linear system of PPE, the SPH calculates the pressure explicitly by a weakly-compressible scheme based on function of state. The implicit scheme provides a more accurate pressure calculation and the incompressibility of the flow is better ensured. Besides, in the case of short-duration violent impact loads, some pressure oscillation related to the fluid compressibility should be expected in the explicit weakly-compressible scheme. Thus, the MPS was adopted in the present Thesis as it is deemed as a better suited particle-based method for the investigation of nonlinear hydrodynamic phenomena.

The drawback of the implicit scheme for the pressure calculation is that a linear system of order N^2 , for the case of two-dimensional models, must be solved at each time step. In the MPS PPE linear system, the matrix of coefficients is sparse with its non-zero coefficients concentrated close to the main diagonal, but it changes every time step due to the change of the arrangement of the particles. Although the numerical

solution of a sparse matrix is much faster than that of a dense matrix, the solution of the PPE linear system is still the bottleneck of the MPS method regarding its computational cost, mainly considering that the matrix along the simulation.

Different strategies could be adopted aiming to reduce the processing time required for a particle simulation in which the computational domain has a large number of particles. The first strategy consists in the use of parallel processing techniques for faster computation.

In such context, Fernandes et al. (2015) developed a hybrid parallel computing framework for an MPS-based simulation system. The hybrid parallelization combines shared memory parallelization and distributed memory parallelization. Shared memory consists in the use of multiple cores of a single node that share the same memory storage but multiple processors to perform the calculations. Distributed memory consists in the simultaneous use of multiples nodes of a computer Cluster, each node with its own memory storage. In this approach, the computational domain is divided into sub-domains, which contains a fraction of the total particles of the model, and each sub-domain is calculated by a different node of the computer Cluster.

Despite its effectiveness, parallelization techniques require specific computer architecture, such as multi-core processors or cluster of PCs, and the demand huge computational resources in order to achieve a decrease in the processing time.

As the essence of the problem lies on the large number of particles required for the modeling of practical engineering, an effective approach might be the reduction of the number of particles, but without losing its level of detail and the accuracy of the results. This approach is particularly useful for the investigation of phenomena in which the local complex hydrodynamic loads occur in a small portion of the domain, while the global loads that affect a much larger portion of the domain could not be disregarded. As an example, there is the case of the green water phenomenon in a floating platform in a harsh weather environment. In order to model the boarding

water and the impact pressure of the fluid in the deck structures, a high resolution should be adopted to model deck structures that measure only few meters. However, in order to model the complete phenomena, the interaction between the floating platform and the waves should be modeled as well, which involves structures with dimensions in the order on hundreds of meters. As the modelling of such case usually is performed by using numerical towing tanks, the fluid domain must be large enough in order to avoid the effects of wave reflection and the effects of the bottom of the tank in the wave dynamics. Summarizing, a computational domain in the order of several hundreds of meters should be modelled by particles with its dimension in the case of few centimeters.

Figure 5.1 – Inside an LNG MarkIII membrane tank with corrugations



Source: Gaztransport & Technigaz (GTT) website (access on May/2019).

Other example is the case of sloshing in membrane type LNG tanks. Damage to small internal corrugations due to sloshing impact were reported for MARKIII LNG membrane tanks (Bogaert, Brosset, & Kaminski, 2010). The corrugations are small features with height of few centimeters, which are designed to deal with the tank thermal expansion and contraction due to the cryogenic LNG containment. Meanwhile, the LNG membrane tanks have dimensions in the order of 40 meters. The different length scales between the tank and the corrugations could be clearly observed in Figure 5.1. So, in order to adequately model the hydrodynamic impact load on the

corrugations, a resolution of few millimeters should be adopted to model such large tanks, which is unfeasible for particle simulations even by using parallel processing on computer Clusters.

In this context, two strategies could be used to the modelling of the problem: the coupling between the MPS to less computer-intensive methods and the use of multiresolution techniques for MPS-only simulations. The case of the coupling between the MPS method to other methods could be adopted for cases in which the phenomena responsible for the global loads is not so complex and other less computer-intensive methods are suitable. This approach is similar to that adopted by Kleefsman et al. (2005) to model the green water phenomenon on floating structures. In this work, while a small portion of the computational domain and the local loads were modelled by a CFD Finite Volume Method (FVM), the global loads and the incoming wave field were calculated by a less computer-intensive Boundary Element Method (BEM).

Nevertheless, such coupling strategy is not adequate for cases in which both the global loads and the local loads are caused by very complex phenomena, such as the case of the sloshing impact in tanks with corrugations. In this case, the use of multi-resolution MPS simulations seems to be the best approach.

The development of multi-resolution techniques is one of the main topics in the state-of-the-art of MPS method. Several different techniques were proposed in the last decade, such as Tanaka et al. (2009) (2018), Tang et al. (2014), Chen et al. (2015) and Shibata et al. (2012) (2017). Each one of these works proposes a different solution for a multi-resolution MPS method; each one presents its important contributions, its own advantages and disadvantages as well, which will be properly presented later in the literature review. In this context, the present study is focused on the proposal of a novel multi-resolution technique, which is named herein “border-mapping” technique and tackles important aspects that were not yet solved by the previously proposed techniques in literature.

5.3 OBJECTIVE

In order to define the objectives of the present study, it is important to enumerate the main aspects that an adequate multi-resolution technique should feature. For sake of simplicity, although not properly a coupling, it is useful to make an analogy between the multi-resolution technique and a coupling between two sub-domains with different resolutions for clarity of the arguments. Hence:

- 1) The coupling between the sub-domains of different resolutions should be in the strong-form, i. e., the conservation equations must be solved jointly for all the sub-domains.
- 2) The coupling must be two-way, i. e., the information between two sub-domains of different resolutions flows in both directions, from fine region to coarse region and vice-versa.
- 3) As the particles pass through the boundary between two-subdomains with different resolutions, its resolution must change and the pre-defined resolutions of each sub-domain must be properly maintained during that process.
- 4) The calculation of the pressure in the MPS method is highly sensitive to local changes in the particle distributions. So, for a better pressure calculation, a multi-resolution technique must avoid abrupt changes in the particle distribution in the border between sub-domains.

Summarizing, the objective of the present study is to propose and develop a multi-resolution technique which presents a two-way strong-form coupling between sub-domains with different resolutions. Besides, as particles flow between them, its pre-defined resolutions must be kept uniform during the simulation and the particle distribution in the borders should be changed as smoothly as possible.

5.4 LITERATURE REVIEW

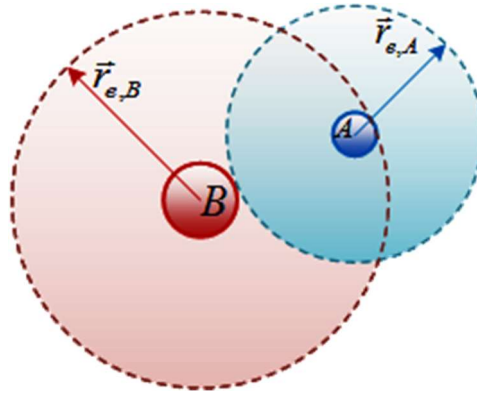
As previously mentioned, the two most widespread particle-based CFD methods are the SPH and the MPS methods. One of the key differences between the original formulations of these methods lies in the algorithm for the calculation of the pressure. The MPS adopts an implicit calculation of the pressure by a linear system of PPE while the SPH adopts an explicit calculation based on weakly-compressible scheme by an equation of state. As a consequence, the formulation of a multi-resolution technique becomes more challenging for the MPS method than for the weakly-compressible SPH. So, although there are several multi-resolution techniques proposed to the SPH method, the current literature review will be solely focused on multi-resolution proposals to the MPS method.

In this section, the previously proposed multi-resolution techniques for the MPS method are described based on some key aspects. The first one is how the computational domain is divided in regions with different resolutions, herein called sub-domains. The second aspect is how the method keeps the resolution within each sub-domain uniform as the simulation progresses, i. e., how the method changes some particles as they flow from one sub-domain to other sub-domain. The third aspect is the weighting function that the technique adopts to deal with particles of different sizes.

This final aspect is particularly important because the compact support, also known as the particle neighborhood, is usually defined by a radius proportional to the size of the particle. A consistent weighting function should hold the Newton's third law, which means that two neighbor particles must be in the neighborhood of each other and affect each other equally in opposite directions. However, in the case of particles of different sizes close to each other, it is possible to one particle being in the neighborhood of the other but the opposite not happen, such as presented by Figure 5.2. In this case, the particle A is inside the neighborhood of particle B, which is outside the neighborhood of particle A. This situation must happen in the boundary

between sub-domains of different resolutions and should be adequately addressed by the multi-resolution techniques.

Figure 5.2 – Neighborhood of particles with different sizes



Source: figure from the author.

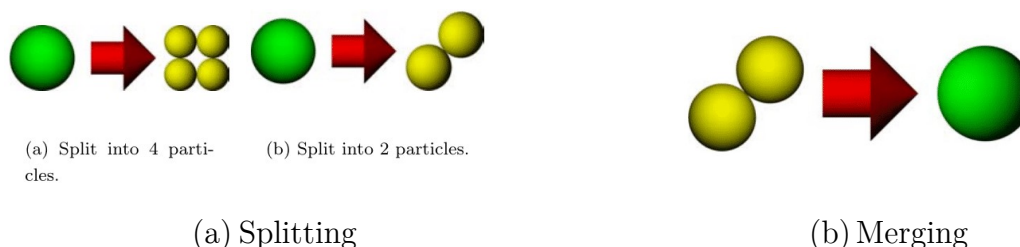
The important contributions of each previously proposed technique, as well as its shortcomings, will be described in the present section by considering the four features of a suitable multi-resolution technique as outlined in the objectives (section 4.3).

The first multi-resolution technique for the MPS method was proposed by Tanaka et al. (2009), only for two-dimensional cases. In this work, two different strategies were adopted in order to divide the computational domain. In the first one, the sub-domains with different resolutions were defined initially and along the simulation particles with different resolutions are allowed to freely mix. In the second strategy, the particles with different resolutions are confined to their respective sub-domain by adopting splitting and merging algorithms.

In this second strategy, when a particle flows from the low-resolution region to the high-resolution region, splitting occurs when it crosses the border between high and low resolution domains. Two splitting ratios were evaluated by the authors: from 1 to 2 particles and from 1 to 4 particles (Figure 5.3-a). When the particles flow in the opposite way, from the high-resolution region to the low-resolution region, they are

merged. The merging was made by adopting a ratio of 2 to 1 (Figure 5.3-b) and the two merged particles are not necessarily of the same size.

Figure 5.3 – Splitting and merging algorithm – Tanaka et al. (2009)



Source: Tanaka et al. (2009).

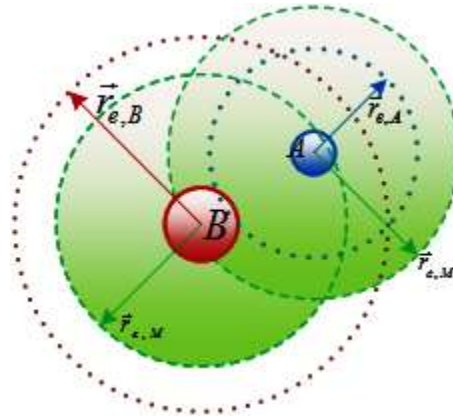
The two different proposals have its own shortcomings. The multi-resolution technique that allows the particles to mix is suitable for very few practical cases, as the low-resolution-particles might reach the high-resolution region and vice-versa. So, the accuracy of the results in the high-resolution region is gradually reduced as the simulation advances.

In the second strategy, which applies splitting and merging to keep the resolution of the regions, there are two drawbacks. The first drawback is that the ratios of splitting and merging are different, so the defined resolution of each region is not properly kept as the size of the particles gradually changes. The second drawback is that the particle distribution that results from the two splitting schemes is not isotropic. The abrupt change in the particle distribution due to particle splitting might result in an artificial and large numerical oscillation of the local pressure. Thus, the pressure field of the multi-resolution simulation shows a much more unstable profile than the pressure field of the equivalent single resolution simulation.

Regarding the weight function adopted by Tanaka et al. (2009), the Newton third law is ensured by adopting a neighborhood radius for each pair of particles, which is defined based on the average value of the neighborhood radius previously expected for the two particles, as presented by Figure 5.2. As each pair of particles has its own neighborhood radius, the neighbor particles of a given particle could have several

different neighborhood radiuses and the compact support of a given particle might be highly non-symmetrical.

Figure 5.4 – Neighborhood of particles



Source: figure from the author.

Tanaka et al. (2018) improved substantially this multi-resolution technique with splitting and merging by replacing the original MPS formulation by the Least-Squares MPS (LSMPS) (Tamai & Koshizuka, 2014). The LSMPS is a higher-order formulation which is able to deal with highly irregular particle distributions, but the tradeoff is a higher computational cost as a matrix of coefficients, a momentum matrix and a momentum vector should be calculated for each derivative operator at each particle. Nevertheless, the obtained results presented much improved results for the calculated pressure.

A different approach called Overlapping Particle Technique (OPT) was proposed by Shibata et al. (2012) for two-dimensional MPS simulations. This technique, in a practical sense, basically consists in two separated MPS simulations, one covering the entire computational domain, modeled with low-resolution particles, and the other covering only the critical area, modeled with high-resolution particles. The boundaries of the high-resolution region are then modeled as inlet/outlet boundary conditions in which the velocity and pressure of the flow is defined based on an interpolation from the values previously obtained in the low-resolution simulation for the boundary

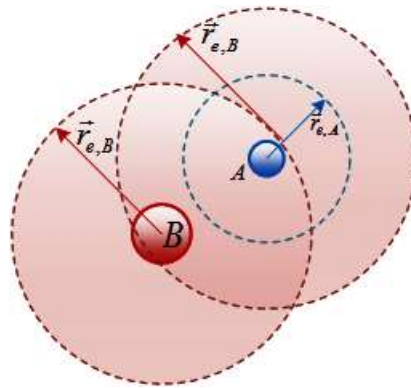
location. Summarizing, it is a weak-form, one-way coupling between two simulations using different resolutions.

One advantage of this technique is that it is suitable for the original weight function of the MPS. Other advantage is that the resolutions of the different regions are effectively maintained during the entire simulation. On the other hand, additional numerical error is introduced in the boundaries when generating or removing particles or by interpolating the physical quantities. As a consequence, the mass of the system is not properly conserved and techniques for the mitigation of the mass loss are required.

Tang et al. (2014) extended the OPT multi-resolution technique for three-dimensional simulations and proposed an improved algorithm for particle generation and removal. Shibata et al. (2017) further developed the OPT technique for a two-way coupling between the domains of different resolutions. The interpolation of the velocity and pressure in the overlapping boundary was modified to a formulation based on the LSMPS. Besides, several improvements to the formulation of the inlet/outlet boundaries were proposed in order to reduce the error in the mass conservation.

Chen et al. (2015) proposed a strategy similar to Tanaka et al. (2009) (2018) for the division of the computational domain, with algorithms of particle splitting and merging to keep the resolution within the sub-domains. Besides, a weight function based on a cubic spline kernel of the SPH was used. Different gradient operator and Laplacian were proposed as well. In order to ensure the Newton's third law, the particle with the larger neighborhood radius is adopted as the neighborhood radius of two particles with different resolution (Figure 5.5).

Figure 5.5 – Neighborhood of particles– Chen et al. (2015)

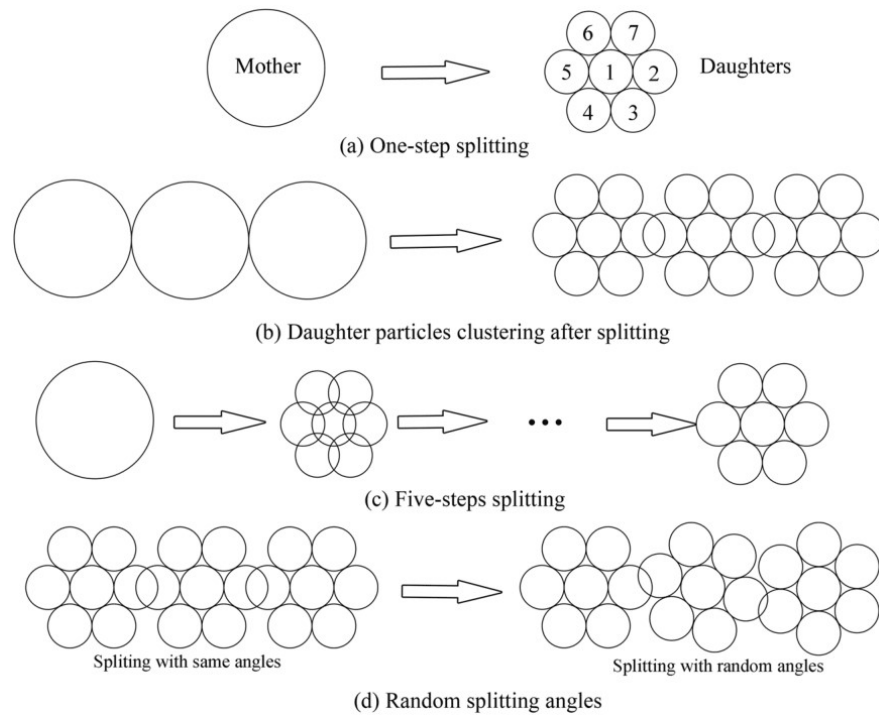


Source: figure from the author.

Chen et al. (2015) adopted a different splitting algorithm in order to obtain a more isotropic high-resolution particle distribution and mitigate numerical pressure oscillations in the border between the sub-domains. The splitting algorithm adopts a ratio from 1 to 7 particles, distributed in a hexagonal geometry as shown by Figure 5.6. The splitting algorithm is divided into sub-steps, in order to gradually rotate the hexagonal distribution of particles aiming to reduce particle clustering. The merging algorithm, presented by Figure 5.7, is similar to that previously adopted by Tanaka et al. (2009) (2018), with ratio from 2 to 1 in order to merge two particles not necessarily of the same size.

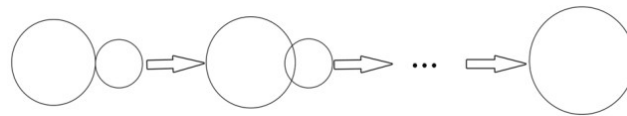
The multi-resolution technique proposed by Chen et al. (2015) has its shortcomings. At first, as information is created and lost by the splitting and merging algorithms, a larger numerical error should be expected due to the very large ratio of 1 to 7 adopted in splitting algorithm. Besides, the neighborhood radius of the high-resolution particles is the same of the low-resolution particles, which results in a very large neighborhood radius for the fine-resolution particles. What is more, due to the different ratios used in splitting and merging, in both the high and the low resolution sub-domains, the resolution of the particles gradually change as the simulation advances.

Figure 5.6 – Splitting algorithm – Chen et al. (2015).



Source: Chen et al. (2015).

Figure 5.7 – Merging algorithm – Cheng et al. (2015).



Source: Chen et al. (2015).

In the multi-resolution technique proposed by Tsuruta et al. (2016), the sub-domains with different resolutions are adopted. As it is focused only in keeping the resolution of high-resolution sub-domain, only a splitting technique was considered. The splitting algorithm allows different ratios, since all the generated daughter particles have the same distance from the centroid of the mother particle. As the fine-resolution particles are allowed to flow to low-resolution sub-domains without merging, mixing of particles with different resolutions occurs in the low-resolution sub-domains and the total number of particles of the model only increases as the simulation advance.

Besides, Tsuruta et al. (2016) adopts a weight function that takes into account particles of different sizes. To ensure Newton's third law, a unique neighborhood radius

is adopted, such as in Figure 5.5. Then, fine-resolution particles are expected to have very large neighborhood radii in relation to its size. As particles with different sizes interact with each other, the neighborhood of a given particle becomes more irregular and non-isotropic, which results in “void spaces”. To correct such void spaces, a technique called Space Potential Particles (SPP) (Tsuruta, Khayyer, & Gotoh, 2015) is adopted. It introduces “ghost particles” that account for the missing portion of particle number density of a given particle neighborhood.

5.4.1 Summary of the different multi-resolution techniques

Table 5.1 summarizes the main features of the existing multi-resolution techniques shown above and how they fit to the objective of achieving a strong-form, two-way coupling multi-resolution technique, without mixing of particle with different size and provide a simple and consistent particle distribution in the interface between subdomains. The features that agree with the objectives of the present work are highlighted in **green** as the aspects that do not are highlighted in **red**. The major shortcoming of each approach is outlined in the last line of the Table 5.1 and highlighted in **orange**.

For sake of simplicity, only the most recent version of a given technique is presented herein.

Table 5.1 – Features of the multi-resolution techniques for MPS method

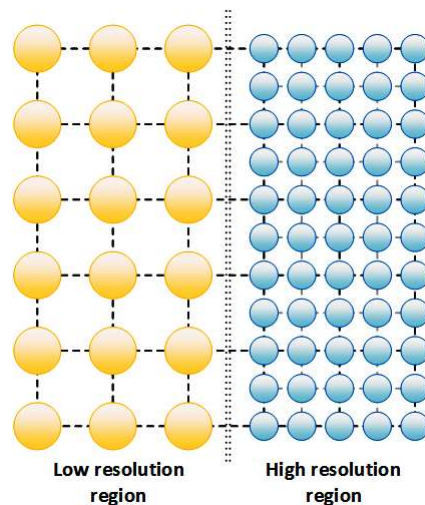
| | Tanaka et al. (2018) | Shibata et al. (2017) | Chen et al. (2015) | Tsuruta et al. (2016) |
|--|--|-----------------------------------|--------------------------------------|--------------------------------------|
| Coupling | Strong-form Two-way | Weak-form One-way Two-way | Strong-form Two-way | Strong-form Two-way |
| Splitting | Ratios 1:2/1:4 | No | Ratio 1:7 | Any ratio |
| Merging | Ratio 2:1 | No | Ratio 2:1 | No |
| Effectively keeps the resolution? | Slightly change | Yes | Slightly change | Only fine-resolution |
| Particle interaction model | Modified for variable-size particles + LSMPS | LSMPS | Modified for variable-size particles | Modified for variable-size particles |
| Supports the original particle model? | No | Yes | No | No |
| Neighborhood radius | Average value | One for each resolution | Single for all resolutions | Single for all resolutions |
| Additional improvements | Free surface and wall BC + Particle shifting | Some to enhance mass conservation | Smoother particle splitting | Space Potential Particles + more |
| Other shortcoming? | Non-isotropic particle distribution | Error in the total mass | Large ratio between fine/coarse | Only particle refinement |

5.5 MULTIREOLUTION MPS METHOD BY “BORDER MAPPING” TECHNIQUE

5.5.1 Overview

The border region between two sub-domains of different resolutions is presented in Figure 5.8. For sake of simplicity, only the cubic regular particle arrangement is shown to show the basic concepts of the proposed technique. In the case of the particles close to the border, the compact support of each particle reaches the other sub-domain and contains particles with different resolutions so that suitable treatments should be done regarding the computation using the weighting function.

Figure 5.8 – Border between two sub-domains



Source: figure from the author.

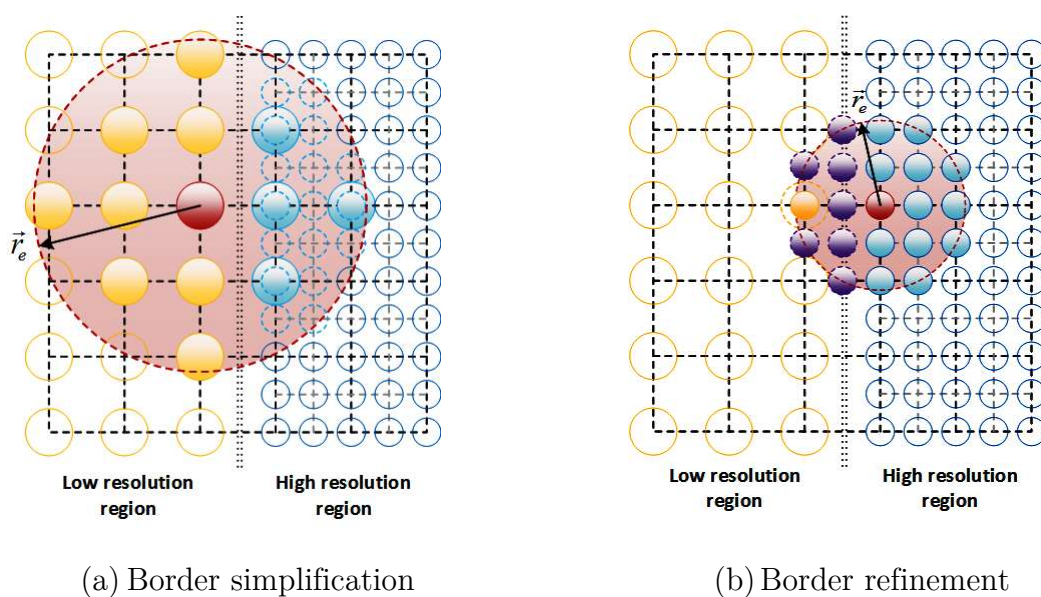
The multi-resolution techniques found in the literature deal with particles of different sizes by splitting/merging (Tanaka, Cardoso, & Bahai, 2018) (Chen, Sun, Liu, & Xi, 2015) (Tsuruta, Gotoh, & Khayyer, 2016) or by generating/removing particles similarly an inlet/outlet boundary condition (Shibata K. , Koshizuka, Matsunaga, & Masaie, 2017). In common, such techniques are based on a strictly Lagrangian point-of-

view, in which the fluid domain is composed by particles that corresponds to macro-scale fluid particles that carry its mass and physical properties.

In the so-called “border-mapping” technique proposed here, the problem is solved using a different paradigm. Instead of a Lagrangian point-of-view, an Eulerian point-of-view of the fluid through the subdomains is adopted. In this approach, the particle-based discrete fluid domain is viewed as an unstructured grid, with an irregular but uniform distribution of nodes in which the physical properties of the flow are known. These nodes are equivalent to the center of the fluid particles. In Figure 5.8, the unstructured grid is represented by dashed line in the background of the particles.

Based on such approach, the border-mapping technique aims to obtain an equivalent particle distribution in each side of the border between the subdomains so that a particle close to the border could consider only particles of same resolution within its neighborhood. The algorithm of the border-mapping technique is composed by two processes: the high-resolution border simplification and the low-resolution border refinement. Their conceptual scheme is presented by Figure 5.9.

Figure 5.9 – Conceptual scheme of the “border mapping” technique



Source: figure from the author.

The objective of the border simplification (Figure 5.9-a) is to obtain a low-resolution particle distribution in the near-border region of the high-resolution sub-domain. Meanwhile, the objective of the border refinement (Figure 5.9-b) is to obtain a high-resolution particle distribution in the near-border region of the low-resolution sub-domain. The length ratio between the low-resolution particles and the high-resolution particles is 2:1. Notwithstanding, successive levels of higher-resolution regions could be modeled to achieve finer resolutions in the critical region of the computational domain.

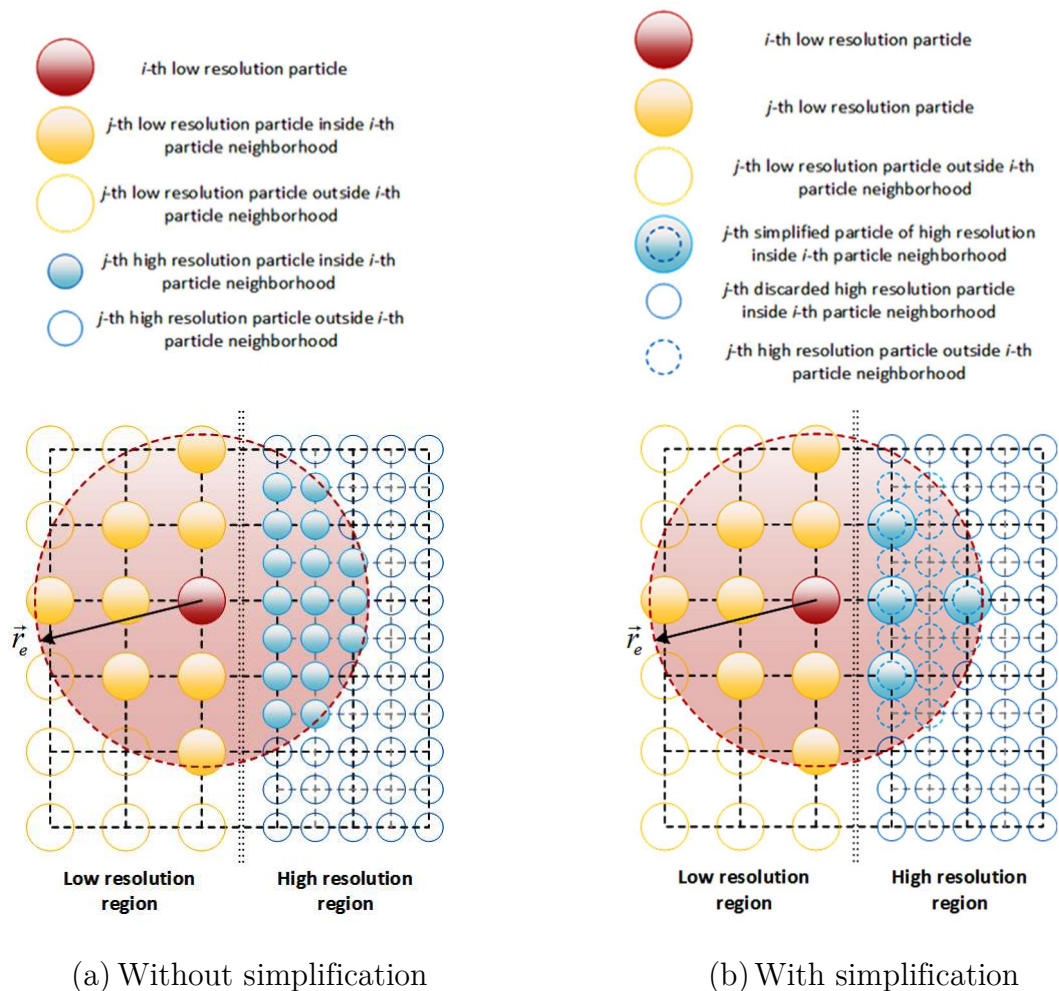
By associating the particle-based fluid domain to a triangular grid, the equivalent resolutions could be obtained by mesh triangulation operations to reduce or to increase the number of triangles while maintaining the position of the original nodes. As the original position of the node, i. e., particles, is kept, abrupt changes in the particle distribution are avoided and, as a consequence, a more stable calculation of the pressure in the border region is expected. This is an important feature because in the traditional splitting/merging algorithms remove a mother particle from a certain position and introduce daughter particles or vice versa in different locations, which usually result in abrupt changes to the local particle distribution and unstable computations.

Summarizing, the proposed technique has a **strong-form, two-way coupling** between sub-domains of different resolutions. Besides, the simplification and refinement ratios are the same in a way **the resolution** of the particles within each sub-domain **is kept during the entire simulation**. Finally, as the simplification and refinement algorithms intend to keep the position of the original particles, a **smooth particle distribution** and pressure calculation are then expected.

5.5.2 Simplification of the fine-resolution region

Figure 5.10 presents a conceptual scheme of the simplification of the high-resolution region close to the border. A low resolution particle with a distance to the border smaller than its neighborhood radius is expected to have an “overpopulated” neighborhood, i. e., a neighborhood with a larger number of neighbor particles than it should have, as presented by Figure 5.10-a. As a consequence, its particle number density will be wrongly overestimated if calculated by original MPS weight function.

Figure 5.10 – Conceptual scheme of the simplification



Source: figure from the author.

The simplification aims to obtain a particle distribution that closely resembles a low-resolution distribution in the near-border region of the high-resolution domain.

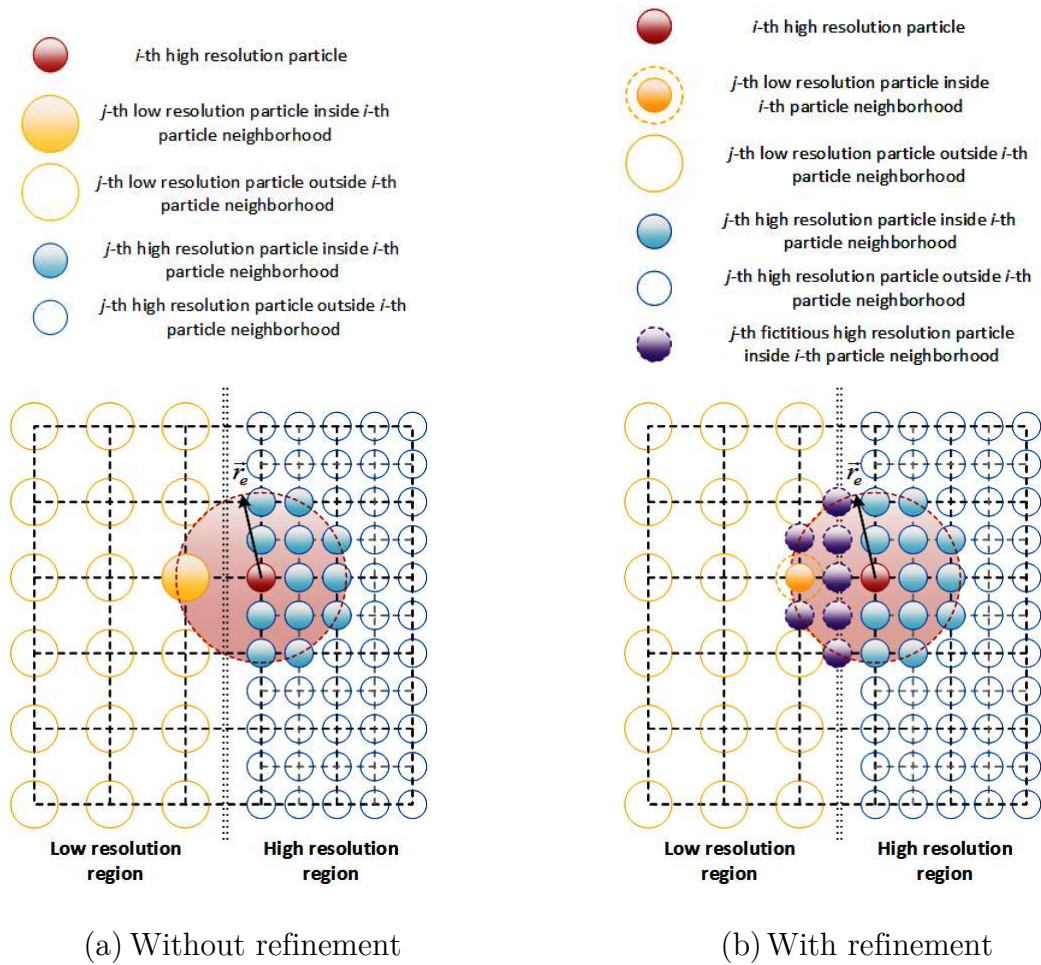
This is achieved by dividing the high-resolution particles close to the border into two-types: the “simplified particles” and the “non-simplified particles” (or “discarded particles”), as depicted by Figure 5.10-b. For the low-resolution particle close to the border, the non-simplified particles are disregarded in its neighborhood. As a result, a consistent low-resolution particle is assured inside their compact support. In the present proposal for two-dimensional modeling, the ratio between the number of “simplified particles” and the number of “non-simplified particles” should be approximately 1:3.

5.5.3 Refinement of the coarse-resolution region

Figure 5.11 presents a conceptual scheme of the refinement of the low-resolution region close to the border. A high-resolution particle with a distance to the border smaller than its neighborhood radius is expected to have an “underpopulated” neighborhood, i. e., a neighborhood with a smaller number of neighbor particles than it should have, as presented by Figure 5.11-a. As a consequence, its particle number density will be wrongly underestimated if calculated by original MPS formulation.

The refinement aims to obtain a particle distribution that closely resembles a high-resolution distribution in the near-border region of the low-resolution domain. This is achieved by the introduction of the so-called “fictitious particles”, as presented by Figure 5.11-b. With the “fictitious particles” and the existing low-resolution particles that are assumed as high-resolution particles, a consistent high-resolution particle distribution can be obtained in the compact support of the near-border high-resolution particles. The ratio between the number of “fictitious particles” and the number of low-resolution particles close to the border should be approximately 3:1.

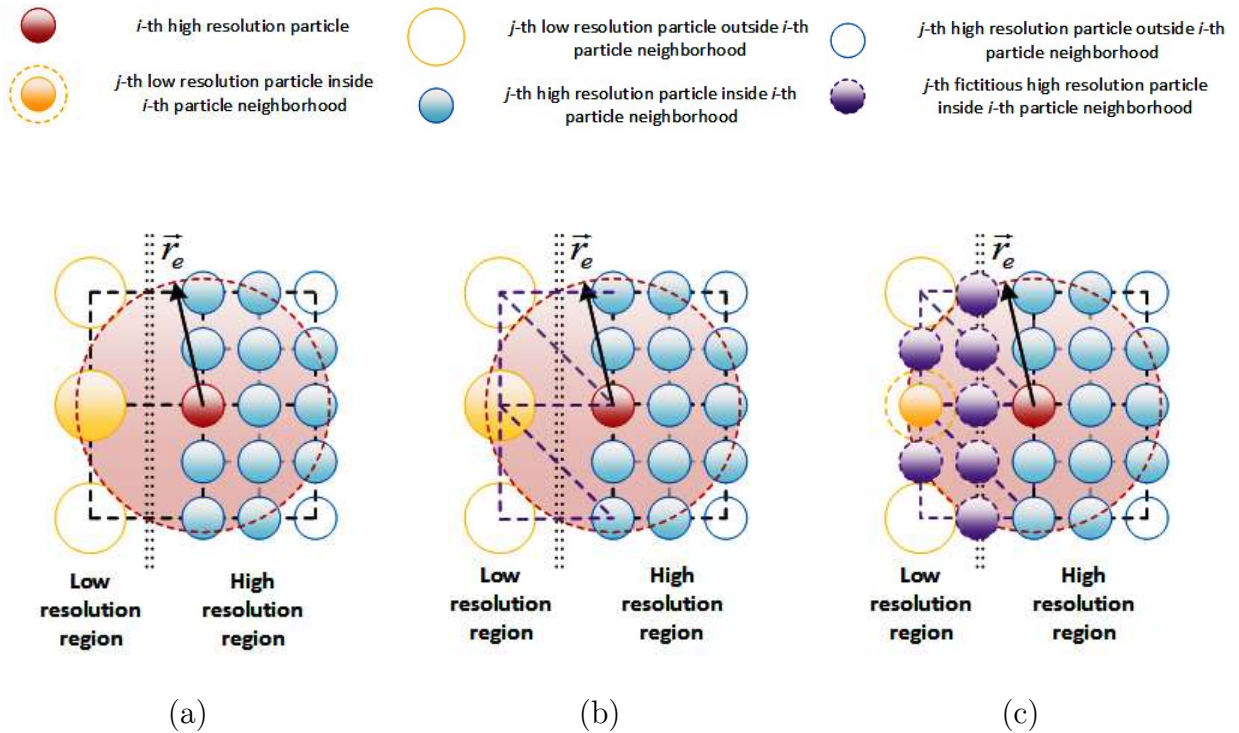
Figure 5.11 – Conceptual scheme of the refinement



Source: figure from the author.

The algorithm adopted to introduce the “fictitious particles” in the border region is illustrated by Figure 5.12. The first step is the triangulation of the grid whose nodes consist in the low-resolution particles and the “high-resolution simplified particles” closer to the border (Figure 5.12-b). Such particles used as vertex of the triangles are henceforth called “reference particles”. Next, the “fictitious particles” are created at the center of the edges of the triangles (Figure 5.12-c). In the final step, the physical properties of the “fictitious particles” are calculated based on an interpolation from the values of the “reference particles”.

Figure 5.12 – Creation of a fictitious particle



Source: figure from the author.

5.5.4 Algorithm to keep the resolution: update of the border particles

As the particles flow from one sub-domain to other sub-domain with a different resolution, when a particle crosses the border of the domains with different resolutions, some treatment should be applied to maintain the resolution within each subdomain.

In the case of the flow from the high-resolution sub-domain to the low-resolution sub-domain, the “high-resolution simplified particles” are converted to low resolution particles as they pass through the border. On the other hand, the “high-resolution non-simplified particles” are simply removed. For the two-dimensional modeling the mass is conserved because, for each converted “simplified particle”, about three “non-simplified particles” are expected to be removed.

In the case of the flow from the low-resolution sub-domain to the high-resolution sub-domain, the “fictitious particles” are converted to high-resolution particles as they cross the border. Meanwhile, as a low-resolution particle pass through the border, it is

converted into a high-resolution particle. For the two-dimensional modeling, the mass is conserved because, for each low-resolution particle converted to a high-resolution particle, about three additional high-resolution particles are created from “fictitious particles”.

5.5.5 Algorithm of the multi-resolution MPS

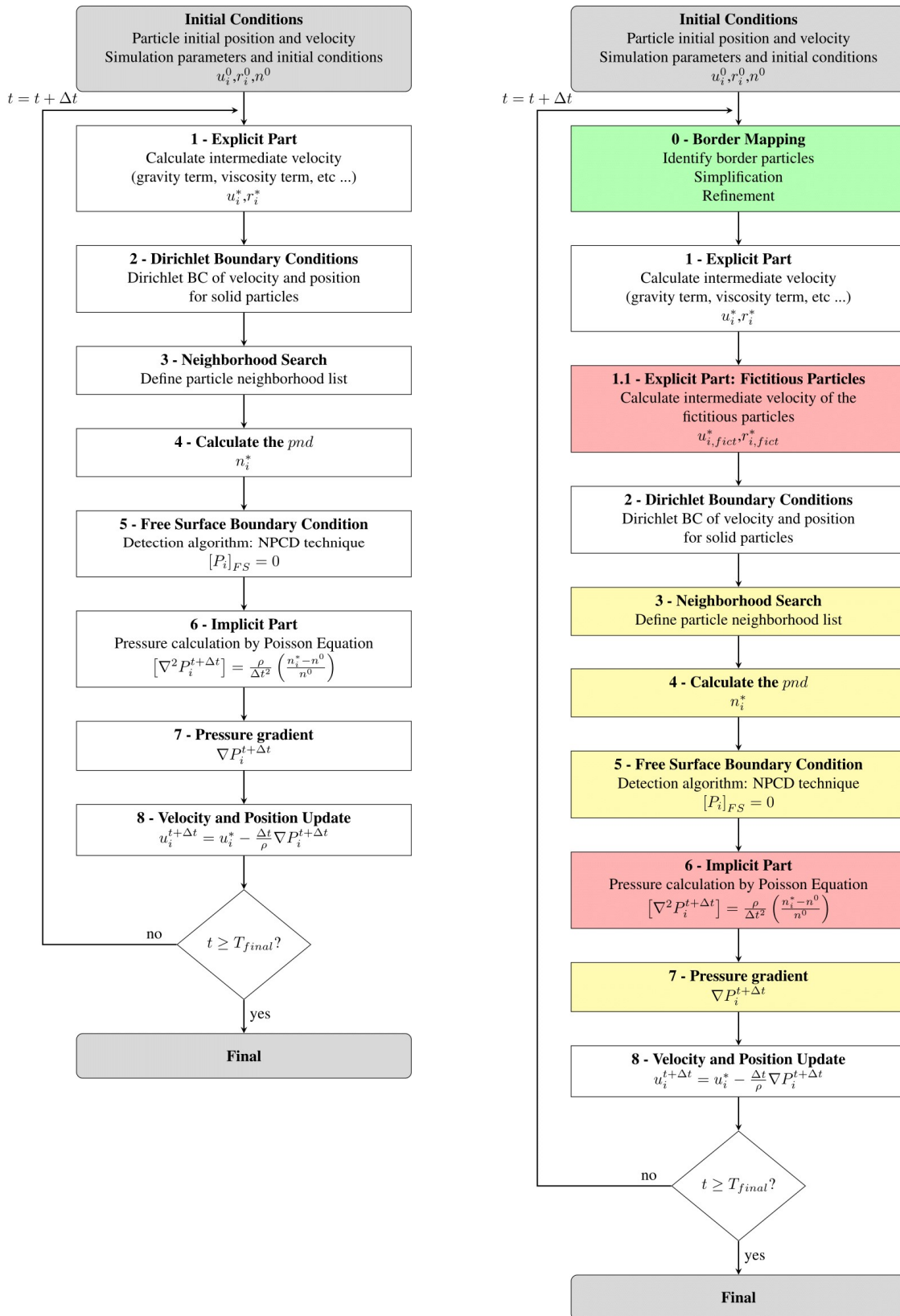
Figure 5.13-b shows the algorithm of the proposed multi-resolution technique. Besides, the algorithm of the single-resolution MPS formulation is shown by Figure 5.13-a to provide a clear picture of the modifications that should be introduced. The main steps of the multi-resolution algorithm are:

- 1) **Initial conditions:** the particle model with the initial conditions of the simulation should be already modeled using the multi-resolution approach, with the initial state of the particles for each sub-domain modeled in its proper resolution. Besides, the boundaries of each sub-domain are represented by a closed polygon and are input data as well.
- 2) **Border-mapping:** except for the case of the simulation’s first time-step, the first step of the border-mapping algorithm is the update of the particles as they flow from one sub-domain to other sub-domain. Updated the particles, the second step of the border-mapping is the simplification and, next, the third step is the refinement or the border particles.
- 3) **Explicit part:** in the explicit part all the terms of the right-hand side of the momentum conservation equation (Eq. 2.2) are estimated, except for the pressure gradient. In the case of the multi-resolution scheme, such contributions should also be calculated for the “fictitious particles”. Further detail about the calculation of the explicit terms for the “fictitious particles” are given in the next sections.

- 4) **Update of the intermediate state of the particles:** The position and velocity of the particles are updated based on the contributions calculated explicitly. Moreover, the neighbor search, the update of the particle number density of the particles and the detection of the free-surface particles are also carried out in this step. These procedures should be carried out for the “fictitious particles” as well.
- 5) **Implicit part:** the matrix of coefficients and the source term vector are defined. In the case of the particles close to the border between sub-domain, the PPE linear system is defined by considering the equivalent particle distribution obtained by the border-mapping technique. Then, the linear system is solved and the pressure in the particles is obtained.
- 6) **Pressure gradient:** the pressure gradient of the particles is then calculated. In the case of the particles close to the border between sub-domain, the pressure gradient is calculated by considering the equivalent particle distribution obtained by the border-mapping technique. Besides, the contribution due the pressure gradient should also be calculated for the “fictitious particles”.
- 7) **Update of the state of particle:** The intermediate state of the particles, which was obtained from the contributions explicitly calculated, is corrected by considering the contribution of the pressure gradient.

The steps from 2 to 7 in the list above are then repeated until the final time of the simulation.

Figure 5.13 – Algorithm of the multi-resolution and single-resolution MPS



(a) Original formulation

(b) Multi-resolution formulation

Source: figure from the author.

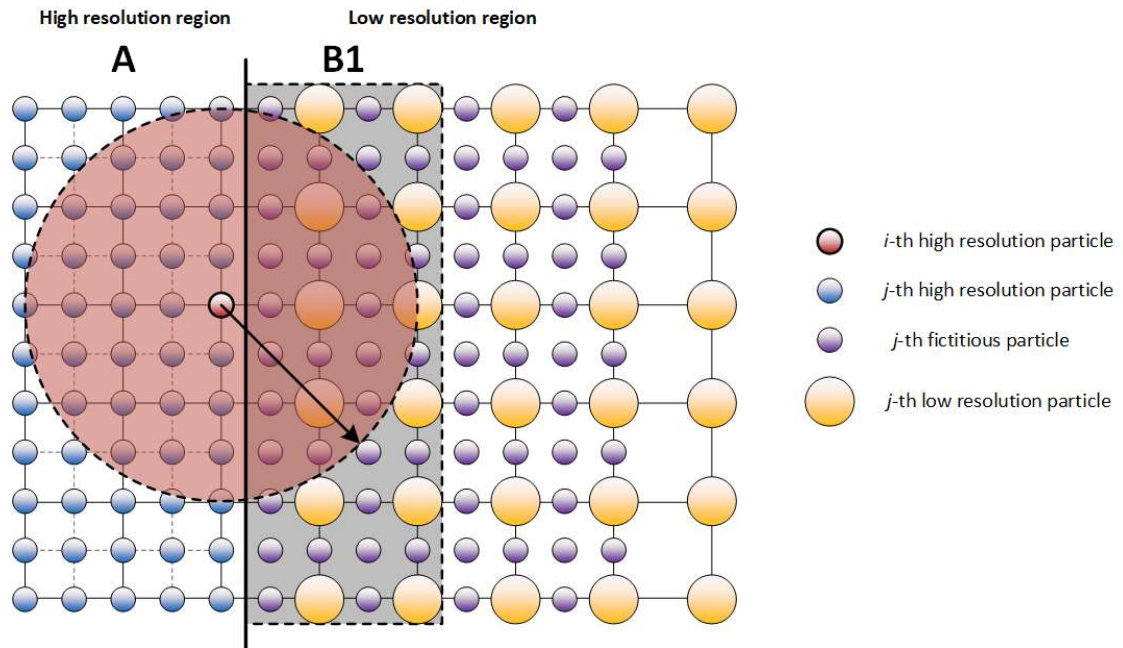
5.5.6 Explicit Part

Figure 5.14-a illustrates the case of a high-resolution particle close to the border and its neighborhood, which is composed by high-resolution particles from the region “A” and low-resolution particles and “fictitious particles” from the region “B1”. After the explicit part of the algorithm, the position and velocity of the high-resolution particles and the low-resolution particles within this compact support are updated to an intermediate state. So, the “fictitious particles” should also be updated to this intermediate state in order to obtain a consistent particle distribution in the border region prior to the calculation of the pressure. Thus, the explicit terms are also calculated for the “fictitious particles” in the region “B1”.

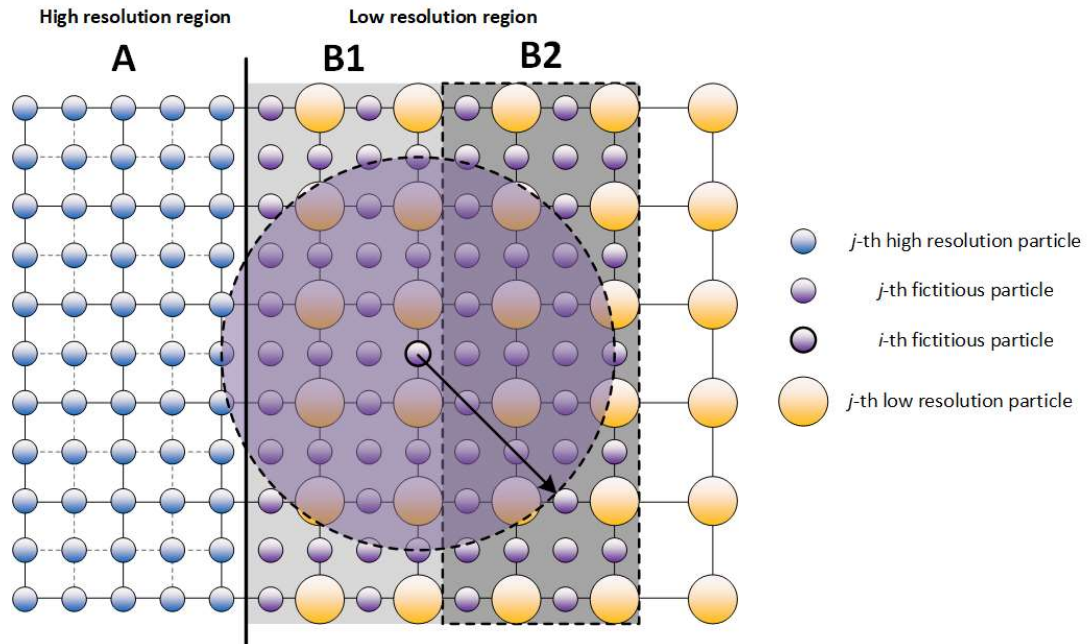
Figure 5.14-b shows the neighborhood of a “fictitious particles” in the region “B1”. As some explicit terms are also calculated by adopting a compact support, an equivalent high-resolution particle distribution must be obtained for the neighborhood of the “fictitious particles” in the region “B1”. Hence, a second layer of “fictitious particles”, in the region “B2” of Figure 5.14-b, is required to the proper calculation of the explicit terms for the “fictitious particles” at the region “B1”. The explicit terms are not calculated for the “fictitious particles” in the region “B2”.

The region “B1” comprises the “fictitious particles” with a distance to the border up to $r_{e,H}$, where $r_{e,HR}$ is the neighborhood radius of the high-resolution particles. The region “B2” comprises the “fictitious particles” with a distance to the border in the range between $r_{e,H}$ and $2 \times r_{e,H}$.

Figure 5.14 – Layers of the border region – Explicit calculation



(a) High-resolution particle close to the border



(b) Fictitious particle in the border first layer

Source: figure from the author.

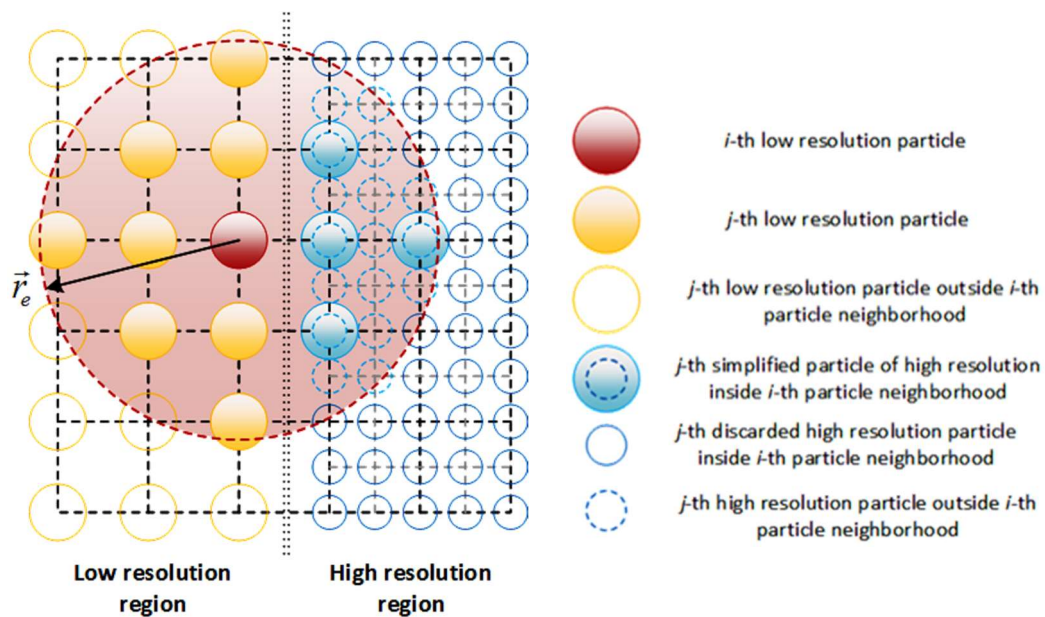
5.5.7 Implicit calculation of pressure

The neighborhood of a low-resolution particle close to the border between sub-domains is depicted by Figure 5.15. Two sets of particles are observed in this neighborhood:

- **Set A:** low-resolution particles,
- **Set B:** high-resolution particles, which are divided into:
 - **Set B1:** “simplified” high-resolution particles,
 - **Set B2:** “non-simplified” high-resolution particles ($B_2 = B \setminus B_1$).

For the calculation of the pressure and the modeling of the numerical operators in this case, the equivalent low-resolution particle distribution is composed by the particles from the set $\{A \cup B_1: |\vec{r}_i - \vec{r}_j| \leq r_e\}$.

Figure 5.15 – Neighborhood of a low-resolution particle close to the border



Source: figure from the author.

So, the particle number density of a low-resolution particle in the border region is given by:

$$[pnd]_i = \sum_{j \neq i} w(\vec{r}_j - \vec{r}_i), \quad (|\vec{r}_j - \vec{r}_i| \leq r_e) \wedge (j \in \{A \cup B_1\}) \quad (5.1)$$

For the linear system of the PPE in the case of a low-resolution border particle, the matrix of coefficients $[A]$ and the solution vector $[B]$ are given by Eq. 5.2 and Eq. 5.3, respectively. The solution vector is given herein based on the original formulation of the source term containing only the particle number density deviation condition. Notwithstanding, the solution vector based on other formulation could be obtained straightforwardly from Eq. 5.3.

$$[A_{ij}] = \begin{cases} -\sum_{k \neq i} w(|\vec{r}_k - \vec{r}_i|), & (i = j) \wedge (|\vec{r}_k - \vec{r}_i| \leq r_e) \wedge (j \in \{A \cup B_1\}) \\ w(|\vec{r}_j - \vec{r}_i|), & (i \neq j) \wedge (|\vec{r}_j - \vec{r}_i| \leq r_e) \wedge (j \in \{A \cup B_1\} \setminus BC) \\ 0, & (i \neq j) \wedge (|\vec{r}_j - \vec{r}_i| > r_e) \\ 0, & (i \neq j) \wedge (|\vec{r}_j - \vec{r}_i| \leq r_e) \wedge (j \in B_2) \end{cases} \quad (5.2)$$

$$[B_i] = -\frac{\rho\delta}{2d\Delta t^2} (pnd_i^* - pnd^0) - \sum_{\substack{k \neq i, \\ k \in (BC \cap \{A \cup B_1\}), \\ |\vec{r}_k - \vec{r}_i| \leq r_e}} P_k w(|\vec{r}_k - \vec{r}_i|) \quad (5.3)$$

where BC is the set of particles containing the free surface particles.

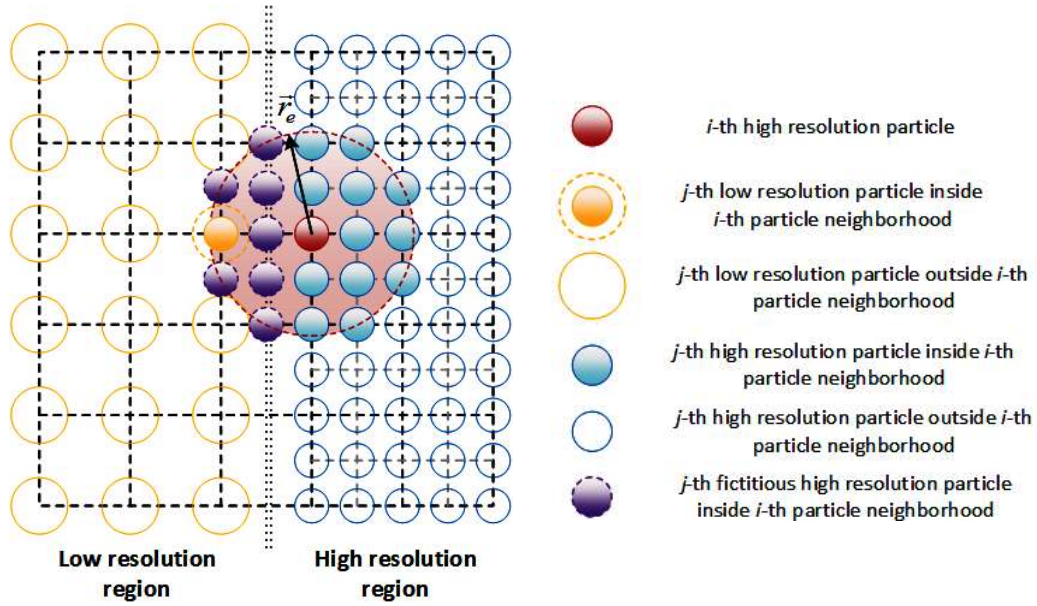
The second term in the right-hand side of the solution vector accounts for the contributions of the free surface particles in the equivalent particle distribution $\{(A \cup B_1) \cap BC: |\vec{r}_i - \vec{r}_j| \leq r_e\}$. The difference between the matrix of coefficients in this case is regarding the contribution of the “non-simplified” high-resolution particles, which is set as zero.

The neighborhood of a high-resolution particle close to the border between sub-domains is depicted by Figure 5.18. In this case, three sets of particles are observed in this neighborhood:

- **Set A:** low-resolution particles,
- **Set B:** high-resolution particles,
- **Set C:** fictitious particles.

For the calculation of the pressure and the modeling of the numerical operators in this case, the equivalent high-resolution particle distribution is composed by the particles from the set $\{A \cup B \cup C: |\vec{r}_i - \vec{r}_j| \leq r_e\}$.

Figure 5.16 – Neighborhood of a high-resolution particle close to the border



Source: figure from the author.

Hence, the particle number density of a high-resolution particle close to the border is given by:

$$[pnd]_i = \sum_{j \neq i} w(|\vec{r}_j - \vec{r}_i|), \quad (j \neq i) \wedge (|\vec{r}_j - \vec{r}_i| \leq r_e) \wedge (j \in \{A \cup B \cup C\}) \quad (5.4)$$

For the linear system of the PPE in the case of a high-resolution border particle, the matrix of coefficients $[A]$ and the solution vector $[B]$ are given by the Eq. 5.5 and Eq. 5.6, respectively.

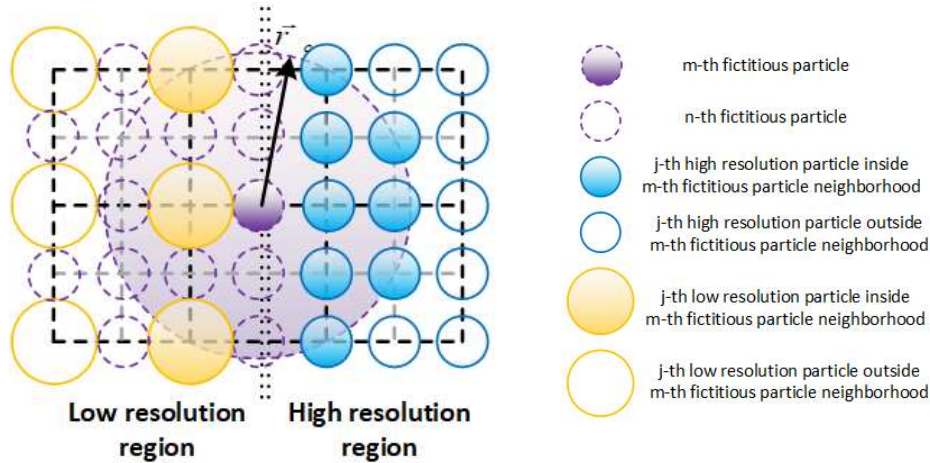
$$[A_{ij}] = \begin{cases} -\sum_{k \neq i} w(|\vec{r}_k - \vec{r}_i|), & (i = j) \wedge (|\vec{r}_k - \vec{r}_i| \leq r_e) \wedge (j \in \{A \cup B \cup C\}) \\ w(|\vec{r}_j - \vec{r}_i|), & (i \neq j) \wedge (|\vec{r}_j - \vec{r}_i| \leq r_e) \wedge (j \in \{A \cup B \cup C\} \setminus BC) \\ 0, & (i \neq j) \wedge (|\vec{r}_j - \vec{r}_i| > r_e) \end{cases} \quad (5.5)$$

$$[B_i] = -\frac{\rho\delta}{2d\Delta t^2} (pnd_i^* - pnd^0) - \sum_{\substack{k \in (BC \cap \{A \cup B \cup C\}), \\ |\vec{r}_k - \vec{r}_i| \leq r_e}} P_k w(|\vec{r}_k - \vec{r}_i|) \quad (5.6)$$

In the matrix of coefficients, the contributions from the fictitious particles that not belong to the free surface should be accounted. Otherwise, in the solution vector, the contribution of the fictitious particles detected as free surface particles should be accounted $\{(A \cup B \cup C) \cap BC: |\vec{r}_i - \vec{r}_j| \leq r_e\}$.

Nevertheless, the fictitious particles do not belong to the set of particles whose pressures are calculated by the PPE linear system, thus their nomenclature as “fictitious”. In fact, the position of the fictitious particles is set in order to obtain an equivalent particle distribution, while their physical properties, such as velocity and pressure, are interpolated from the particles nearby. The set of high-resolution particles and low-resolution particles in the compact support which is used for the interpolation of the fictitious particles physical parameters is defined as the **Set D** of particles $\{D: (j \in A \cup B) \wedge |\vec{r}_j - \vec{r}_m| \leq r_c\}$, which is depicted by Figure 5.17.

Figure 5.17 – Neighborhood of a “fictitious particle” close to the border



Source: figure from the author.

The **set D** comprises particles from the sets A and B within the interpolation radius (r_c) of a given fictitious particle. Then, the pressure P_m of the m -th fictitious particle is defined as the interpolation of the pressure P_j of the j -th particles of the set D, as follows:

$$P_m = \sum_j \alpha_{mj} P_j, \quad (m \in C) \wedge (j \in D) \quad (5.7)$$

where α_{mj} is coefficient of interpolation of the j -th real particle in relation to the m -th fictitious particle. In the present work, a simple formulation based on the weight function and the area of the particles from the set D is adopted to define α_{mj} :

$$\alpha_{mj} = \frac{A_j w(|\vec{r}_m - \vec{r}_j|)}{\sum_l A_l w(|\vec{r}_m - \vec{r}_l|)}, \quad (j, l \in D) \wedge (m \in C) \quad (5.8)$$

where A_j is the area of the j -th particle of the set D and $\sum_l A_l w(|\vec{r}_m - \vec{r}_l|)$ is the summation of the product between the area and the weight of all the real particles in the interpolation compact support of the m -th fictitious particle. Notwithstanding, higher order interpolation schemes could be adopted to estimate the coefficient α_{mj} in order to achieve improved accuracy.

By replacing the Eq. 5.7 in the Eq. 5.5 and the Eq. 5.6, the final form of the matrix of coefficients (Eq. 5.9) and the solution vector (Eq. 5.10) of the PPE linear system for the high-resolution particles close to the border is obtained:

$$[A_{ij}] = \begin{cases} -\sum_{k \neq i} w(|\vec{r}_k - \vec{r}_i|) - \sum_m w(|\vec{r}_m - \vec{r}_i|), & (i = j) \dots \\ & (k \neq i) \wedge (|\vec{r}_k - \vec{r}_i| \leq r_e) \dots \\ & (m \in C) \\ w(|\vec{r}_j - \vec{r}_i|) + \sum_m w(|\vec{r}_m - \vec{r}_i|) \alpha_{mj}, & (i \neq j) \wedge (|\vec{r}_j - \vec{r}_i| \leq r_e) \dots \\ & (m \in C) \wedge (j \in D \setminus BC) \\ w(|\vec{r}_j - \vec{r}_i|), & (i \neq j) \wedge (|\vec{r}_j - \vec{r}_i| \leq r_e) \wedge (j \notin L) \\ \sum_m w(|\vec{r}_m - \vec{r}_i|) \alpha_{mj}, & (i \neq j) \wedge (|\vec{r}_j - \vec{r}_i| > r_e) \dots \\ & (m \in C) \wedge (j \in D \setminus BC) \\ 0, & (i \neq j) \wedge (|\vec{r}_j - \vec{r}_i| > r_e) \wedge (j \notin L) \end{cases} \quad (5.9)$$

$$[B_i] = -\frac{\rho \delta}{2d\Delta t^2} (pnd_i^* - pnd^0) - \sum_{\substack{k \neq i, \\ k \in (BC \cap \{A \cup B\}), \\ |\vec{r}_k - \vec{r}_i| \leq r_e}} P_k w(|\vec{r}_k - \vec{r}_i|) - \sum_{\substack{m \in C, \\ |\vec{r}_m - \vec{r}_i| \leq r_e}} \sum_{j \in D \cap BC} P_j \alpha_{mj} w(|\vec{r}_m - \vec{r}_i|) \quad (5.10)$$

5.6 RESULTS

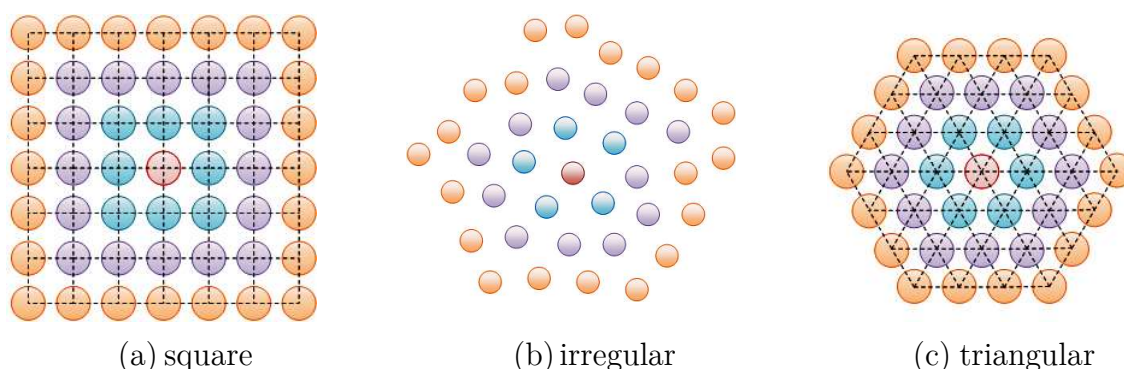
Aiming to show the effectiveness of the multi-resolution MPS method by “border mapping” technique, the results of the test and the validation are organized as follows:

- First, a study regarding the statistical distribution of the distance between neighbor particles is presented, as its results will guide the development of the simplification and the refinement algorithms.
- Next, details about the implementation and the results from the refinement and simplification techniques are presented.
- In the final sections, the multi-resolution technique is evaluated considering its ability to correctly calculate the pressure, ensure the mass conservation and decrease the simulation processing time.

5.6.1 Concepts on the particle distribution in MPS simulations

In the MPS method, the particles are distributed in a unstructured grid nodes almost uniformly spaced between each other. During a simulation, three typical arrangements of the particle distributions, as shown in Figure 5.18, might occur.

Figure 5.18 – Sketch of different typical particle distributions



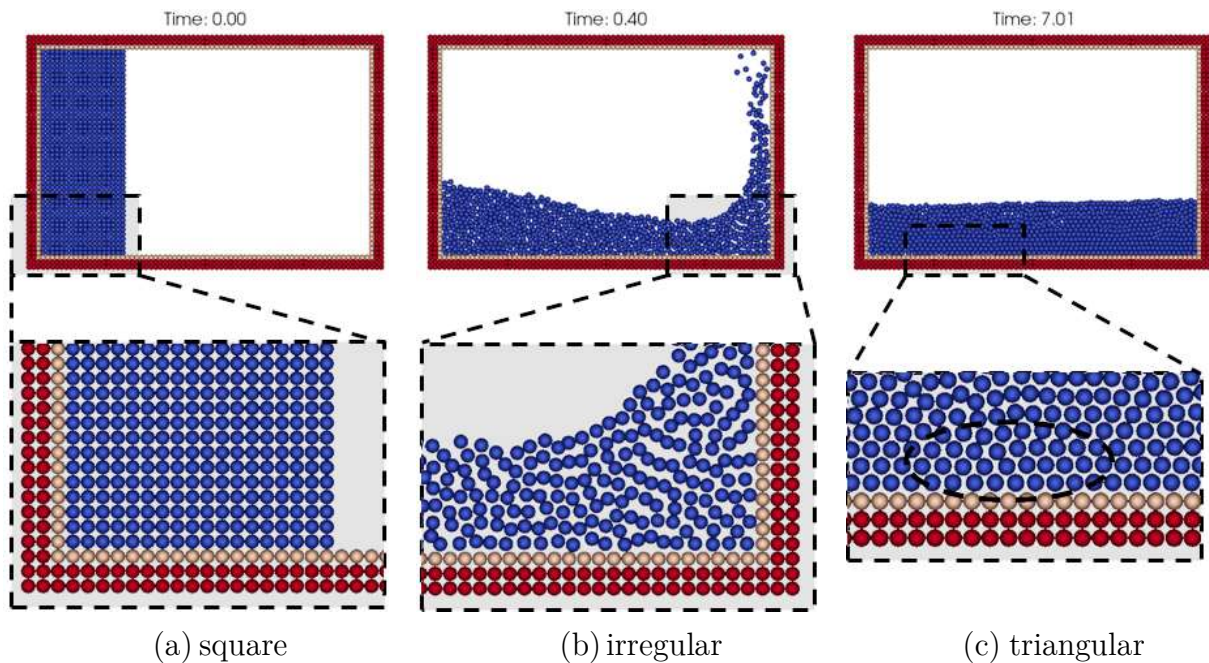
Source: figure from the author.

Each particle has multiple “layers” of neighboring particles, from the closest to the farthest, the first layer (blue), the second layer (purple) and the third layer (orange)

of neighboring particles are illustrated in Figure 5.18. The first layer comprises particles with distance between each other around l_0 , the second layer around $2 \times l_0$, the third layer around $3 \times l_0$ and so on until the dimension of the neighborhood radius.

Figure 5.19 shows these three different particle distributions in a MPS simulation of a two-dimensional Dam-Break case. The “square” arrangement (Figure 5.18-a, Figure 5.19-a) is usually adopted as initial condition of the simulations as it is easy to generate the initial particle grid. However, the square arrangement is an unstable condition. As the simulation advances and highly violent free surface displacements occur, the particle distribution becomes irregular (Figure 5.18-b, Figure 5.19-b). The third typical arrangement is the “triangular” arrangement (Figure 5.18-c, Figure 5.19-c), which is a stable condition for the particles and it is reached as the particles loose kinetic energy.

Figure 5.19 – Different arrangements on a Dam-Break simulation

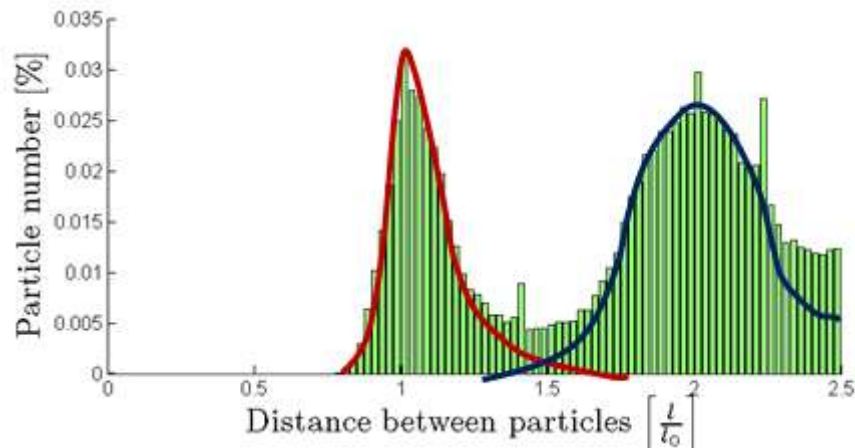


Source: figure from the author.

As the distance between neighbor particles are well defined for the square and triangular arrangements, the refinement and simplification algorithms are relatively simple for these cases. However, the case of the irregular arrangement is much more

complex. Figure 5.20 gives a histogram containing the distribution of the distance to the neighboring particles of the first and second layers for the Dam-Break case shown in Figure 5.19.

Figure 5.20 – Histogram of the distance between neighbor particles



Source: figure from the author.

The two peaks in the histogram, at l_0 and at $2l_0$, are related to the average distance between the first layer and the second layer of neighbor particles, respectively. The distribution related to the first layer of neighbors (red line) presents a narrower bandwidth than the distribution related to the second layer of neighbors (blue line), which indicates a larger deviation in relation to the average distance.

The present analysis was focused only on the distribution related to the first and the second layers of neighbor particles because the ratio between the low-resolution and high-resolution particles to be adopted by the border-mapping proposal is 1:2. For the simplification and refinement algorithms, it is useful to define the upper and lower limits of distance between particles of the two first layers of neighbor particles.

The case of the lower limit of the first layer of neighbor is clear, as no pair of particles with distance lower than $0.75l_0$ was registered in Figure 5.20. On the other hand, there is a range between $1.25l_0$ and $1.75l_0$ in which the distributions of the first layer and the second layer of neighbors overlap each other. So, pairs of particles with distance between $1.25l_0$ and $1.75l_0$ could not be assigned straightforwardly as the

neighbors of the first or the second layer. In this issue lies the main challenge for the development of the refinement and simplification algorithms.

5.6.2 Simplification algorithm

In the simplification algorithm, an equivalent low-resolution distribution should be obtained from a high-resolution distribution. The simplification of the particle grid is achieved by the classification of the high-resolution particles into “simplified particles” and “non-simplified particles”. For such purpose, two different algorithms were evaluated. The first algorithm was based solely on the distance between the particles. The second algorithm linked particles of the first layer of neighbors and performed the simplification by set operations.

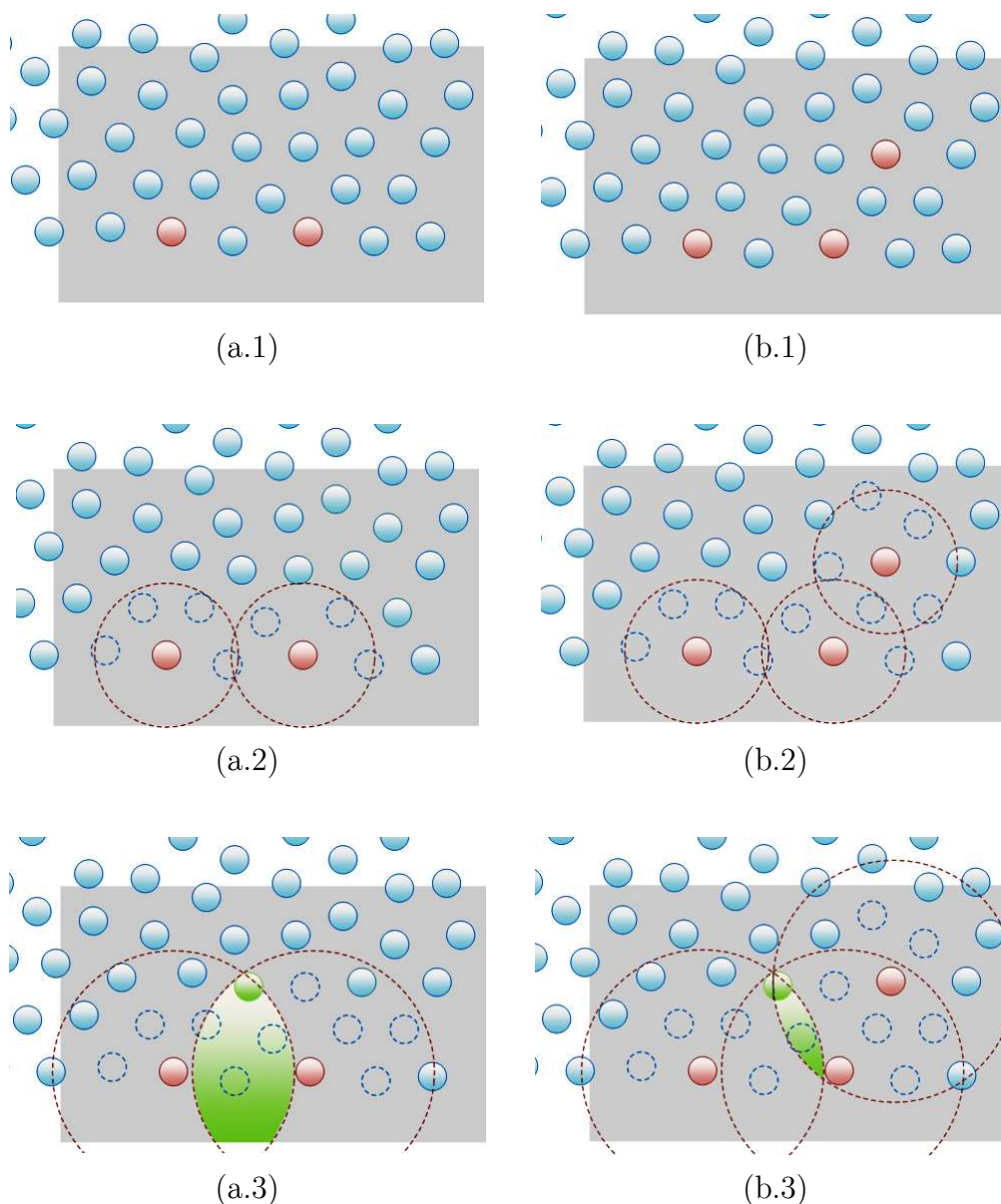
The process of the first algorithm is illustrated in Figure 5.21. Depending on the geometry of the border between the sub-domain, the simplification process should consider two or three “reference particles”. In the border-mapping technique, the low-resolution particles closer to the border must be adopted as the first set of reference particles. So, the cases of two reference particles and three reference particles are presented side-by-side in Figure 5.21-a.

The first step of the algorithm (Figure 5.21-b) consists in the removal of the first layer of neighbor particles, which are the particles that have a distance to the reference particles lower than $1.5l_{0,H}$. This distance is equivalent to the low-resolution lower limit of $0.75l_{0,LR}$. Such particles are immediately classified as “non-simplified particles”.

In the second step of the algorithm (Figure 5.21-c), the next “simplified particle” is defined among the set of remaining particles based on the intersection of the particles with distance to the reference particles lower than $1.75l_{0,LR}$. Next, the newly found “simplified particle” is adopted as “reference particle” for the next iteration of

the algorithm. The algorithm is repeated until all the particles of the high-resolution border region are classified into “non-simplified” and “simplified” particles.

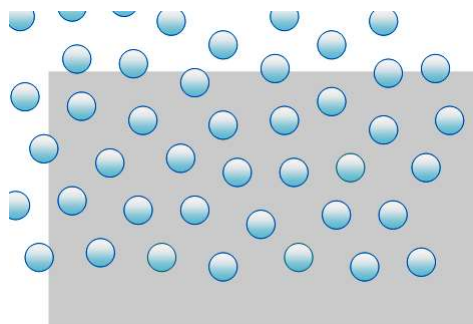
Figure 5.21 – Algorithm 1 of simplification – distance between particles



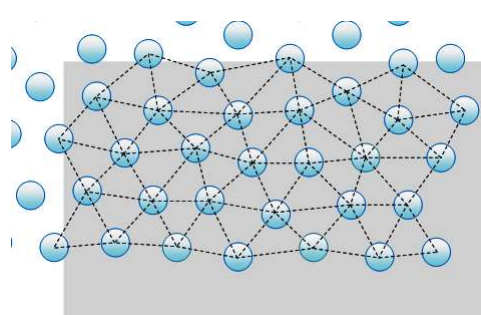
Source: figure from the author.

As the upper limit of the distance between particles in the first layer of neighbors is not well defined, multiple particles were found as candidates to the next “simplified particle” after the second step. In such cases, it was difficult to define a suitable criterion based only on the distance between the particles. Then, a second algorithm was developed for the simplification, which is presented by Figure 5.22.

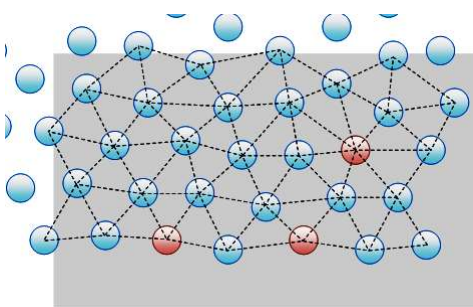
Figure 5.22 – Algorithm 2 of simplification: set operations



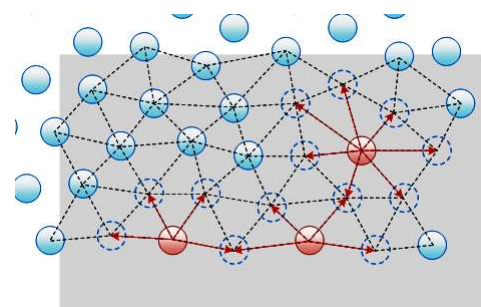
(a) Initial condition



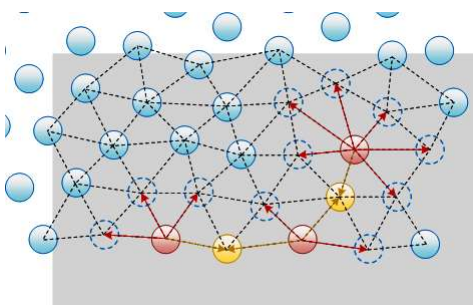
(b) Triangulation



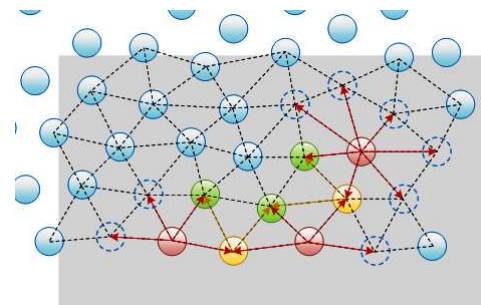
(c) Reference particles



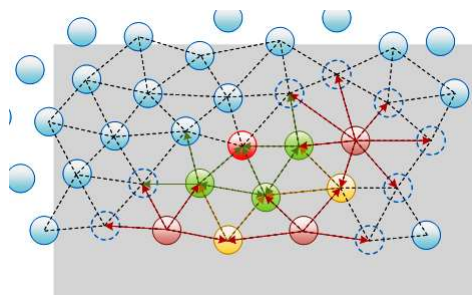
(d) Remove the first layer of neighbors of the reference particle



(e) Common neighbors of the first layer of the reference particle



(f) Common neighbor between reference particles and the particles found in (e)



(g) Next simplified particle

Source: figure from the author.

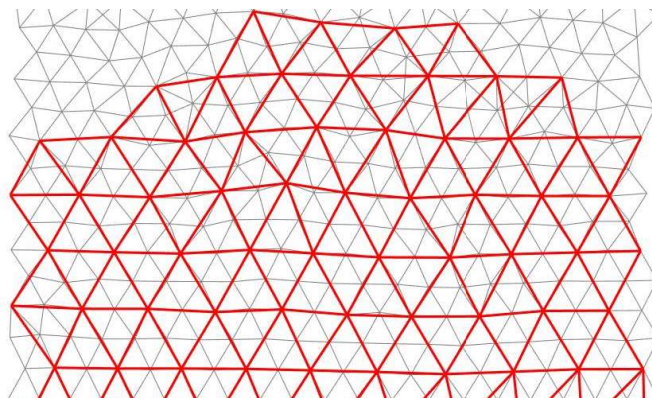
The second algorithm for the simplification is based on set operations to define the next “simplified particles”. Given a set of high-resolution particles in the border between the sub-domains (Figure 5.22-a), the first step consists in the triangulation of the particle grid in order to define the set of neighbor particles of the first layer of neighbors (Figure 5.22-b). Then, the remaining steps of the algorithm are entirely performed based on the list containing the set of neighbor particles.

At first, the first layer of neighbors of the reference particles are classified as “non-simplified” particles (Figure 5.22-d). Among such particles, those which are neighbors of the first layer of more than one reference particle are identified (yellow particles from Figure 5.22-e). Next, the particle neighboring both a reference particle (dark red) and a yellow particle are identified (green particles of Figure 5.22-f). Finally, the next “simplified” particle is found as the particle that is neighbor of all the green particles found in the last step. Such as in the previous algorithm, the newly found “simplified particle” is adopted as “reference particle” for the next iteration of the algorithm. The algorithm is repeated until all the particles of the high-resolution border region are classified into “non-simplified” and “simplified” particles.

Although this algorithm seems to be overly complex because all the set operations, its main concept is quite simple: it aims to find a high-resolution particle in the second layer of neighbors of all the considered reference particles, but this particle could not belong to the first layer of neighbors of a reference particle as well.

As an example, Figure 5.23 presents the result of this second simplification algorithm applied for the grid of a MPS simulation of still water in a rectangular tank. The grid in black line was obtained after the final step of the simulation and both triangular and irregular particle distributions could be observed at the bottom-half and the top-half of the figure, respectively. Then, the equivalent low-resolution grid, which is represented by the red lines, is obtained by adopting the simplification algorithm.

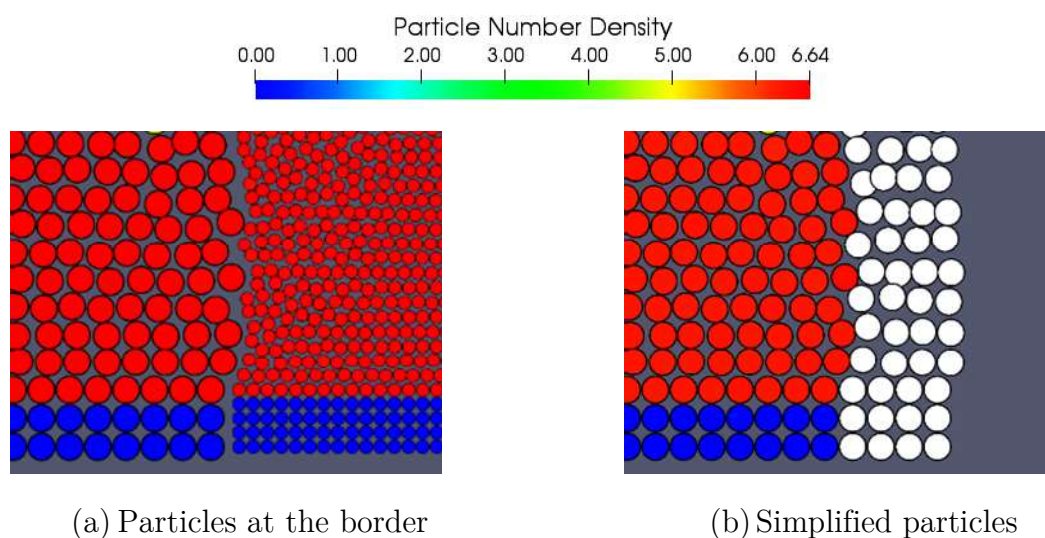
Figure 5.23 – Simplification of a particle grid from a MPS simulation



Source: figure from the author.

The color scale of Figure 5.24 shows the particle number density calculated in the border region of a multi-resolution simulation for the case of still water in a rectangular tank. Among the high-resolution particles in the border, the equivalent low-resolution particle distribution is represented by the “simplified” particles (the white particles at Figure 5.24-b). In this result, the particle number density calculated for the low-resolution particles close to the border is consistent, which indicates that the particle distribution of the “simplified” particles might be consistent as well.

Figure 5.24 – Simplified particles in the border of a MPS simulation



(a) Particles at the border

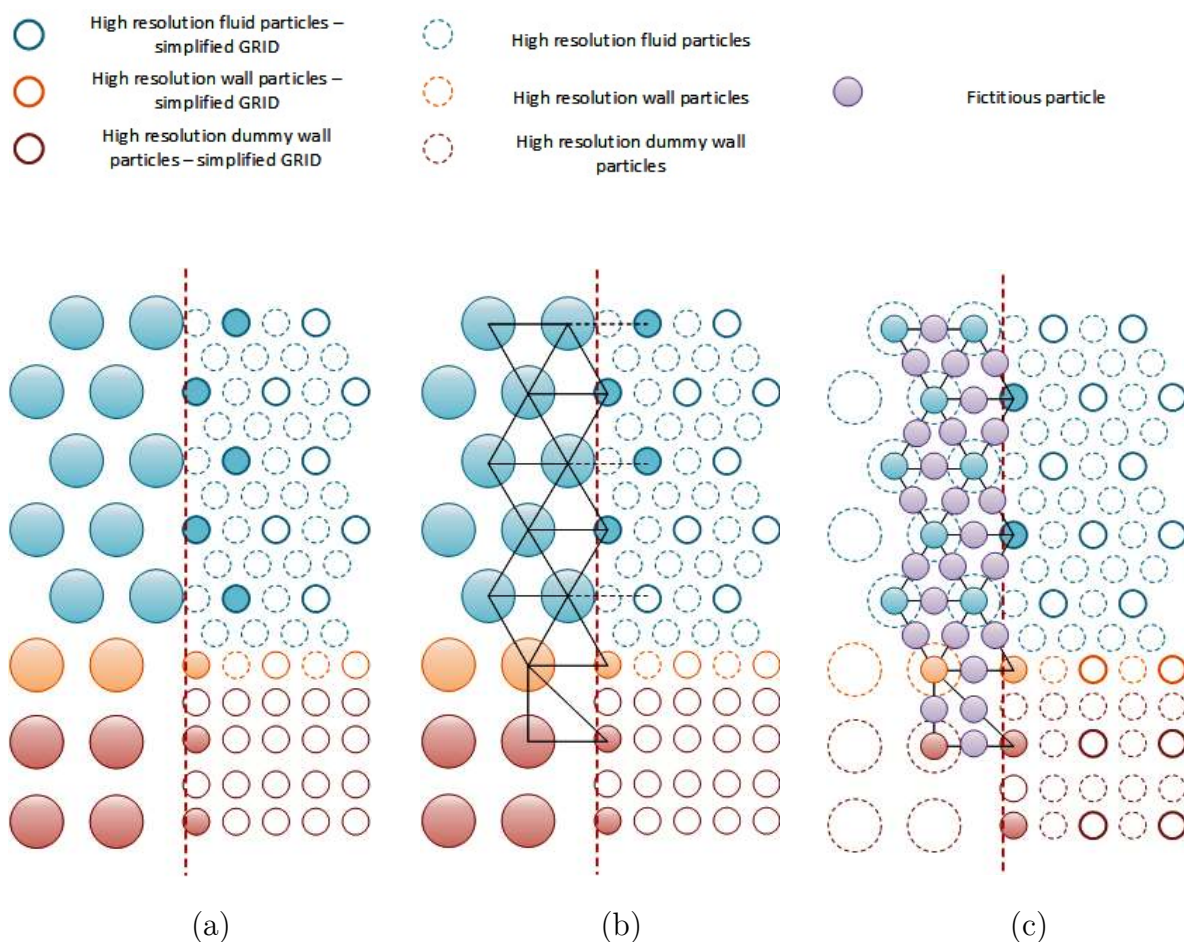
(b) Simplified particles

Source: figure from the author.

5.6.3 Refinement algorithm

In the refinement algorithm, an equivalent high-resolution distribution should be obtained from a low-resolution distribution. The refinement of the particle grid is achieved by the creation of the so-called “fictitious particles”. The algorithm for the refinement of the low-resolution particles close to the border is illustrated by Figure 5.25.

Figure 5.25 – Refinement algorithm



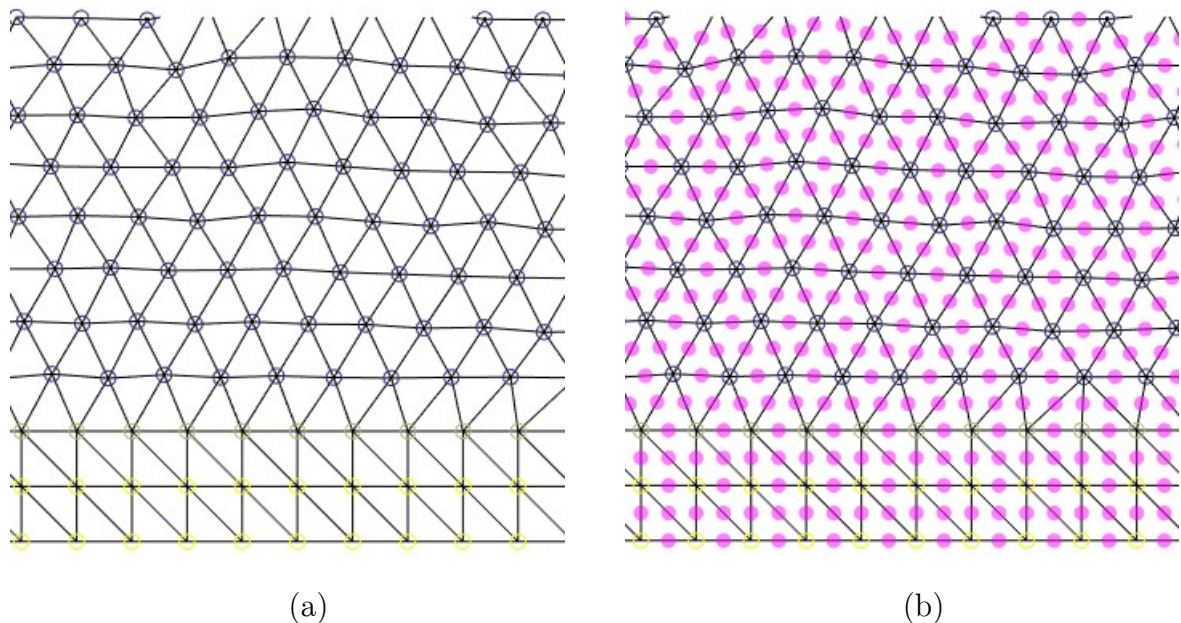
Source: figure from the author.

In Figure 5.25-a, the colored particles indicate the “reference particles” of the refinement algorithm, while the white particles are disregarded. The set of “reference particles” consists in the low-resolution particles and the high-resolution “simplified particles” that should be identified by the simplification algorithm prior to the

refinement. Next, the reference particles are triangulated (Figure 5.25-b) and the “fictitious particles” should be created in the center of the edges of each triangle (Figure 5.25-c).

As an example, Figure 5.26 presents the result of the refinement algorithm applied for the grid of a MPS simulation of still water in a rectangular tank, same case previously presented by Figure 5.23. The grid in black line was obtained after the final step of the simulation and the triangular, irregular and square particle distributions could be observed at the figure. Then, the equivalent high-resolution grid is obtained by the creation of the “fictitious particles” (pink particles in Figure 5.26-b).

Figure 5.26 – Refinement of a particle grid from a MPS simulation

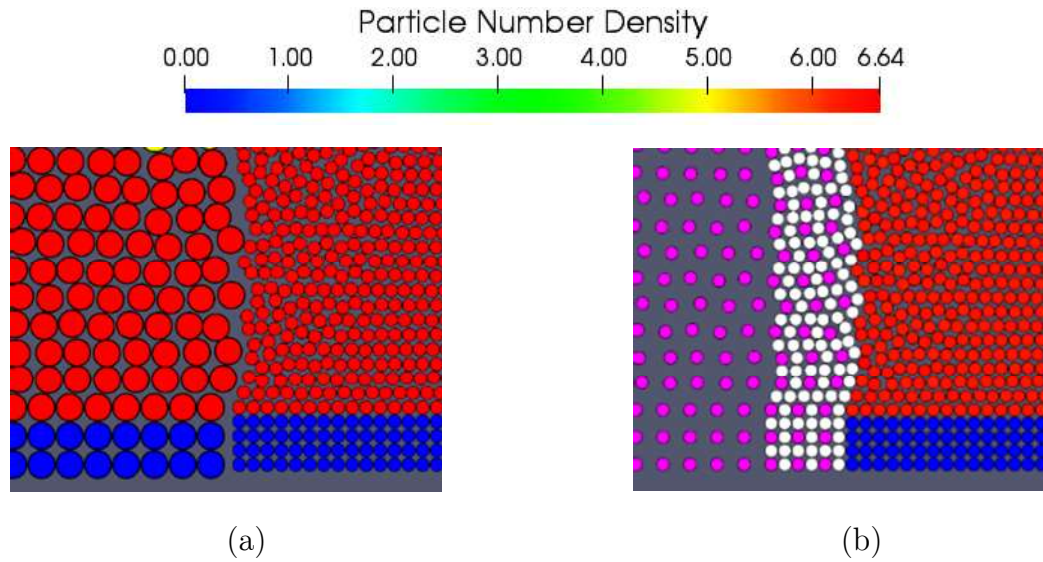


Source: figure from the author.

The color scale of Figure 5.27 shows the particle number density calculated in the border region of a multi-resolution simulation for the case of still water in a rectangular tank, the same case previously presented by Figure 5.24. The equivalent high-resolution particle distribution in the border region is represented by the “fictitious particles” (white particles at Figure 5.27-b) and the low-resolution particles (pink particles at Figure 5.27-b). In this result, the particle number density calculated

for the high-resolution particles close to the border is consistent, which indicates that the particle distribution of the “fictitious particles” might be consistent as well.

Figure 5.27 – Fictitious particles in the border of a MPS simulation

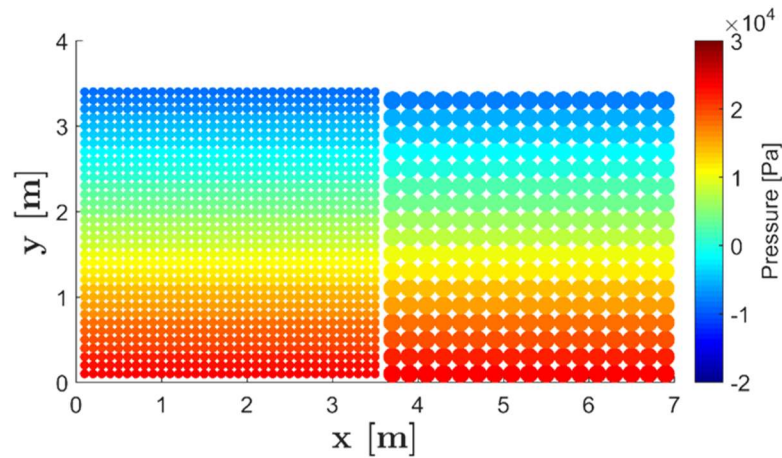


Source: figure from the author.

5.6.4 Pressure calculation

The focus of the present section is to evaluate the calculation of the pressure in the border region by adopting the proposed scheme. As a first simple test, a regular grid with square particle distribution of the case of still water in a rectangular tank is investigated. The tank is divided in the half: the left half is modeled in high-resolution and the right half is modeled in low-resolution. As a neighborhood radius of $r_e = 2.1l_0$ is adopted, the two most external layers of particles are set as boundary particles and the hydrostatic pressure profile are assigned to them. Then, the linear system of the PPE is solved. The pressure profile for this simple case is presented by Figure 5.28 and the results obtained were qualitatively in agreement with the hydrostatic pressure field.

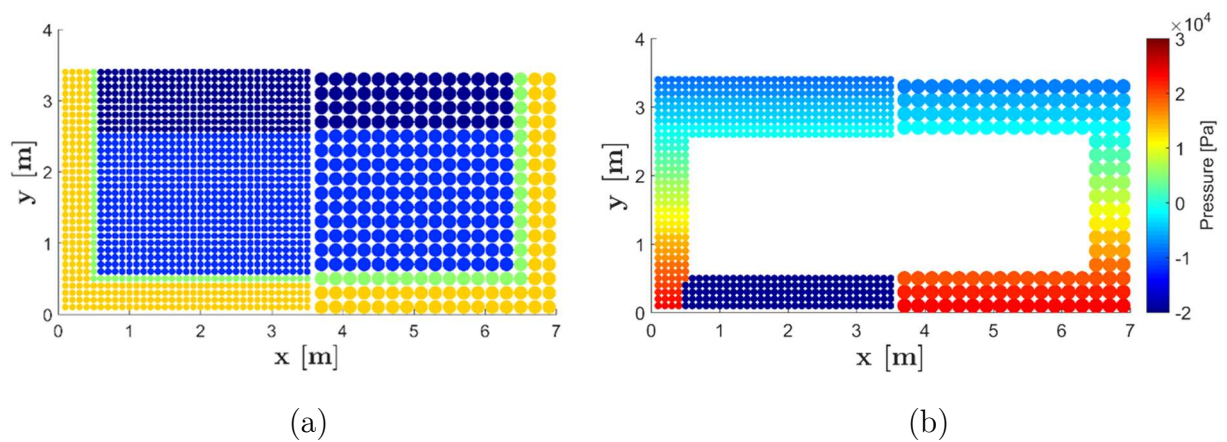
Figure 5.28 – Pressure field of a hydrostatic case



Source: figure from the author.

In order to introduce an additional level of complexity, by adopting the same square particle distribution, the boundary conditions of the numerical model are modified. For this case, the materials of the particles are shown by Figure 5.29-a, and the modified pressure boundary condition is shown by Figure 5.29-b. The hydrostatic pressure profile is attributed to the most external layer of particles, except by the bottom of the tank in the high-resolution sub-domain, where a negative pressure is imposed (Figure 5.29-b).

Figure 5.29 – Initial conditions of the test case

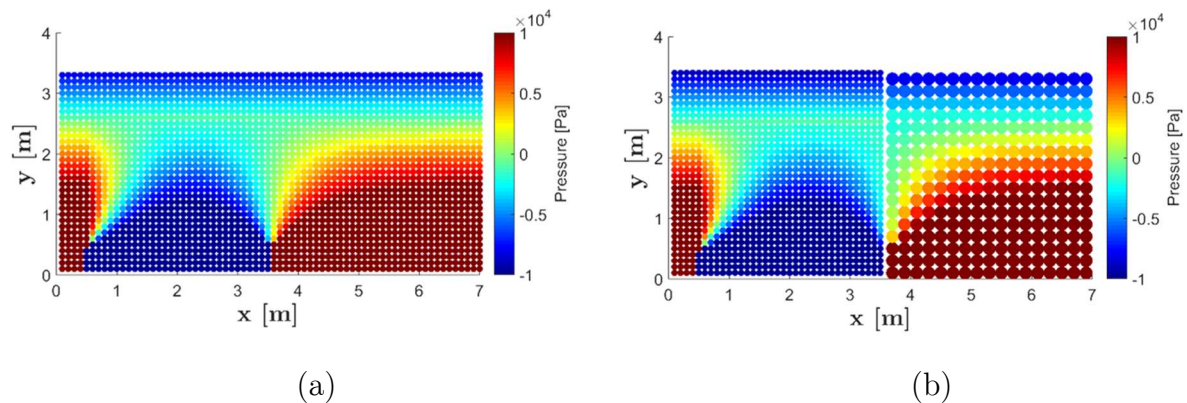


Source: figure from the author.

In addition to this, a similar case but with entire domain modeled using high-resolution particles. While the multi-resolution case has 153,000 particles, the single resolution case has 245,000 particles.

The pressure distribution obtained in both cases is presented by Figure 5.30. The pressure profile obtained in the single resolution and the multi-resolution were consistent and agreed well qualitatively. Besides, due to the difference in the number of particles of each model, the solution of the PPE linear system of the multi-resolution test case was more than 6 times faster than that for the single resolution model. The same hardware was used for the computations of both cases.

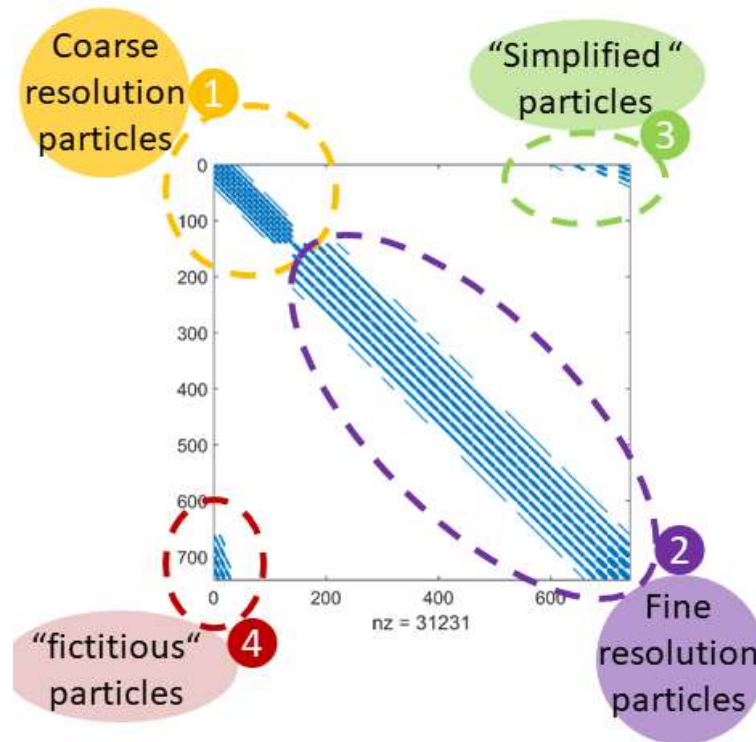
Figure 5.30 – Pressure distribution of the test case: single resolution case and multi-resolution case



Source: figure from the author.

Another interesting aspect of the pressure calculation that worths mentioning is the configuration of the matrix of coefficients of the PPE in the multi-resolution simulation. For the case of Figure 5.28, the matrix of coefficients of the PPE linear system is presented by Figure 5.31. The colored points in the square matrix of the Figure 5.31 are related to the non-zero elements of the matrix of coefficients.

Figure 5.31 – Non-zero elements of the PPE matrix of coefficients



Source: figure from the author.

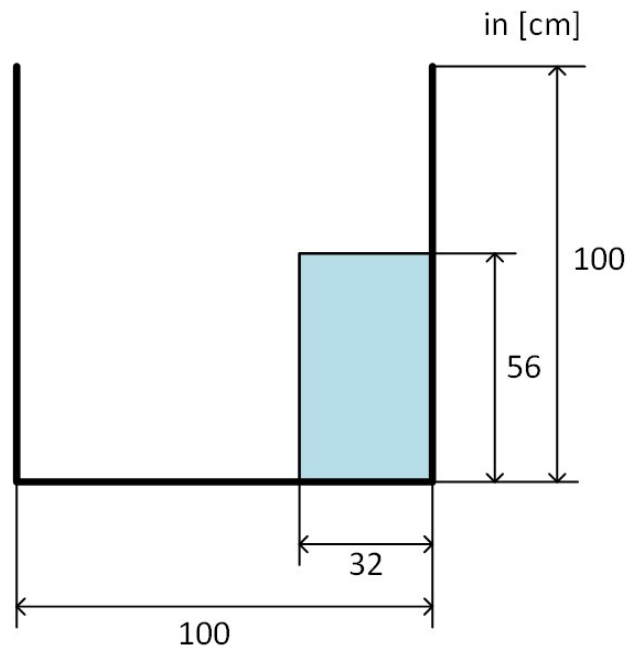
As previously mentioned, the PPE linear system in the MPS method has a sparse matrix in which the non-zero elements are concentrated in its diagonal. In the case of the multi-resolution scheme, the diagonal of the matrix shows the non-zero elements related to pairs of particles with the same resolution. The smaller portion of non-zero elements in the top-left corner (①) are related to the low-resolution particles and the larger portion of non-zero elements in the bottom-right corner (②) are related to the high-resolution particles. In the case of the multi-resolution scheme, non-zero elements that relate particles with different resolutions are observed outside the main diagonal. In the top-right corner (③) are the non-zero elements related to the high-resolution “simplified particles” while in the bottom-left corner (④) are the non-zero elements related to the “fictitious particles”.

5.6.5 Mass conservation

In the sections 5.6.2 and 5.6.3, the effectiveness of the simplification and refinement algorithms was assessed based on the consistency of the equivalent particle distribution and the particle number density calculated in the border of high and low resolution domains for the case of a still water rectangular tank. Notwithstanding, if particles flow from one sub-domain to another, the refinement and simplification affect the mass of the system as particles are generated and removed in the border. So, the aspect of the mass conservation in the multi-resolution technique is addressed in the present section.

The test case in this section is a two-dimensional Dam Break case. The model configuration and its main dimensions are presented by Figure 5.32.

Figure 5.32 – Dimensions of the Dam Break test case

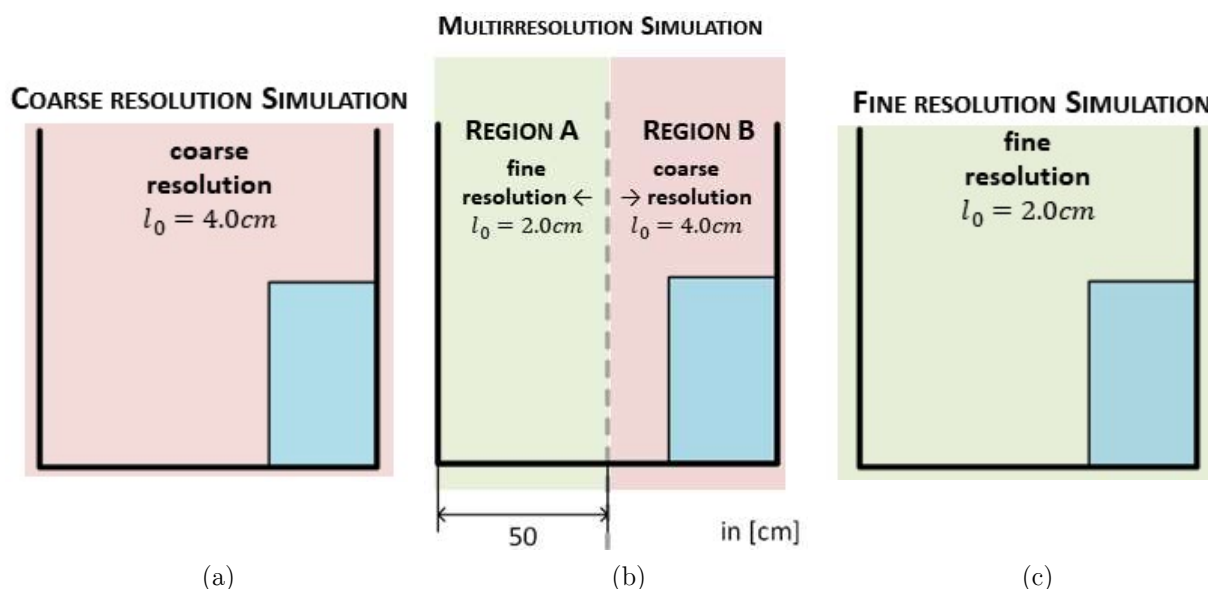


Source: figure from the author.

Three different cases are then simulated: a multi-resolution case in which the fluid column is initially modeled by using low-resolution particles and the border between the sub-domains is placed in the center of the tank (Figure 5.33-b). The mass

of the multi-resolution model are compared to those of two single resolution models: one with entire computational domain modeled in low-resolution (Figure 5.33-a) and other with the entire computational domain modeled in high-resolution (Figure 5.33-c).

Figure 5.33 – Division of the computational domain – Dam Break case

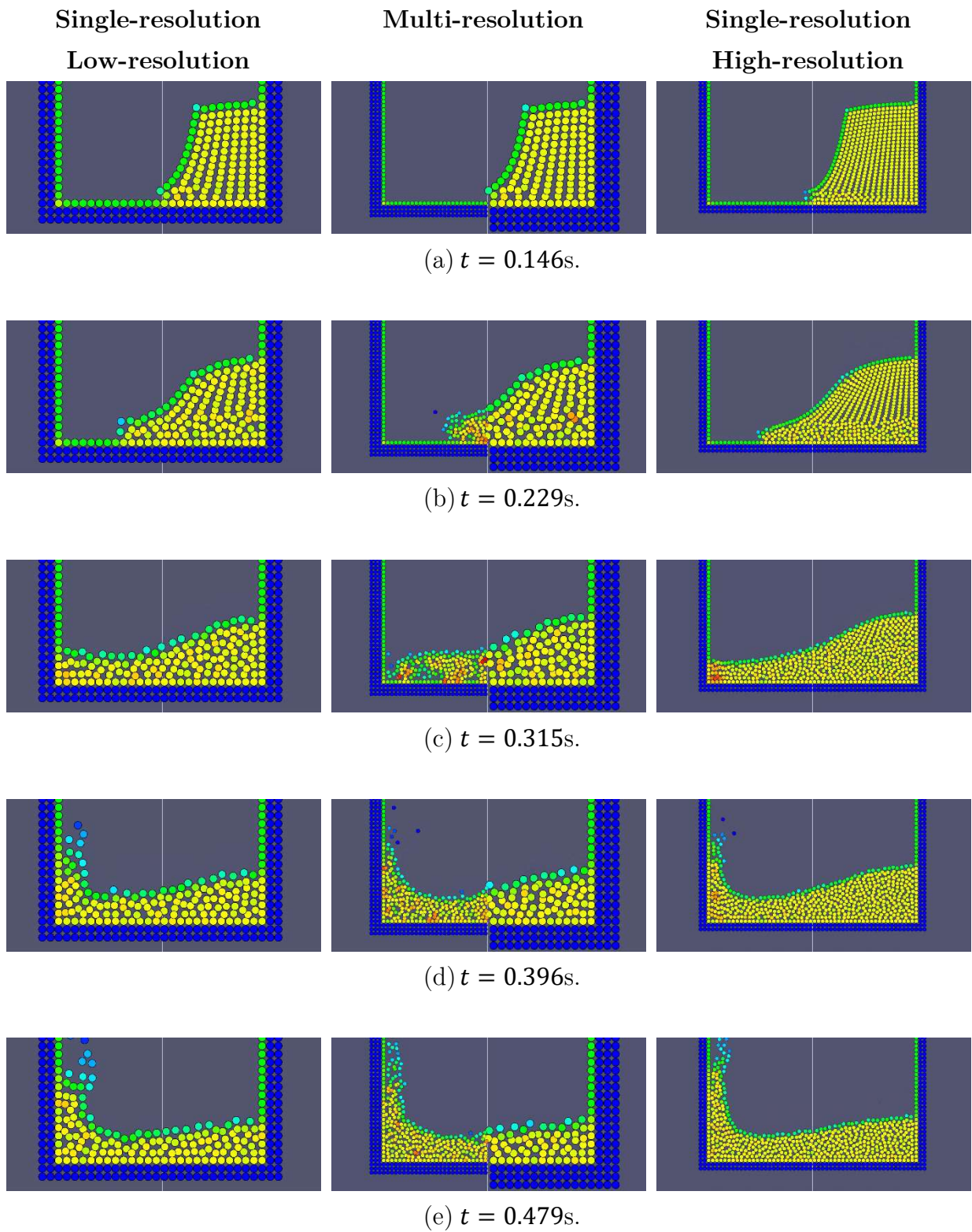


Source: figure from the author.

Figure 5.34 shows snapshots of the MPS simulation of these three cases side-by-side. The left column shows the single-resolution/low-resolution simulation, the center column shows the multi-resolution simulation and the right column shows the single-resolution/high-resolution simulation. The color scale of the particles indicates the particle number density, with the free-surface particles colored green, the inner fluid particles colored yellow and the dummy particles in blue.

In the multi-resolution simulation, as the wave front of water column reaches the border between the sub-domain, the “fictitious particles” are converted into high-resolution particles and the low-resolution particles are converted into high-resolution particles as well. In general, the behavior of the flow is qualitatively similar between the three simulations. The distribution of the particle number density in the high-resolution sub-domain of the multi-resolution simulation is not properly smooth (Figure 5.34-c) and demands further investigation.

Figure 5.34 – Snapshots of the MPS simulation – Dam Break case

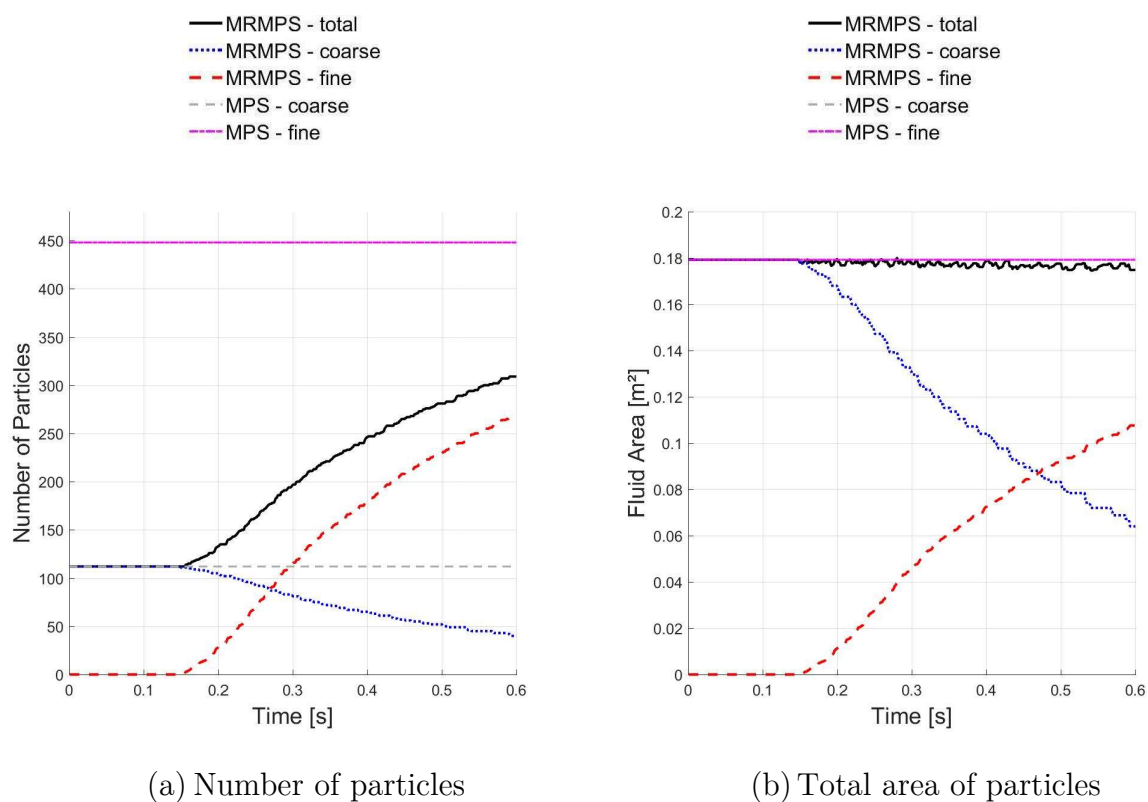


Source: figure from the author.

The quantitative analysis of the mass conservation is provided by Figure 5.35, which presents the time series of the number of particles and the time series of the total area of the particles, which is proportional to the mass in the case of the two-dimensional simulation. Only the fluid particles were considered.

In Figure 5.35-a, the multi-resolution simulation has the same number of particles as the single-resolution/low-resolution simulation until it reaches the border. Then, the number of high-resolution particles increase at a rate four times the decrease rate of the number of low-resolution particles. In Figure 5.35-b, the mass is well conserved in the multi-resolution simulation, as the decrease rate of the mass of low-resolution particles is equal to the increase rate of high-resolution particles.

Figure 5.35 – Time series of (a) the number and (b) the total area of the particles of each resolution – Dam Break case

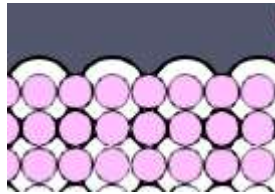


Source: figure from the author.

The very small mass loss in the multi-resolution simulation is attributed to the refinement process of the free surface region. As in our approach the height of the free

surface is considered at the center of the particles, it is equivalent in both low-resolution and high-resolution. However, an additional area of half the particle area is accounted above its center for each free surface particle in Figure 5.35-b and this additional is larger for low-resolution particles. This issue is portrayed by Figure 5.36.

Figure 5.36 – Refinement at the free-surface

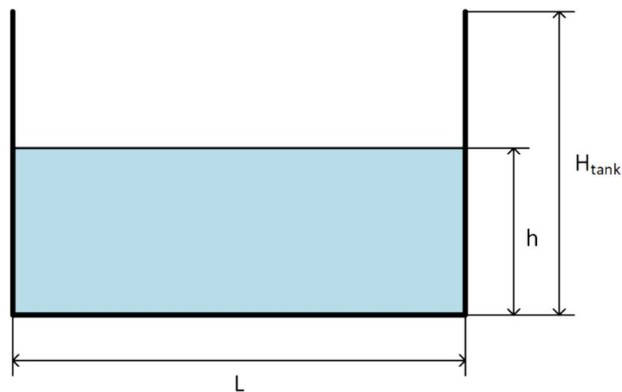


Source: figure from the author.

5.6.6 Processing time

For the analysis of processing time, the case of still water in a rectangular tank is adopted. The configuration and main dimensions of the case are shown by Figure 5.37, where $L = 120$ m, $h = 8$ m and $H_{tank} = 10$ m.

Figure 5.37 – Dimensions of the still water rectangular tank

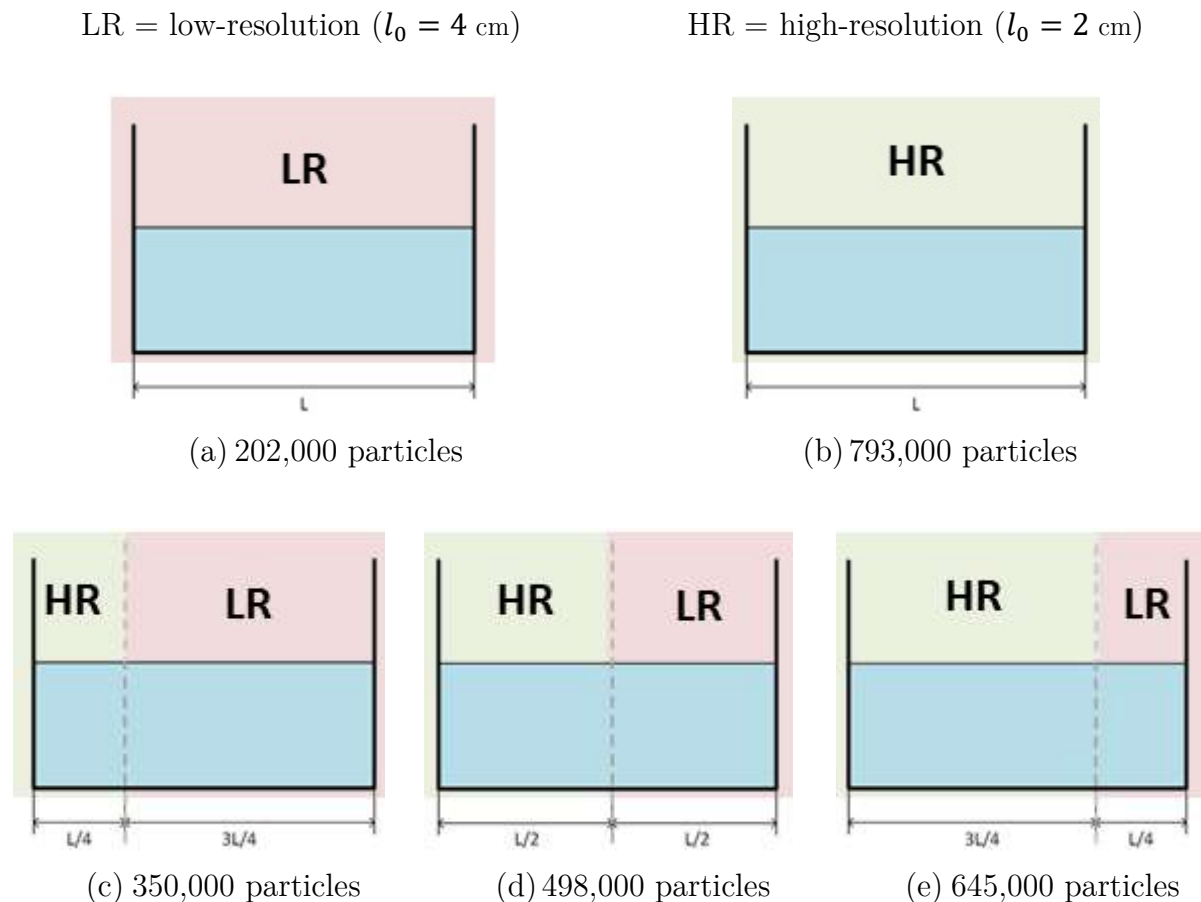


Source: figure from the author.

In order to evaluate the performance of the multi-resolution scheme, five different cases were simulated. For this investigation, the low-resolution is defined as $l_0 = 4$ cm and the high-resolution is defined as $l_0 = 2$ cm. Two of these cases were simulated with the entire computational domain modeled in a single resolution, one

with low-resolution (Figure 5.38-a) and the other with high-resolution (Figure 5.38-b). The other three cases (Figure 5.38-c,d,e) were simulated with the multi-resolution technique, each one was modeled with a gradually larger portion of the domain with high-resolution particles. The division of the computational domain was defined in order to have a border with the same perimeter for the three cases, so that the time spent in the refinement and simplification algorithms is the same for the three cases. In Figure 5.38 the total number of particles of each model is presented as well.

Figure 5.38 – Division of the computational domain – still water rectangular tank

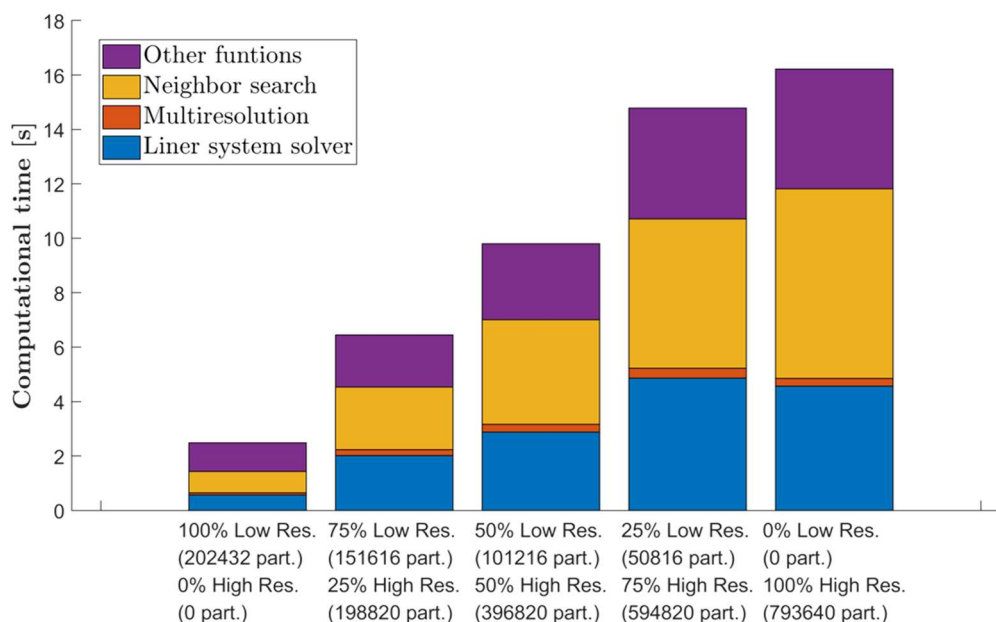


Source: figure from the author.

Figure 5.39 presents a bar graph with the average processing time for the five cases, with the portions of the processing time related to the multiresolution (simplification/refinement), the neighbor search and the solution of the linear system

highlighted. One important aspect to consider is that the numerical solver for the linear system of the PPE is different between the single-resolution simulations and the multi-resolution simulations. As the matrix of coefficients of the single-resolution simulation is diagonal and symmetrical, the Conjugate Gradient (CG) method could be adopted. Otherwise, as previously shown by Figure 5.31, the matrix of coefficients of the multi-resolution simulation is not strictly diagonal neither symmetrical. So, the CG solver could not be used and a Generalized Minimal Residual (GMRES) solver was adopted instead. For matrices of same size, the CG solver is approximately twice faster than the GMRES solver. Hence, there is a tradeoff between the decrease in the processing time as the number of particles of the model decrease but there is the need to adopt a slower numerical solver.

Figure 5.39 – Processing time for the still water rectangular tank in multi-resolution simulation



Source: figure from the author.

The results from Figure 5.39 show that the total processing time could be substantially reduced by adopting the multi-resolution simulation. Besides, despite the algorithms adopted for the simplification and the refinement not being yet optimized,

they account for a minimal portion of the total processing time. As mentioned in the introduction, the neighbor search and the solution of the PPE linear system account for the major portion of the processing time. As expected, the processing time required for the neighbor search steadily increased as the total number of particles increased. The two bars in the right of Figure 5.39 show that the time spent to solve the PPE was longer for the multi-resolution case with 645,000 particles than the single-resolution case with 798,000 particles. Summarizing, the multi-resolution technique could be an effective technique in order to reduce the computational cost of the MPS simulations.

5.7 CONCLUSION

A novel multi-resolution technique named “border-mapping” was proposed in the present study for the MPS method with the aim to reduce the computational cost of the particle-based simulations. The border-mapping technique achieves equivalent low-resolution and high-resolution particle distributions in the truncated border between sub-domains of different resolutions in a way that the original formulation of MPS method could be adopted. To obtain such equivalent particle distributions, refinement and simplification algorithms able to deal with irregular particle distributions were proposed. The border-mapping technique provides a strong-form, two-way coupling between the subdomains of different resolutions. Besides, the simplification/refinement algorithms maintain the resolution of the particles of the different sub-domains during the entire simulation. As these techniques obtain the equivalent particle distributions based on the original particle distributions at the border, they avoid abrupt changes in the particle distribution and are expected to provide better pressure estimation there.

In the present work, the irregular distribution of particles in the MPS method was investigated. Its results were adopted as input to develop the simplification and refinement algorithms. These algorithms were qualitatively verified at first, as both provided consistent particle distributions and the particle number density at the border was calculated properly for the test cases. Different test cases were simulated for the verification of the pressure calculation at the border and the mass conservation of the technique. Finally, the performance of the multi-resolution technique to reduce the processing time was assessed. The last results obtained still demand further improvement, debugging and development, as some numerical instabilities were observed. Notwithstanding, the results were very promising.

As next steps and future works, the border-mapping technique is suitable for any projection-based particle method, so it could be adopted for the Incompressible Smoothed Particle Hydrodynamics (ISPH) or the Consistent Particle Method (CPM)

as well. Moreover, the various improvements to the MPS method, such as high-order numerical operators, could be adopted to further enhance the stability of the simulation system. Furthermore, some aspects of the present proposal could be combined with other aspects from previously proposed multi-resolution techniques. As an example, the refinement/simplification could be adopted only to update the particles in the sub-domain while the pressure is calculated based on a particle interaction model able to deal with particles of different resolution, and so on. Finally and more important, the border-mapping technique should be developed for the three-dimensional formulation, which will be substantially more challenging regarding the simplification/refinement algorithms.

6 CHAPTER SIX: CONCLUSION

6.1 CONCLUDING REMARKS

The present thesis was focused on the development and the application of a MPS-based simulation system to the investigation of nonlinear hydrodynamic phenomena in naval and offshore engineering. In such context, three different studies were carried out. In the present section, the main contributions of each study are briefly outlined.

The first study of the present work was the **investigation of the sloshing suppression by perforated swash bulkheads**. The work could be divided in two main parts. The first part consisted on a fundamental investigation of the effect the geometrical parameters of the perforated bulkheads in the sloshing mitigation. The main conclusions of this part are:

- 1) The MPS was successfully validated for the sloshing in tanks with perforated swash bulkheads,
- 2) Perforated swash bulkheads with higher open-area ratio presented better mitigation for the sloshing first non-compartmented mode,
- 3) Perforated swash bulkheads with lower open-area ratio presented better mitigation for the sloshing first compartmented mode,
- 4) As the open-area ratio of the perforated bulkhead increases, the natural frequency of the sloshing first and second resonant modes gradually shifts,
- 5) Since the open-area ratio remains similar, the geometry of the holes and its arrangement had little effect on sloshing,
- 6) The perforated bulkhead strongly affects the added mass of the system, by the blockage of the flow mid-tank. The major contributions to the

damping are related to the free surface nonlinearities. The damping from viscous friction and vortex formation were considered very small contributions.

The second part of this study was focused on the development of technological solution which is the proposal of an optimized perforated bulkhead for sloshing mitigation in different filling levels. The main conclusions of this part are:

- 1) Given the tradeoff in the first and the second resonant mode related to the open-area ratio, there is an optimized open-area ratio that provides the best overall sloshing mitigation,
- 2) A relation for the optimized open-area ratio as function of the filling ratio was obtained,
- 3) Three models of perforated bulkhead with optimized geometry were proposed and its effectiveness for sloshing mitigation were confirmed.

The second study of the present thesis was the **investigation of the resonance of fluid trapped within narrow gaps between two structures**. This work is another fundamental investigation of a complex phenomenon carried out by taking advantage of the flexibility of MPS method. This analysis was focused in a two-dimensional simplified layout of the problem with a relatively low fluid depth. The main conclusions of this study are:

- 1) The MPS method was successfully validated for the gap resonance,
- 2) Two different types of resonant modes were observed in the simulations,
 - a. The piston-type resonance and
 - b. The sloshing-type resonance.
- 3) The piston-type resonant flow presented strong non-linear behavior,

- 4) Two peaks were observed in the frequency domain for the piston-type resonant flow,
- 5) These two peaks were explained by analogies to two simple mechanical models,
 - a. The first peak resembles a mechanical system containing only the fluid trapped in the gap, with minimal interaction with the fluid on the other side of hull,
 - b. The second peak resembles a U-tube flow, in which the fluid in the narrow gap strongly interacts with the fluid on the other side of hull,
- 6) The first two sloshing resonant modes were observed,
- 7) As the amplitude of the motion increases, the natural period of the sloshing resonant modes slightly shifts to a longer period.

At last, the third study of the present thesis comprises the **development of a multi-resolution technique for the MPS method**, named border-mapping technique. The technique was initially proposed for the two-dimensional case. It adopts a different paradigm in relation to the previously proposed techniques found in the literature. The border-mapping technique adopts a refinement and a simplification algorithms in order to obtain equivalent particle distribution on the border between sub-domains of different resolution. As the main results of this technique:

- 1) The proposed technique is a strong-form, two-way coupling,
- 2) The resolution of the sub-domains is kept during the entire simulation,
- 3) As equivalent particle distributions are obtained from the existing particle distributions, abrupt changes in the particle distribution in the border region are avoided,

- 4) The original particle interaction model of the MPS method could be adopted,
- 5) A simplification algorithm for the high-resolution particle distribution was proposed and a consistent equivalent low-resolution particle distribution was obtained,
- 6) A refinement algorithm for the low-resolution particle distribution was proposed and a consistent high-resolution particle distribution was obtained,
- 7) The pressure was adequately calculated at the border between sub-domains by the technique,
- 8) The mass conservation of the technique was verified by a Dam-Break case,
- 9) The proposed multi-resolution technique successfully reduced the processing time.

6.2 FURTHER WORK AND PROPOSED IMPROVEMENTS

In this section, the next steps and the prospect of further investigations related to three topics of the present Thesis are briefly outlined.

In the investigation of sloshing mitigation in the tanks with perforated swash bulkheads, future works could be:

- 1) As the present work was focused on bulkhead geometries with the holes homogeneously distributed, the open-area ratio was almost constant along the depth. So, the effect of different open-area ratios along the vertical direction of the bulkhead by non-homogeneous open-area distribution is an interesting aspect that might be investigated.
- 2) The analysis carried out herein was focused only in the case of a perforated swash bulkhead placed mid-tank, in a symmetrical layout. Cases with the perforated bulkhead placed in a different position, which results in two compartments with different length, could be studied.
- 3) The present study was focused on the mitigation of the sloshing loads in order to protect the tank inner structures. For naval and offshore practical cases, the sloshing also affects the motion of the floating structures. Thus, the investigation of the coupled effect of the vessel motions due to waves and the loads due to sloshing on tanks equipped with optimized perforated bulkheads could also be investigated,

In the **investigation of the resonant flow in the gap between two structures**, the next steps might be to:

- 1) Investigate the effect of the tank depth to the two peaks of the piston-resonant mode, as only a tank with small depth was investigated,
- 2) Propose an experimental setup in order to confirm the two types of piston-mode resonance observed in the numerical results,
- 3) Investigate the effect of the hull shape to the piston-resonant mode,
- 4) Introduce gradually more complex aspects to the simplified two-dimensional setup, such as floating bodies instead of the imposed motion and so on.
- 5) Study the phenomenon in three-dimensional simulations.

In the **development of the border-mapping multi-resolution technique for the MPS method**, further works could be:

- 1) To improve the stability of the multi-resolution simulation system,
- 2) As the current version is based on the original formulation of the MPS method, additional improvements of the MPS method could be introduced,
- 3) Some aspects of the current multi-resolution technique could be combined with other multi-resolution techniques. As an example, the simplification/refinement algorithms could be used to keep the resolution of the sub-domains while a particle interaction model that deals with particles of different sizes is adopted to model the differential operator and calculate the pressure.
- 4) At last and more important, the next step of this study is the development of a multi-resolution technique based on the border-mapping scheme for the three-dimensional formulation.

7 REFERENCES

AALBERS, A. B. (1984). **The water motions in a moonpool.** Ocean Engineering, Vol. 11, n. 3, pp. 557-579.

AGÊNCIA NACIONAL DE PETRÓLEO (ANP) (NATIONAL AGENCY OF PETROLEUM/BRAZIL) (2018). **Opportunities in the brazilian oil & gas industry: ongoing actions & 2018-2019 upcoming bidding rounds.**

AKITA, Y. (1967). **Dynamic pressure of cargo oil due to pitching and effectiveness of swash bulkhead in long tanks.** Japan Shipbuilding and Marine Engineering, v. 2, pp. 42-55.

AMARO JUNIOR, R., CHENG, L.-Y., & NISHIMOTO, K. (2015). **The influence of geometrical parameters on the performance of perforated breakwater.** Proceedings of the 1st Pan-American Congress on Computational Mechanics (PANACM-2015). Buenos Aires, Argentina.

ARAI, J., KOSHIZUKA, S., & MUROZONO, K. (2013). **Large eddy simulation and a simple wall model for turbulent flow calculation by a particle model.** International Journal for Numerical Methods in Fluids, 71, 772-787.

BELLEZI, C. A., & CHENG, L.-Y. (2011). **Analysis of wave-in-deck impact on offshore platforms by Moving Particles Semi-Implicit (MPS) method (in portuguese) (Análise do impacto de onda no convés inferior de plataforma offshore por método Moving Particles Semi-Implicit (MPS)).** Proceedings of the 32nd Ibero Latin-American Congress on Computational Methods in Engineering. Ouro Preto, Brazil.

BELLEZI, C. A., CHENG, L.-Y., & NISHIMOTO, K. (2013). **Particle based numerical analysis of green water on FPSO deck**. Proceedings of the ASME 2013 32nd International Conference on Ocean, Offshore and Arctic Engineering - OMAE-2013. Nantes, France.

BELLEZI, C. A., FERNANDES, D. T., CHENG, L.-Y., TSUKAMOTO, M. M., & NISHIMOTO, K. (2015). **Investigation of green water in FPSO by a particle based numerical offshore tank**. Proceedings of the IV International Conference on Particle-based Methods: Fundamental and Applications. Barcelona, Spain.

BELLEZI, C. A., MARCUS, F. A., LIANG-YEE, C., & NISHIMOTO, K. (2009). **Analysis of nonlinear hydrodynamics by MPS method: smoothing of the pressure oscillations (in portuguese)(Análise de Hidrodinâmica Não-linear por Método MPS: Suavização da Flutuação de Pressão)**. 30^o Iberian-Latin-American Congress on Computational Methods in Engineering.

BELLEZI, C. A., MENDES, S. B., & CHENG, L.-Y. (2011a). **Study of the slamming in wedges, cylinders and parabolas by Moving Particles Semi-Implicit (MPS) method (in portuguese)(Estudo do Slamming em cunha em V, cilindro e parábola por método Moving Particles Semi-Implicit (MPS))**. Proceedings of the 32nd Ibero-Latin American Congress on Computational Methods in Engineering (CILAMCE 2011). Ouro Preto, Brazil.

BELLEZI, C. A., CHENG, L.-Y., OKADA, T., ARAI, M. (2019). **Optimized perforated bulkhead for sloshing mitigation and control**. Ocean Engineering, 187.

BOGAERT, H., BROSSET, L., & KAMINSKI, L. M. (2010). **Interaction between wave impacts and corrugations of MarkIII containment system for LNG carrier: findings from the SlosheI project**. Proceedings of the Twentieth

International Offshore and Polar Engineering Conference (ISOPE 2010), (pp. 109-118). Shanghai, China.

CHEN, X., SUN, Z.-G., LIU, L., & XI, G. (2015). **Improved MPS method with variable-size particles**. International Journal for Numerical Methods in Fluids.

CHEN, X., WAN, D., & HUANG, W. (2016). **Numerical simulations of effects of two different baffles on liquid sloshing by MPS method**. Proceedings of the Twenty-sixth International Ocean and Polar Engineering Conference - ISOPE 2016, (pp. 931-938). Rhodes, Greece.

CHENG, L.-Y., & ARAI, M. (2002). **A Numerical treatment of the boundary conditions for stable assessment of hydrodynamic impact pressure**. OMAE2002.

CHENG, L.-Y., AMARO JUNIOR, R. A., & BELLEZI, C. A. (2018). **Wave impact loads by MPS method with an improved pressure source term**. In J. S. (JASNAOE) (Ed.), Proceedings of the 2018 Autumn Meeting of the Japan Society of Naval Architects and Ocean Engineers, (pp. 17-21). Chiba, Japan.

CHENG, L.-Y., AMARO JUNIOR, R. A., MELLO, P. C., BELLEZI, C. A., & NISHIMOTO, K. (2015). **Numerical-experimental analysis of sloshing phenomenon in prismatic tanks (in portuguese) (Análise numérico-experimental do fenômeno de sloshing em tanque prismático)**. Proceedings of the XXXVI Ibero Latin-American Congress on Computational Methods in Engineering (CILAMCE-2105). Rio de Janeiro, Brazil.

CHENG, L.-Y., BELLEZI, C., AMARO JUNIOR, R., ARAI, M., & OKADA, T. (2016). **A numerical study on the effects of the perforated swash bulkheads on sloshing behaviors of liquid cargo tanks**. The Proceedings of the 26th

International Ocean and Polar Engineering Conference (ISOPE-12016), (pp. 923-930). Rhodes, Greece.

CHORIN, A. J. (1967). **The numerical solution of the Navier-Stokes equations for an incompressible fluid.** Bulletin of the American Mathematical Society, 73(6), pp. 928-931.

DEAN, R. G., & DALRYMPLE, R. A. (1991). **Water Wave Mechanics for Engineers and Scientists** (1st ed.). World Scientific Publication.

EXXONMOBIL. (2018). **2018 Outlook for Energy: A view to 2040.**

FALTINSEN, O. M., & TIMOKHA, A. N. (2009). **Sloshing.** Cambridge University Press.

FALTINSEN, O. M., FIROOZKOOHI, R., & TIMOKHA, A. N. (2011a). **Analytical modelling of liquid sloshing in a two-dimensional rectangular tank with a slat screen.** Journal of Engineering Mathematics, v. 70, pp. 63-109.

FALTINSEN, O. M., FIROOZKOOHI, R., & TIMOKHA, A. N. (2011b). **Steady state sloshing in a rectangular tank with a slat-type screen in the middle: quasi-linear modal analysis and experiments.** Physics of Fluids, v. 23, p. 19 pages.

FALTINSEN, O. M., ROGNEBAKKE, O. F., & TIMOKHA, A. N. (2007). **Two-dimensional resonant piston-like sloshing in a moonpool.** Journal of Fluid Mechanics, 575, 359-397.

FENG, X., & BAI, W. (2015). **Wave resonances in a narrow gap between two barges using fully nonlinear numerical simulation.** Applied Ocean Research, Vol. 50, pp. 119-129.

FENG, X., & BAI, W. (2015). **Wave resonances in a narrow gap between two barges using fully nonlinear numerical simulations**. *Applied Ocean Research*, 50, 119-129.

FERNANDES, D. T., CHENG, L.-Y., FAVERO, E., & NISHIMOTO, K. (2015). **A domain decomposition strategy for hybrid parallelization of moving particles semi-implicit (MPS) method for computer cluster**. *Cluster Computing*, 18 (4), pp. 1363-1377.

FIROOZKOOHI, R. (2013). **Experimental, numerical and analytical investigation of the effect of swash bulkheads on sloshing**. Norwegian University of Science and Technology. Trondheim, Norway: Doctoral thesis.

FIROOZKOOHI, R., & FALTINSEN, O. M. (2010). **Experimental and numerical investigation of the effect of swash bulkhead on sloshing**. *Proceedings of the Twentieth International Ocean and Polar Engineering Conference - ISOPE2010*, (pp. 252-259). Beijing, China.

FIROOZKOOHI, R., FALTINSEN, O. M., & ARSLAN, T. (2015). **Investigation of finite water depth sloshing in a tank in presence of slat screens using model tests and CFD**. *Proceedings of the twenty-fifth International Ocean and Polar Engineering Conference - ISOPE2015*, (pp. 924-930). Kona, Hawaii, USA.

FONFACH, J. M., MANDERBACKA, T., & NEVES, M. A. (2016). **Numerical Sloshing Simulations: Comparison Between Lagrangian and Lumped Mass Models Applied to Two Compartments with Mass Transfer**. *Ocean Engineering*, 114, pp. 168-184.

GINGOLD, R. A. & MONAGHAN, J. J. (1977). **Smoothed particle hydrodynamics: theory and application to non-spherical stars.** Monthly Notices of the Royal Astronomical Society, 181, pp.375-389.

HUIJSMANS, R. H., PINKSTER, J. A., & DE WILDE, J. A. (2001). **Diffraction and radiation of waves around side-by-side moored vessels.** Proceedings of the 4th International Ocean Offshore and Polar Engineering Conference (ISOPE 2001). Oslo, Norway.

INTERNATIONAL TOWING TANK CONFERENCE (ITTC). (2017). **Recommended Procedures and Guidelines: Sloshing Model Tests (7.5-02-07-02.7).**

ISSHIKI, H. (2011). **Discrete differential operators on irregular nodes (DDIN).** International Journal for Numerical Methods in Engineering, 88:12, pp. 1323-1343.

KANEKO, S., & ISHIKAWA, M. (1999). **Modeling of Tuned Liquid Damper with Submerged Nets.** Journal of Pressure Vessels and Control, 121, pp. 334-343.

KARIMI, M. R., BROSSET, L., GHIDAGLIA, J. M., & KAMINSKI, M. L. (2014). **A study on the conservatism of Froude scaling for sloshing model tests.** Proceedings of the 24th International Ocean and Polar Engineering Conference (ISOPE 2014), 3, pp. 303-306. Busan, South Korea.

KENDON, T. E., PAKOSDY, C., BAARHOLM, R., BERTHELSEN, P. A., STANSBERG, C., & ENGER, S. (2010). **Wave-in-deck impact: comparing CFD, simple methods and model tests.** Proceedings of the ASME 29th International Conference on Ocean, Offshore and Arctic Engineering (OMAE 2010). Shanghai, China: American Society of Mechanical Engineers (ASME).

KLEEFSMAN, T. K., LOOTS, E. G., VELDMAN, A. E., BUCHNER, B., BUNNIK, T., & FALKENBERG, E. (2005). **The numerical simulation of green water loading including vessel motions and the incoming wave field**. Proceedings of the ASME 24th International Conference on Offshore Mechanics and Arctic Engineering (OMAE 2005). Halkidiki, Greece: American Society of Mechanical Engineers.

KOSHIZUKA, S., & OKA, Y. (1996). **Moving particles semi-implicit method for fragmentation of incompressible fluid**. Nuclear Science and Engineering, 123, 421-434.

KOSHIZUKA, S., NOBE, A., & OKA, Y. (1998). **Numerical analysis of breaking waves using the Moving Particles Semi-Implicit method**. International Journal for Numerical Methods in Fluids, 26, pp. 751-769.

KOSHIZUKA, S., TAMAKO., H., & OKA, Y. (1995). **A Particle Method for Incompressible Viscous Flow with Fluid Fragmentation**. Journal of Computational Fluid Dynamics, pp. 29-46.

KRISTIANSEN, T., & FALTINSEN, O. M. (2010). **A two-dimensional numerical and experimental study of resonant coupled ship and piston-mode motion**. Applied Ocean Research, 32, 158-176.

LAWS, E. M., & LIVESEY, L. J. (1978). **Flow through screens**. Annual Review of Fluid Mechanics, 6, pp. 33-50.

LEE, B. H., PARK, J. C., KIM, M. H., & HWANG, S. C. (2011). **Step-by-step improvement of MPS method in simulating violent free surface motions and impact-loads**. Computer Methods in Applied Mechanics and Engineering, 200, 1113-1125.

LEE, B.-H., PARK, J.-C., & KIM, M. (2010). **Two-dimensional vessel-motion/liquid-sloshing interactions and impact loadings by using a particle method**. Proceedings of the ASME 2010 29th International Conference on Ocean, Offshore and Arctic Engineering - OMAE2010. Shanghai, China.

LEE, H.-H., LIM, H.-J., & RHEE, S. H. (2012). **Experimental Investigation of Green Water on Deck for a CFD Validation Database**. Ocean Engineering, 42, p. 47-60.

LLOYD'S REGISTER. (2012). **Guidance on the operation of membrane LNG ships to reduce the risk of damage due to sloshing**. Lloyd's Register.

LOVE, J. S., & TAIT, M. J. (2010). **Nonlinear simulation of a tuned liquid damper with damping screens using a modal expansion technique**. Journal of Fluid and Structures, 26, pp. 1058-1077.

MAISONDIEU, C., MOLIN, B., KIMMOUN, O., & GENTAZ, L. (2001). **Simulation bidimensionnelle des écoulements dans une baie de forage: Etude des modes de la résonance et des amortissements (2D flow simulation in a moonpool: Natural modes and damping evaluation)**. Actes des Huitièmes Journées de l'Hydrodynamique, (pp. 251-264). Nantes.

MARAVANI, M., & HAMED, M. S. (2010). **Numerical modeling of sloshing motion in a tuned liquid damper outfitted with a submerged slat screen**. International Journal for Numerical Methods in Engineering, v. 65, pp. 834-855.

MIYAGI, C. H. (2003). **Development of an experimental apparatus for the investigation of two-dimensional hydrodynamic impact (in portuguese) (Desenvolvimento de um aparato experimental para o estudo do impacto**

hidrodinâmico bidimensional). São Paulo: Doctorate Thesis, University of São Paulo.

MOLIN, B. (2001). **On the piston and sloshing modes in moonpools**. Journal of Fluid Mechanics, 430, 27-50.

MOLIN, B., & REMY, F. (2013). **Experimental and numerical study of the sloshing motion in a rectangular tank with a perforated screen**. Journal of Fluids and Structures, 43, pp. 463-480.

MOLIN, B., REMY, F., CAMHI, A., & LEDOUX, A. (2009). **Experimental and numerical study of the gap resonances in-between two rectangular barges**. Proceedings of the 13th International Congress of International Maritime Association of Meiterranean (IMAM 2009). Istanbul, Turkey.

MOLIN, B., REMY, F., KIMMOUN, O., & STASSEN, Y. (2002). **Experimental study of the wave propagation and decay in a channel through a rigid ice-sheet**. Applied Ocean Research, Vol. 24, pp. 247-260.

MONAGHAN, J. J., & GINGOLD, R. (1983). **Shock Simulation by the Particle Method SPH**. Journal of computational Physics, pp. 374-389.

NATIONAL AGENCY OF PETROLEUM, NATURAL GAS AND BIOFUELS (ANP). (2018). **Opportunities in the Brazilian Oil and Gas Industry: Ongoing Actions and 2018-2019 Upcoming Bidding Rounds**.

NEWMAN, J. N., & SCLAVOUNOS, P. D. (1988). **The computation of wave loads on large offshore structures**. Proceedings of the International Conference on Behavior of Offshore Structures (BOSS). Trondheim, Norway.

SAWAYANAGI, M., & MATSUMOTO, Y. (1977a). **Experimental study on the sloshing pressure of rectangular tanks - Report 1 (in japanese)**. Mitsui Technical Review, v. 98, pp. 32-46.

SAWAYANAGI, M., & MATSUMOTO, Y. (1977b). **Experimental study on the sloshing pressure of rectangular tanks - Report 2 (in japanese)**. Mitsui Technical Review, v. 99, pp. 1-16.

SAWAYANAGI, M., & MATSUMOTO, Y. (1978). **Experimental on the sloshing pressure of rectangular tanks - Report 3 (in japanese)**. Mitsui Technical Review, v. 101, pp. 1-19.

SHIBATA, K., KOSHIZUKA, S., & TAMAI, T. (2012). **Overlapping particle technique and application to green water on deck**. Proceedings of 2nd International Conference on Violent Flows . Nantes, France.

SHIBATA, K., KOSHIZUKA, S., MATSUNAGA, T., & MASAIE, I. (2017). **The overlapping particle technique for multi-resolution simulation of particle methods**. Computer Methods in Applied Mechanics and Engineering, 325, pp. 434-462.

SHIBATA, K., KOSHIZUKA, S., SAKAI, M., & TANIZAWA, K. (2012). **Lagrangian Simulations of Ship-Wave Interactions in Rough Seas**. Ocean Engineering.

SOUTO-IGLESIAS, A., DELORME, L., PÉREZ-ROJAS, L., & ABRIL-PÉREZ, S. (2006). **Liquid moment amplitude assesment in sloshing type problems with smoothed particles hydrodynamics**. Ocean Engineering, 33, pp. 1462-1484.

SOUTO-IGLESIAS, A., PÉREZ-ROJAS, L., & ZAMORA RODRÍGUEZ, R. (2004). **Simulation of anti-roll tanks and sloshing type problems with smoothed particle hydrodynamics**. Ocean Engineering, 31, pp. 1169-1192.

- SUEYOSHI, M., & NAITO, S. (2002). **A Numerical Study of Very Large Motion of Floating Body by Particle Method**. Asia and Pacific Maritime Congress. Kobe, Japan: Asia and Pacific Workshop on Marine Hydrodynamics.
- TAIT, M. J., EL DAMATTY, A. A., ISYUMOV, N., & SIDDIQUE, M. R. (2005). **Numerical flow models to simulate tuned liquid dampers (TLD) with slat screens**. Journal of Fluids and Structures, 20, pp. 1007-1023.
- TAIT, M. J., ISYUMOV, N., & EL DAMATTY, A. A. (2008). **Performance of Tuned Liquid Dampers**. Journal of Engineering Mechanics, 134 (5), pp. 417-427.
- TAMAI, T., & KOSHIZUKA, S. (2014). **Least squares moving particle semi-implicit method**. Computational Particle Mechanics, 1(3), pp. 277-305.
- TANAKA, M., & MASUNAGA, T. (2010). **Stabilization and smoothing of pressure in MPS method by Quasi-Compressibility**. Journal of Computational Physics, 229 (11), pp. 4279-4290.
- TANAKA, M., CARDOSO, R., & BAHAI, H. (2018). **Multi-resolution MPS method**. Journal of Computational Physics, 359, pp. 106-136.
- TANAKA, M., MASUNAGA, T., & NAKAGAWA, Y. (2009). **Multi-resolution MPS Method (injapanese)**. Transactions of the Japanese Society of Computational Engineering and Science (JSCES).
- TANG, Z. Y., ZHANG, Y. X., LI, H. Z., & WAN, D. C. (2014). **Overlapping MPS method for 2D free surface flows**. Proceedings of the 24th International Ocean Offshore and Polar Engineering Conference - ISOPE 2014. Busan, South Korea.

TKACHENKO, O. Y., KAZACHKOV, A. R., LYKAH, V. A., MINAKOVA, K. A., & SYRKIN, E. S. (2015). **Dynamics of oscillation processes in siphon U-tubes.** Bulletin of Kharkiv National University: series of physics, 23, pp. 84-90.

TSUKAMOTO, M. M. (2006). **Development of particle method representing floating bodies with highly non-linear waves (in portuguese)(Desenvolvimento de método de partículas na representação de corpos flutuantes em ondas altamente não-lineares).** Master Thesis, University of São Paulo.

TSUKAMOTO, M. M. (2011). **Analytical modeling and numerical simulation of a moving sloshing suppression device (in portuguese)(Modelagem analítica e simulação numérica de um sistema móvel de supressão de sloshing).** Doctorate thesis, University of São Paulo.

TSUKAMOTO, M. M., CHENG, L.-Y., & MOTEZUKI, F. K. (2016). **Fluid interface detection technique based on neighborhood particles centroid deviation (NPCD) for particle methods.** International Journal for Numerical Methods in Fluids.

TSUKAMOTO, M. M., CHENG, L.-Y., & NISHIMOTO, K. (2011). **Analytical and numerical study of the effects of an elastically-linked body on sloshing.** Computer & Fluids, 49, 1-21.

TSURUTA, N., GOTOH, H., & KHAYYER, A. (2016). **A novel refinement technique for projection-based particle methods.** Proceedings of the 11th International SPHERIC Workshop, (pp. 402-410). Munich, Germany.

TSURUTA, N., KHAYYER, A., & GOTOH, H. (2015). **Space potential particles to enhance the stability of projection-based particle methods.** International Journal of Computational Fluid Dynamics, 29:1, pp. 100-119.

VEEN, D., & GOURLAY, T. (2012). **A combined strip theory and Smoothed Particles Hydrodynamics approach for estimating slamming loads on a ship in head seas.** Ocean Engineering, 43, pp. 64-71.

WANG, L., JIANG, Q., & ZHANG, C. (2017). **Improvement of moving particle semi-implicit method for simulation of progressive water waves.** International Journal for Numerical Methods in Fluids, 85, pp. 69-89.

XUE, M.-A., LIN, P.-Z., ZHENG, J.-H., MA , Y.-X., YUAN, X.-L., & NGUYEN, V.-T. (2013). **Effects of perforated baffle on reducing sloshing in rectangular tank: experimental and numerical analysis.** China Ocean Engineering, 27, pp. 615-628.

XUE, M.-A., ZHENG, J., LIN, P., & YUAN, X. (2017). **Experimental study on vertical baffles of different configurations in suppressing sloshing pressure.** Ocean Engineering, 136, pp. 178-189.

YU, L., XUE, M.-A., & ZHENG, J. (2019). **Experimental study of vertical slat-screens effects on reducing shallow water sloshing in a tank under horizontal excitation with a wide range of frequency.** Ocean Engineering, 173, pp. 131-141.

